Fluid Mechanics of Blood Motion Resulting from Common Bloodletting Events

by

Patrick M. Comiskey
B.S., Milwaukee School of Engineering, 2014

Thesis submitted in partial fulfillment of the requirements
for the degree of Doctor of Philosophy in Mechanical Engineering
in the Graduate College of the
University of Illinois at Chicago, 2019

Chicago, Illinois

Defense Committee:

Alexander L. Yarin,	Chair and Advisor
Kenneth Brezinsky,	Mechanical and Industrial Engineering, UIC
Kumar Natesaiyer,	United States Gypsum Corporation
Roberto Paoli,	Mechanical and Industrial Engineering, UIC
Suman Sinha–Ray,	Mechanical and Industrial Engineering, UIC

This thesis is dedicated to my grandfather, Ronald W. Hlavacek, for his loving guidance,

my late father, James G. Comiskey, for teaching me the value of hard work,

my mother, Cynthia S. Comiskey, for her unwavering love and support,

and my fiancée, Heather R. Payette, for making it all worth it.

ACKNOWLEDGMENTS

When I was young, my grandfather gifted me a set of architectural drawing stencils which fostered a love for design and creation further than I ever thought possible. This passion slowly morphed into mechanical engineering through excursions that he took me on such as annual trips to the Chicago Auto Show and visits to the Volo Auto Museum. I am forever grateful for the loving support that my grandfather gave me and I will always treasure that original set of drawing stencils.

I would like to thank my mother and late father for raising me with the love and support which allowed me to follow my dreams. They were invariably willing to help me in any way possible and I will always remember their generosity. I wish that my father would have been able to see me graduate with my Ph.D. degree, but I am comforted in knowing that he was always proud of me, no matter what I had accomplished. My brothers Bryan and Sean provided continuous support and encouragement, and I am grateful to have them both. Life isn't straightforward, and frivolous things have severed their good relationship, but I hold out for the day that all will be reconciled.

Without the support of my fiancée, I would not have made it this far. She is astonishingly patient and has deferred many of her dreams so that I could pursue higher education. Her compassion, drive, and wit, are inspiring and gave me the ability to complete this thesis. I am lucky to say that one day I will be her husband.

ACKNOWLEDGMENTS (Continued)

I would also like to acknowledge my thesis advisor, Distinguished Professor Alexander L. Yarin. His immense depth of knowledge and phenomenal teaching allowed me to grow to a level I would have otherwise not been able to. His abilities as a scientist are second to none and I will forever treasure his stories surrounding the fascinating life that he has led. I am honored to have been one of his doctoral students.

The support and friendship of my lab mates has been invaluable and I will always cherish the camaraderie we had. I want to especially thank Christopher Staszel and Abhilash Sankaran with whom I spent many long days and nights working on homework and troubleshooting research issues with. My Ph.D. would not have been possible without their friendship. I want to also thank all of my life–long friends and close family, as they gave me the ability to forget work for a moment every so often. I want to thank all of the staff and doctors at Ann & Robert H. Lurie Children's Hospital of Chicago, especially Dr. Elfriede Pahl, Dr. R. Andrew de Freitas, and the incredible surgical team, for giving me a chance in life. Finally, I want to thank Dr. Les Inch for keeping me on track.

Without the above individuals, this work would not have been possible.

PMC

Portions of this thesis have been published previously in peer–reviewed journals. Sections 2.1, and 3.1, as well as Chapter 4 were published in Reference [1], reprinted by permission from Springer Nature [Blood rheology in shear and uniaxial elongation. Kolbasov, A., Comiskey, P. M., Sahu, R. P., Sinha–Ray, S., Yarin, A. L., Sikarwar, B. S., Kim, S., Jubery, T. Z., and Attinger, D., Rheologica Acta 55, 901–908]. Copyright (2016) Springer Nature. Sections 2.2, and 2.3, along with parts of Chapter 6 were published in Reference [2], reprinted with permission from [Comiskey, P. M., Yarin, A. L., Kim, S., and Attinger, D., Physical Review Fluids, 1, 043201, 2016]. Copyright (2016) by the American Physical Society. Section 2.4 and parts of Chapter 7 were published in Reference [3], reprinted with permission from [Comiskey, P. M., Yarin, A. L., and Attinger, D., Physical Review Fluids, 3, 063901, 2018]. Copyright (2018) by the American Physical Society. Sections 2.5, and 3.4, as well as Chapter 8 and Appendix C and D have been submitted for publication in Reference [4]. Sections 2.6, and 3.5, as well as Chapter 9 have been published in Reference [5], reprinted by permission from Springer Nature [Friction coefficient of an intact free liquid jet moving in air. Comiskey, P. M., and Yarin, A. L., Experiments in Fluids, 59, 65]. Copyright (2018) Springer Nature. Section 3.3 and parts of Chapter 6 were published in Reference [6], reprinted with permission from [Comiskey, P. M., Yarin, A. L., and Attinger, D., Physical Review Fluids, 2, 073906, 2017]. Copyright (2017) by the American Physical Society. Section 3.2 and Chapter 5 has been published in Reference [7]. Portions of Chapter 6 have been submitted for publication in Reference [8]. And finally, sections of Chapter 7 have been submitted for publication in Reference [9]. Permission letters given by each publisher are located in Appendix F.

CONTRIBUTION OF AUTHORS

The characterization of blood rheology in Sections 2.1, 3.1, and Chapter 4 are parts of a published work [1] where Mr. Alexander Kolbasov is the primary author and I am the secondary author. Mr. Kolbasov, myself, and Dr. Rakesh Prasad Sahu conducted the experiments and participated in writing the manuscript. Dr. Suman Sinha–Ray, and Dr. Alexander L. Yarin, assisted in the development of the direction of the work as well as helped interpret experimental results and contributed to the writing of the manuscript. Dr. Basant Singh Sikarwar, Mr. Sungu Kim, Dr. Talukder Zaki Jubery, and Dr. Daniel Attinger conducted experiments, analyzed data, and contributed to the writing of the manuscript. The work on backward spattered blood droplets due to a conical bullet in Sections 2.2, and 2.3, along with parts of Chapter 6 were published in Reference [2] for which I am the primary author and participated in analyzing experimental data, developing the theory, and analyzing the results. Dr. Yarin contributed to the writing of the manuscript, the development of the theory, and the analysis of the results. Mr. Kim and Dr. Attinger designed the experimental setup, partook in its execution, helped analyze and interpret experimental data, and assisted in writing the manuscript. The work on forward spattered blood droplets due to a specific bullet type in Section 2.4 and parts of Chapter 7 were published in Reference [3] for which I am the primary author and interpreted experimental data, developed the theory, and analyzed the results under the close guidance of Dr. Yarin who contributed to all aforementioned tasks. Dr. Attinger contributed to the writing of the manuscript and interpretation of the results. For the work

CONTRIBUTION OF AUTHORS (Continued)

on the propagation of muzzle gases and quantifying their effect on backward spattered blood droplets discussed in Sections 2.5, and 3.4, as well as Chapter 8 and Appendix C and D, which has been submitted for publication Reference [4], I am the primary author and I developed the theory and created the results. Dr. Yarin contributed in writing the manuscript, development of the theory, and the interpretation of the results. The work on intact blood jets discussed in Sections 2.6, and 3.5, as well as Chapter 9 and published in Reference [5] for which I am the primary author, I designed and conducted the experiments as well as expanded on the already developed theory. Dr. Yarin contributed to the writing of the manuscript and provided the basis for the theory. For the work on backward spattered blood droplets due to a cylindrical blunt bullet discussed in Section 3.3 and parts of Chapter 6 and published in Reference [6], I am the primary author and contributed to the development and interpretation of the experiment, developed the theory, and created the theoretical results to compare the experiment with. Dr. Yarin contributed to the writing of the manuscript and the theory, whereas Dr. Attinger developed the experiment, supervised it, analyzed the data, and contributed to the writing of the manuscript. The work on the analysis of high–speed videos to better understand the fundamental physics which occurs in blood spatter due to a gunshot discussed in Section 3.2 and Chapter 5 and has been published in Reference [7], I am the primary author and analyzed and interpreted the experimental data. Dr. Yarin and Dr. Attinger both helped write the manuscript and interpreted the data. For the work on the expansion of the created backward spatter models and dissemination to the forensic science community discussed in portions of Chapter 6 which has been submitted for publication in Reference [8], I am the primary author

CONTRIBUTION OF AUTHORS (Continued)

and created the statistical models. Dr. Yarin and Dr. Attinger contributed to writing the manuscript and guided the direction of the statistical models. The generalized model for forward spattered blood drops for an arbitrary bullet discussed in portions of Chapter 7 which has been submitted for publication in Reference [9], I am the primary author and I interpreted the experimental data, developed the mathematical model, and performed the comparisons. Dr. Yarin contributed to the mathematical model, the text of the manuscript, and the analysis of the results. Dr. Attinger helped with the experimental data, interpretation of the results, and the writing of the manuscript. The Kutta–Merson numerical scheme described in Appendix A and used throughout my thesis was introduced to me by Dr. Yarin. Appendix B for the evaluation of the Fredholm integral equation which arises in the work on the forward spatter of blood due to an arbitrary bullet was developed by me and is based off of theory from Dr. Ilia Roisman and Dr. Yarin. The extension of the theory for the intact jet with non–Newtonian fluids discussed in Appendix E was developed by myself and Dr. Yarin. In all work, my advisor, Dr. Yarin, contributed to the writing of each manuscript, the theoretical development of models, helped develop experimental setups and properly analyze the data, as well as contributed to the analysis of the final results.

TABLE OF CONTENTS

TABLE OF CONTENTS (Continued)

CHAPTER **PAGE**

TABLE OF CONTENTS (Continued)

CHAPTER **PAGE**

LIST OF TABLES

LIST OF FIGURES

LIST OF FIGURES (Continued)

FIGURE **PAGE**

LIST OF FIGURES (Continued)

LIST OF FIGURES (Continued)

LIST OF FIGURES (Continued)

LIST OF FIGURES (Continued)

LIST OF ABBREVIATIONS

ACD	Acid citrate dextrose
BPA	Bloodstain pattern analysis
CSI	Crime scene investigation
DPI	Dots per inch
EDTA	Ethylenediaminetetraacetic acid
FFT	Fast Fourier transform
FMJ	Full metal jacket
GSR	Gunshot residue
HP	Hollow point
IABPA	International Association of Bloodstain Pattern Analysis
LHS	Left–hand side
MFRC	Midwest Forensics Resource Center
ODE	Ordinary differential equation
PIV	Particle image velocimetry
RM	Rabinowitch–Mooney
RHS	Right–hand side

SUMMARY

The goal of this thesis is to investigate the application of fluid mechanics in forensic science in bloodletting events such as blood spatter due to a gunshot. Bloodstain pattern analysis experts often rely upon trace evidence and deductive reasoning to solve a crime but can sometimes ignore standard scientific principles established in fluid mechanics. This can leave an uncomfortable amount of uncertainty in the results of an analysis performed at a crime scene. Oftentimes, the transgression committed during the crime scene reconstruction is rooted in a fundamental misunderstanding of fluid mechanics. As such, this work is an attempt to bridge the gap between the fluid mechanics and forensic science community by applying sound fluid mechanical theory and principles to problems within forensic science.

There are several fundamental problems in forensic science that can be investigated and explored using tools found in fluid mechanics. For instance, what effect does the non–Newtonian behavior of blood have on atomization and the subsequent flight of blood droplets? What physical mechanisms are present in the atomization of blood prompted by the impact of a bullet? Can the original location of the victim and shooter be elucidated using only the information present in patterns of bloodstains? For victims shot at close range, what is the effect of the expanding muzzle gases resulting from the chemical reaction propelling the bullet on splashed blood droplets? This thesis intends to answer all of these questions and subsequently expand the field of fluid mechanics and forensic science simultaneously.

The first part of this work is to investigate the rheology of blood. Standard measurements with recognized techniques are utilized to determine the surface tension and shear viscosity of swine blood. Swine blood is used as a substitute for human blood because it is biologically similar and safer to work with. It's found that blood reveals a power–law shear thinning behavior in simple shear flow. Comparisons with data on elongational viscosity shows that it can be up to three orders of magnitude higher than that of shear viscosity. Therefore, the viscoelasticity of blood should not be ignored as the atomization and dripping processes present in forensic science applications are affected.

The next chapter deals with a quantitative analysis of high–speed videos found in literature on the atomization of blood due to a gunshot. The videos show a variety of target and bullet types and are analyzed with particle image velocimetry and various image analysis tools. Average velocity histories, typical size and number ranges, blood spatter spray angles, and other qualitative results are presented. It is shown that blood droplets traveling in the direction of the bullet, termed forward spatter, are faster than those traveling in the direction opposite of the bullet, termed backward spatter. Moreover, the blood droplets are seen to possess an acceleration after leaving the target which indicates there is a collective aerodynamic affect, similar to that which can be seen in a flock of geese flying in a V formation.

With this knowledge in mind, two backward blood spatter (spatter in the direction opposite of bullet motion) models were developed. One, for an idealized case of a blunt, or cylindrical bullet, and the other, for an idealized sharp, or conical bullet. The initial velocities and acceleration of the blood droplets are determined through impact–driven fluid mechanics and the

resultant atomization is attributed to the Rayleigh–Taylor instability. This instability occurs when a fluid of greater density, in this case blood, is accelerated towards one of lighter density, i.e. air. The acceleration is found analytically from the specific solutions to the impact–driven fluid mechanical problems, and then, the number of blood droplets and their respective sizes are determined through the instability analysis. The flight of the blood droplets then entrains a significant amount of surrounding air due to viscous suction and the two–phase flow diminishes the aerodynamic drag of drops trailing the faster ones, thus resulting in the collective effect occurring in reality. The drop trajectories are also affected by gravity and air drag forces. The theoretical results are then compared with experimental data and the comparisons for the distribution of stains with properties such as stain area and impact angle are found to be good.

Forward blood spatter (spatter in the direction of bullet motion) is tackled next and because of a cascade of instabilities involved as compared to backwards spatter, a different atomization model is appropriate. Here, a chaotic disintegrating model is used and the liquid target is fragmented through the growth of lacunae due to the angular stretching of the target from the motion of the bullet. Then, the target fractures into blood droplets which is predicted through the framework of percolation theory. The viscoelasticity of blood is important for this phenomena because the faster motion results in a build–up of elastic stresses which develop in the blood droplet "tails" which connect the individual droplets to the liquid bulk in a web of liquid. These droplet tails slow down the blood droplets until the connections undergo brittle fracture at which point their motion is governed by the same principles as the blood droplet trajectories in backward spatter. The model is generalized to accommodate bullets of

any arbitrary shape and the distribution of the number of droplets and average stain area are compared with experimental data. The results are shown to be good.

The importance of propagating muzzle gases from the chemical reaction of propelling the bullet on backward spattered blood droplets is then investigated. There are several constituents of the muzzle gases, propellant gases being one of them, and it is known that they form a turbulent vortex ring. This turbulent vortex ring is shown to be self–similar and carry gunpowder particles which leads to the deposition of gunshot residue. The results of the self–similar flow, vorticity, and concentration of gunpowder fields are calculated. The equations of motion of the trajectories of blood droplets are then modified to accommodate an interaction with the flow field from the turbulent vortex ring. The changes in the final locations and distributions of the number of stains and their respective stain areas are presented. It is found that muzzle gases result in a large difference in the expected bloodstain pattern.

Finally, intact jets of blood are considered which is an important topic for bloodletting events such as arterial gushing. A theoretical model for the intact jets of liquid is developed which allows for a generalized coefficient of friction function to be used. This coefficient is found empirically through experiments conducted in this work. The theoretically predicted intact liquid jet trajectories match nearly perfectly with the experimental data.

CHAPTER 1

INTRODUCTION

1.1 History of Bloodstain Pattern Analysis

The first comprehensive study of bloodstain pattern analysis (BPA) was conducted in 1895 by Eduard Piotrowski [10]. He attempted to determine how and where bloodstains form after blunt trauma to the head, however, after his pioneering work, scientific interest in the topic waned for several decades. Then, in 1939 BPA research slowly started to gain traction when Victor Balthazard published a study on determining the angle of impact from a bloodstain [11], the formula and methodology which he developed is still in use by police departments today. In 1944, LeMoyne Snyder published a widely read book describing many phenomenological aspects of bloodstains and the proper way to analyze and get useful information from them [12], but it was not until 1955, however, that many consider to be the establishment of modern day BPA practices. It was at this time that BPA was first used in a court of law [13]. The case surrounded the question of whether Dr. Sam Sheppard, a neurosurgeon, murdered his wife Marilyn Reese. Dr. Sheppard was initially found guilty, but, on appeal, the forensic evidence presented by Dr. Paul Kirk proved that Dr. Sheppard was innocent and the case solidified the importance of BPA expert opinion in crime scenes. The field then scientifically progressed through the work of experts such as Herbert Leon MacDonell who wrote an important book in 1971 [14], and formalized the science by establishing the International Association of Bloodstain

Pattern Analysts (IABPA) in 1983. Scientific research in BPA steadily progressed, but in 2013, it was noted by Dr. Daniel Attinger, et al. that there are many areas of BPA in which a fundamental knowledge of physics is lacking [15]. The paper lists several avenues for fluid mechanics to bridge that gap, and since then, there has been a plethora of research addressing this issue [2–9, 16–22].

1.2 Role of Fluid Mechanics

According to Ref. [15], there are many facets of fluid mechanics that can facilitate the growth of BPA. An overview of the crossover between the two subjects is shown in that paper in Table 4c. In that table, there are a series of fluid mechanic and BPA topics where relations between the two are drawn. Several important crossovers exist, namely in the physical properties of blood, such as its rheology and surface tension. These properties can affect the resultant bloodstain size, the cast–off pattern, and the formation of possible satellite droplets which allows inferences such as impact conditions and the type of weapon. The atomization, or liquid jet/sheet breakup of blood plays a critical role in the number of bloodstains and their resultant spatter pattern. This has potential to link spatter patterns to specific classes of weapons. The trajectories of blood droplets in flight is another big issue within BPA which fluid mechanics can digest, because it contains the mathematical tools to include physical effects such as drag, gravity, and aerodynamic drop–drop interactions. This allows final possible parameters such as the angle of impact of a droplet and its final location to properly be determined.

1.3 Thesis Objectives

As pointed out by Ref. [15], there are many aspects of BPA which can be improved upon through the application of fluid mechanics. The objective of this thesis is to apply techniques based upon fundamental fluid mechanics in an attempt to improve the understanding of BPA. This is completed by developing a deeper understanding of the rheology of blood discussed in Ch. 4. Then, the atomization process of blood spatter due to a gunshot is quantitatively explored with particle image velocimetry (PIV) and image processing techniques in Ch. 5. Using the knowledge gained from these two studies, two mathematical models were developed for backward spattered blood spray due to a gunshot discussed in Ch. 6. Then, forward blood spatter is modeled in Ch. 7 and the theoretical model is generalized to account for bullets of arbitrary shape. The effect of muzzle gases on backward spattered blood droplets is explored in Ch. 8. Finally, Ch. 9 describes a theoretical model to track the trajectories of intact jets of liquid for any friction coefficient, and experiments with water jets were conducted and compared.

CHAPTER 2

BACKGROUND AND LITERATURE REVIEW

2.1 Blood Rheology

(This section has been previously published in Rheologica Acta by Kolbasov, and Comiskey, et al. 2016, in Ref. [1].)

Blood is one of the most common liquids with relevance to disciplines as varied as the food industry, medicine, and forensics. It is a complex aqueous liquid that starts to coagulate as soon as it flows out of the human body. Approximately half of the volume of blood consists of particles such as red and white blood cells and an important property is the hematocrit, which is the relative volume of red blood cells in that sample of blood [23, 24].

Several properties of blood have been already characterized, for instance, the density of blood, 1060 kg/m^3, is close to that of water and blood is known to be a non–Newtonian fluid. The shear viscosity of blood decreases with shear rate in simple–shear flow, i.e. blood is a shear–thinning fluid. Moreover, blood viscosity also increases with a decrease in temperature and an increasing hematocrit. Based on experimental measurements, correlations have been proposed for the shear viscosity of blood which models the dependence upon hematocrit, shear rate, and temperature [25]. Other empirical correlations are available, for instance in Ref. [26] based on Casson's equation, for shear rates from 2 to 10^5 s^{-1}. Previous work has been addressed for the shear–thinning aspects of blood rheology [25, 26], as well as the viscoelastic properties [27–29].

A detailed understanding of blood rheology is important in biology, where it plays a role in the flow structure and affects viscous dissipation during circulation [27]. For instance, shear–thinning effects are known to affect blood flow and wall shear stress in coronary arteries [30–32]. Similarly, blood rheology matters for forensic disciplines such as BPA, a discipline which the US National Academies recently advocated for stronger scientific foundations, given the "complex nature of fluid dynamics" [33]. Indeed, rheology affects most aspects of a violent crime or accident, such as (a) the dripping process of blood, where viscosity and elasticity control the final stages of drop formation [34]; (b) the breakup of jets [35,36] and sheets [35–37], especially in the transition from dripping to jetting [38]; (c) the oscillations of drops during flight [39]; (d) the fate of droplets and jets upon impact [40–43]; and (e) the evaporation–driven flow in drying bloodstains [44]. Understanding the rheology of blood is therefore important for crime scene reconstruction and Ref. [15] provide values of shear rates relevant to BPA. Indeed, blood flow will be significantly influenced by blood rheology in any situation where the Reynolds, Deborah, or capillary numbers have finite values.

For polymer solutions, viscoelasticity is typically caused by coil–stretch transition of macromolecules, which happens in strong elongational flows [45]. For blood, there is no clear link between its viscoelasticity and its microscopic or molecular structure, which explains the mostly phenomenological rheological approach adopted in hemodynamics [46–49]. Recently, Ref. [28] measured the relaxation time of blood with a custom–made capillary breakup extensional rheometer resulting in values of 7.8 ± 0.6 and 1.5 ± 0.2 ms for human blood and blood plasma, respectively, both at 37 °C. This result shows that whole blood and blood plasma can be

viscoelastic. Viscoelasticity might influence blood spatters and bloodstain pattern analysis. For instance, viscoelasticity influences the deformation, spreading, and atomization of drops according to the data available in Refs. [50–56].

2.2 Bloodstain Pattern Analysis

(Parts of this section have been previously published in Physical Review Fluids by Comiskey, et al. 2016, in Ref. [2].)

A blood spatter pattern is a collection of bloodstains produced by blood droplets from a source location to a target surface. One of the main issues in forensic analysis of blood spatter patterns is to determine where a blood spatter originates from. This serves the purpose in crime scene reconstruction of determining the position of the source of blood. This type of knowledge is expected by the analyst communities [33] as it provides a deeper understanding of what occurred during the crime. The position of the source of blood is typically obtained by backward reconstruction of the trajectories, from the target to the source. A sound fluid–mechanical theory of drop atomization, trajectories, and drop impact would be relevant to the interpretation of blood spatters resulting from gunshot wounds such as the infamous case of Phil Spector, where the question arose if blood from backspatter could travel a distance of approximately 1.8 m [57]. Using a model for the flight of blood droplets and the inspection of bloodstains, the backward reconstruction of drop trajectories can be performed [15].

The terminology used for trajectory reconstruction can be described as follows; the area of origin is the three–dimensional origin location and its projection onto a horizontal plane is the area of convergence. The area of convergence corresponds to the projection of the trajectories

on a horizontal plane. To determine the area of origin, BPA experts use the angle of impact from several stains through visual inspection [15]. This angle is the acute angle at which a blood drop impacts the deposition surface, e.g. a floor.

As stated in 1939 in Ref. [11], reconstructing trajectories is very difficult and still is today. One method for trajectory reconstruction is the assumption that blood droplets travel in a straight line [33]. This is called the trigonometric method or method of strings and is routinely used in crime scene analysis [58–62] and was first used for crime scene reconstruction in the 1950's [13]. The uncertainties associated with the inspection of blood stains for parameters needed for the method of strings reconstruction is reviewed in Ref. [15]. The actual trajectories are curved, due to the effect of gravity which is amplified by aerodynamic drag. Since gravity and drag act, respectively, vertically and parallel to the trajectory, it is valid to assume that the projection of the trajectories on a horizontal plane consists of straight lines. This justifies the use of straight lines to determine the region of convergence.

However, the use of straight lines to predict the vertical position of the source, i.e. the region of origin, involves a systematic error. For instance, Refs. [63, 64] report errors in the determination of the region of origin. Similarly, Ref. [65] verifies experimentally that the method of strings "[overestimates] the height of the point of origin and the error associated with this technique is significant (50% on average)".

2.3 Backward Blood Spatter

(This section has been previously published in Physical Review Fluids by Comiskey, et al. 2016, in Ref. [2].)

BPA research has recently proposed methods to reconstruct curved trajectories, particularly in backward blood spatter cases, that is blood spatter traveling in the direction opposite of bullet motion[1]. For example, Ref. [17] describes "a method of reconstructing the area of origin in a nonlinear manner" and incorporates the effects of drag in trajectory calculations using probability densities. A statistical procedure based on aggregate statistics and the basic equations of projectile motion have been shown to determine the area of origin of a blood spatter for cases when the spatter is launched within a narrow range of polar angles [16]. Since ballistic reconstruction involves the knowledge of impact velocity and drop size, recent BPA work has focused on deducing that information by stain inspection, as proposed in Ref. [66]. The authors of Ref. [19] reconstructed drop trajectories using ballistic calculations, considering gravity and drag forces, and determined the region of origin with about four times higher accuracy than under the assumption of straight trajectories.

It should be emphasized that none of the existing theories used for predictions of blood trajectories address basic questions such as what the physical mechanism of drop formation in blood spatter is and how it determines the drop size distribution and the initial velocities and angles. Even though a drop size can be reconstructed from an available bloodstain, the initial drop velocity and direction cannot be established this way, which adds additional unknowns in any method of the prediction of drop trajectory. In fact, the key element of the problem is in these initial conditions rather than in predicting trajectories, albeit the methods of pre-

[1]Frequently in BPA literature it is not specified that the trajectory reconstruction models are only valid for backspatter, however, it is often the case that only backward spatter is in focus.

dicting trajectories should also be upgraded to account for the collective effect on the air drag experienced by drops in dense clouds.

Spatter originates from blood at body temperature ($\sim 37^{\circ}$C), while drops typically travel through colder air and impact a colder surface. The effect of cooling in flight and impact has been investigated in other fields [67] but not in the context of BPA. This issue might be important because the physical properties of blood vary considerably with temperature which might affect in–flight atomization as well as drop spreading and splashing on impact. The evaporation of drops during flight might be another issue and this would be most important for small drops due to their large surface–to–volume ratios.

There are four additional obstacles to the ballistic reconstruction of blood drop trajectories. Namely: (i) the area of drop origin can be different from the area of origin of blood spatter because the process of drop generation can involve a sequence of topological changes (secondary, tertiary, etc., atomization in flight) like the breakup of liquid sheets [68]. (ii) Air through which blood drops fly is not always quiescent and sometimes it plays an active role in drop transport. For instance, experiments involving respiration–caused blood spatter have demonstrated the importance of understanding the role of the surrounding air [69], which helped carrying sub-millimeter drops further away than occurs in still air. (iii) When spatters have a predominant direction, such as for gunshot backspatter patterns, the trajectory reconstruction approach for earlier drops requires one to account for the formation flight effect, important in spatters generated from a jet or stream of blood (arterial gushing, expectorate, or gunshot). For instance, in situations when blood spatter is caused by a bullet entering a body, e.g. as in the case of Phil

Spector allegedly murdering Lana Clarkson by a gunshot into her open mouth, multiple blood drops issued at a high speed of the order of 10 m/s or more, formed a rapidly moving turbulent two–phase jet entraining air. Similar situations are familiar in relation to sprinkler jets, where it was shown that drop motion is dominated by the collective effect, which diminishes the effect of air drag [70, 71]. (iv) Blood is a non–Newtonian liquid that is a suspension of red and white blood cells and platelets in lymph. Blood is known to be a shear–thinning fluid that can be described by the power–law model in simple shear flows. Also, viscoelastic properties of blood were revealed experimentally in Ref. [28]. To what extent the non–Newtonian rheological properties of blood affect blood spatter, especially the initial atomization stage, is currently unknown.

2.4 Forward Blood Spatter

(This section has been previously published in Physical Review Fluids by Comiskey, et al. 2018, in Ref. [3].)

The physical mechanism of blood spatter generation has so far been studied in detail for backward spatter, but not for forward spatter. These spatter pattern ejecta types are different and may result in quite different spatter patterns [7]. In the latter work, it was revealed that the maximum velocity of forward spattered drops is approximately two times higher than that of their backward spattered counterparts. Moreover, it was found that there are more drops generated in forward spatter and they are grouped in a more compact fashion in flight. These physical facts have several consequences for the development of modeling methods. For instance, the faster velocities may result in drops with larger deformations in flight, which can possibly

render the common drag coefficient correlations, such as the Schiller–Naumann or Clift–Gauvin correlations [15, 72], inaccurate, or even trigger further atomization events. The effect of drops cooling in flight has been studied before, such as in Ref. [73], but never in the context of BPA, where the cooling from body temperature to ambient air might affect atomization, spreading, splashing, etc.

There is essentially no scientific literature on the mechanisms of forward spatter pattern formation, and this could be due to the difficult nature of the problem. It is clear, however, that the damaged tissue ahead of the bullet is the material from which the forward spatter ejecta originates [74]. Understanding the formation of forward blood spatters might help crime scene reconstruction, supplementing information obtained from ballistic reconstruction of bullet trajectories. The latter information is sometimes confusing or complex because bullets can travel long distances without striking an object within the crime scene or might not even be recovered at all. Thus, accurately determining the trajectory of the bullet is not always possible, especially if there are multiple bullets involved throughout a crime scene. It may be a challenge to associate a specific hole or bullet to a given forward spatter pattern. Combining the reconstruction of the bullet and blood drop trajectories may yield the location of the victim. In addition, in cases involving multiple shooters, forward spatter patterns in conjunction with bullet comparisons may help identify which gun/shooter fired the fatal shot. Lastly, muzzle gases may have less of an effect on forward spatter pattern distribution than on backward spatter.

2.5 Muzzle Gases

(This section has been submitted for publication by Comiskey and Yarin, 2019, in Ref. [4].)

Vortex rings are formed by vorticity generated in fluid issued from a nozzle or an orifice, and growing instabilities at the cores of such vortex rings can cause transition to turbulence [75, 76]. The laminar–turbulent transition occurs in the range of the initial Reynolds number $10^3 \leq Re_0 \leq 10^4$, and turbulent vortex rings are observed at $Re_0 > 10^4$, where $Re_0 = u_0 R_0/\nu$ and u_0, R_0, and ν, are the initial velocity, radius, and kinematic viscosity of the turbulent vortex ring, respectively [77]. The radius of a turbulent vortex ring increases linearly with its propagation distance [76, 77] which implies self–similar behavior. Self–similar scaling laws have been recognized previously and validated by experimental data [77, 78].

Muzzle exhaust flow, or muzzle gases, originating from the muzzle of a gun involves a cascade of multiple complex phenomena and a thorough description of the structure is discussed in Ref. [79]. The muzzle exhaust flow, which begins before the bullet exits the muzzle of the barrel, results from an intense explosion of the propellant powder. This propels the bullet and produces a spherical shock wave called the precursor blast wave, and its propagation can be described by the theory of a strong explosion [80–82]. Then, the air ahead of the bullet is rapidly accelerated to a supersonic speed resulting in the Prandtl–Meyer expansion fan at the muzzle [83, 84]. The expansion fan is terminated by a normal shock called the Mach disk [85], and a system of shocks exists between the Mach disk and the blast wave. The bullet then exits the muzzle of the barrel and passes through the Mach disk. If the bullet is supersonic, it can then overtake the precursor blast wave. Immediately after the bullet leaves the muzzle, the propellant gas flow can exit and it forms a turbulent vortex ring which then propagates in the direction of the bullet [85]. Unburnt propellant powder is carried by this turbulent vortex ring

and when it is deposited on a surface is termed gunshot residue (GSR). The leading edge of this propellant gas flow is called the contact surface.

Occurring simultaneously with the muzzle exhaust flow is a series of muzzle flashes which are bright luminous zones due to a complex temperature distribution resulting from propellant powder combustion [86]. First, there is a primary flash or muzzle glow which is of relatively low luminosity and situated directly adjacent to the muzzle. Directly after the primary flash exists a high intensity intermediate flash which is located further from the muzzle, thus resulting in a dark region between the primary and intermediate flash. An incomplete combustion of the in–bore propellant powder leaves combustible material to travel downstream which can produce a secondary flash that releases an amount of energy comparable to that during the initial in–bore combustion [86]. This occurs because of entrained propellant gases which recompress when passing through a shockwave front and raise the temperature igniting the rest of the combustible propellant [85–87]. This locally confined increase in gas pressure can also act to reverse the pressure gradient in the flow field, and as such, the gas motion at this location is decreased significantly, and in some cases, can be reversed entirely [87].

Thorough experimental investigations were conducted to determine gas velocity throughout the entire muzzle exhaust flow process with a 7.62 mm caliber rifle [87]. It was observed that the flow field within the Prandtl–Meyer expansion fan accelerates quickly and can attain a maximum velocity of 2400 m/s. After the Mach disk, the flow rapidly decelerates to 150 m/s or less. This was also confirmed in a separate experimental study in Ref. [88]. When the expansion again commences downstream, the gas velocity is on the order of several hundred meters per

second. With the same caliber rifle, temperature measurements for the three muzzle flashes were conducted where it was found that the primary flash can reach temperatures of 1645 K, the intermediate flash 1940 K, and the secondary flash 2500 K [86]. Pressure measurements with the same 7.62 mm caliber rifle revealed subatmospheric pressure in the Prandtl–Meyer expansion zone, and then a significant increase in pressure at the Mach disk [85]. The contact surface (the propellant gas–air interface) had a peak pressure of 350 kPa, and it was noted that the propellant gas flow is heavily dependent upon the muzzle exit pressure which is affected by the type of propellant powder, gun, bullet, and atmospheric conditions.

The complex nature of the muzzle exhaust flow was found to follow several empirical laws for the Mach disk, contact surface, and the precursor blast wave [85, 89, 90]. For example, it was observed that the contact surface can reach a distance normalized by the muzzle diameter of ~ 100. It should be emphasized that this value does not indicate the maximum distance reached because experimental limitations were met. Note also that the complex nature of the formation of muzzle exhaust flow has been treated theoretically using crude approximations. The basic unsteady nature of the initially reacting flow field means that simple approximations such as a quasi–steady free submerged jet [87] could be inadequate, and previous numerical simulations such as that in Ref. [90] could be inaccurate because the chemical kinetics of the muzzle flash are not accounted for.

The propellant gas, which propagates downstream, is of great interest to crime scene investigators because it can help identify the distance of the shooter from the target and also establish if an individual was at the crime scene [91, 92]. In order to determine the presence

of GSR, any potential residue must be removed from the surface through a variety of common collection techniques depending upon the deposition surface. The sample is then tested with various methods such as atomic absorption spectrometry and scanning electron microscopy to detect trace amounts of organic and inorganic GSR. The constituents of GSR originate from various sources including the propellant powder, the primer (a section in the shell casing which contains a highly explosive charge and is used to ensure proper ignition), the shell casing, and the bullet resulting in a possibility of 48 organic compounds and 52 inorganic compounds which may contribute to the composition of GSR [92].

The spatial distribution of GSR from the muzzle of a gun has been experimentally tested for various scenarios in order to determine the maximum range the residue can reach. For example, a target 1 m downrange contains easily detectable amounts of GSR [93]. If the target is moved further downrange, to 7.62 m, there is still a detectable amount of GSR originating from four weapons, a Ruger .22 caliber pistol, a Colt .32, and .45 caliber revolvers, and a Glock .45 caliber pistol [94]. The maximum possible axial and lateral distance which GSR can reach was shown to be 18 m, and 3 m, respectively, and the largest mass deposited was axially located at 13.5 m [95]. The distances at which GSR is deposited can be greatly affected by the surrounding environment. An open environment resulted in ten times lower the amount of detectable GSR as compared to a closed shooting range [96]. The concentration of particles in muzzle gases was found to be on the order of $10^5 - 10^8$ particles/cm^3 [79]. These experiments show that there is a wide range of final locations for GSR depending upon shooting conditions, the type of ammunition, and the type of gun used.

The furthest distance that propellant gases (and thus, GSR) can reach is important to crime scene reconstruction in the case of the backward spattering of blood because the propellant gases can deflect blood droplets flying toward the shooter [7, 97]. On the other hand, the blast wave was not observed to have a significant effect on the blood droplets probably because it reaches the wound earlier than the formation of blood droplets in backspatter [97]. A probabilistic approach was proposed in Ref. [98] to determine a link between the distribution of GSR and the shooter location, but the acquisition of the model parameters is difficult.

2.6 Intact Liquid Jets

(This section has been previously published in Experiments in Fluids by Comiskey, et al. 2018, in Ref. [5].)

Free liquid jets moving in air are a common phenomenon, since decorative fountains, fire extinguishers, and different sprinklers are frequently seen in our everyday life. One of the first studies attempting to better understand free liquid jets was sensibly related to large water jets used to suppress fires [99]. This extensive work quantified friction loss in hoses, roughness of various nozzles, effects due to back pressure, and even attempted to formulate a simple theory to match the trajectories of large firefighting jets. Practical nozzle designs were further discussed in Refs. [100–102], which Ref. [102] in particular, made additional theoretical predictions of jet trajectories using a model based on projectile motion neglecting air resistance. Early work in the field was dominated by experimental tests intended to design the best fire suppression or agricultural systems [103]. It resulted in many practically important observations such as the

optimal (determined by the maximum range reached by liquid) initial inclination angle of the jet in the 30–40° range reported by Ref. [104] or 35° reported by Ref. [102].

Theoretically, the trajectories of liquid jets have often been predicted using the equations of projectile motion, where air resistance is either neglected such as in Refs. [100,105] or empirically accounted for as in Refs. [104,106]. This results in trajectories which form parabolic arcs [104, 106–108], even though the effect of the aerodynamic drag has been used to explain the difference between theory and experiments [108]. For large sprinkler jets, it was found that air drag should be accounted for as Ref. [70] showed in their numerical model of multiphase turbulent atomizing jets. Recently, Ref. [109] developed a theoretical model which assumes the jet to be intact and unaffected by air drag until a breakup point, at which the jet instantaneously becomes a droplet train system whose motion is affected by air drag. Moreover, for the multiphase atomizing jets relevant in agricultural and forensic applications, it was shown that the aerodynamic drag experienced by individual drops is determined by their collective interaction similar to the aerodynamic interaction of birds flying in V formation [7, 70, 110].

Liquid in free liquid jets can either be Newtonian, such as water in decorative fountains and sprinklers, or non–Newtonian as in fiber–forming processes [111, 112] and in intact jets of blood which can form when a sharp object lacerates a main blood vessel [113–115]. The latter situation is of particular interest here. The ejection of intact blood jets is called arterial gushing and originates from a high–pressure location within the body such as the neck [113,115]. Such phenomena can occur when knives or other cutting instruments are used as a murder weapon, which, is on the rise. In the United States, knives or other cutting instruments accounted for

12.9% of murders in 2005 and 13.1% in 2014, even though violent crime was down 16.2% during that period [116, 117].

The transition from dripping to an intact liquid jet can happen at a large enough outflow velocity [118, 119]. As the outflow velocity increases, such jets break up due to the surface–tension driven capillary instability, then, at a higher velocity, by the bending instability and the atomization process, with the latter two mechanisms being driven by the dynamic interaction with the surrounding air [35, 72, 118–125]. Free jets of non–Newtonian polymeric liquids in many practically important applications are unaffected by these instabilities and stay intact even though their velocities of motion relative to air are very high, for example, in fiber–forming processes such as melt spinning, solution and melt blowing, etc. [111, 112, 118, 125]. Accordingly, in this latter group of works, the significant effect of the coefficient of friction drag acting on elongated cylindrical bodies was in focus. It was established that it cannot be described by the standard Blasius or Schultz–Grunow and other theoretical and empirical correlations based on the boundary layer theory and dependent on the Reynolds number based on the longitudinal length scale [126]. In the case of elongated cylindrical bodies, the boundary layer thickness becomes larger than the cross–sectional diameter, and as a result, the average friction coefficient is determined by the Reynolds number based on the diameter, Re_{d}, rather than on the longitudinal scale. Accordingly, several semi–empirical and empirical correlations for the friction coefficient of intact straight solid cylinders (wires) or liquid jets moving in air were established in the $0.04 \leq Re_{\mathrm{d}} \leq 400$ range. For example, Ref. [127] proposed the expression for the friction coefficient in the form of $C_{\mathrm{fd}} = 0.4 Re_{\mathrm{d}}^{-0.7}$, while Refs. [118, 128] employed $C_{\mathrm{fd}} =$

$0.65Re_{\mathrm{d}}^{-0.81}$, where the dimensionless friction coefficient is defined as the friction force (traction) T, rendered dimensionless by the product of the jet surface area S and the dynamic pressure of the surrounding air $\rho_{\mathrm{a}}V_{\tau}^{2}/2$. Here, ρ_{a} is the air density and V_{τ} is the tangential velocity of a liquid jet; in addition, the Reynolds number is defined as $Re_{\mathrm{d}} = 2aV_{\tau}/\nu_{\mathrm{a}}$, with $d = 2a$ being the cross–sectional jet diameter (with the radius denoted as a), and ν_{a} being the kinematic viscosity of air. Several other works in which a wire was either supported in a wind tunnel, or was moving through air at rest resulted in the expressions of the type $C_{\mathrm{fd}} = \gamma Re_{\mathrm{d}}^{-\beta}$, with γ in the 0.23–1.78 range and β in the 0.62–0.81 range valid in different intervals of Re_{d} in the 5–400 range [111, 112]. The applicability of these expressions for the average friction coefficient of curved intact free liquid jets arising in decorative fountains, sprinklers, and forensic applications has never been examined. An ad hoc hypothesis of their applicability is questionable.

The internal geometry of the nozzle is one of the most fundamental components in the formation of an intact free liquid jet. In such applications as decorative fountains and small sprinklers, the nozzles are typically designed to provide a gradual transition toward the exit and are operated with a backpressure which keeps the working fluid attached to the nozzle walls. If the working fluid becomes detached from the nozzle walls, however, a constricted jet can be created. Such a jet can travel distances further than normally obtained, because the destabilizing effects from the nozzle walls are eliminated [129]. Such jet detachments appear on sharp orifices and stiff nozzle generatrices, e.g. of the so–called Borda mouthpiece [130], and result from an essentially inviscid flow kinematics (leading to vena contracta) supplemented by the momentum balance in the form of the Bernoulli equation [131, 132].

CHAPTER 3

RESEARCH OUTLINE

3.1 Blood Rheology

(Parts of this section have been previously published in Rheologica Acta by Kolbasov, and Comiskey, et al. 2016, in Ref. [1].)

The physical properties of blood play an important role in crime scene investigation (CSI) because they affect everything from bloodstain formation to the atomization of blood. As such, the rheological behavior of blood should be investigated in the context of forensic science. To accomplish this task, the rheology of swine blood in shear was experimentally investigated and discussed in uniaxial elongation. As a substitute for human blood, swine blood was used because it has physical properties which are comparable [68, 133, 134]. For example, red blood cells in rouleaux at low shear rates are similar in swine blood and human blood, but that is not the case in the blood of cattle or sheep [135–137]. Shear viscosity measurements were carried out with a rotational and capillary viscometer, the results of which are discussed in Sec. 4.3 and ramifications for forensic science are mentioned in Sec. 4.4.

3.2 Atomization of Blood

(Parts of this section have been previously published in Forensic Science International by Comiskey, et al. 2017, in Ref. [7].)

Because the uncertainties of different BPA techniques can be significant, up to a 50% overestimation of the height of the origin of a blood spatter [68], a better understanding of the mechanisms of blood droplet formation and flight is required. Such efforts would be significantly facilitated by a thorough analysis of the available experiments data, one facet of which is explored in Ch. 5 where high–speed videos taken by Ref. [138] are analyzed. It should be emphasized, however, that some experimental simplifications do not necessarily reflect the real crime scene situations. For example, oftentimes, human blood is substituted for swine blood for safety reasons, and because of expected similarities in size and concentration of blood cells, and in rheology [2], albeit it is definitely not a perfect substitute [133].

After a thorough experimental investigation, of the atomization of blood resulting from a gunshot, it was determined that backward, and forward spattered blood behave quite differently. As a result, the mathematical models required to describe the physical situation are inherently different. The atomization of backward spattered blood is based off of the Rayleigh–Taylor instability because dense blood droplets accelerated towards air adhere to this instability as described in Sec. 6.5. This forms the basis of two mathematical models, one for idealized sharp bullets as shown in Sec. 6.3, and another of an idealized blunt bullet in Sec. 6.4. Forward spatter atomizes on a different time scale because of the added effect of the bullet resulting in a cascade of instabilities and therefore, the blood target chaotically disintegrates which is discussed in Sec. 7.3.1 for a single bullet type, and in Sec. 7.4.1 for a bullet of an arbitrary shape.

3.3 Bloodstain Pattern Prediction

(Parts of this section have been previously published in Physical Review Fluids by Comiskey, et al. 2017, in Ref. [6].)

Once a cloud of blood drops is generated due to the atomization of a blood target from a gunshot, its behavior in a sense is reminiscent of that of a sprinkler or diesel–engine jets studied previously in Ref. [70, 71]. Such jets entrain significant volumes of air and the resulting two–phase flow diminishes the aerodynamic drag of drops moving behind leading ones, similarly to the V formation of a flying flock of birds [110]. Then, the prediction of drop trajectories in such jets makes use of the initial drop sizes and initial velocities resulting from their respective atomization model, accounting for gravity and air drag forces, with the latter being diminished by drop–drop interactions through air mentioned above in Ref. [70]. It should be emphasized that few other studies account for gravity and air drag (albeit without accounting for the drop–drop interaction) to predict blood spatter patterns such as in Refs. [16, 17, 19], however, they do not consider the physical mechanism of drop formation.

The prediction of these patterns gives the ability of BPA experts a powerful tool to determine the events of a crime scene with minimal real–world input. The intent is that with a given bloodstain pattern, the models and methods developed here for backward and forward spatter allow the elucidation of the location of the bloodletting event and therefore the victim, and possibly the shooter. These trajectory equations which allow for this are described in Sec. 6.6, 7.3.2, and 8.2.3.

3.4 Effect of Muzzle Gases

(Parts of this section have been submitted for publication by Comiskey and Yarin, 2019, in Ref. [4].)

Muzzle gases propagating in the direction of the bullet as a result of the chemical reaction firing that bullet is of great interest to BPA experts because the resultant flow field can deflect soaring blood droplets. In particular, a portion of the overall structure of the muzzle gases called the propellant gases, are of utmost importance. This is because propellant gases form a turbulent vortex ring and not only act to deflect blood droplets, but also disperse passive admixture leading to GSR.

The present work aims to incorporate and quantify the effect of the turbulent vortex ring on the backward spatter of blood. Note that prediction of blood stain area and location is important in the framework of their further analysis in the hydrodynamic and forensic context [139]. The theoretical treatment of the aerodynamics of self–similar turbulent vortex rings is described in Sec. 8.2.1. The theory of dispersion of passive admixture (the GSR particles) by a turbulent vortex ring is given in Sec. 8.2.2. The theoretical framework for the effects of a turbulent vortex ring on blood droplets in backward spatter is described in Sec. 8.2.3. The results on the GSR dispersion by a turbulent vortex ring are presented and discussed in Sec. 8.3.1, and the interaction of a turbulent vortex ring with backward spattered blood droplets is discussed in Sec. 8.3.2. Finally, conclusions are drawn in Sec. 8.4.

3.5 Friction Coefficient and Blood Jets

(Parts of this section have been previously published in Experiments in Fluids by Comiskey, et al. 2018, in Ref. [5].)

The friction coefficient (sometimes referred to as the coefficient of friction) is an important parameter between the relationship of the force of friction and the subsequent normal reaction. For an intact jet of fluid, this is related to the aerodynamic force which acts on the jet due to the shear stress at the surface of the jet. This term is an empirical relation and is often determined for specific problems, therefore the developed equation is oftentimes only applicable to narrow fields of study. To mitigate this problem, a theoretical model discussed in Sec. 9.3 was constructed for the equations of motion of an intact jet of liquid for any friction coefficient. This allows the model to be versatile as it does not need to be bound by the Reynolds number range considered in Sec. 9.2.

The nozzles used in the experiments of Ch. 9 generated intact liquid jets because their internal geometry closely followed that of a pressure washer except designed to work at a low backpressure. The present work aims at establishing the average friction coefficient of intact liquid jets moving in quiescent air under conditions characteristic of decorative fountains, smaller sprinklers, and forensic applications. These cases are drastically different from those whose friction coefficient has already been found such as in fiber forming processes like melt spinning.

CHAPTER 4

INVESTIGATION OF BLOOD RHEOLOGY

This chapter has been previously published in Ref. [1], reprinted by permission from Springer Nature [Blood rheology in shear and uniaxial elongation. Kolbasov, A., Comiskey, P. M., Sahu, R. P., Sinha–Ray, S., Yarin, A. L., Sikarwar, B. S., Kim, S., Jubery, T. Z., and Attinger, D., Rheologica Acta 55, 901–908].

4.1 Introduction

Despite being at the same time a very common and precious fluid, the rheological properties of blood have not been thoroughly investigated. The goal of this chapter is to characterize the rheology of swine blood in the context of BPA. This is accomplished by performing measurements in shear flow and discussing experiments performed in uniaxial elongation. The experimental data shows that blood is a shear–thinning fluid which exhibits viscoelastic behavior. Elongational viscosity can be 1000 times higher than the shear viscosity and implications in biology and forensics are described.

4.2 Materials and Methods

The blood used in the experiments was from the National Animal Disease Center (Ames, IA) and was anticoagulated with 1% heparin and kept at 7 °C during transport before the experiment. In preparation for each experiment, the blood samples were placed on a Labquake (Thermo Scientific) rocker to ensure no coagulation until the blood samples reached room

temperature. Prior to use, the relative humidity and temperature of the room, as well as the temperature of the blood, were documented. The blood samples were then taken off the rocker and used in the various instruments to conduct the required experiments. Hematocrit was also measured for each blood sample through a HemataStat–II centrifugation device, according to manufacturer's instructions.

4.2.1 Shear Viscosity Measurements with a Rotational Viscometer

Simple shear experiments were conducted using three samples of swine blood: sample A (fresh blood, hematocrit 49%), sample B (1–day–old blood, 44% hematocrit), and sample C (1–day–old blood, 40% hematocrit; this type of blood was used in the experiments with a capillary viscometer described in Sec. 4.2.2, with the results presented in Fig. 1 for comparison with sample B). These three different types of samples were used to elucidate the influence of hematocrit in shear flow. In order to elucidate the effect of the difference in blood preparation on the experimental results, the blood from sample B was separated into two groups. All the blood was first brought to room temperature (24 °C) by placing blood–containing vials in a beaker with water at room temperature on a shaker table. Then, the vials with blood from both groups were slowly turned upside down 10 times. The first group of samples was used after that, whereas the samples from the second group were additionally passed through a 23–gauge needle 10 times to elucidate the effect of blood preparation on the shear flow of blood.

Viscosity of blood in simple shear flow was first measured using an LV–II+ cone and plate Brookfield viscometer with cone spindle CPE–40 (cone angle 0.8° and radius 2.4 cm). During each trial, the sample temperature was maintained at 24 °C by the temperature–control system

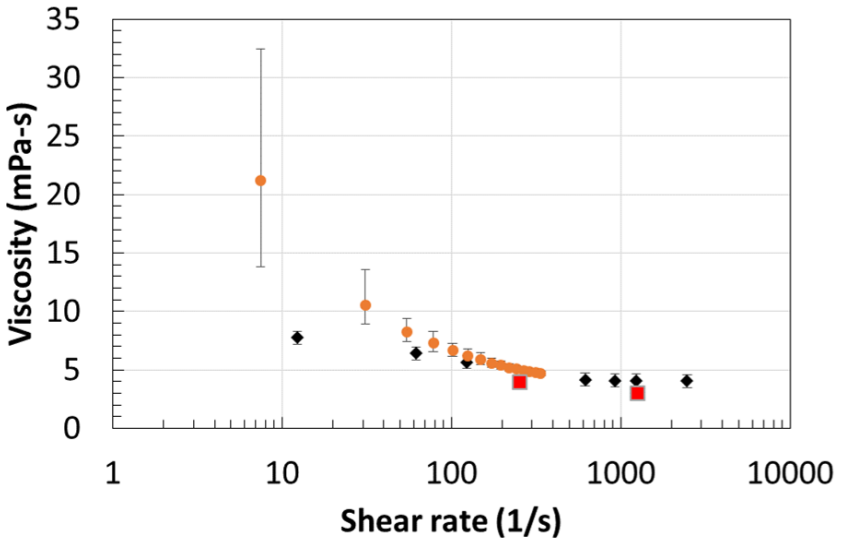

Figure 1. Shear viscosity versus shear rate in simple shear flow. Data shown by circles were obtained by the rotational viscometer and correspond to blood with the hematocrit of 44% (sample B). The experimental data shown by diamond and square symbols were measured using a capillary viscometer driven by a syringe pump (discussed in Sec. 4.2.2). Diamond symbols correspond to blood with the hematocrit of 44% sample B). Square symbols correspond to blood with the hematocrit of 40% (sample C). All blood samples were of types B and C. Error bars represent the maximum and minimum standard deviations. Fig. from Ref. [1].

of the viscometer (model TC–102D). The shear rates studied were in the 7–60, 7–350, and 200–400 s^{-1} ranges, and the shear rate was varied by equal increments, each being maintained for 30 s with a reading being performed before the next speed change. For hysteresis, the shear rate was tested in equal increments for both the ramp up and ramp down cases.

The combined results for the flow curves measured in the simple–shear flow are shown in Figs. 1–3. The results can be approximated using the Ostwald–de Waele power–law rheological constitutive equation which reduces to the following expression in the simple shear flow for the shear stress, τ_{shear},

$$\tau_{\text{shear}} = K\left(\dot{\gamma}\right)^{n}, \tag{4.1}$$

where $\dot{\gamma}$ is the shear rate, K is the consistency index, and n is the flow behavior index.

The non–Newtonian shear viscosity is defined as,

$$\mu_{\text{shear}} = \frac{\tau_{\text{shear}}}{\dot{\gamma}} = K\left(\dot{\gamma}\right)^{n-1}. \tag{4.2}$$

4.2.2 Shear Viscosity Measurements with a Capillary Viscometer

The shear viscosity of an incompressible fluid can be determined through the internal steady–state flow in a thin capillary. This is called a capillary viscometer and works based off of pressure and volumetric flow rate measurements [140]. The capillary viscometer used here measured the shear viscosity of blood through a power–law model in conjunction with the Rabinowitch–Mooney (RM) equation following Refs. [140, 141].

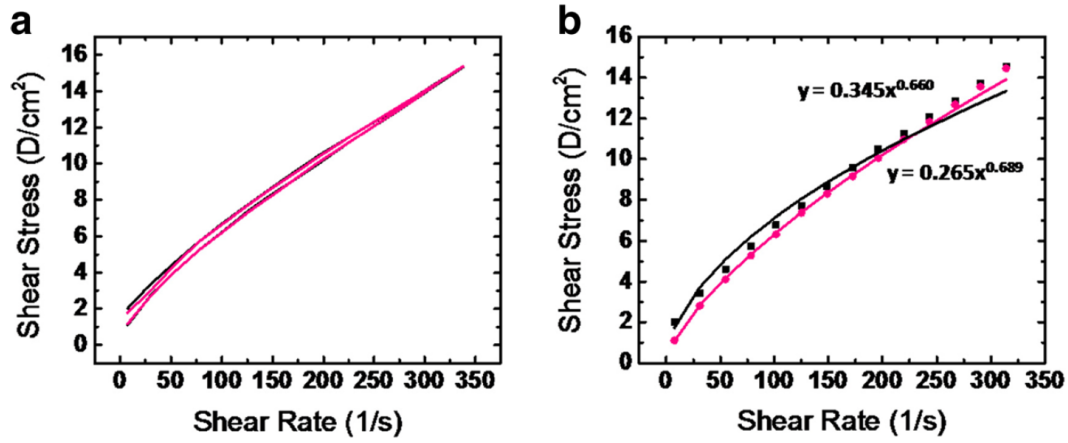

Figure 2. Shear stress versus shear rate in simple shear flow. The experimental data shown by the magenta line was obtained with blood that was not passed through the syringe. The rotational viscometer was used. The blue line was obtained with blood that was passed through the syringe. Blood samples B with a hematocrit of 44% were used. (a) The data is shown by lines. (b) The data is shown by symbols, and the fitted functions are shown by curves. Fig. from Ref. [1].

The experiments used flow rates ranging from 0.01 to 2 mL/min with a Reynolds number $Re < 600$ to maintain laminar flow. The measurements were performed in the fully developed flow region with an entry length, L_e, that is negligible with respect to the entire length of the tube, i.e. $L_e < 0.01\ L$, described in Ref. [142]. A 60 mL syringe was used, and the viscometer was designed to measure the viscosity of blood in the shear rate range of 10–1500 s^{-1}. A syringe pump was used to pump blood into the microcapillary tube, and an Omega DPG 110 differential pressure transducer was employed to measure the pressure drop across the tube at flow rates between 0.01–1.5 mL/min. Calibration was performed to determine the hydraulic diameter of the tube which was larger than 500 μm to avoid any viscosity underestimation caused by

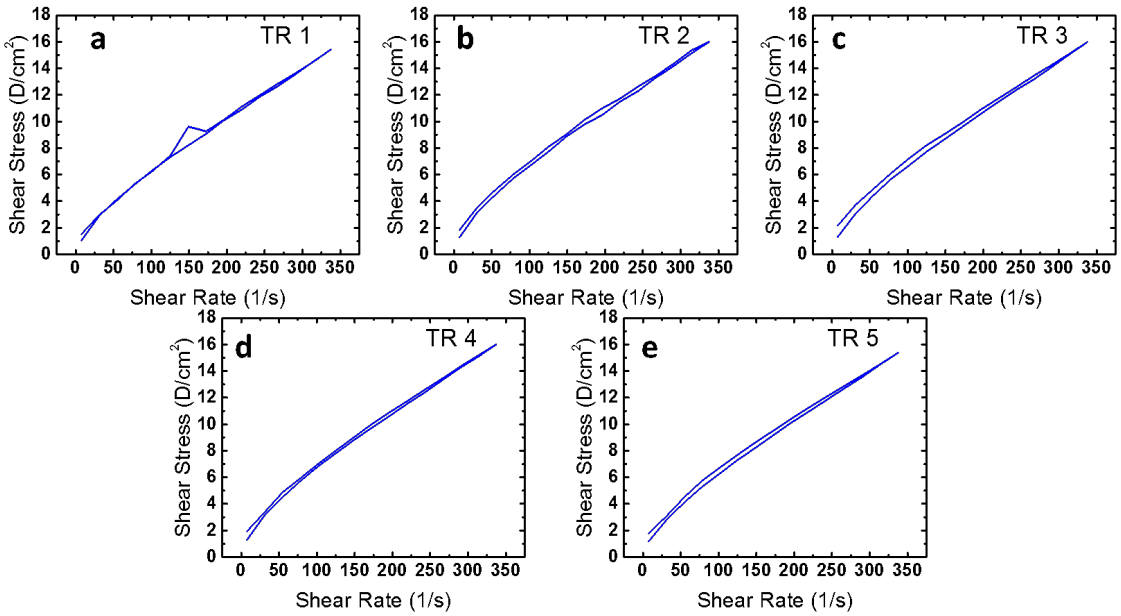

Figure 3. The ramp up and down shear stress versus shear rate in simple shear flow measured by the rotational viscometer for five consecutive trials with blood samples B, with a hematocrit of 44%. Fig. from Ref. [1].

the depletion of blood cells near the walls, a phenomenon known as the Fahraeus–Lindqvist effect, which is significant in tubes with diameters smaller than 300 μm [143]. Before starting the viscosity measurements, the room and blood temperatures were measured with a digital thermometer as 24.6 and 24.6 °C, respectively. The blood hematocrit was also measured by a centrifugation device (HemataSTAT II), as $49 \pm 1\%$.

4.3 Results

Equation (4.2) was fitted to the experimental data for samples A and B, and the results for the consistency and flow behavior indices are listed in Table I. Figure 1 shows that the effect of hematocrit on the measured shear viscosity values was minimal in the 100–1000 s^{-1} shear rate range, as the comparison between the results of the rotational viscometer for sample B and capillary viscometer for sample C shows. An example of the fitting is shown in Fig. 2.

Figure 2 shows that the experimental results are not affected by blood pre–treatment. The hysteresis of the shear viscosity measurements appears to be negligible except for low values of shear rate which is seen in Fig. 3. The viscometer is known to be inaccurate at low shear rates and is likely the source of the hysteresis.

Note also that the maximum shear stresses measured in Figs. 2 and 3 are significantly lower than the shear stresses reported to induce instantaneous cell lysis (about 400 Pa) [144] but close to the shear stresses (10–100 Pa) reported to induce platelet activation [144–147].

As Fig. 1 shows, a very good agreement was obtained between the capillary and rheometer measurements over the shear rates ranging from 100 to 2000 s^{-1}. The capillary viscometer

TABLE I

Consistency and flow behavior indices measured in simple shear experiments for samples A (fresh blood hematocrit 49%) and B (1–day–old blood, hematocrit 44%). Table from Ref. [1].

Shear rate range [1/s]	Hemato-crit [%]	Age [days]/ sample type	Trial	n (ramp up)	K (ramp up) [Pa × s^n]	n (ramp down)	K (ramp down) [Pa × s^n]
7.5–225	49	0/A	1	0.48	1.05	0.64	0.44
7.5–225	49	0/A	2	0.51	0.86	0.65	0.43
7.5–337.5	49	0/A	1	0.64	0.46	0.68	0.38
7.5–337.5	44	1/B	1	0.68	0.30	0.76	0.19
7.5–337.5	44	1/B	2	0.63	0.42	0.71	0.25
7.5–337.5	44	1/B	3	0.65	0.34	0.71	0.25
7.5–337.5	44	1/B	4	0.63	0.38	0.74	0.20
7.5–337.5	44	1/B	5	0.65	0.33	0.73	0.22
7.5–337.5	44	1/B	6	0.70	0.26	0.73	0.21
7.5–337.5	44	1/B	7	0.66	0.34	0.70	0.26
7.5–337.5	44	1/B	8	0.64	0.38	0.71	0.25
7.5–337.5	44	1/B	9	0.66	0.33	0.70	0.26
7.5–337.5	44	1/B	10	0.67	0.30	0.73	0.21
7.5–60	49	0/A	1	0.28	2.81	0.53	1.11
7.5–60	49	0/A	2	0.30	1.87	0.58	0.58
7.5–60	49	0/A	3	0.42	1.17	0.56	0.62
200–400	49	0/A	1	0.68	0.55	0.66	0.64
200–400	49	0/A	2	0.44	2.11	0.85	0.19

measurements have a relative uncertainty of 4% due to the uncertainty of the instruments used for the pressure and temperature measurements.

The equilibrium surface tension of blood was also measured using the pendant drop method described in Ref. [140] resulting in $\gamma_{\mathrm{la}} = 60.45$ mN/m.

4.4 Conclusion

The experimental data on the elongational viscosity of blood in Ref. [1] shows that it can be three orders of magnitude higher than the shear viscosity. The rheological measurements presented reveal that the tensorial rheological constitutive equation of swine blood cannot be reduced to the Ostwald–de Waele power–law model. Indeed, in uniaxial elongation, the behavior of blood flow is clearly viscoelastic. For a situation such as blood dripping from a weapon due to the Rayleigh–Taylor instability, the viscoelasticity of blood cannot be ignored because a thread of blood from the liquid bulk to the drop is formed. This effect is also essential in blood drop splashing as the drop impact forms a web of blood due to high elastic stresses. As a result, the viscoelasticity of blood should be considered in the description and analysis of such processes.

It should be emphasized that the fact that blood reveals a power–law behavior in shear flows still does not mean that the tensorial Ostwald–de Waele power–law model or any yield stress model (e.g. the Casson model) could represent a real tensorial rheological constitutive equation of blood, since none of them are capable to account for the viscoelasticity. The uniformly valid tensorial rheological equation of blood seems to be viscoelastic with shear–thinning behavior in shear.

CHAPTER 5

HIGH–SPEED VIDEO ANALYSIS OF BLOOD SPATTER

This chapter has been previously published in Ref. [7].

5.1 Introduction

High–speed videos of blood spatter due to a gunshot taken by the Ames Laboratory Midwest Forensics Resource Center (MFRC) [148] are analyzed. The videos used in this analysis were focused on a variety of targets hit by a bullet which caused either forward, backward, or both types of blood spatter. The analysis process utilized particle image velocimetry (PIV) and particle analysis software to measure drop velocities as well as the distributions of the number of droplets and their respective side view area. The results of this analysis revealed that the maximal velocity in forward spatter can be about 47 ± 5 m/s and 24 ± 8 m/s for backward spatter. Moreover, our measurements indicate that the number of droplets produced is larger in forward spatter than it is in backward spatter. In forward and backward spatter, the droplet area in the side–view images is approximately the same. The upper angles of the close–to–cone domain in which droplets are issued in forward and backward spatter are, $27 \pm 9^\circ$ and $57 \pm 7^\circ$, respectively, whereas the lower angles of the close–to–cone domain are $28 \pm 12^\circ$ and $30 \pm 18^\circ$, respectively. The inclination angle of the bullet as it penetrates the target is seen to play a large role in the directional preference of the spattered blood. Also, muzzle gases, bullet impact angle, as well as the aerodynamic wake of the bullet are seen to greatly influence the flight of

the droplets. The intent of this investigation is to provide a quantitative basis for current and future research on BPA of either forward or backward blood spatter due to a gunshot.

5.2 Experimental Video Analysis

The MFRC videos were produced from experiments performed primarily at the Minnesota Bureau of Criminal Apprehension Forensic Science Laboratory, in Minnesota, USA, with some performed at the Christchurch Laboratory of the Institute of Environmental Science and Research, in Christchurch, New Zealand [149]. The camera used to record the experiments was a Photron Fastcam–SA1 High–Speed Digital Video camera with most videos using either a Tamron 90 mm macro lens, Micro Nikkor 55 mm, or Micro Nikkor 105 mm lens. Proper lighting was specific to each experiment which resulted in a variety of apertures and shutter speeds used to produce the highest quality videos possible. Room temperature human blood with an anti coagulant was used within 72 h of the draw date for every experiment.

Of the series of over 500 videos, over 200 are posted on the MFRC Blood Pattern Analysis Videos webpage, 19 of them are directly related to blood spatter due to a gunshot, and four of those show different muzzle discharges [148]. The targets consisted of a blood soaked sponge, fabric covering the sponge, tape encompassing the entire sponge, and a silicone–encased sponge. The targets were placed at distances in the 1–182 cm range from the muzzle of the gun. Of the 19 videos available for blood spatter induced by a gunshot, five were chosen for a quantitative analysis with PIV in the present work because they either contained both forward and backward spatter, or, their spatter pattern was resolved enough (in time and space) for an accurate analysis. The five experiments used in this analysis are described in Table II.

TABLE II

Experiments from the MFRC used in this analysis. The experiment number corresponds to a part of the title of a particular video on the MFRC website.

Experiment number	Bullet caliber	Target type	Targe distance [cm]
7Aa1	.22	Bare Sponge	182
7Ab1	.44	Bare Sponge	182
7Cb3	.44	Tape–covered Sponge	182
7Db1	.44	Silicone–covered Sponge	182
7Db2	.44	Silicone–covered Sponge	182

Each frame of the high–speed videos were taken at time intervals of 0.1 ms. In the present work, PIV analysis was conducted to characterize the motion of the blood droplets. The PIV method relies on recording the positions of fluid particles (here droplets) for two time instances in quick succession on the order of a millisecond. Statistical correlation of the two images with the position of the particles allows for the determination of the velocity field, that is, the spatial distribution of velocities. Here, PIV is conducted from approximately the time the bullet impacted the sponge to two milliseconds in each experiment. The program used for PIV was PIVlab 1.41 which is an application built for the numerical computing language MATLAB [150]. The analysis was done with a fast Fourier transform (FFT) algorithm with four interrogation passes from 64, 32, 16, and finally 8 square pixels. A linear interpolator was used with a Gauss 2×3–point sub–pixel estimator and the contrast of each image was automatically locally enhanced before processing. A region of interest mask of 100×200 pixels was drawn about a centimeter from the target for backspatter, and half a centimeter from the

target for forward spatter. The dimensions for the region of interest were chosen so that it would be sufficiently large enough to capture the created spray of blood droplets, yet not too large as to increase the likelihood of a false reading by including phantom vectors. The location of the region of interest away from the target was dictated by the distance at which droplets became recognizable, as it was centered about the splash of blood droplets. Post–processing vector validation was performed, in which physically impossible vectors were deleted as outliers.

Each experiment was also analyzed for the area of each droplet, measured as the area of the droplet in flight as seen directly from frames of the high–speed videos, and the number of droplets located within a region of interest. This was done using ImageJ [151], utilizing the particle analysis toolset. A rectangular region of interest, 100×200 pixels large, was placed at approximately the same respective location as done in the PIV tests. Each experiment was analyzed at approximately 2 ms, a time which was chosen because the droplets became very easily distinguishable from the background. Automatic local thresholding was performed on each image following the method of Phansalkar, et al. [152] with a thresholding radius of 15 pixels, $k = 0.25$, and $r = 0.5$. This converted each image into a binary image which was then analyzed with the particles toolset. There were no pixel–size limiting or circularity–based restrictions imposed on the analysis.

5.3 Results and Discussion

The PIV technique described in Sec. 5.2 was employed to find the velocity magnitude at the midplane of the region of interest, parallel to the target face. For each time interval between the frames of interest, the velocity magnitude along this midplane was averaged and then these

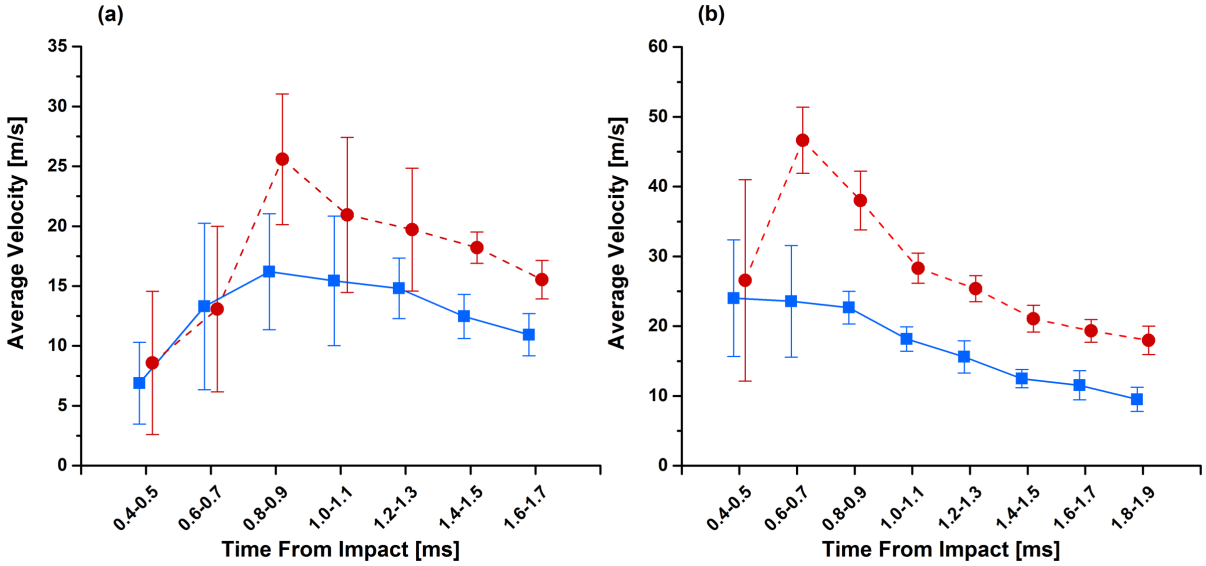

Figure 4. PIV results for experiment 7Aa1 are shown in panel (a), and for experiment 7Ab1 in panel (b). The red dashed line with circular data points represents the results from forward spatter, and the solid blue line with square data points is for backward spatter. The error bars are the standard deviations of the sets of data. Note that the data points are slightly offset from their corresponding time reckoned from the bullet impact moment in order to more easily distinguish the error bars.

velocities were plotted against the time reckoned from the bullet impact on the target. For the bare sponge experiments number 7Aa1 and 7Ab1 from Table II, this process results in Fig. 4. These two experiments are directly comparable with one another because they differ only in the caliber of bullet used and both experiments resulted in forward and backward spatter.

Figure 4 shows that the larger caliber bullet used in experiment 7Ab1 results in an overall larger average velocity for both forward and backward spattered droplets. The difference is apparent from the first data point of the analysis at a time from the bullet impact in the 0.4–0.5 ms range, all the way to the end of the experiment. For either caliber, the forward spattered

velocity is larger than that of the backward spattered velocity, even though in Fig. 4(a), the velocity gap is only noticeable starting at the 0.8–0.9 ms mark from the bullet impact time, which may be due to a large number of droplets difficult to resolve. A larger forward spatter velocity makes physical sense due to the entraining effect of the bullet traveling in the direction of the blood spatter. It is also interesting to note that as the time from the bullet impact increases, the standard deviation of the data, as indicated by the error bars, decreases due to a more uniform flow field in the corresponding part of the region of interest. The trend of the steep gradient upward and steady decrease in average velocity (cf. Fig. 4) indicates that at the onset of the analysis which was at 0.4 ms after the bullet impact, the blood droplets are accelerated. This means (from the second law of Newton applied to an individual droplet) that droplets analyzed at the onset of the PIV analysis practically do not experience air drag but on the contrary, are pulled forward by the aerodynamic wake of the fast moving, small–sized, preceding droplets from the initial splash. This is similar to the aerodynamic interaction of birds flying in V formation [110]. After about 0.6–0.9 ms, the blood droplets finally begin to slow down due air drag, since at the later stage droplets have already sufficiently separated and their mutual aerodynamic interaction has been diminished. It should be emphasized that not only in forward spatter droplets are initially accelerated, but also in backward spatter (cf. Fig. 4). Therefore, this acceleration cannot be attributed to the aerodynamic effect of the bullet preceding droplets in forward spatter but to the mutual entrainment of droplets described above.

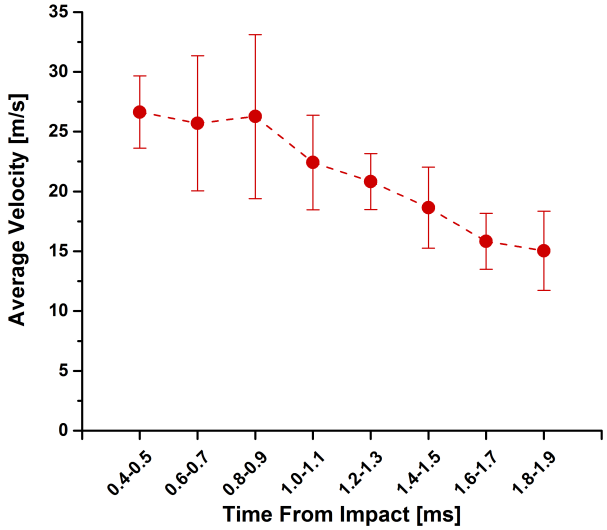

Figure 5. PIV result for the forward spattered blood data of experiment 7Cb3. The error bars are the standard deviation of the set of data.

The tape–covered sponge of experiment 7Cb3 only produced forward spattered droplets and the results from the PIV analysis are shown in Fig. 5. Since the same bullet caliber and shooting distance as in experiment 7Ab1 were used, the results in Fig. 5 can be directly compared to the forward spatter case of Fig. 4(b).

Covering the sponge with tape prevents the onset of backward spatter. Due to the spread of the error bars, an accelerated droplet motion due to the aerodynamic wake of the preceding droplets is still plausible, however, it is not directly seen in Fig. 5. The magnitude of the average velocity is approximately that of the forward spattered case shown in Fig. 4(b). The trend of a decrease in the error bar spread at a longer time is still seen, albeit to a lesser extent.

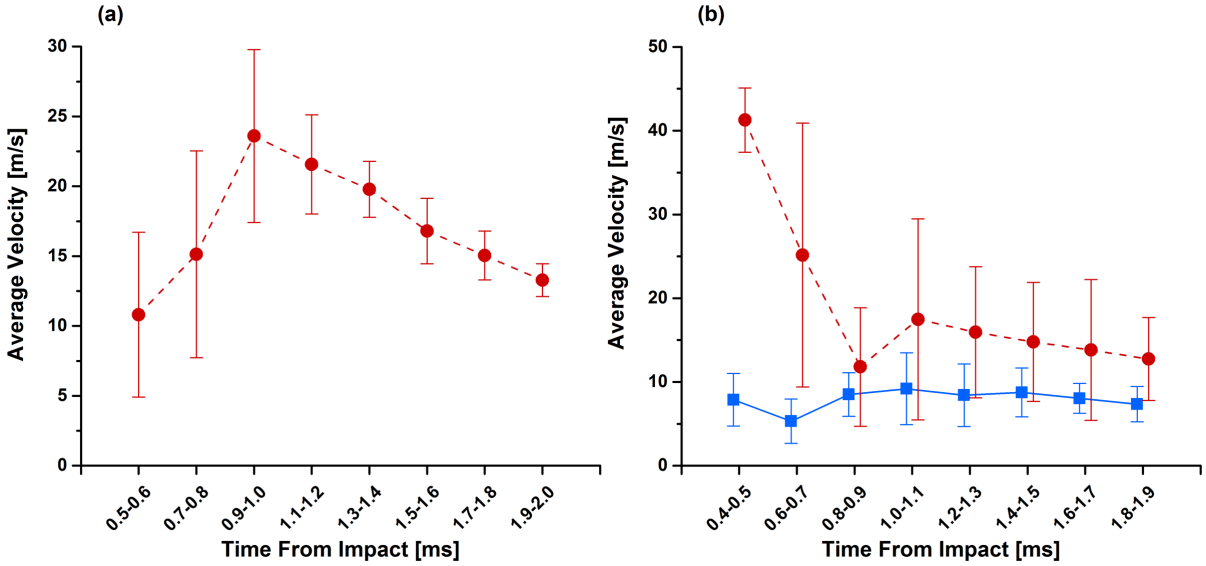

Figure 6. Droplet velocities for experiment 7Db1 shown in panel (a), and 7Db2 shown in panel (b). The red dashed lines with circular data points represent the results for forward spatter, and the solid blue line with square data points is for backward spatter. The error bars are the standard deviations of the set of data. Note that the data points are once again slightly offset from their corresponding time from impact value in order to more easily distinguish the error bars.

The two experiments with silicone–covered sponges, 7Db1 and 7Db2, were conducted using the same caliber of bullet and the same shooting distance. The results for the 7Db1 and 7Db2 experiments are presented in Fig. 6.

Even though experiments 7Db1 and 7Db2 were conducted under exactly the same conditions as indicated in Table II, 7Db1 only resulted in forward spatter, whereas 7Db2 revealed both forward and backward spatter. This sheds light on the complexity of performing repeatable BPA experiments: it means that for this set of experiments, there are some uncontrolled factors which result in two very different outcomes. Upon careful inspection of the high–speed videos,

it seems that the silicone–encased sponge in experiment 7Db2 held more blood. Even more critically, the blood seems to have pooled to the backside of the target where backward spatter would form. Therefore, the presence of backward spatter in only one of these trials could simply be explained by the undocumented blood filling process of the silicone–encased sponge, or by gravity–driven transport of blood. Regardless of this deficiency, Fig. 6(b) still reveals the important result of a faster average blood velocity for forward spattered droplets versus backward spattered droplets.

It should be emphasized that the PIV results shown in Figs. 4–6 do not contain data with the initial velocities of the droplets. All data points were taken starting at 0.4 ms after the bullet impacted the target (except for experiment 7Db1 where data started at 0.5 ms due to the inability to accurately resolve the droplets at an earlier moment of time, the early frames are completely blurry). The analysis was only conducted for the time interval when the droplets became clear enough to get accurate results. Droplets were formed before 0.4 ms, but with the current high–speed videos, PIV cannot be utilized to measure their velocity. The high–speed videos seem to show at least two regimes of the expulsion of droplets, the first of which has not been measured by PIV here. The first regime is a very fast moving spray which occurs almost instantaneously after the impact. After about 0.4 ms, the second regime begins to take place where the web of blood issued from the target consists of recognizable droplets moving at a much slower pace. An example of these two regimes can be seen in Fig. 7 which is a frame taken from the high–speed video of experiment 7Aa1.

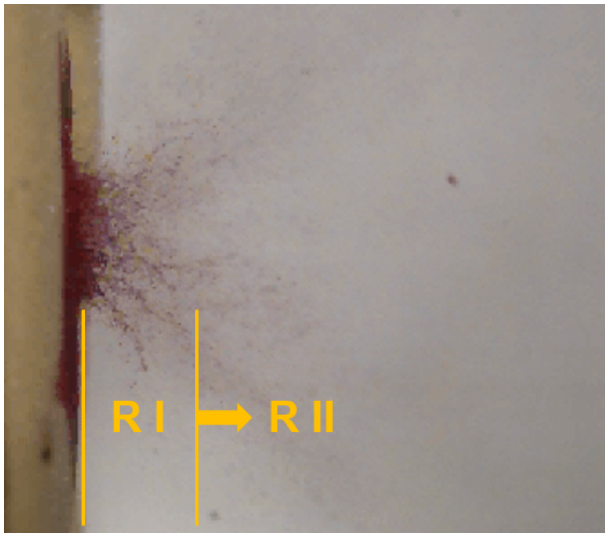

Figure 7. Cropped image of the backward spatter region of experiment 7Aa1 at 0.1 ms after the bullet impact [148]. The two labels, R I and R II, represent the two regimes found. The first regime, R I, is where recognizable droplets which are relatively large and travel relatively slowly begin to form; they were analyzed by PIV. Note, that as time goes on, the boundary between R I and R II moves towards the right of the image and at about 0.4 ms, individual droplets in R I are easy to resolve.

As described in Sec. 5.2, the number of droplets was counted with the particle analysis toolset of ImageJ within a region of interest replicating the one used in the PIV analysis. The results for the number of droplets in each experiment are shown in Fig. 8.

For the three experiments which contained both forward and backward spattered droplets, there were always more forward spattered droplets. In comparing experiments 7Aa1 and 7Ab1, which differ only in the caliber of the bullet, experiment 7Ab1, corresponding to the larger caliber, produced more droplets in both forward and backward spatter. It also seems as if the

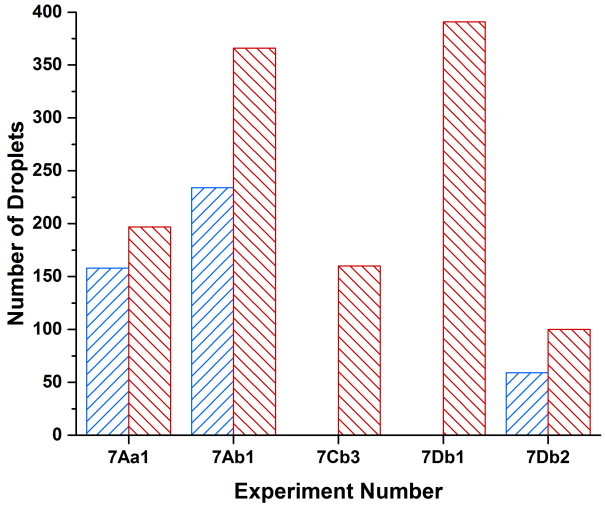

Figure 8. The number of droplets in the PIV region of interest for each experiment. The red bars with negatively sloped crosshatching are for the forward spatter and the blue bars with positively sloped crosshatching are for backward spatter.

experiments with an open–faced bare sponge produce more droplets overall when accounting for the experimental inconsistencies of 7Db1 and 7Db2.

Using the particle analysis toolset of ImageJ, the side view area of each individual droplet can also be determined. An average of all these values in each experiment is shown in Fig. 9.

For the experiments which revealed both forward and backward spattered droplets, there is an insignificant difference between the average side view area of droplets in the case of a bare sponge. The silicone–covered sponge in experiment of 7Db2 resulted in much larger backward spattered droplets, albeit that might be due to the blood pooling towards that direction in the sponge as discussed above.

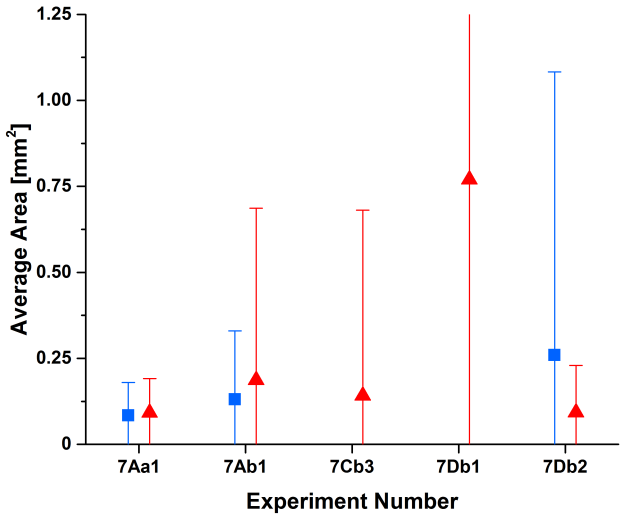

Figure 9. Average side view area of the droplets in all experimental cases. The red triangles represent forward spattered droplets and the blue squares represent the backward spattered ones. The error bars show the standard deviation. For experiment 7Db1, the error bar for the area about 0.75 mm^2 is too wide to be included in full in this frame.

Using data from the high–speed videos of each experiment at 0.5 ms after the bullet impact, the maximum angular spread of the forward and backward spatter was established by drawing tangents to the issued drop clouds near the target faces and reckoning their angles from the bullet axis. This resulted in the average upper angles of the close–to–cone domain in which droplets are issued for the forward and backward spatter of $27 \pm 9°$ and $57 \pm 7°$, respectively, whereas the lower angles of the close–to–cone domain are $28 \pm 12°$ and $30 \pm 18°$, respectively. The detailed information on these angles is given in Fig. 10, with the lower semi–angles shown as negative.

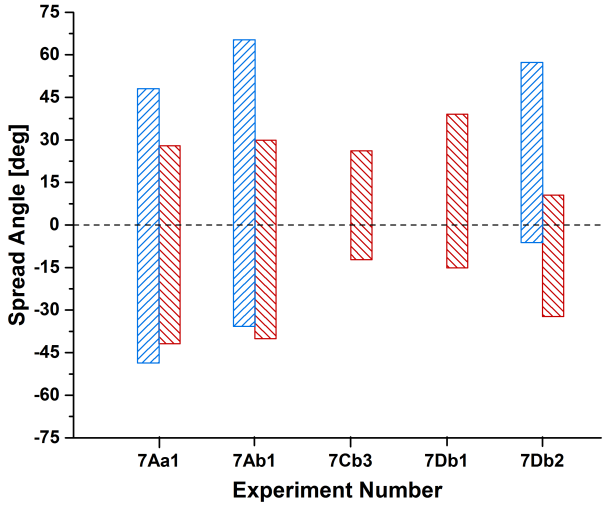

Figure 10. Spread angles of the close–to–cone domain in which droplet clouds are issued at 0.5 ms. The dashed line is the axis of symmetry of the bullet, the red bars correspond to the forward spatter and the blue bars to the backward spatter.

Figure 10 shows that backward spattered droplets have a wider spread angle than the forward spattered ones. The bare sponge experiments 7Aa1 and 7Ab1 revealed an almost symmetric upper and lower angles of the spatter domains in forward and backward spatter. Such symmetry is less prominent in the other experiments which indicates that covering a sponge with silicone or tape results in an uneven distribution of droplets. This is important because the initial droplet cloud significantly determines their further trajectories and shows that the effect of victim's clothes may be crucial for crime scene reconstruction. It should be emphasized that blood droplets were seen to form from the target periphery not penetrated by the bullet and continued to be formed long after the bullet left the target. The above–mentioned

angles correspond to 0.5 ms after the bullet impact. However, they vary in time, albeit not too much, i.e. staying close to the values shown in Fig. 10.

The effect of muzzle gases on the blood spattered droplets is more pronounced in experiments where the distance between the muzzle of the gun and target was short. An example of this is shown in a high–speed video not analyzed above, whose experiment number was 7Aa7 which was a .22 cal bullet impacting a blood–impregnated sponge at 50 cm. Several frames of this video are shown in Fig. 11.

While the motion of the muzzle gases is difficult to discern in the still images, it is clearly visible in the video. The effect of the muzzle gases is the following: as time progresses, the droplets do not only move outward from the surface of the sponge, but are also entrained by muzzle gases impinging onto the sponge and turn towards the left, which is against gravity and against backward spatter motion. This phenomena has been discussed in literature before [97], and clearly should not be ignored.

Two more observations worth noting were made when viewing the selection of MFRC videos. Both of them are revealed in the forward spattered section of experiment 7Db2, of which a series of four video frames are shown in Fig. 12.

First, note that the angle of the bullet coming out of the target is not normal to the target face. The forward spattered droplets seem to follow the axis of penetration and as a result, they travel at a downward angle of inclination. Note that this trend is opposite to what is seen for backward spattered droplets in Fig. 11. For that experiment, the bullet traveled horizontally, parallel to the floor, and therefore impacted the sponge target at an angle. The backward

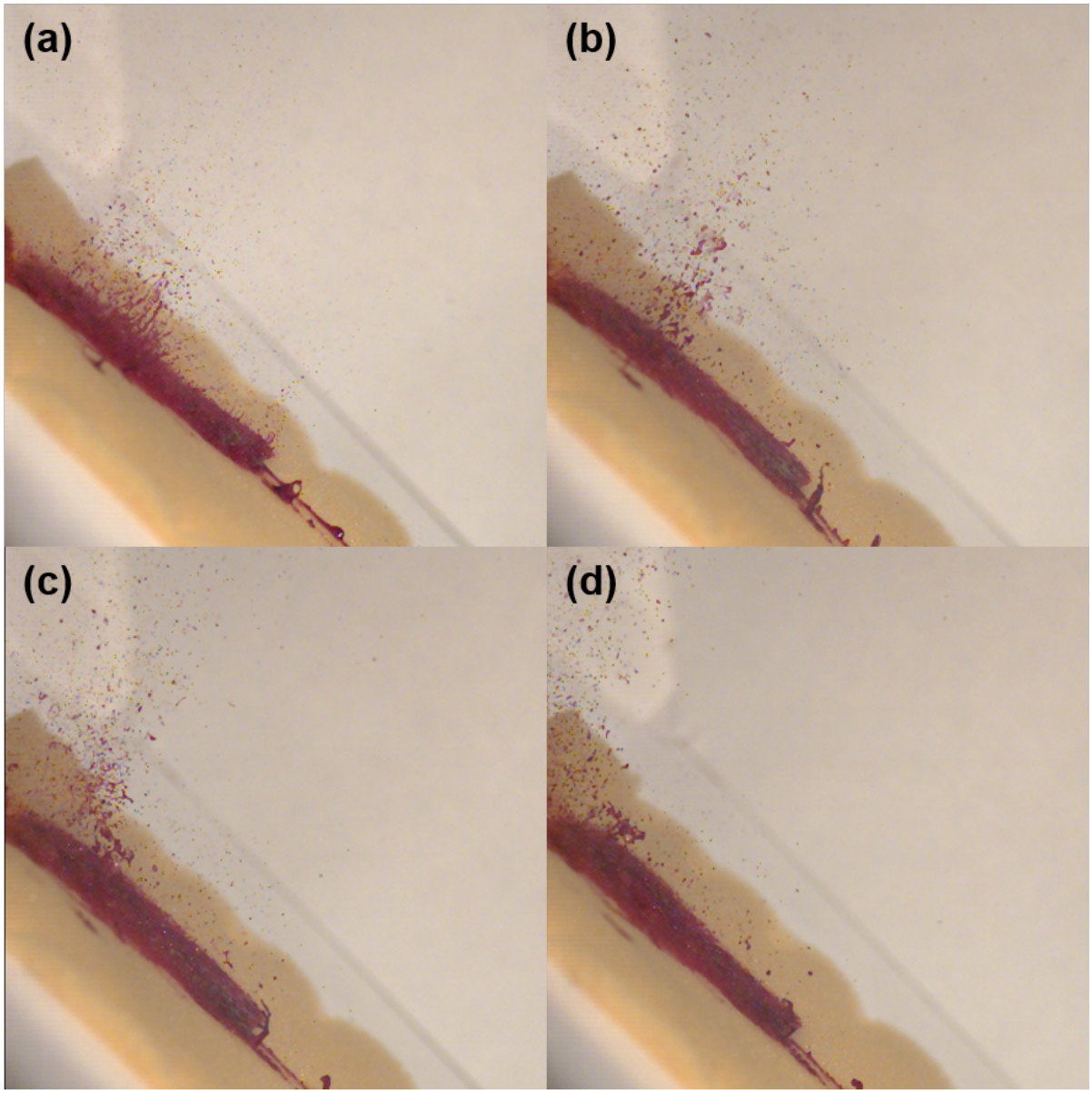

Figure 11. Frames from experiment 7Aa7 where panel (a) corresponds to 2.4 ms, (b) 6.4 ms, (c) 7.9 ms, and (d) 9.4 ms after the horizontally traveling bullet impacted the inclined sponge [148].

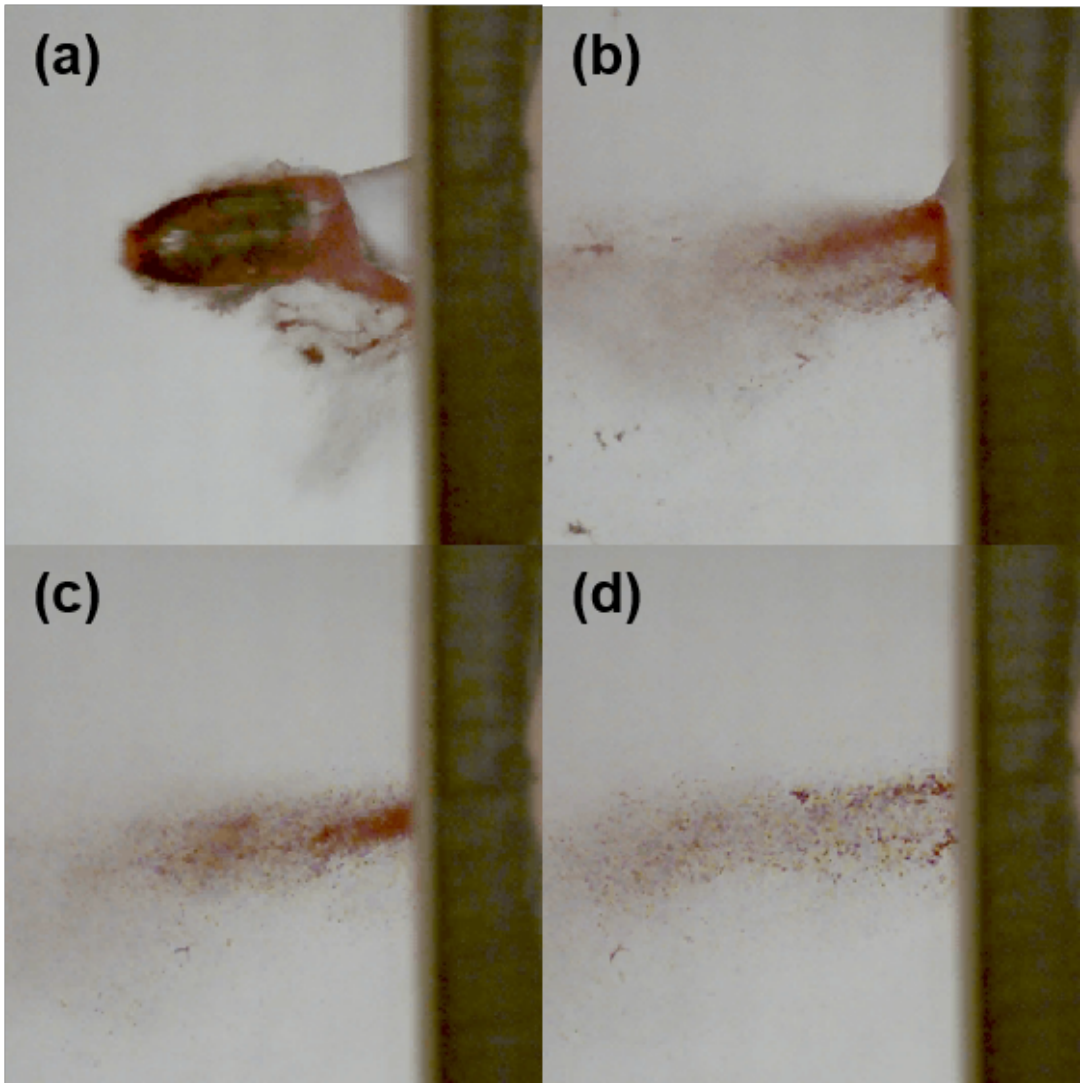

Figure 12. Frames from the forward spattered portion of experiment 7Db2 [148]. Panel (a) is 0.2 ms, (b) 0.8 ms, (c) 1.1 ms, and (d) 1.5 ms after the bullet impacted the silicon–encased sponge target.

spattered droplets are then issued normally to the face of the target, not in preference with the axis of the bullet as seen in forward spatter in Fig. 12.

The final important observation in Fig. 12 is that the issued blood droplets do not continue to travel as their initial trajectory would tend to suggest. For example, looking at the top grouping of droplets in Fig. 12(b), notice that they move downward towards the centerline of where the bullet was in Fig. 12(c), and then they continue to move in that direction as indicated in Fig. 12(d). The same phenomenon happens with the bottom grouping of droplets in Fig. 12(b), except in reverse. This means that the droplets initially traveling upwards, end up projected downwards, and vice versa for the group initially traveling downwards. The process may be difficult to visualize with only four frames of experiment 7Db2, but it is clearly visible in the MFRC video online. This phenomena can occur because of two possibilities. First, it might be that the aerodynamic wake forming behind the bullet is causing the droplets to spiral about the axis of penetration, a process which would be very difficult to see from this viewpoint and might manifest itself as this artifact. Second, the low pressure zone within the wake of the bullet may be causing the droplets to travel opposite to their initial direction. With the current set of MFRC videos, it is impossible to accurately deduce a reason. It should be emphasized that in the other videos used in this analysis which contained forward spatter, this phenomenon was only observed in experiment 7Db2.

5.4 Conclusion

Five different videos from the MFRC were quantitatively analyzed with PIV and droplet detection software. The videos are freely available to the public [148] as well as the droplet

detection software used which was ImageJ. A toolset called "analyze particles" was used after the image was converted to binary with the use of a standard, automatic local thresholding method. The PIV software was PIVlab 1.41 which is a free application that works within the MATLAB environment [150]. The average velocity of both forward spattered and backward spattered droplets, number of droplets, and average side view area were found.

When comparing experiment numbers 7Aa1 and 7Ab1, it was observed that a larger caliber bullet results in more, faster, and larger droplets in both forward and backward spatter. Covering the blood–impregnated sponge target with tape, as was done in experiment 7Cb3, reduced the amount of droplets created, and only produced forward spatter. These droplets were of about the same size as in the experiment with a comparable bullet size, 7Ab1. The average spread angles of the close–to–cone domain of the droplet cloud in the forward and backward spatter for the upper domain were measured as $27 \pm 9^\circ$ and $57 \pm 7^\circ$, respectively, whereas for the lower domain they were $28 \pm 12^\circ$ and $30 \pm 18^\circ$, respectively. Encasing the sponge in silicone produced mixed results which may be attributed to the blood filling process of the sponge. It was also noted that the blood spatter experiments clearly produced two regimes of spatter. In one of the regimes, a fine mist traveled rapidly and was created immediately after the bullet impacted the target. In another regime larger droplets propagated much slower, and within this regime the analysis contained in this work was performed. The inclination angle of the spattered blood droplets was seen to be influenced by the impact angle of the bullet which is not the case for backward spattered droplets. Additionally, the effect of muzzle gas was prominent and the aerodynamic wake of the bullet may influence the trajectory of the blood spatter.

It was found that in both forward and backward spatter, the droplets analyzed with PIV were moving with an acceleration. This is because those droplets which constitute a dense cloud practically do not experience air drag, and on the contrary are pulled forward by the aerodynamic wake of the preceding droplets spattered initially, at earlier time moments. This effect is similar to the aerodynamic interaction of birds flying in V formation. Only at the later stage when droplets are sufficiently separated, their mutual aerodynamic interaction has been diminished and they started to experience aerodynamic drag and decelerate. The MFRC video database, despite its limits in space and time resolution, contain an immense information that can facilitate the development of BPA models.

Note that the videos analyzed were chosen from the entire MFRC database because they were of high enough quality to extract reliable information on the physical mechanisms of backward and forward blood spatter. It should be emphasized that there is no known recording of the volume of blood which was used in each experiment. From viewing the videos, however, it is clear that a sufficient amount of blood was soaked into the sponge target because a spot of blood several times larger than the impacting bullet are clearly visible on each target. Nevertheless, in this work it is shown that even with such limited accompanying information, the database is a rich source for the exploration of the physical mechanisms of blood spatter aimed in the present work.

The physical aspects of the process established in this chapter facilitate and confirm the foundations of the detailed numerical models discussed in Chs. 6, 7, and 8, which describe in

detail velocities, sizes and trajectories of blood drops formed in back and forward spatter after a gunshot, as well as their impact angles and velocities, and the stain size they form.

CHAPTER 6

BACKWARD SPATTER OF BLOOD SPRAY

Parts of this chapter have been previously published in Ref. [2], reprinted with permission from [Comiskey, P. M., Yarin, A. L., Kim, S., and Attinger, D., Physical Review Fluids, 1, 043201, 2016], copyright (2016) by the American Physical Society, and Ref. [6], reprinted with permission from [Comiskey, P. M., Yarin, A. L., and Attinger, D., Physical Review Fluids, 2, 073906, 2017], copyright (2017) by the American Physical Society, as well as submitted for publication in Ref. [8].

6.1 Introduction

A theoretical model for predicting blood–spatter patterns resulting from blood droplets in backward spattering from a gunshot wound is discussed. Two bullet shapes, a blunt body and a sharp cone, respectively, are considered as limiting cases and described mathematically. The blunt bullet type belongs to the class of impact hydrodynamics with the pressure impulse generating the blood flow whereas the sharp bullet belongs to a Wagner–type problem. For both cases, the physical process generating a backward spatter of blood is linked to the Rayleigh–Taylor instability which is due to the acceleration of blood toward the surrounding quiescent air, allowing the determination of the initial distribution of drop sizes and velocities. The motion of many blood drops in air is considered with governing equations accounting for gravity and air drag as well as drop–drop interactions through air, diminishing the air drag on drops following in

the leaders wake. The models predict the atomization process, the trajectories of the backward spattered blood drops from the wound, as well as important distributions such as the number of stains and their respective areas. The theoretical results are then compared with experimental data and reveal satisfactory agreement.

6.2 Experiment

The experiments herein are a subset of an open source data set of high–resolution, 600 dots per inch (DPI), scanned images of blood spatter from a gunshot [21]. There, the experimental conditions are described in detail, and allows the forensic science community to test their models on publicly available data. Backward spattered blood droplets due to a gunshot were created at the indoor shooting range at Izaak Walton League Park in Ames, Iowa, USA. While the indoor shooting range provided quiescent air for the experiments, the environmental conditions varied with the time of the year of the specific experiments. Relative humidity was measured between 44% and 76%, with a precision of ± 5% and the room temperature was between 14.5 and 23.5 °C. The rifle used was a .223 cal Rock River Arms, LAR–15 16" barrel M–4, fit with a Yanki YHM Phantom 223 suppressor firing two different types of bullets, one hollow point (HP), and the other full metal jacket (FMJ). The HP bullet was a BEE .224 cal with a .223 Remington casing, 26.5 grain BLC–2 powder, and Winchester Small Rifle Primer. The FMJ bullet was a 5.56 mm caliber Federal Ammunition XM193 with a mass of 55 grain. The velocity of the HP bullet was measured with a chronograph as 897 m/s, and the FMJ bullet was measured to be 922 m/s.

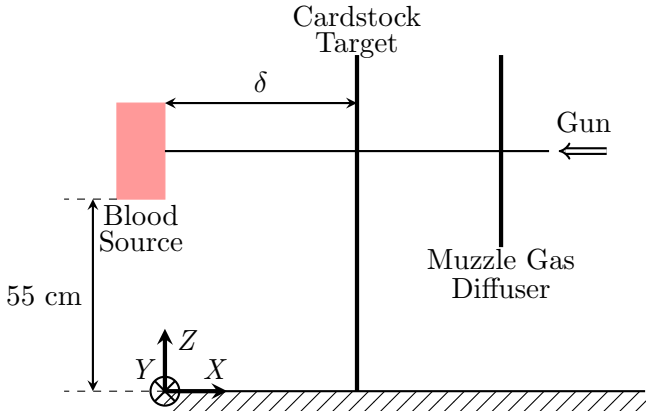

Figure 13. Schematic of the experimental setup used to generate backward spattered blood droplets impacting on a vertical substrate. Variables are dependent upon which experiment was conducted as specified in Table III. The coordinate trihedron is located on the floor, with the X–axis being parallel and coplanar (with respect to the Z–X plane) to the path of the bullet which was aimed at the target center.

The bullets were shot at either a closed hollow cavity or polyurethane foam sheet filled with 10–13 mL of swine blood. For the experiments conducted with the soaked foam target, the blood was anticoagulated with acid citrate dextrose (ACD) and had 41% hematocrit. The temperature of the blood injected into the foam was 35 ± 2 °C. For the experiments where blood was contained in a closed hollow cavity, the blood was used at room temperature and anticoagulated with heparin and had 38–39% hematocrit. In each case, the blood was drawn two days before the experiment was conducted. A schematic of the experimental setup is depicted in Fig. 13

Having in mind the effect of expanding muzzle gases interacting with blood droplets in flight as discussed in Ch. 5 and Ref. [97], the experimental setup was designed such that the

TABLE III

Parameters of the experiments of different backward blood spatter situations. The variables are defined in Fig. 13, FMJ stands for the full metal jacket bullet, HP for the hollow point bullet, V_{Blood} for the volume of blood used in the target, and the blood source corresponds to either a soaked polyurethane foam (a) or a hollow cavity (b). For all experiments, the bullet impacted the target normally and the substrate was smooth cardstock.

Experiment Number	Bullet	Blood Source	δ [cm]	V_{Blood} [mL]
Rp11#	FMJ	(a)	50	13
Rp12#	FMJ	(a)	50	13
Rf13#	HP	(a)	50	13
Rf14#	HP	(a)	50	13
Rp41	FMJ	(b)	10	10
Rp42	FMJ	(b)	30	10
Rp43	FMJ	(b)	30	10
Rp44	FMJ	(b)	30	10
Rp45	FMJ	(b)	60	10
Rp46	FMJ	(b)	60	10
Rp47	FMJ	(b)	60	10
Rp48	FMJ	(b)	120	10
Rp49	FMJ	(b)	120	10
Rp50	FMJ	(b)	120	10
Rp101	FMJ	(b)	90	10

bullet penetrated through a sheet of cardstock which acted as a diffuser to obstruct the muzzle gases from traveling downstream. The substrate which was impacted by the blood droplets was smooth cardstock.

6.3 Model for a Sharp Bullet

Bullet impact phenomena are short–term events taking place on the scale of 30 μs or even shorter, estimated with the depth of penetration of about 1 cm and the velocity of about

340 m/s. In such cases, viscous forces are always negligible compared to the inertial ones, as the Reynolds number is of the order of 10^7. Moreover, in impact hydrodynamics when pressure is high and flow processes are short, the effect of any rheological behavior (viscous or non–Newtonian) is always negligibly small compared to the pressure impulse, and only the inertial effects play a role, i.e. the initial flow field is potential, with the potential being determined by the impulse [153]. Then, under the conditions of the Lagrange theorem, which are fully applicable in the present case, the flow field will stay potential during its subsequent evolution [83]. Therefore, the splash of blood resulting from a bullet impact can effectively be considered in the framework of the inviscid potential flow approximation as in the classical Wagner problem [83, 131, 153–156].

In the experiments in Sec. 6.2, a bullet impacted a blood–impregnated sponge with open porosity and very low hydraulic resistance. The situation therefore effectively resembles the situation of a bullet impacting a pool of blood, which then splashes. It is assumed that there is no significant difference whether blood is being emitted from a free surface or from a highly porous sponge with open porosity during the stage of interest when pressure is high and flow processes are short. It is also assumed that the mechanical behavior of actual skin (a porous organ containing blood vessels including capillaries) hardly matters and thus blood splashing from a free surface seems to be a plausible model of real gunshot backspatters.

Denote the flow potential by φ and consider the axisymmetric Laplace equation, which it should satisfy in blood backspatter generated by a bullet impact,

$$\nabla^2\varphi = \frac{1}{r}\frac{\partial}{\partial r}\left(r\frac{\partial\varphi}{\partial r}\right) + \frac{\partial^2\varphi}{\partial z^2} = 0, \tag{6.1}$$

with r and z being radial and axial coordinates, respectively. Note that the z–axis corresponds to the direction of bullet impact and is directed from the free surface into the liquid bulk.

In the present work, the theoretical approach is developed and tested for a purely conical bullet shape (cf. Fig. 14) as a first approximation. A theory for a blunt bullet impact is discussed in Sec. 6.4. It should be emphasized that in both bullet type cases (or transitional shapes) backspatter of blood will be traced to the Rayleigh–Taylor instability, as is shown Sec. 6.5.

In the present case a bullet is considered as a slender body of revolution and effectively acts as a system of sources of strength q distributed along its main axis. In such cases the resulting potential can be found as [83],

$$\varphi\left(r,z\right) = -\frac{1}{4\pi}\int \frac{q\left(\xi\right)}{\sqrt{\left(\xi - z\right)^2 + r^2}}\mathrm{d}\xi, \tag{6.2}$$

where the integration is conducted over the bullet axis, with ξ being the axial dummy variable and q a function of the velocity and shape of the bullet.

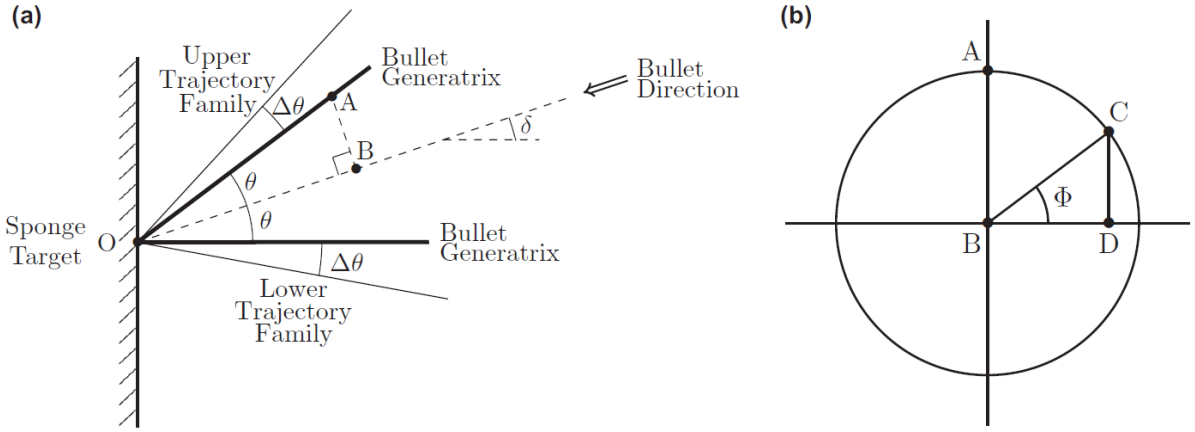

Figure 14. (a) Origin of trajectory families of blood drops in backspatter. Only two trajectory families corresponding to $\Phi = \pi/2$ (the uppermost trajectory family) and $\Phi = 3\pi/2$ (the lowermost trajectory family) are shown. (b) Normal cross section of the conical tip with the azimuthal angle Φ.

When the bullet tip has reached depth $h(t)$ below the free surface, with t being time, the condition that the surface is free is accommodated by the mirror reflection of the submerged conical part of the bullet. This allows one to introduce the integration limits as follows,

$$\varphi(r,z) = -\frac{1}{4\pi}\int_{-h}^{h} \frac{q(\xi)}{\sqrt{(\xi - z)^2 + r^2}} \mathrm{d}\xi. \tag{6.3}$$

It should be emphasized that the free surface is assumed to be located at $z = 0$, approximately at the same place where it was at the moment of the bullet impact, which is a good approximation for sufficiently slender bullets.

The strength of the sources distributed over the submerged and mirror–reflected axis of the bullet is established using the fact that the bullet surface is impenetrable for blood and thus,

$$\left.\frac{\partial \varphi}{\partial r}\right|_{\text{bullet surface}} = \frac{1}{2\pi}\frac{q(\xi)}{r|_{\text{bullet surface}}}. \tag{6.4}$$

Since at the bullet surface the normal component of blood motion is equal to the normal component of the bullet velocity, one can find from Eq. (6.4) that,

$$\frac{1}{2\pi}\frac{q(\xi)}{r|_{\text{bullet surface}}} = \begin{cases} \theta\dot{h} & \text{for} \quad 0 \le \xi \le h \\ -\theta\dot{h} & \text{for} \quad -h \le \xi \le 0 \end{cases}, \tag{6.5}$$

where the dot over h denotes time differentiation and θ is the semiangle of the bullet tip.

Accordingly,

$$q(\xi) = \begin{cases} 2\pi\, r|_{\text{bullet below surface}} \times \theta\dot{h} & \text{for} \quad 0 \le \xi \le h \\ 2\pi\, r|_{\text{bullet above surface}} \times \left(-\theta\dot{h}\right) & \text{for} \quad -h \le \xi \le 0 \end{cases}. \tag{6.6}$$

Note that the conical geometry of the bullet tip yields,

$$\begin{array}{l} r|_{\text{bullet below surface}} = (h-\xi)\tan\theta \approx (h-\xi)\,\theta \quad \text{for} \quad 0 \le \xi \le h \\ r|_{\text{bullet above surface}} = (h-\xi)\tan\theta \approx (h+\xi)\,\theta \quad \text{for} \quad -h \le \xi \le 0 \end{array}. \tag{6.7}$$

Note also that Eq. (6.7) becomes less accurate for bullet tips significantly different from a thin cone, albeit still qualitatively true. Then Eqs. (6.6), and (6.7) yield,

$$q(\xi) = \begin{cases} 2\pi\theta^2 (h-\xi) \times \dot{h} & \text{for} \quad 0 \le \xi \le h \\ -2\pi\theta^2 (h+\xi) \times \dot{h} & \text{for} \quad -h \le \xi \le 0 \end{cases}. \tag{6.8}$$

After the distribution of the sources (and also sinks corresponding to the mirror image of the submerged bullet tip) are found, Eqs. (6.3) and (6.8) result in the following expression for the flow potential,

$$\varphi(r,z) = -\frac{1}{2}\theta^2\dot{h}\int_0^h \frac{h-\xi}{\sqrt{(\xi-z)^2+r^2}}\mathrm{d}\xi + \frac{1}{2}\theta^2\dot{h}\int_{-h}^0 \frac{h+\xi}{\sqrt{(\xi-z)^2+r^2}}\mathrm{d}\xi. \tag{6.9}$$

Blood velocity at the free surface (where it is splashed against the direction of bullet motion) is found as,

$$v_z|_{z=0} = \left.\frac{\partial\varphi}{\partial z}\right|_{z=0} = -\theta^2\dot{h}\left[\frac{h}{r} + \ln\frac{r}{h+\sqrt{h^2+r^2}}\right]. \tag{6.10}$$

For example, at the free surface in contact with the penetrating bullet, i.e. at $r = \theta h$, at the moment of impact when $\dot{h} = V_0$, with V_0 being the bullet impact velocity, Eq. (6.10) yields,

$$\left.\frac{\partial\varphi}{\partial z}\right|_{z=0,\ r=\theta h} = -\theta^2\dot{h}\left[\frac{1}{\theta} + \ln\frac{\theta}{1+\sqrt{1+\theta^2}}\right] \approx -\theta\dot{h} = -\theta V_0. \tag{6.11}$$

This backspatter velocity is negative since it is directed against the positive bullet velocity V_0 and, moreover, it is much lower than the latter, since for slender bullets $\theta \ll 1$. If one takes

for the estimate $\theta = 0.24$ (which corresponds to the semiangle of 14°) and a bullet velocity of 340 m/s, the initial backspatter velocity is 80 m/s.

Evaluating the integrals in Eq. (6.9) and using the first of Eqs. (6.7) allows one to find the potential distribution at the surface of the submerged bullet tip,

$$\varphi|_{\text{bullet surface}} = -\frac{1}{2}\theta^2 \dot{h} \left[-2\,(h-z)\ln\theta + 2z + (h-z)\ln 4 + h\ln\left(\frac{z^2}{h^2-z^2}\right) + z\ln\left(\frac{h-z}{h+z}\right)\right]. \tag{6.12}$$

The nonsteady Bernoulli equation in the slender–body approximation yields the pressure p at the bullet surface as,

$$p|_{\text{bullet surface}} = -\rho \left.\frac{\partial \varphi}{\partial t}\right|_{\text{bullet surface}}, \tag{6.13}$$

where ρ is the blood density. The drag force F experienced by the penetrating bullet in the slender body approximation is found using the integral over the axially symmetric wetted surface of a slender conical bullet,

$$F = -2\pi\theta^2 \int_0^h p|_{\text{bullet surface}}\,(h-z)\,\mathrm{d}z. \tag{6.14}$$

Then Eqs. (6.12)–(6.14) yield,

$$F = \lambda\pi\theta^4\rho\left(\dot{h}\right)^2 h^2 + \lambda\frac{\pi}{3}\theta^4\rho\left(\ddot{h}\right)h^3, \tag{6.15}$$

where the dimensionless factor,

$$\lambda = \ln(2\theta) + 1. \tag{6.16}$$

It should be emphasized that for a slender bullet $\lambda < 0$ and thus the force $F < 0$, i.e. acting against the direction of bullet motion. Note also that the first term on the right–hand side (RHS) in Eq. (6.15) expresses the shape drag, whereas the second one expresses the added–mass drag.

Newton's second law for the motion of the bullet reads,

$$F = m\ddot{h}, \tag{6.17}$$

where m is the bullet mass. Substituting the expression for the drag force from Eq. (6.15) into Eq. (6.17), the equation describing bullet motion when it penetrates the blood is found,

$$\frac{\mathrm{d}^2 h}{\mathrm{d}t^2} = \frac{\lambda\pi\theta^4\rho\,(\mathrm{d}h/\mathrm{d}t)^2\,h^2}{m - \lambda\pi\theta^4\rho h^3/3}, \tag{6.18}$$

which should be solved subjected to the initial conditions,

$$t = 0: \quad h = 0,\ \frac{\mathrm{d}h}{\mathrm{d}t} = V_0. \tag{6.19}$$

Using Eq. (6.10), the acceleration of the free liquid surface A is found as,

$$A = \left.\frac{\partial v_z}{\partial t}\right|_{z=0} = -\theta^2 \frac{\mathrm{d}^2 h}{\mathrm{d}t^2}\left[\frac{h}{r} + \ln\frac{r}{h+\sqrt{h^2+r^2}}\right] - \theta^2\left(\frac{\mathrm{d}h}{\mathrm{d}t}\right)^2\left[\frac{1}{r} + \frac{1}{\sqrt{h^2+r^2}}\right]. \tag{6.20}$$

The estimates based on Eqs. (6.18)–(6.20) show that at $\mathrm{d}h/\mathrm{d}t \sim V_0 = 340$ m/s, the bullet deceleration $\mathrm{d}^2h/\mathrm{d}t^2 \sim -121$ m/s^2. Accordingly, for $h \sim r \sim 1$ cm, the second term on the RHS in Eq. (6.20) is much larger than the first one and thus the acceleration of the liquid surface that results in backspatter is,

$$A \approx -\theta^2 V_0^2\left[\frac{1}{r} + \frac{1}{\sqrt{h^2+r^2}}\right] \approx -\frac{\theta^2 V_0^2}{r}. \tag{6.21}$$

The drop velocity, according to Eq. (6.10) is then,

$$v_z|_{z=0} = -\frac{\theta^2 V_0 h}{r}. \tag{6.22}$$

Note that in Eqs. (6.21)–(6.22) $r \geq \theta h$. It should be emphasized that blood moves with acceleration A toward air. Since the blood density is higher than the air density, such flow is prone to the Rayleigh–Taylor instability [157], and discussed in Sec. 6.5.

Equation (6.22) shows that the most important information pertaining to the bullet is the semiangle of its tip θ and the bullet impact velocity V_0. Sensitivity of the results to the

uncertainty in these values is not presently addressed and is considered as a task for future work.

Denote the blood drops originating from the zone $b_i \leq r \leq b_{i+1}$ as a bin i. The mass M_i of the blood drops in backspatter originating from this bin during time $\tau = ch/V_0$ is found as,

$$M_i = \tau\rho \int_{b_i}^{b_{i+1}} |\, v_z|_{z=0}| \, 2\pi r dr = 2\pi\rho \, (h\theta)^2 \, (b_{i+1} - b_i) \, c, \tag{6.23}$$

where c is a dimensionless factor. The number of drops n_i in such a bin is approximately equal to,

$$n_i = \frac{M_i}{\rho\pi l_{*,i}^3/6}, \tag{6.24}$$

where the characteristic drop size $l_{*,i}$ is assumed to be the diameter. Note that the characteristic time of the backspatter could be taken as the characteristic time of the Rayleigh–Taylor instability, which would yield in the present case $\tau \approx (\sigma/\rho)^{1/4} \, h^{3/4}/V_0^{3/2}$. This estimate is, however, quite uncertain, since the formation of multiple drops might take several characteristic times and be different for different radial coordinates r. Therefore, a uniformly valid time scale $\tau = ch/V_0$ is used, which introduced the factor c in Eq. (6.23). Its choice is discussed in Sec. 6.8.

6.4 Model for a Blunt Bullet

The blunt (HP) bullet has a front edge which resembles a disk. The impact duration $\tau \sim 1$ μs, and the impact velocity $V_0 \approx 1000$ m/s, is at least of the order of the speed of sound in blood and is supersonic relative to air. Then, the impact pressure is of the order

$\Delta p \sim \rho V_0 C_s$, where C_s is the speed of sound in blood and ρ is its density. Essentially, this is the situation where $\Delta p \to \infty$, $\tau \to 0$, and the impulse $\Pi = \int_0^\tau \Delta p \mathrm{d}t = \mathcal{O}(1)$, with t being time. Such situations are characteristic of impact–driven fluid mechanics, where the flows are inevitably potential, with the potential $\varphi = -\Pi/\rho$ [72, 131, 132, 153].

The flow potential once again satisfies the axisymmetric Laplace equation,

$$\nabla^2 \varphi = \frac{1}{r}\frac{\partial}{\partial r}\left(r\frac{\partial \varphi}{\partial r}\right) + \frac{\partial^2 \varphi}{\partial z^2} = 0, \tag{6.25}$$

with r and z being the radial and axial coordinates, respectively. The z–coordinate is reckoned along the axis of symmetry of the bullet, is zero at the free surface, and is positive in the direction away from the free surface into the liquid bulk.

The solution of the potential in Eq. (6.25) is finite at the z–axis in the liquid bulk,

$$r = 0: \quad \varphi < \infty. \tag{6.26}$$

At the free surface, the boundary conditions read,

$$z = 0: \quad \frac{\partial \varphi}{\partial z} = V_0 \text{ at } 0 < r < a, \tag{6.27}$$

$$z = 0: \quad \varphi = 0 \text{ at } a < r < \infty, \tag{6.28}$$

where a is the radius of the blunt bullet edge.

In the far field within the liquid bulk the no–flow boundary condition is imposed,

$$z = \infty : \quad \frac{\partial \varphi}{\partial z} = 0. \tag{6.29}$$

The problem (6.25)–(6.29) is singular because of the boundary conditions (6.26) and (6.28) (the axis of the cylindrical coordinate system, and the radially infinite domain, respectively). Accordingly, being solved using variable separation, it possesses a continuous spectrum ν, with the result being expressed in the form of the following Fourier–Bessel integral,

$$\varphi = \int_0^\infty D_\nu J_0 (\nu r) \, e^{-\nu z} \mathrm{d}\nu, \tag{6.30}$$

where D_ν is a constant, i.e. it does not depend on either r or z.

Accordingly, the z–component of flow velocity at the moment of impact is,

$$v_z = \frac{\partial \varphi}{\partial z} = -\int_0^\infty D_\nu \nu J_0 (\nu r) \, e^{-\nu z} \mathrm{d}\nu. \tag{6.31}$$

Accordingly, the boundary conditions (6.27) and (6.28) with the help of Eqs. (6.30) and (6.31) take the following form,

$$-\int_0^\infty D_\nu \nu J_0 (\nu r) \, \mathrm{d}\nu = V_0 \quad \text{for} \quad 0 < r < a, \tag{6.32}$$

$$-\int_0^\infty D_\nu J_0 (\nu r) \, \mathrm{d}\nu = 0 \quad \text{for} \quad a < r < \infty. \tag{6.33}$$

Introducing $\xi = r/a$ and $\eta = \nu a$, Eqs. (6.32) and (6.33) are transformed to the following form,

$$\int_0^\infty D_\nu \nu J_0(\eta\xi)\,\mathrm{d}\eta = -V_0 a^2 \quad \text{for} \quad 0 < \xi < 1, \tag{6.34}$$

$$\int_0^\infty D_\nu J_0(\eta\xi)\,\mathrm{d}\eta = 0 \quad \text{for} \quad 1 < \xi < \infty. \tag{6.35}$$

It is easy to check that Eqs. (6.34) and (6.35) are satisfied with,

$$D_\nu = \frac{2}{\pi} V_0 a^2 \left(\frac{\cos\eta}{\eta} - \frac{\sin\eta}{\eta^2}\right). \tag{6.36}$$

Substituting Eqs. (6.36) and (6.30), we arrive at the following expression for the flow potential at the blunt bullet edge,

$$\varphi|_{z=0} = \frac{2}{\pi} V_0 a \int_0^\infty \left(\frac{\cos\eta}{\eta} - \frac{\sin\eta}{\eta^2}\right) J_0(\eta\xi)\,\mathrm{d}\eta \quad \text{for} \quad 0 < \xi < 1. \tag{6.37}$$

The integrals in Eq. (6.37) can be evaluated, which yields,

$$\varphi|_{z=0} = -\frac{2}{\pi} V_0 \sqrt{a^2 - r^2} \quad \text{for} \quad 0 < r < a. \tag{6.38}$$

Also, Eqs. (6.30) and (6.36) yield the radial and axial velocity components at the free surface $1 < \xi < \infty$,

$$v_r|_{z=0} = \frac{\partial \varphi}{\partial r} = -\frac{2}{\pi} V_0 \int_0^\infty \left(\cos\eta - \frac{\sin\eta}{\eta} \right) J_1(\eta\xi)\, \mathrm{d}\eta, \tag{6.39}$$

$$v_z|_{z=0} = \frac{\partial \varphi}{\partial z} = -\frac{2}{\pi} V_0 \int_0^\infty \left(\cos\eta - \frac{\sin\eta}{\eta} \right) J_0(\eta\xi)\, \mathrm{d}\eta. \tag{6.40}$$

Evaluating the integrals in Eqs. (6.39) and (6.40), one obtains,

$$v_r|_{z=0} = 0 \quad \text{for} \quad a < r < \infty, \tag{6.41}$$

$$v_z|_{z=0} = -\frac{2}{\pi} V_0 \left[\frac{a}{\sqrt{r^2 - a^2}} - \arcsin\left(\frac{a}{r}\right) \right] \quad \text{for} \quad a < r < \infty. \tag{6.42}$$

The latter equation can be found in Ref. [153]. Note also that $v_z|_{z=0} < 0$, i.e. the flow at the free surface is directed outward, toward air. The impulsive motions are established on the time scale $\tau = ca/V_0$ where c is a dimensionless factor. Accordingly, the acceleration of blood at the free liquid surface, A, can be evaluated using Eq. (6.42) as,

$$A(r) \approx -\frac{2}{\pi} \frac{V_0^2}{ca} \left[\frac{a}{\sqrt{r^2 - a^2}} - \arcsin\left(\frac{a}{r}\right) \right]. \tag{6.43}$$

The impact velocity that generates the impulsive motions V_0 is less than the bullet approach velocity V_a, because the propagation of the sound wave within the liquid absorbs a part of the kinetic energy of the bullet. Accordingly [72, 154, 155],

$$V_0 = V_a \frac{1}{1 + 4\rho a^3 / (3m)}, \tag{6.44}$$

where m is the bullet mass. For the bullet used in the experiments (cf. Sec. 6.8), the approach velocity is $V_\mathrm{a} \approx 1000$ m/s, while $a = 0.285$ cm, and $m = 2.916$ g, which results in $V_0 = 988.90$ m/s.

6.5 Rayleigh–Taylor Instability

The interface between a dense fluid which is accelerated towards a less dense one is unstable [157]. This instability is termed the Rayleigh–Taylor instability and it can be seen to occur in a variety of situations ranging from the mushroom clouds in nuclear explosions to water suspended above oil. For backward blood spatter splashed as a result of a gunshot, the more–dense blood is accelerated towards air due to the bullet impact. As such, the solution of the perturbation equations allows one to find the most unstable wavenumber of that fluid interface as [157],

$$k_* = \sqrt{\frac{|A| (\rho_\mathrm{b} - \rho_\mathrm{a})}{3\sigma}}, \tag{6.45}$$

where A is the acceleration of the blood with density ρ_b towards air with density ρ_a, and σ is the surface tension.

The most unstable wavenumber is related to the most unstable wavelength through, $k_* = 2\pi/l_*$, and transforms Eq. (6.45) to,

$$l_* = \frac{2\pi}{\sqrt{\rho_\mathrm{b} \left|A\right| / (3\sigma)}} w, \tag{6.46}$$

where w is a dimensionless factor. The fastest growing wavelength of the Rayleigh–Taylor instability determines only the order of magnitude of the drop size, and therefore, the factor w is needed in Eq. (6.46) for an exact match. Its choice is discussed in Sec. 6.8.

Equation 6.46 determines the characteristic blood drop diameters in backward spatter as a results of the acceleration of blood towards air, i.e. A, due to a bullet and is discussed in Secs. 6.3 and 6.4.

6.6 Blood Drop Cloud Trajectories

One can assume that drops of different size groups and initial velocities form subfamilies (also known as bins), each following different trajectories. This means that the original cloud of blood drops of different sizes resulting from the Rayleigh–Taylor instability consists not of a continuous spectrum of drop sizes, but of an approximate discrete one, which is a reasonable approximation when many different sizes are involved. In other words, a discrete distribution replaces the so–called diffusion approximation for the drop–size distribution. Then each group of drops (each bin) interacts with the other groups through air and develops its own trajectory according to the laws of mechanics. Consider one of these bins and pose the problem that allows one to describe its trajectory in backspatter starting from the initial wound. Assume that drops of this size group form a continuum that can be considered as a pseudogas moving

through air (it should be emphasized that this pseudogas possesses an effective density but not a viscosity). Then air and the pseudogas form a system of two interpenetrating continua, which is known to be an effective approach in the fluid mechanics of two–phase flows [158]. Denote a parcel of drops originating from a bin by i and moving with an entrained air as a blob i. Introduce the instantaneous averaged velocity of the blob i by u_i and the instantaneous averaged velocity of air accompanying this blob due to the entrainment in motion by all its drops U_i. The interaction of an individual drop with the surrounding air corresponds to the air drag force $F_{\mathrm{D},i}$, which can be introduced using the drag coefficient $C_{\mathrm{D},i}$ [158],

$$C_{\mathrm{D},i} = \frac{F_{\mathrm{D},i}}{(1/2)\,\rho_{\mathrm{a}}\,(u_i - U_i)\,|u_i - U_i|\,\pi l_{*,i}^2}, \tag{6.47}$$

where ρ_{a} is the air density. The drag coefficient is a function of the Reynolds number for an individual drop $\mathrm{Re}_i = u_i 2l_{*,i}/\nu_{\mathrm{a}}$, with ν_{a} being the kinematic viscosity of air. The following correlation for the drag coefficient is used in the present case and applied to individual drops in the blob i [15, 159],

$$C_{\mathrm{D},i} = 0.28 + \frac{6}{\mathrm{Re}_i^{0.5}} + \frac{21}{\mathrm{Re}_i} \quad \text{for} \quad 0.1 \le \mathrm{Re}_i \le 4000. \tag{6.48}$$

This formula is used in BPA research and other fluid mechanical applications [15, 159] and its accuracy and the range of validity is comparable to those of the standard drag curve given by the Schiller–Naumann formula. Note also that in the simulations discussed in Sec. 6.8 the values of Re_i were always in the range of validity of Eq. (6.48), from 0.1 to 4000.

Then the momentum balance of air in the air–drop blob projected onto the tangent of the trajectory is given by,

$$\frac{\mathrm{d}}{\mathrm{d}t}\left(\rho_{\mathrm{a}} V U_i\right) = \sum_i n_i C_{\mathrm{D},i} \frac{1}{2} \rho_{\mathrm{a}} \left(u_i - U_i\right) \left|u_i - U_i\right| \pi l_{*,i}^2. \tag{6.49}$$

Here V is the volume of air in the air–drop blob. It should be emphasized that the effect of gravity on air motion is immaterial compared to the drop motion discussed below, i.e. the effect of gravity on the motion of an air–drop blob is determined by its effect on drop motion, while air is entrained via the interfacial drag force as in Eq. (6.49) and the viscous suction of air into the blob discussed below.

The momentum balance of drops of a chosen size group in the air–drop blob is,

$$M_i \frac{\mathrm{d}}{\mathrm{d}t}\left(u_i \boldsymbol{\tau}\right) = -F_{\mathrm{D},i} \boldsymbol{\tau} - M_i g \mathbf{k}, \tag{6.50}$$

where $\boldsymbol{\tau}$ is the unit vector tangent to the trajectory, g is gravity acceleration, and $\mathbf{k}$ is the unit vector of the vertical direction. Projecting Eq. (6.50) onto the tangent $\boldsymbol{\tau}$ to the trajectory yields,

$$M_i \frac{\mathrm{d}u_i}{\mathrm{d}t} = -n_i C_{\mathrm{D},i} \frac{1}{2} \rho_{\mathrm{a}} \left(u_i - U_i\right) \left|u_i - U_i\right| \pi l_{*,i}^2 - M_i g \frac{1}{u_i} \frac{\mathrm{d}H}{\mathrm{d}t}, \tag{6.51}$$

where H is the current elevation of the blob relative to the ground. On the other hand, the momentum balance of drops of a chosen size group (bin) in the air–drop blob, Eq. (6.50), projected onto the normal to the trajectory yields,

$$\frac{\mathrm{d}^2 H}{\mathrm{d}t^2} = -g\frac{\left[u_i^2 - (\mathrm{d}H/\mathrm{d}t)^2\right]}{u_i^2} + \frac{1}{u_i}\frac{\mathrm{d}H}{\mathrm{d}t}\frac{\mathrm{d}u_i}{\mathrm{d}t}. \tag{6.52}$$

A moving air–drop blob acts on the surrounding air as an axisymmetric air jet occupying the same space. The outside air experiences suction toward the jet core sustained by the viscous forces. The mass of air passing through the jet cross section in unit time G increases due to the suction proportional to the location along the trajectory characterized by the arc length ξ [140],

$$G = 2\pi\rho_\mathrm{a}\int_0^\infty U y dy = 8\pi\mu_\mathrm{a}\xi, \tag{6.53}$$

where the radial coordinate reckoned from the trajectory is denoted by y and μ_a is air viscosity. The volumetric flux of air through the jet cross section $\dot{V}$ is thus equal to,

$$\dot{V} = \frac{G}{\rho_\mathrm{a}} = 8\pi\nu_\mathrm{a}\xi, \tag{6.54}$$

with $\nu_\mathrm{a} = \mu_\mathrm{a}/\rho_\mathrm{a}$ being the kinematic viscosity of air.

An air–drop blob has a characteristic size of $V^{1/3}$ and it takes time $V^{1/3}/u_i$ to pass the cross section. Therefore, $V = \dot{V}\left(V^{1/3}/u_i\right)$ and thus the blob volume increases in time as,

$$V(t) = \left[8\pi\nu_{\mathrm{a}}\frac{\xi(t)}{u_i(t)}\right]^{3/2}. \tag{6.55}$$

In turbulent jet–like motion, the kinematic viscosity ν_{a} is in fact the eddy viscosity. In the framework of the semiempirical Prandtl mixing length theory it is possible to show that $\nu_a = \kappa_1 u_{i0,\max} V_{\mathrm{blood}}^{1/3}$, where $u_{i0,\max}$ and V_{blood} are the maximal initial velocity of a drop bin and volume of blood in the backspatter ($V_{\mathrm{blood}} = \sum_i M_i/\rho$), respectively, and the semiempirical constant $\kappa_1 = 0.016 - 0.019$ [140]. Accordingly, Eq. (6.55) for the air–drop volume can be transformed to,

$$\frac{V(t)}{V_{\mathrm{blood}}} = \kappa\left[\frac{\xi(t)}{V_{\mathrm{blood}}^{1/3}}\frac{u_{i0,\max}}{u_i(t)}\right]^{3/2}, \quad \kappa = 0.255 - 0.33. \tag{6.56}$$

The current arc length corresponding to the blob location along the trajectory is found as,

$$\frac{\mathrm{d}\xi}{\mathrm{d}t} = u_i, \tag{6.57}$$

and the current horizontal coordinate of the blob location along the trajectory is found as,

$$\frac{\mathrm{d}X}{\mathrm{d}t} = \sqrt{\left(\frac{\mathrm{d}\xi}{\mathrm{d}t}\right)^2 - \left(\frac{\mathrm{d}H}{\mathrm{d}t}\right)^2}. \tag{6.58}$$

The six equations, Eqs. (6.49), (6.51), (6.52), and (6.56)–(6.58), govern the motion of each blob and allow one to predict all six unknown functions, $U_i(t)$, $u_i(t)$, $V(t)$, $\xi(t)$, $H(t)$, and $X(t)$ and thus determine the trajectory as $H = H(X)$ from its origin at a bullet wound to a solid surface onto which the blob impacts as a result of backspatter. It should be emphasized that blobs with drops of different sizes will follow different trajectories and will be deposited at different places, thus forming a blood spatter pattern and the above–mentioned equations determine their mutual interaction (through air) in flight.

Having in mind a numerical solution of the system of governing equations, the equations are rendered dimensionless using the following scales: The initial drop velocity (determined by the Rayleigh–Taylor instability discussed in Sec. 6.5) $u_{i0,\max} = \theta^2 V_0/b_1$, the maximal initial velocity corresponds to bin $i = 1$ is used as a scale for air and drop velocities U_i and u_i; the initial volume of the drop blob (also determined by the Rayleigh–Taylor instability discussed in Sec. 6.5), $V_{\text{blood}}^{1/3}$ is used as a scale for the arc length ξ, the horizontal and vertical locations of the blob X and H, respectively, and for the drop size $l_{*,i}$ (also determined by the Rayleigh–Taylor instability discussed in Sec. 6.5); V_{blood} is used as a scale for the air volume in the blob V; $V_{\text{blood}}^{1/3}/u_{i0,\max}$ is used as a scale for time t. Equations (6.49), (6.51), (6.52), and (6.56)–(6.58) are transformed to the dimensionless form,

$$\frac{\mathrm{d}\overline{U}_i\overline{V}}{\mathrm{d}t} = \left(\sum_{i=1}^{N} n_i\right) \frac{1}{2} C_{\mathrm{D},i} \left(\overline{u}_1 - \overline{U}_i\right) \left|\overline{u}_1 - \overline{U}_i\right| \pi \bar{l}_{*,i}^2, \tag{6.59}$$

$$\frac{\mathrm{d}\overline{u}_i}{\mathrm{d}t} = -\frac{1}{2} n_i C_{\mathrm{D},i} \frac{\rho_{\mathrm{a}}}{\rho_{\mathrm{b}}} \left(\overline{u}_i - \overline{U}_i\right) \left|\overline{u}_i - \overline{U}_i\right| \pi \overline{l}_{*,i}^2 - \frac{1}{Fr^2} \frac{\overline{f}}{\overline{u}_i}, \tag{6.60}$$

$$\frac{\mathrm{d}\overline{H}}{\mathrm{d}t} = \overline{f}, \tag{6.61}$$

$$\frac{\mathrm{d}\overline{f}}{\mathrm{d}t} = -\frac{1}{Fr^2} \frac{\left(\overline{u}_i^2 - \overline{f}^2\right)}{\overline{u}_i^2} + \frac{\overline{f}\left(\mathrm{d}\overline{u}_i/\mathrm{d}t\right)}{\overline{u}_i}, \tag{6.62}$$

$$\overline{V}\left(t\right) = \kappa \left[\frac{\overline{\xi}\left(t\right)}{\overline{u}_i\left(t\right)}\right]^{3/2}, \quad \kappa = 0.255 - 0.33, \tag{6.63}$$

$$\frac{\mathrm{d}\overline{\xi}}{\mathrm{d}t} = \overline{u}_i, \tag{6.64}$$

$$\frac{\mathrm{d}\overline{X}}{\mathrm{d}t} = \sqrt{\left(\frac{\mathrm{d}\overline{\xi}}{\mathrm{d}t}\right)^2 - \left(\frac{\mathrm{d}\overline{H}}{\mathrm{d}t}\right)^2}. \tag{6.65}$$

It should be emphasized that Eq. (6.59) approximately expresses the fact that air entrainment is dominated by the fastest moving drops "leading" the cloud, as was previously demonstrated regarding the two–phase flows characteristic of sprinkler jets and diesel sprays [70, 71]. A similar phenomenon is commonly implied regarding the formation flight (or V formation) of a geese flock [110]. Equation (6.59) is integrated directly for the product $\overline{U}_i\overline{V}$. Also, $\overline{f}$ in

Eqs. (6.61) and (6.62) is an auxiliary variable used to split the second–order equation into two first–order ordinary differential equations (ODE's).

The governing equations (6.59)–(6.65) and the expression (6.48) incorporate the following dimensionless groups, the Reynolds and the Froude numbers, *Re* and *Fr*, respectively,

$$Re_i = Re_0 \overline{u}_i \bar{l}_{*,i} \quad \text{for} \quad Re_0 = \frac{u_{i0,\max} 2V_{\text{blood}}^{1/3}}{\nu_{\text{a}}}, \quad Fr^{-2} = \frac{g V_{\text{blood}}^{1/3}}{u_{i0,\max}^2}, \tag{6.66}$$

where $\bar{l}_{*,i} = l_{*,i}/V_{\text{blood}}^{1/3}$. Solutions of Eqs. (6.59)–(6.65) are subjected to the initial conditions,

$$t = 0: \quad \overline{U}_i = 0,\ \overline{u}_i = \frac{u_{i0}}{u_{i0,\max}},\ \overline{\xi} = 0,\ \overline{X} = 0,\ \overline{H} = \overline{H}_0,\ \overline{f} = \frac{u_{i0}}{u_{i0,\max}} \sin\psi,\ \overline{V} = 0, \tag{6.67}$$

where $\overline{H}_0 = H_0/V_{\text{blood}}^{1/3}$, with H_0 being the initial elevation and ψ the initial inclination angle from the horizontal. More details about ψ are given in the Sec. 6.7. The governing equations (6.59)–(6.65) with the initial conditions (6.67) are solved numerically using the Kutta–Merson method with an automatically chosen and variable time step depending on the requested accuracy.[1]

---

[1]The Kutta–Merson numerical scheme is usually not available in modern numerical methods literature and is therefore described in Appendix A.

6.7 Fanning of Blood Drop Clouds

To predict the sideways dispersion of blood spatter, consider a circular cross section of the conical part of a bullet by a surface normal to its main axis. Denote by Φ the angular positions over the circle, with $\Phi = 0$ corresponding to the rightmost point on the RHS, $\Phi = \pi/2$, to the uppermost point on the top, etc. Blood drops are spattered in planes incorporating the cone generatrices, while each such plane corresponds to a given value of Φ. The splash direction at the moment of impact can differ from the bullet generatrix by an angle $\Delta\theta$ due to the flowerlike opening of HP bullets, bullet mushrooming, the effect of the sponge (and skin, in reality), etc. (see Fig. 14).

Assume first that blood is splashed exactly over the generatrix of the conical part of the bullet, i.e. $\Delta\theta = 0$. Then, by straightforward geometrical considerations (see Fig. 14) it is possible to show that the trajectory family corresponding to a certain value of Φ has the initial angle of inclination to the horizon ψ given by the formula,

$$\psi = \psi_0 + \Delta\psi, \tag{6.68}$$

where the following notation for ψ_0 and $\Delta\psi$ is adopted,

$$\sin\psi_0 = \sin\theta\sin\Phi, \quad \sin\Delta\psi = \frac{\sin\delta}{\sqrt{1 + \tan^2\theta\cos^2\Phi}}. \tag{6.69}$$

Equations (6.68) and (6.69) finalize the initial conditions (6.67). Then trajectories of drops corresponding to all bins i (having the same initial inclination ψ for any direction Φ of interest)

can be found by numerical integration of the system Eqs. (6.59)–(6.65) subject to the initial conditions of Eq. (6.67). Thus, for each drop its horizontal landing distance X_Φ from the origin can be predicted. The corresponding X and Y coordinates on the floor [the longitudinal coordinate X belongs to the central plane ($\Phi = \pi/2$, or $\Phi = 3\pi/2$), while Y is the lateral coordinate reckoned from this plane (see Fig. 13)] are found as,

$$X = X_\Phi \frac{\cos\delta\cos\theta}{\sqrt{\cos^2\delta\cos^2\theta + \sin^2\theta\cos^2\Phi}}, \tag{6.70}$$

$$Y = X\frac{\tan\theta\cos\Phi}{\cos\delta}. \tag{6.71}$$

It should be emphasized that if $\Delta\theta \neq 0$, then θ in Eqs. (6.70) and (6.71) should be replaced by $\pm(\theta + \Delta\theta)$ for the upper and lower trajectory families, respectively [see Fig. 14(a)].

6.8 Results and Discussion

The scanned images of the cardstock sheet, which was located vertically at a distance of 50 cm from the target and perforated by a sharp and blunt bullet, were discretized radially from the penetration location to the furthest drop into ten concentric disk–shaped areas of equal width. In each ring–shaped segment, the number of stains was counted and summed to find the number of stains per segment. Also, the average stain area and the impact angle per segment were found. These values were attributed at the location of the mid radius of each segment. This procedure resulted in ten data points for the number of drops, the average stain

area, and the total stain area as the functions of the radial coordinate from the blunt bullet penetration location on the vertical collector sheet.

It should be emphasized that the theory of Secs. 6.4 and 6.3 attributes formation of blood drops in backspatter to the very first moment of the impact of the edge of the bullet onto the target. Therefore, the theoretical predictions are unaffected by the following disintegration of the bullet, which can happen in the experiments. To compare the theoretical data with the results of the experiment described in Sec. 6.2, several parameters must first be defined. The following values were used in the simulations: the blunt bullet impact velocity $V_0 = 988.90$ m/s (corresponding to a bullet approach velocity of $V_\mathrm{a} \approx 1000$ m/s) the sharp bullet impact velocity $V_0 = 100.0$ m/s, radius of the impact area of the blunt bullet, $a = 0.285$ cm, the spatter spread angle for the blunt bullet, $\Delta\theta = 14^\circ$, the spatter spread angle for the sharp bullet, $\Delta\theta = 15^\circ$, the sharp bullet's cone half angle, $\theta = 5.73^\circ$, the sharp bullet's depth of penetration, $h = 0.5$ cm, the azimuthal discretization in the angular direction, $\Delta\Phi = \pi/12$, the height of the impact, $H_0 = 56.0$ cm, and the dimensionless factors for a blunt bullet as $w = 0.112$ and $c = 786.6$ whereas for a sharp bullet $w = 2.375$ and $c = 483.0$. The drop size generated by a gunshot via the Rayleigh–Taylor instability should be affected by the bullet shape, which explains the variation in the value of w [in the same order of magnitude in Eq. (6.46)]. Also, it should be emphasized that the amount of blood splashed by a blunt bullet is usually larger than that of a sharp, slender bullet. That is reflected by a different, larger value of c used in the blunt bullet. Ultimately, the value of c is affected by the bullet shape, as one of the factors, and the increased value used here reflects that fact.

The chosen value of $\Delta\theta$ can be substantiated on the basis of several published experiments and on our theoretical analysis. The x–ray measurements during impact of metallic projectiles in water in Ref. [160] revealed a conical cavity trailing the projectile with $10^\circ < \Delta\theta < 20^\circ$, for diameters and supersonic (by air) impact velocities comparable to that of our study. Interestingly, Ref. [160] reported similar values of $\Delta\theta$ for projectiles with various shapes, such as spheres, cylinders with spherical tips, and blunt cylinders. Similar values of $10^\circ < \Delta\theta < 20^\circ$ were reported in Ref. [161] for impacts of spheres in water at both low and high Bond numbers. The authors of Refs. [162, 163] used shadowgraphy to estimate the pressure field in the fluid around the projectile.

A theoretical justification of the value of $\Delta\theta$ in the present case of a blunt bullet atomization of blood can be made as follows. For both the sharp and blunt bullet case, the radial velocity of splashed liquid is equal to zero, and thus the initial ejection is expected to be strictly normal to the free surface. This is indeed observed in the intact crownlike splashes resulting from drop impact onto a liquid surface (cf. Fig. 6 in Ref. [164]). However, in the present case the ejected liquid is atomized practically from the very beginning, which results in the suction of a significant mass of air, which inevitably happens at the periphery of the spattered two–phase blob unaffected by any aerodynamic effects caused by a bullet (cf. Fig. 10 in Ch. 5). Accordingly, the ejected drop blob essentially forms an axisymmetric two–phase submerged turbulent jet. It should be emphasized that due to the air entrainment, the air–drop blob widens to compensate for the decrease of its velocity due to the action of the eddy viscosity and sustains the invariant value of the longitudinal momentum flux [140]. Accordingly, the

asymptotic boundary of the two–phase jet associated with the one–tenth longitudinal velocity, u in comparison to the corresponding axial velocity value, u_m is given by $y_{0.1} = \eta_{0.1} a_{\mathrm{T}} x$, where $\eta_{0.1}$ is the value of the self–similar coordinate corresponding to the boundary, and a_{T} is the semiempirical constant of the Prandtl mixing length theory ($a_{\mathrm{T}} = 0.045 - 0.055$) [140]. Since the self–similar velocity profile in the jet cross–section is given by $u/u_m = \left(1 + \eta^2/8\right)^{-2}$, the value of $\eta_{0.1}$ is found as $\eta_{0.1} = \left[8\left(\sqrt{10} - 1\right)\right]^{1/2} = 4.16$. Then, $\tan\Delta\theta = \mathrm{d}y_{0.1}/\mathrm{d}x = \eta_{0.1} a_{\mathrm{T}} = 0.229$ (with the value $a_{\mathrm{T}} = 0.055$ being used). Accordingly, $\Delta\theta = 13^\circ$, which is close to both values of $\Delta\theta$ used in the calculations.

Note that in Refs. [72,161], theoretical models for the evolution of the splash curtain formed at high Weber number are presented, still in the velocity range well below that of a gunshot. Also, the work of Ref. [165] explains theoretically that the cavity shape is identical for various projectile shapes, provided that the ratio of their cross–section times drag coefficient over their mass would be the same, which was verified in Ref. [166].

The case of backspatter caused by a sharp bullet belongs to the class of entry (Wagner) problems where a wedgelike or an axisymmetric body penetration into liquid is accompanied by a splashed liquid jet rising over the body generatrix and forming a thin sheet prone to atomization. The entry problems, which are essentially different from the instantaneous impact problem of blunt bullet impact, were studied in detail in the following works and references therein [72, 153–156, 167, 168]. Recently, it was shown experimentally that the splashed liquid jet rising over the body generatrix, as a consequence of the entry of the body, is displaced from the body surface due to the air gulping, which can further affect the liquid atomization process

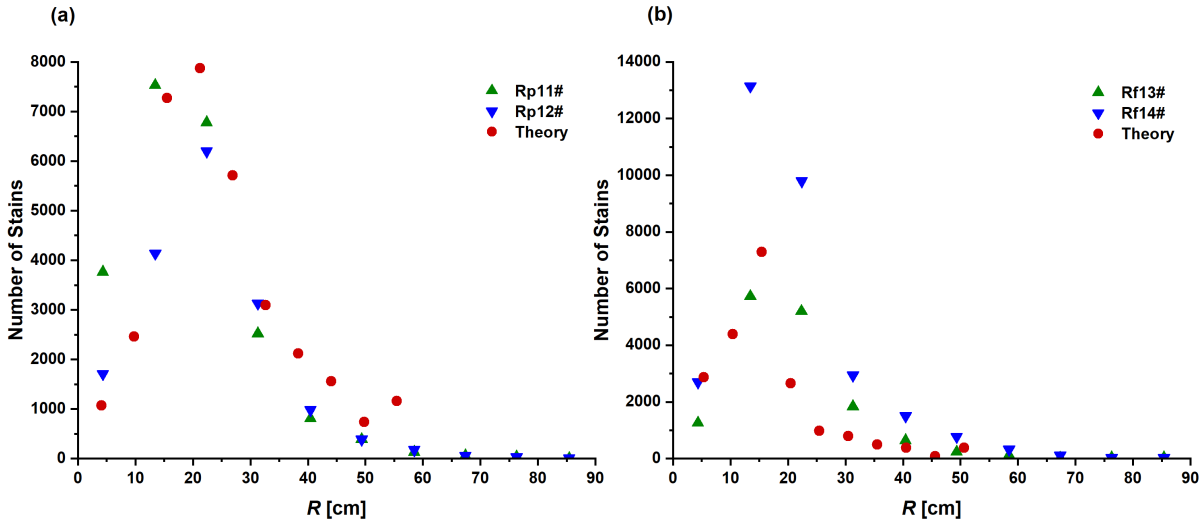

Figure 15. Number of stains on a vertical wall in the case of (a) a sharp bullet and (b) a blunt bullet. Red circles show the theoretical predictions and triangles correspond to experimental trial numbers in Table III.

in such situations [169]. In typical BPA cases, muzzle gases can also deflect the ejected blood drops as shown in Ch. 5 and quantified in Ch. 8. In particular, the effect of the muzzle gases and the underlying bones could cause $\Delta\theta \approx 90°$, as in Ref. [170]. For the present case however, the influence of the muzzle gases has been made negligible by design of the experimental setup.

It should be emphasized that the cardstock target was discretized into 10 even rings spanning the minimum and maximum radial distances from the bullet penetration hole. The median distance of each ring from the center of the hole is R. For the number of stains, the stains in each ring were added together, for the stain area and impact angle, they were averaged in each ring. Comparisons of the predicted and measured number of stains resulting from the sharp and blunt bullets are shown in Fig. 15

The experimental stain area resulting from a single–drop impact was determined by the pixel density found via a purpose–built in–house program. The theoretically predicted stain area resulting from a single–drop impact is found from the spread factor [43, 171, 172],

$$\chi = 0.61 \left(\frac{We_{\text{impact}}}{Oh_{\text{impact}}} \right)^{0.166}, \tag{6.72}$$

where $\chi = D_{\max}/l_{*,i}$, with $D_{\max}$ being the final stain diameter and the final (impact) Weber and Ohnesorge numbers being, respectively,

$$We_{\text{impact}} = \frac{\rho l_{*,i} u_{i,\text{impact}}^2}{\sigma}, \quad Oh_{\text{impact}} = \frac{\sqrt{We_{\text{impact}}}}{Re}. \tag{6.73}$$

Here $\rho = 1.06$ g/cm^3 and $\sigma = 60.45$ g/s^2 are the density and surface tension of blood found in Ch. 4, respectively, and Re is the Reynolds number of the impacting blood droplet at high shear rates[1], $\mu_{\text{shear}} = 5$ mPa–s, also discussed in Ch. 4. Since in the present case of backspatter drop impact on a vertical cardstock sheet, the impacts are not normal and therefore the spread factor alone cannot account for the arising stain area, and a relation with the impact angle must be found. Using the approach employed for crime scene reconstruction [173], the relation

[1]This is not how the spread factor was calculated in Ref. [2], rather, the Reynolds number of the droplet cluster was used and the impact velocity was taken as the magnitude, not the component that is normal to the impacted surface. See Fig. 5 in Ref. [2] and references therein.

between the longest size of drop stain, L, resulting from an oblique impact, and the stain size after normal impact, χl_* can be taken as,

$$L = \chi \frac{l_*}{\sin\alpha}, \tag{6.74}$$

with the angle α shown in Fig 16. Accordingly, the effective stain area, S, is evaluated as,

$$S = \frac{\pi l_*^2 \chi^2}{4\sin\alpha}. \tag{6.75}$$

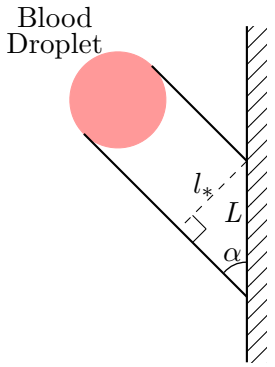

Figure 16. Stain formation in oblique drop impact onto a vertical surface.

For the same conditions as in Fig. 15, a comparison of the theoretical predictions with the experimental data for the average stain area (it should be emphasized that this is averaged in each ring) is shown in Fig. 17.

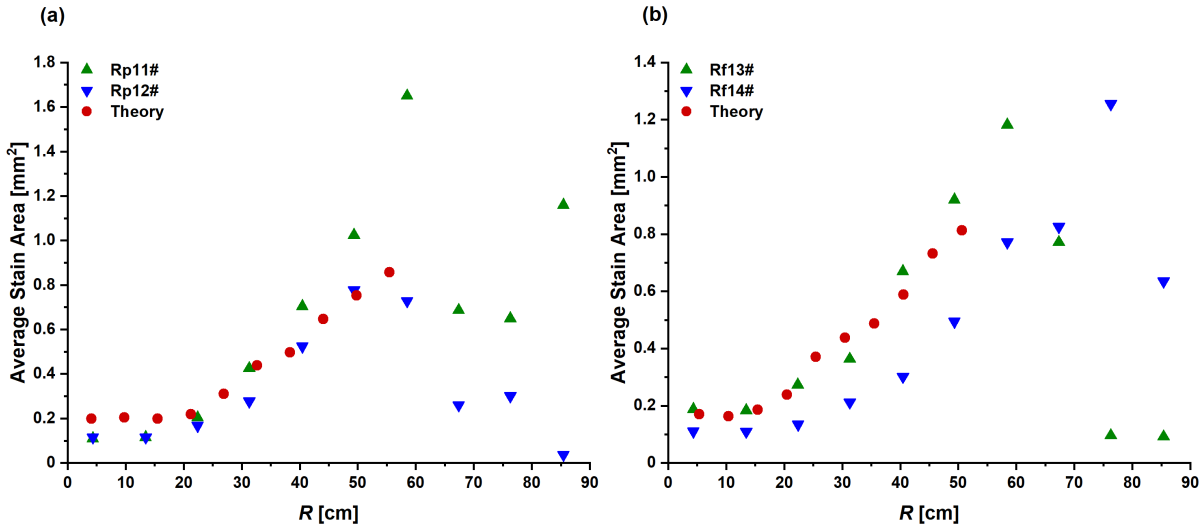

Figure 17. Average stain area of droplets impacting onto a vertical wall for (a) a sharp bullet and (b) a blunt bullet. Same notations as in Fig. 15.

The average impact angles predicted and measured under the same conditions as in Figs. 15 and 17 are shown in Fig. 18.

The two predictive models of backward spatter of blood can offer further insight to better understand various physical scenarios which BPA experts can use to quantitatively analyze crime scenes. Applying both models with the same parameters fitted to the experiments used in Figs. 15–18 and changing the distance between the blood source and the vertical cardstock target from 25–250 cm in steps of 25 cm, allows for cross–sections of the evolution of the blood droplet spray to be seen. The cumulative stained area was plotted as a function of the area of the stains in the spatter, a statistical concept that has been found useful to describe beating

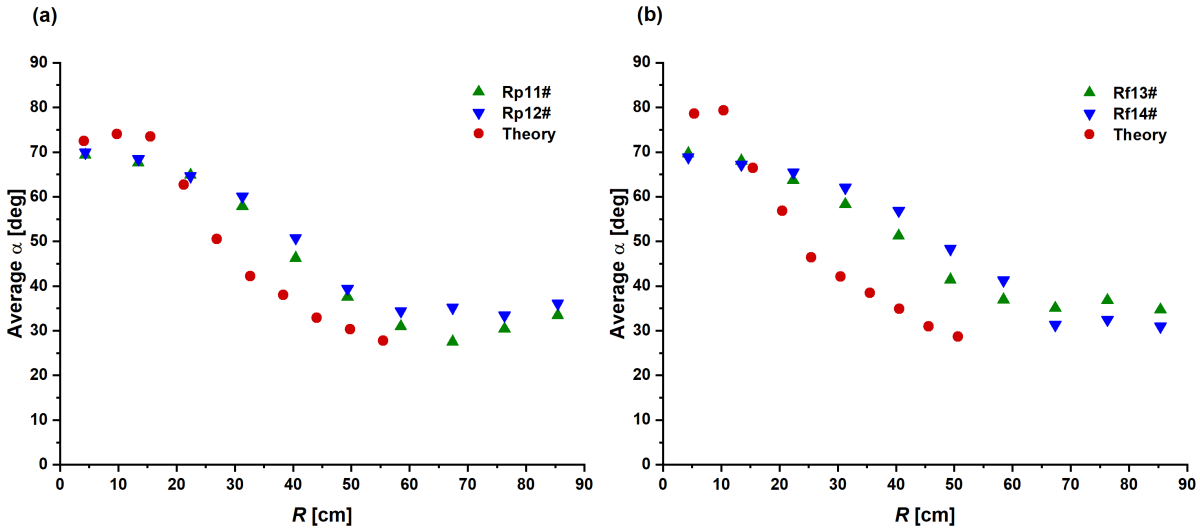

Figure 18. Average impact angle relative to a vertical wall for (a) a sharp bullet and (b) a blunt bullet. Same notations as in Figs. 15 and 17. A value of $\alpha_{\text{avg}} = 90^{\circ}$ corresponds to normal impact.

spatters [174]. Then, the value corresponding to 50% of the cumulative distribution, denoted as A_{50} and plotted as a function of the vertical substrate location, is shown in Fig. 19.

The best fit lines of Fig. 19 are useful for interpolating distance between those at which data points were taken. An appropriate fit was created with the equation,

$$A_{50} = A_0 + (B)\, e^{-\exp(-\lambda)-\lambda+1}, \tag{6.76}$$

where $\lambda = (Z - C)/D$ and the values of the parameters are listed in Table IV.

It is interesting to note that in Fig. 19, the sharp bullet produces larger droplets and at closer vertical deposition distances than its blunt bullet counterpart. The prediction from the

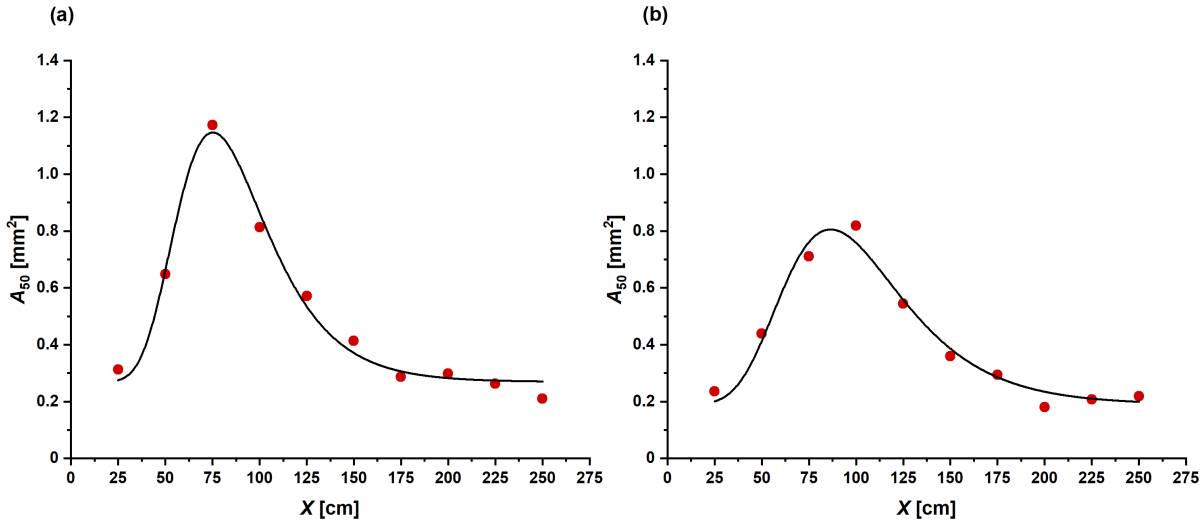

Figure 19. Area corresponding to 50% of the cumulative distribution of area as a function of the vertical impact substrate distance. Panel (a) is for a sharp bullet and (b) for a blunt bullet. The red circles are the results of the theoretical codes and the black line a best fit function.

numerical simulations in Fig. 19 that A_{50} reaches a maximum at an intermediate distance between blood source and vertical target spatter was tested against a series of gunshot backspatter experiments from [21]. As Fig. 20 shows, both experiments and numerical simulations show a comparable maximum for A_{50} at a distance of about 75–90 cm. This agreement between experiments and numerical simulations is a sign that the developed model captures the relevant fluid dynamics. Moreover, it opens a path towards quantitative crime scene reconstruction of the relative position of the blood source and the spatter based on a statistical examination of the stains.

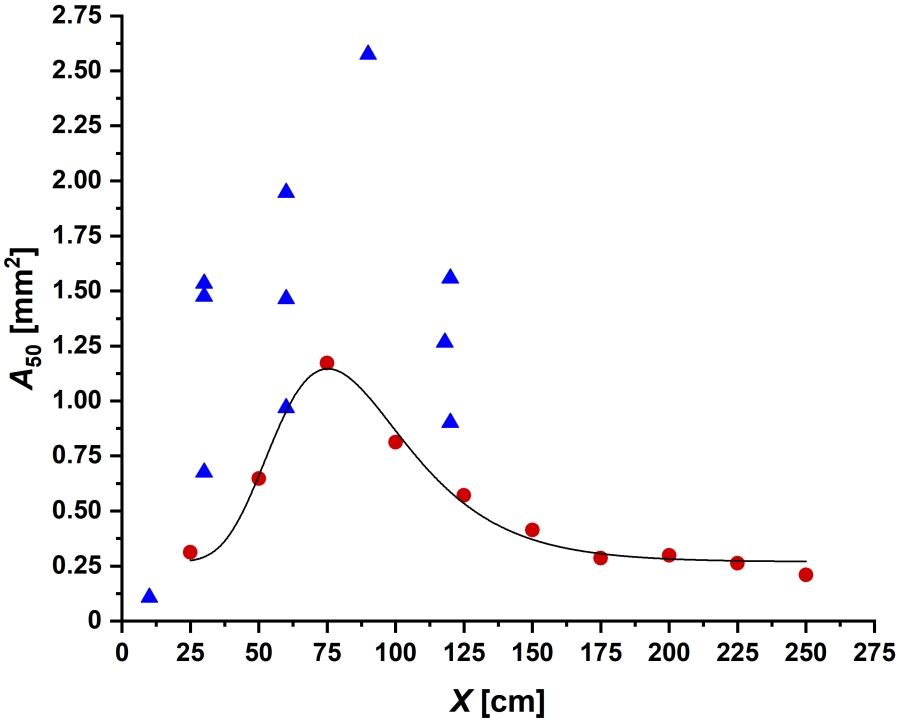

Figure 20. Comparison between experiments and the numerical simulation of A_{50} for the sharp bullet case. The blue triangles represent experimental trials Rp41–Rp50, and Rp101 in Table III, and the red circles and lines are the results of the numerical simulations shown in Fig. 19(a).

TABLE IV

Parameters in the best fit correlation of Eq. (6.76), used for the stain area corresponding to 50% of the cumulative distribution of area. The values within the parenthesis represent standard error and the last row is the coefficient of determination.

Parameters	Sharp Bullet	Blunt Bullet
A_0	0.269 (0.022)	0.190 (0.029)
B	0.877 (0.046)	0.616 (0.042)
C	75.219 (1.408)	86.481 (2.278)
D	24.033 (1.657)	31.643 (3.166)
R^2	0.978	0.959

The A_{50} value for each vertical deposition distance acts as a border between the small and large droplets. The geometric centroids, C_Y, of those less than or equal to this value as compared to those larger than A_{50}, can help facilitate a qualitative analysis performed by BPA experts on the distance to the vertical impact substrate by comparing to the quantitative analysis here. Plotting the lowest bounded centroid (from droplets $> A_{50}$) and the highest bounded centroid (from droplets $\leq A_{50}$) as a function of the vertical deposition distance is seen in Fig. 21.

Note that C_Y becomes the same and equal to approximately 60 cm for both bullet types after a certain distance. The best fit lines of Fig. 21 were found based off of the average of the two centroids and a good fit was found with a simple exponential decay function,

$$C_Y = C_0 + Fe^{-GZ}, \tag{6.77}$$

where the parameters are shown in Table V.

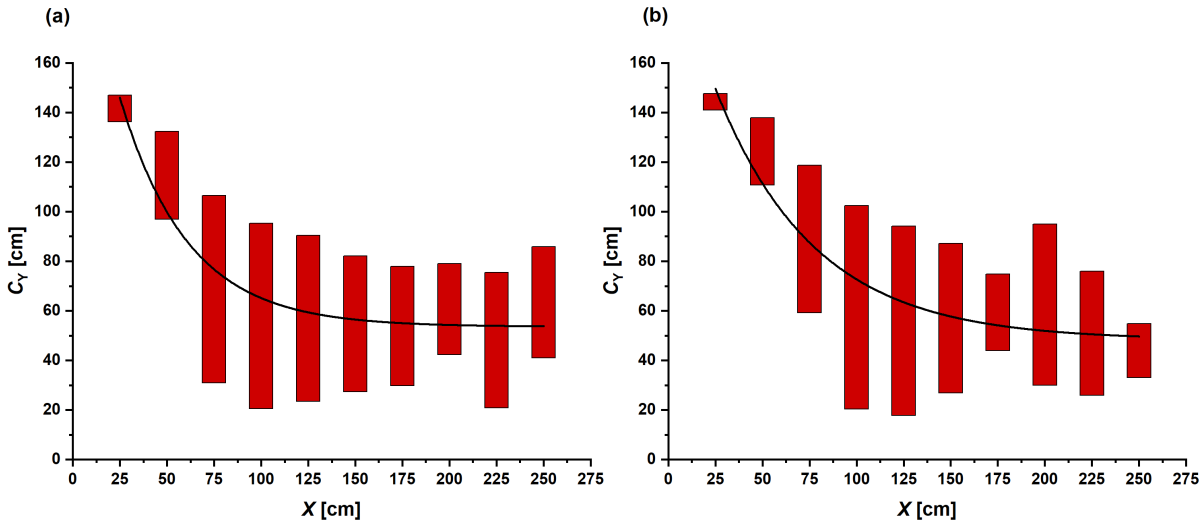

Figure 21. The geometric centroid bounded by small and large droplets corresponding to A_{50}. Panel (a) is for a sharp bullet and (b) for a blunt bullet. The red bars are the result of the theoretical codes and the black line is the best fit.

TABLE V

Parameters in the best fit correlation of Eq. (6.77) used for the centroid locations C_{Y}. The values within the parenthesis represent standard error and the last row is the coefficient of determination.

Parameters	Sharp Bullet	Blunt Bullet
C_0	53.591 (4.319)	48.273 (5.973)
F	184.433 (36.009)	162.898 (22.526)
G	0.028 (0.006)	0.0190 (0.004)
R^2	0.937	0.946

6.9 Conclusion

A series of experiments were conducted by the present group and the resultant experimental images with the raw data deposited in Ref. [21]. Four of those sets of experimental data were chosen and compared with the physically based models for sharp and blunt bullets, described in Sec. 6.3 and 6.4, respectively. These models predict that the Rayleigh–Taylor instability is responsible for blood droplet formation in backward spatter and their initial size distribution. The velocity and acceleration distribution of blood in the target are found solving the corresponding fluid mechanical problem, thus allowing for the prediction of the resulting trajectories of the droplets accounting for gravity, air drag and droplet–droplet aerodynamic interactions. The number of stains, the average stain area, and the average impact angle on the cardstock target predicted by the physical models were compared with experimental data and revealed reasonably good agreement. Also, the models were used to provide a further insight into the phenomena of backward spattered blood by predicting the locations of the stain area corresponding to a 50% cumulative distribution and the geometric centroid of the spatter pattern.

CHAPTER 7

FORWARD SPATTER OF BLOOD SPRAY

Parts of this chapter have been previously published in Ref. [3], reprinted with permission from [Comiskey, P. M., Yarin, A. L., and Attinger, D., Physical Review Fluids, 3, 063901, 2018], copyright (2018) by the American Physical Society, and submitted for publication in Ref. [9].

7.1 Introduction

A theoretical model for the chaotic disintegration of a liquid due to an arbitrarily shaped projectile is proposed. A unique solution for a bullet in the shape of an ovoid of Rankine is found. The model uses percolation theory to predict the fragmentation process of blood resulting in forward spatter to determine the number of droplets, as well as their sizes and initial velocities resulting from the flow field generated by a 9 mm bullet (close to the shape of an ovoid of Rankine), a .45 auto bullet, and a 7.62×39 mm bullet. Blood viscoelasticity, which slows down the initial velocities of the droplets, is accounted for. The size distribution of blood drops is determined, which allows for the prediction of a blood spatter cloud being ejected from the rear side of the target where the bullet exits. Then, the blood droplet spray are numerically predicted accounting for gravity and air drag, which is affected by the collective aerodynamic interaction of drops through air. The model predicts the number and area of individual stains, as well as the stain distribution as a function of distance from the region of origin. Experimental data are then compared with theoretical predictions and agreement is found to be good.

7.2 Experiment

The experimental forward spatter patterns were created at the Kansas City Police Department Crime Lab in Kansas City, MO. In an attempt to construct a reproducible blood source, a closed blood–filled reservoir was prepared as follows. A 4×4 cm^2 section of paper was peeled back from one side of foam board and approximately 5 mm of exposed foam in a central 2×2 cm^2 section was then removed and the cavity was filled with 2 mL of whole human blood containing ethylenediaminetetraacetic acid (EDTA) anticoagulant from a single individual. Clear packaging tape was then used to attach the paper back over the blood–filled section. The blood was allowed to cool to $20 - 22°$C and prior to shooting, the foam board was gently agitated to ensure homogenous displacement and limit coagulation within each cavity. Five cavities were created for five replicated shooting trials for each bullet type.

Each cavity containing 2 mL of blood was shot only once with either a 9 mm Luger FMJ bullet which is close in shape to an ovoid of Rankine, a 7.62×39 mm and a .45 auto bullet. The .45 auto bullet is similar in shape to the 9 mm one while the 7.62×39 mm bullet has a much different shape, two of which can be seen in Fig. 22. A chronograph (Competitive Edge Dynamics Model M2) was used to measure the average muzzle velocity from the five trials which was found as 350.89 ± 4.16 m/s for the 9 mm bullet, 234.47 ± 0.74 m/s for the .45 auto bullet, and 714.44 ± 31.48 m/s for the 7.62×39 mm bullet.

The blood spatter was produced on a butcher paper substrate strip (0.41×4 m^2) located on the floor behind the target. The substrate was then digitally scanned at 600 DPI and analyzed for the number of stains and their areas as a function of the distance traveled from the rear

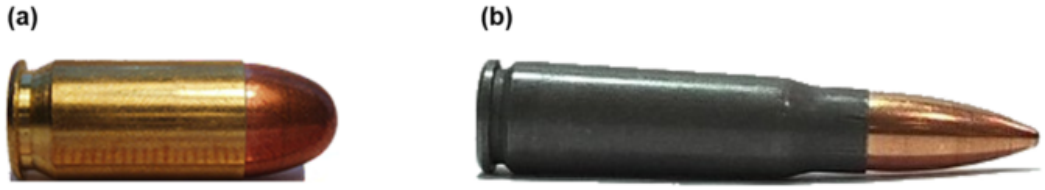

Figure 22. Images of two of the bullets used in the experiments: (a) the .45 auto bullet, and (b) the 7.62×39 mm bullet.

side of the target. These parameters were binned in the 25–400 cm range from the rear side of the target in strips 25 cm wide. Figure 23 depicts a schematic of the experimental setup and the corresponding binning method.

Note that the reported experimental results are the combination of the number of stains and their average areas over the five conducted trials for each bullet. Namely, the number of stains were added for the five experiments, and then, the stain area was averaged stripwise. The theoretical predictions were organized accordingly. The results were reported in this way to minimize the effect of any minor irreproducibility such as the bullet impacting the target off–center or arriving non–normal to the surface. Moreover, if there are multiple gunshot wounds, it can be difficult for BPA experts to attribute which bloodstain occurred as a result of a specific gunshot wound. Therefore, the total number of stains is a result of interest. Their respective stain areas were averaged over all five replicates to get an impression of the possible distribution of stain sizes.

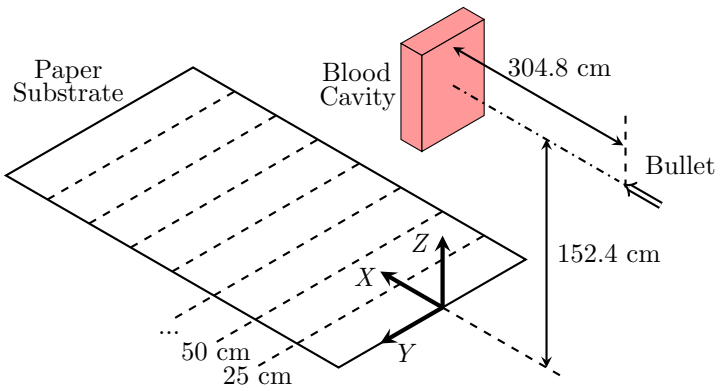

Figure 23. Schematic of the experimental setup for the study of forward spattering of blood. The muzzle of the gun was located 304.8 cm away from the front face of the target and the bullet impact was normal. When the bullet penetrated through the target, the forward blood spatter spray was generated and then deposited onto the paper substrate located on the floor. Note that the schematic is not to scale.

7.3 Theory of the Unique Solution for an Ovoid of Rankine

The formation of blood spatter due to a bullet impact is a short–term event in which the viscous forces are negligibly small compared to the inertial ones because the Reynolds number is of the order of 10^7 as described in Ch. 6. Blood spatter formation in forward spatter involves a cascade of instability phenomena, and in this sense is seemingly more involved than in the case of backward spatter, where at least the first group of spattered drops is formed due to the Rayleigh–Taylor instability associated with acceleration of denser blood toward lighter surrounding air (cf. Ch. 6). It was also found that the maximum velocity of forward spattered drops is approximately two times higher than that of backwards spattered ones partially due to

the entrainment effect of the bullet traveling in the same direction as the forward blood spatter as shown in Ch. 5.

Given the above facts, an appropriate atomization model might be one of chaotic disintegration. Such models were developed previously in the framework of percolation theory to predict the debris formation in terminal ballistics [72, 118, 175]. After atomization, the drops move through air and experience gravity and air drag forces, with the latter being diminished for the inner drops in the cloud due to collective effects associated with the aerodynamic drop–drop interaction described in Chs. 5 and 6 [70, 158]. At rates of strain as high as those characteristic of forward spatter, the viscoelasticity of blood can significantly reduce drop ejection velocities, and thus should be accounted for.

The framework of the theoretical model is built around percolation theory. First, the probability field within the target is established, and the fragmented sections are determined under the condition that the probability of a site being occupied by liquid $P < P^*$, with the latter being the critical probability value (a fully geometrical parameter known from percolation theory). This is described in Sec. 7.3.1. Then in Sec. 7.3.2, the fragmented section is discretized into bins that have the predicted initial velocities, inclination angles, and characteristic sizes. The effect of blood viscoelasticity creates a web of blood that decelerates and reconnects droplets forming a strongly interconnected web and is described in Sec. 7.3.3. Finally, the trajectories of the blood droplet spray are predicted following Ch. 6.

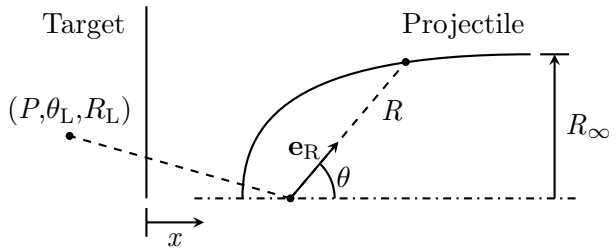

Figure 24. Schematic of the coordinates and variables used in the theoretical model.

7.3.1 Chaotic Disintegration of a Liquid

The problem of forward spatter formation is posed similarly to the formation of debris due to bullet impact and is shown schematically in Fig. 24 [72,175]. The flow field within the blood-impregnated target is potential. The bullet is assumed to be shaped like an ovoid of Rankine, which is equivalent to parallel flow superimposed on a single source. The surface of the axially symmetric ovoid of Rankine in spherical coordinates with the source at the coordinate system origin is given by Ref. [176] as,

$$R = \frac{R_\infty}{2\sin(\theta/2)}, \tag{7.1}$$

where R is the radial coordinate, θ is the zenith angle reckoned from the parallel flow direction, with $\theta = \pi$ corresponding to the tip of the bullet, and R_∞ being the cross–sectional radius of the

ovoid of Rankine at infinity. The potential flow field generated in the target by the penetrating ovoid of Rankine and resulting from its disjoining action possesses the velocity vector,

$$\mathbf{v}_{\mathrm{T}} = -\frac{\dot{x}R_{\infty}^{2}}{4R^{2}}\mathbf{e}_{\mathrm{R}}, \tag{7.2}$$

where $\dot{x}$ is the velocity of the ovoid of Rankine, and $\mathbf{e}_{\mathrm{R}}$ is the unit vector in the radial direction. Note that the coordinate x is reckoned from the front surface of the target outward, which means that $x \leq 0$ is within the target.

The target undergoes fragmentation into drops due to the angular stretching imposed by the penetrating axisymmetric bullet. When the kinetic energy of deformation becomes equal to the surface energy of a liquid element under consideration, the fragmentation process cannot be sustained anymore. Therefore, the smallest (indivisible) drop size, a_0, is determined by the equality [118],

$$\frac{1}{2}\rho a_{0}^{3}\left(\dot{\varepsilon}a_{0}\right)^{2} = \gamma a_{0}^{2}, \tag{7.3}$$

where ρ is the density of the liquid target, 1060 kg/m^3, γ is the surface tension of blood, 60.45 mN/m (cf. Ch. 4), and $\dot{\varepsilon}$ is the local rate of strain. The rate of strain in the target is on the order of,

$$\dot{\varepsilon} \sim \frac{|\dot{x}|\,R_{\infty}^{2}}{R^{3}}, \tag{7.4}$$

which shows that the azimuthal stretching process fades as $1/R^3$. Equations (7.3) and (7.4) yield,

$$a_0 \sim \left(\frac{\gamma}{\rho\dot{\varepsilon}^2}\right)^{1/3} = R_\infty \alpha^{1/3}\overline{R}^2, \tag{7.5}$$

$$V_0 = \frac{4}{3}\pi a_0^3 = \frac{4}{3}\pi R_\infty^3 \alpha \overline{R}^6, \tag{7.6}$$

where V_0 is the volume of the smallest drop, $\overline{R} = R/R_\infty$, and,

$$\alpha = \frac{\gamma}{\rho\left|\dot{x}\right|^2 R_\infty}. \tag{7.7}$$

Note that Eq. (7.5) is essentially an order–of–magnitude estimate, where the factor of the order of one is immaterial [118, 175].

As previously mentioned, the local elements of the target are fragmented due to angular stretching. This causes random lacunae growth identical to multiple observations of liquid fracture (cavitation) caused by a high–speed impact (e.g. bullet) or explosion [177–180]. To account for the random nature of such a fragmentation process, percolation theory can be applied [72, 118, 181, 182]. It should be emphasized that percolation theory is essentially a purely geometric description, which underlies the essence of multiple physical phenomena, and

thus is applicable to any medium (liquid or solid). A volume of an envelope encompassing an element of a target that is undergoing fragmentation, $\mathrm{d}V_{\mathrm{T}}$, can be estimated as,

$$\mathrm{d}V_{\mathrm{T}} = \mathrm{d}V_{\mathrm{T0}} \left(1 + \int_0^t \frac{|\dot{x}|\, R_\infty^2}{R^3} \mathrm{d}t\right)^3, \tag{7.8}$$

where $\mathrm{d}V_{T0}$ is the initial element volume of that element. The corresponding probability that an elementary particle of the size a_0 is within an elementary site inside $\mathrm{d}V_{\mathrm{T}}$ is,

$$P\left(t\right) = \frac{\mathrm{d}V_{\mathrm{T0}}}{\mathrm{d}V_{\mathrm{T0}} \left(1 + \int_0^t \frac{|\dot{x}| R_\infty^2}{R^3} \mathrm{d}t\right)^3}. \tag{7.9}$$

As $t \to \infty$, the probability that a particle of size a_0 occupies an elementary site within $\mathrm{d}V_{\mathrm{T}}$ decreases, since the angular stretching (and thus lacunae growth) continues. Therefore, there exists a certain time moment at which the probability becomes subcritical and thus small enough for an infinite cluster of the occupied elementary sites to cease existing. The critical probability value may be taken as $P^* = 0.311$ for three–dimensional percolation [118, 175, 181, 182]. In the subcritical case only finite clusters can exist, which corresponds to drops of different sizes comprised of a different number of elementary droplets of size a_0.

In the framework of the Lagrangian description of the target deformation in the present axisymmetric case, the probability field within the target $P\left(R, \theta, t\right)$ can be found. The initial radial and angular positions of a material element are denoted as R_0 and θ_0, whereas the current positions of this material element are denoted as R_{L} and θ_{L}. Then, the following set of ordinary

differential equations describes the evolution of the probability field and the current coordinates of the material element in time,

$$\frac{\mathrm{d}}{\mathrm{d}t}\left(P^{-1/3}\right) = \frac{|\dot{x}|\, R_{\infty}^2}{R_{\mathrm{L}}^3}, \tag{7.10}$$

$$\frac{\mathrm{d}R_L}{\mathrm{d}t} = \mathbf{v}_{\mathrm{T}} \cdot \mathbf{e}_{\mathrm{R}} + |\dot{x}| \cos\theta_{\mathrm{L}}, \tag{7.11}$$

$$\frac{\mathrm{d}\theta_L}{\mathrm{d}t} = \frac{1}{R_{\mathrm{L}}} \left(\mathbf{v}_{\mathrm{T}} \cdot \mathbf{e}_{\theta} - |\dot{x}| \sin\theta_{\mathrm{L}}\right), \tag{7.12}$$

where Eq. (7.10) is obtained from Eq. (7.9) by differentiation in time.

Given that $|\dot{x}|\,\mathrm{d}t = \mathrm{d}\,|x|$ (cf. Fig 24 having in mind that $x < 0$ and $\dot{x} < 0$), Eqs. (7.10)–(7.12) take the following dimensionless form,

$$\frac{\mathrm{d}}{\mathrm{d}\,|\overline{x}|}\left(P^{-1/3}\right) = \frac{1}{\overline{R}_{\mathrm{L}}^3}, \tag{7.13}$$

$$\frac{\mathrm{d}\overline{R}_{\mathrm{L}}}{\mathrm{d}\,|\overline{x}|} = \frac{1}{4\overline{R}_{\mathrm{L}}^2} + \cos\theta_{\mathrm{L}}, \tag{7.14}$$

$$\frac{\mathrm{d}\theta_{\mathrm{L}}}{\mathrm{d}\,|\overline{x}|} = -\frac{1}{\overline{R}_{\mathrm{L}}} \sin\theta_{\mathrm{L}}. \tag{7.15}$$

Here $R_{\rm L}$ and x are rendered dimensionless by R_∞. Equations (7.13)–(7.15) are solved using the following initial conditions,

$$|\overline{x}| = 0: \quad P = 1,\ R_{\rm L} = R_0,\ \theta_{\rm L} = \theta_0. \tag{7.16}$$

The analytical solutions of Eqs. (7.13) and (7.14) read [72, 175],

$$\overline{R}_{\rm L} = \left(\frac{\cos\theta_{\rm L} - \cos\theta_0 + 2\overline{R}_0^2 \sin^2\theta_0}{2\sin^2\theta_{\rm L}} \right)^{1/2}, \tag{7.17}$$

$$P = \left(1 + 2\ln \left| \frac{\overline{R}_{\rm L}^2 \sin^2\theta_{\rm L}}{\overline{R}_0^2 \sin^2\theta_0} \right| \right)^{-3}, \tag{7.18}$$

where $\overline{R}_0 = R_0/R_\infty$. The equation for the current angular position of the material element, Eq. (7.15), however, must be simultaneously numerically integrated for different material elements of the target corresponding to different values of R_0 and θ_0, as,

$$\frac{{\rm d}\theta_L}{{\rm d}\,|\overline{x}|} = -\frac{\sqrt{2}\sin^2\theta_{\rm L}}{\left(\cos\theta_{\rm L} - \cos\theta_0 + 2\overline{R}_0^2 \sin^2\theta_0 \right)^{1/2}}. \tag{7.19}$$

Note that Eqs. (7.17) and (7.18) are singular at $\theta_{\rm L} = \theta_0 = \pi$. The singularity in the limit $\theta \to \pi$ is removed by introducing $\delta_\theta = \pi - \theta \ll 1$ as $\theta \to \pi$. Then, Eqs. (7.13)–(7.15) reduce to the following equations,

$$\frac{\rm d}{{\rm d}\,|\overline{x}|} \left(P^{-1/3} \right) = \frac{1}{\overline{R}_{\rm L}^3}, \tag{7.20}$$

$$\frac{\mathrm{d}\overline{R}_{\mathrm{L}}}{\mathrm{d}\,|\overline{x}|} = \frac{1}{4\overline{R}_{\mathrm{L}}^2} - 1 + \mathcal{O}\left(\delta_\theta^2\right), \tag{7.21}$$

$$\frac{\mathrm{d}\delta_\theta}{\mathrm{d}\,|\overline{x}|} = \frac{\delta_\theta}{\overline{R}_{\mathrm{L}}} + \mathcal{O}\left(\delta_\theta^2\right). \tag{7.22}$$

The analytical solutions of the latter three equations read [72, 175],

$$P = \left(1 + 2\ln\left|\frac{\overline{R}_{\mathrm{L}}^2}{4\overline{R}_{\mathrm{L}}^2 - 1}\right| - 2\ln\left|\frac{\overline{R}_0^2}{4\overline{R}_0^2 - 1}\right|\right)^{-3}, \tag{7.23}$$

$$4\overline{R}_0 - \ln\left|\frac{2\overline{R}_0 + 1}{2\overline{R}_0 - 1}\right| = 4\,|\overline{x}| + 4\overline{R}_{\mathrm{L}} - \ln\left|\frac{2\overline{R}_{\mathrm{L}} + 1}{2\overline{R}_{\mathrm{L}} - 1}\right|, \tag{7.24}$$

$$\delta_{\theta\mathrm{L}} = \delta_{\theta 0}\left(\frac{4\overline{R}_0^2 - 1}{4\overline{R}_{\mathrm{L}}^2 - 1}\right)^{1/2}, \tag{7.25}$$

where $\delta_{\theta\mathrm{L}} = \pi - \theta_{\mathrm{L}}$ and $\delta_{\theta 0} = \pi - \theta_0$.

The probability that a material element of elementary size a_0 occupies a site in proximity to the bullet axis is thus found and its current position along that axis is determined by Eq. (7.24). However, at the bullet tip, Eqs. (7.23) and (7.24) become singular since there, $\overline{R}_{\mathrm{L}} = \overline{R}_0 = 1/2$, which means that the asymptotic behavior at this point must also be further explored. Defining

$\delta_{\mathrm{R}} \ll 1$, Eq. (7.23) for $P = P\left(R_{\mathrm{L}}\right)$ and Eq. (7.24) for $R_{\mathrm{L}} = R_{\mathrm{L}}\left(x\right)$ can be linearized about the tip point, $\delta_{\mathrm{R}} = 0$, which yields,

$$P = \left(1 + 8\left|x\right|\right)^{-3} + \frac{24\left(1 - e^{-4|x|}\right)}{\left(1 + 8\left|x\right|\right)^{4}}\delta_{\mathrm{R}} + \mathcal{O}\left(\delta_{\mathrm{R}}^{2}\right). \tag{7.26}$$

The probability that an elementary droplet of size a_0 occupies any site inside the target domain undergoing fragmentation at time t after impact is thus found.

It should be emphasized that an analytical solution for the magnitude of the coordinate of the tip of the fractured zone in the target $|\overline{x}|^{*}$ at time t^{*} reckoned from the front surface of the target can be found using Eqs. (7.23) and (7.24) as,

$$|\overline{x}|^{*} = \overline{H} + \frac{1}{2} - \overline{R}^{*} + \frac{1}{4}\left(\ln\left|\frac{2\overline{R}^{*} + 1}{2\overline{R}^{*} - 1}\right| - \ln\left|1 + \frac{1}{\overline{H}}\right|\right), \tag{7.27}$$

where

$$\overline{R}^{*} = \left(\frac{Q}{4Q - 1}\right)^{1/2}, \tag{7.28}$$

$$Q = \exp = \left(\ln\left|\frac{\left(\overline{H} + 1/2\right)^{2}}{4\left(\overline{H} + 1/2\right)^{2} - 1}\right| + \frac{\left(P^{*}\right)^{-1/3} - 1}{2}\right), \tag{7.29}$$

which uses the fact that $\overline{R}_0 = \overline{H} + 1/2$ with $\overline{H} = H/R_{\infty}$, and H is the target thickness.

To determine the distribution of mass and number of drops (finite clusters) within a volume element in the fractured zone, $\mathrm{d}V_{\mathrm{T}}$, percolation theory is applied. If s is the number of ele-

mentary indivisible droplets of size a_0 in a fragment (a finite cluster) emerging from the target ($s \geq 1$), the volume and mass of the fragment can be found using a_0 from Eq. (7.5) as,

$$V = \frac{4}{3}\pi R_{\infty}^{3}\alpha\overline{R}^{6}s, \tag{7.30}$$

$$m = \frac{4}{3}\pi\rho R_{\infty}^{3}\alpha\overline{R}^{6}s. \tag{7.31}$$

The probability density function corresponding to a cluster of s elementary indivisible droplets of size a_0 is known from percolation theory [118, 175, 181, 182] as,

$$w_s = Ks^{-\tau+1}\exp\left(-bs^{\zeta}\right), \tag{7.32}$$

where τ and ζ are known constants determined by the space dimensionality (here we are dealing with a three–dimensional case), b depends on the spatial location within the target, and K is a normalization parameter,

$$K = \frac{1}{\int_1^{\infty} s^{-\tau+1}\exp\left(-bs^{\zeta}\right)\mathrm{d}s}. \tag{7.33}$$

Using Eqs. (7.30)–(7.33), the total number of fragments of mass m_{f} in the fractured zone of the target, $\mathrm{d}N$, in $\mathrm{d}V_{\mathrm{T}}$ is found as,

$$\mathrm{d}N\left(m_{\mathrm{f}}\right) = \frac{3\mathrm{d}V_{\mathrm{T}}K}{4\pi R_{\infty}^{3}\alpha\overline{R}^{6}}\int_1^{s_{\mathrm{f}}} s^{-\tau}\exp\left(-bs^{\zeta}\right)\mathrm{d}s, \tag{7.34}$$

$$s_{\mathrm{f}}\left(m_{\mathrm{f}}, \overline{R}\right) = \max\left[1,\ \frac{3m_{\mathrm{f}}}{4\pi\alpha\rho R_{\infty}^{3}\overline{R}^{6}}\right]. \tag{7.35}$$

The upper limit of the integration in Eq. (7.34) is s_{f}, given by Eq. (7.35), which is the number of elementary indivisible droplets of size a_0 in the fragment of mass m_{f}. The total mass of the fractured target corresponding to the fragments beginning from the indivisible elementary one of size a_0 to the one of mass m_{f} is given by,

$$\mathrm{d}M\left(m_{\mathrm{f}}\right) = \rho \mathrm{d}V_{\mathrm{T}} K \int_{1}^{s_{\mathrm{f}}} s^{-\tau+1} \exp\left(-bs^{\zeta}\right) \mathrm{d}s. \tag{7.36}$$

Accordingly, the total number of fragments (finite clusters, drops) and mass in the fractured zone of the target are equal to,

$$N\left(m_{\mathrm{f}}\right) = \int_{V_{\mathrm{T}}} \mathrm{d}N\left(m_{\mathrm{f}}\right), \tag{7.37}$$

$$M\left(m_{\mathrm{f}}\right) = \int_{V_{\mathrm{T}}} \mathrm{d}M\left(m_{\mathrm{f}}\right), \tag{7.38}$$

respectively.

Evaluating these integrals using the standard parameter values and the expression familiar in percolation theory [181, 182], namely $\tau = 3/2$, $b = 20.84\left|P^{*} - P\right|^{1/\sigma}$, $\sigma = 0.45$, and $\zeta = 1$, results in,

$$N\left(m_{\mathrm{f}}\right)=-\frac{3\rho\left|\dot{x}\right|^{2}}{2\pi\gamma R_{\infty}^{2}}\int_{V_{\mathrm{T}}}\frac{K}{R^{6}}\left\{\sqrt{b\pi}\left[\operatorname{erf}\left(\sqrt{bs_{\mathrm{f}}}\right)-\operatorname{erf}\left(\sqrt{b}\right)\right]\right.$$
$$\left.+\exp\left(-bs_{\mathrm{f}}\right)s_{\mathrm{f}}^{-1/2}-\exp\left(-b\right)\right\}\mathrm{d}V_{\mathrm{T}}, \tag{7.39}$$

$$M\left(m_{\mathrm{f}}\right)=\rho\int_{V_{\mathrm{T}}}\frac{\operatorname{erf}\left(\sqrt{bs_{\mathrm{f}}}\right)-\operatorname{erf}\left(\sqrt{b}\right)}{\operatorname{erfc}\left(\sqrt{b}\right)}\mathrm{d}V_{\mathrm{T}}, \tag{7.40}$$

where the normalization parameter becomes,

$$K=\left(\frac{b}{\pi}\right)^{1/2}\frac{1}{\operatorname{erfc}\left(\sqrt{b}\right)}. \tag{7.41}$$

Equations (7.39) and (7.40) are numerically integrated over the entire fractured volume, V_{T}, which exists in the target only when $P<P^{*}$. Directly in front of the leading edge of the bullet, V_{T} is encompassed by a cone–like domain whose apex is at the location of the source generating the ovoid of Rankine (cf. Fig. 25). The boundaries of this domain are fully determined by the critical percolation value P^{*}. The semiangle of the cone, β, changes as the bullet approaches the rear surface of the target, and at a time instance of $t>t^{*}$, the fractured zone reaches the rear side of the target and the fragment cone is ejected. Between the time intervals from t (where $t>t^{*}$) to $t+\Delta t$, a new, hollow fragmented cone emerges as a result of the continuous bullet motion whose volume is found as ΔV_{T}. Eventually, this volume ΔV_{T} also leaves the target and the process repeats until $\beta\geq\pi/2$ because at that point, the cone approximation of

the fractured domain is not valid anymore and is replaced by the cylindrical one. This process continues until the bullet can freely leave the target without any further fragmentation.

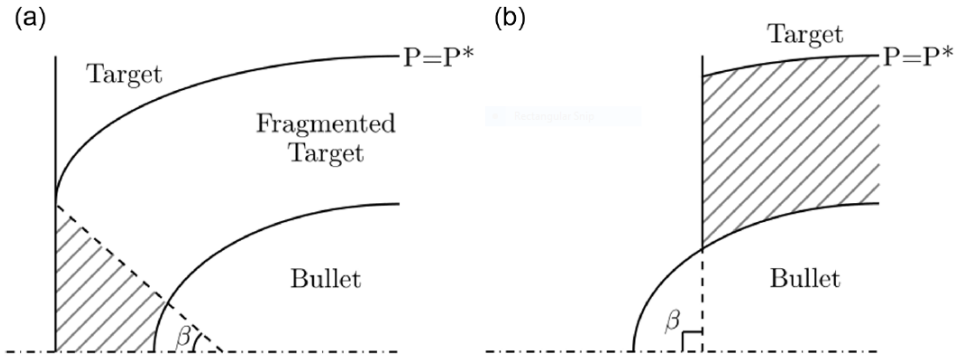

Figure 25. Target discretization types from the bullet as it travels from the right to the left. The gray cross–hatched section represents the portion of the target in which droplets form and are ejected from the target. (a) Section of the target where V_{T} is approximated as a cone, and (b) where V_{T} is approximated as a cylinder.

7.3.2 Drop Trajectories

Discretized ringlike slices of the fractured target volume, V_{T}, are termed bins and denoted by i. The number of drops and their respective masses for each bin are found using Eqs. (7.39) and (7.40). These drops are ejected from the target with velocity magnitude $u_i|_{\mathrm{initial}}$ determined by Eq. (7.2) as,

$$u_i|_{\mathrm{initial}} = \dot{x}\sqrt{\frac{R_\infty^4}{16R^4} + 1 - \frac{R_\infty^2}{2R^2}\cos\theta}, \tag{7.42}$$

at the initial inclination angle, φ, which is found as,

$$\varphi = \cos^{-1}\left[\left(2 - \frac{R_\infty^2}{2R^2}\cos\theta\right)\left(2\sqrt{\frac{R_\infty^4}{16R^4} + 1 - \frac{R_\infty^2}{2R^2}\cos\theta}\right)^{-1}\right]. \tag{7.43}$$

Each drop in the ejected bins has a characteristic size, $l_{*,i}$, calculated as,

$$l_{*,i} = \left[\frac{6\,(M_i/N_i)}{\pi\rho}\right]^{1/3}. \tag{7.44}$$

Each bin is considered as a blood drop spray that entrains air due to the turbulent eddy viscosity, thus forming a two–phase interpenetrating continuum [70, 158]. The resultant trajectory equations are described in detail in Ch. 6. It should be emphasized that the equation for the coefficient of drag used in the present work is the Schiller–Naumann formula [72],

$$C_{\mathrm{D},i} = \frac{24}{\mathrm{Re}_i}\left(1 + 0.15\mathrm{Re}_i^{0.687}\right), \tag{7.45}$$

where Re_i is the Reynolds number for each bin. The current results belong to the range of validity of this widely used correlation. Another option would be the empirical formula for the drag coefficient discussed in Ref. [15].

7.3.3 Effect of Blood Elasticity on Forward Blood Spatter

Consider a single drop of characteristic size $l_{*,i}$, disconnecting from the target at a velocity $u_i|_{\mathrm{initial}}$. Since blood is a complex, non–Newtonian fluid that exhibits viscoelastic behavior as discussed in Ch. 4, elastic stresses can build up in the rapidly stretching drop tails. Such tails are inevitably formed during the ejection of a viscoelastic fluid at a sufficiently high initial

velocity of the drops in a short–time detachment process, i.e. when the Deborah number, De, is $De \gg 1$ (cf. Ref. [1]). Here, the Deborah number is the ratio of the blood elastic relaxation time, λ, to the characteristic time of the tail detachment process $t_{\mathrm{det},i}$, i.e. $De = \lambda / t_{\mathrm{det},i}$. Note that in non–Newtonian fluid mechanics, flows with $De \gg 1$ are called strong flows. Drop tails are inevitably formed as drops separate from ligaments, films, or fully three–dimensional liquid bodies. Tail formation in viscoelastic fluids from strong elongational flows is due to significant elastic stresses. This effect was explored in detail, for example, in Ref. [183]. A similar flow scenario is present as in the current case of projectile–induced flow. It should be emphasized that at $De \gg 1$, the rheological behavior of any material essentially resembles an elastic solid. As a result, high–speed collisions with all liquids including blood cause a shock wave front to propagate followed by a rarefaction wave, which induces cavitation and solidlike brittle fracture. These spallation (fragmentation) phenomena have been experimentally observed to occur in both Newtonian (viscous and in practically inviscid) and non–Newtonian viscoelastic liquids [177–180, 184], where, for example, the brittle fracture of a liquid jet was demonstrated starting from the impact velocity as low as 23 m/s [177]. Because the impact velocity of the bullet in the current case, $|\dot{x}| = 351$ m/s, is much higher than this threshold, it is assumed that the blood droplet tails undergo brittle fracture.

The buildup of the elastic stresses in the drop tail, evident from the estimates in Ref. [1] and substantiated in Sec. 7.5, can decelerate the drop detachment process and diminish its initial ejection velocity. It should be emphasized that in the previous models of backward spatter described in Ch. 6, blood viscoelasticity was not accounted for because the drop detachment

velocities there were significantly lower than in the present case of forward spatter. For example, in a previous experiment where both forward and backward spatter were observed, at 0.45 ms after bullet impact, droplet velocity in the forward spatter case was 40 m/s, whereas for backward spatter it was only 8 m/s (cf. Ch. 5), with the former being higher than the threshold velocity of brittle fracture of 23 m/s [177], whereas the latter was lower. Accordingly, in the present case, consider a drop tail of size L_i, which still spans the detaching drop and the main body of the target. Its evolution is determined by the following kinematic equation and the momentum balance, respectively,

$$\frac{\mathrm{d}L_i}{\mathrm{d}t} = u_i, \tag{7.46}$$

$$\rho\frac{4\pi}{3}\left(\frac{l_{*,i}}{2}\right)^3\frac{\mathrm{d}u_i}{\mathrm{d}t} = -\pi\left(\frac{l_{*,i}}{2}\right)^2 3G\varepsilon_{\mathrm{xx}}, \tag{7.47}$$

where, u_i is the current drop velocity, G is the elastic shear modulus, and $\varepsilon_{\mathrm{xx}} = \left(L_i - l_{*,i}\right)/l_{*,i}$, is the tail strain.

In the momentum balance of the drop, subjected to a resistive elastic force acting on it from the stretching tail as described by Eq. (7.47), a relatively small tail stretching occurs below $L_i \approx l_{*,i}$, and before the fracture would happen, and thus, blood elasticity is described using Hooke's law [28]. Note that $G = E/3$, where E is Young's modulus of blood. The latter can be evaluated using the speed of sound in blood, $c = 1570$ m/s [185], and its density, which yields $E = 2.6$ GPa.

Equations (7.46) and (7.47) yield,

$$u_i = u_i|_{\text{initial}} \cos\left(t_i/T_i\right), \quad T_i = \left(\frac{2}{3}\frac{\rho l_{*,i}^2}{E}\right)^{1/2}. \tag{7.48}$$

Droplet detachment time $t_i = t_{\text{det},i}$, which is obviously less than T_i, increases with its size $l_{*,i}$ and an appropriate correlation between $t_{\text{det},i}$ and $l_{*,i}$ is discussed in Sec. 7.5. It should be emphasized that u_i predicted by Eq. (7.48) is used as the initial velocity in the simulations of drop trajectories.

7.4 Blood Flow Generated by a Bullet of an Arbitrary Shape

7.4.1 Generalized Chaotic Disintegration of a Liquid

For a bullet shaped as an ovoid of Rankine, flow description in the framework of potential flow theory is analytical since it is identical to the flow generated by a pointwise source located in parallel flow [176] which was employed in Sec. 7.3.1. In order to model the forward spattering of blood due to a bullet of an arbitrary shape, such as, for example, as shown in Fig. 22(b), an appropriate system of sinks and sources $\overline{q}\left(\overline{\zeta}\right)$, along the axis of symmetry of a bullet should be found which generates the potential flow about such a bullet. The flow potential generated by an axial system of sources and sinks reads (without parallel flow which can be superimposed on it) [186],

$$\overline{\varphi}\left(\overline{\xi},\overline{\eta}\right) = -\int_{\overline{\xi}_{\text{A}}}^{\overline{\xi}_{\text{E}}} \frac{\overline{q}\left(\overline{\zeta}\right)}{\left[\left(\overline{\xi}-\overline{\eta}\right)^2+\overline{\eta}^2\right]^{1/2}}\mathrm{d}\overline{\zeta}, \tag{7.49}$$

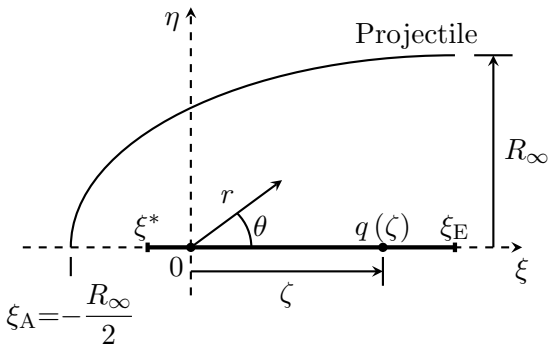

Figure 26. Schematic and variable definitions for a bullet of an arbitrary shape. The thick dark line is where a nonzero value of $q(\zeta)$ exists, and between ξ_A and ξ^* the function $q(\zeta) = 0$. Specifically, the sinks and sources are distributed over the section $\xi^* \leq \xi \leq \xi_E$ of the horizontal axis. An appropriate distribution of $q(\zeta)$ can be found to guarantee the no–penetration condition at an arbitrary axisymmetric bullet surface with the tip at $\xi_A = -R_\infty/2 < \xi^*$. The spherical coordinate system is centered at $\xi = 0$, with r being the radial coordinate of the spherical coordinate system, and θ being the corresponding azimuthal angular coordinate. The polar angular spherical coordinate reckoned about the bullet axis is ε and not shown here.

where ξ is the axial coordinate, η is the radial coordinate normal to the axis of revolution, the subscripts A and E denote axial coordinates of the bullet tip and the end, and ζ is a dummy variable. As shown with the overbar, all coordinates in Eq. (7.49) are rendered dimensionless with the cross–sectional radius of the bullet tail, R_∞, and q and φ are rendered dimensionless by $\dot{\xi}R_\infty$, where $\dot{\xi}$ is the velocity of the bullet. The spherical coordinate system used here is shown in Fig. 26, its origin is located at the distance $R_\infty/2$ to the right from the projectile tip.

The potential of the parallel flow associated with the target material motion at infinity towards the projectile is superimposed on that of the sinks and sources in Eq. (7.49), which yields,

$$\overline{\varphi}\left(\overline{\xi},\overline{\eta}\right)=\overline{\xi}-\int_{\overline{\xi}_{\mathrm{A}}}^{\overline{\xi}_{\mathrm{E}}}\frac{\overline{q}\left(\overline{\zeta}\right)}{\left[\left(\overline{\xi}-\overline{\zeta}\right)^{2}+\overline{\eta}^{2}\right]^{1/2}}\mathrm{d}\overline{\zeta}. \tag{7.50}$$

The corresponding stream function rendered dimensionless by $\dot{\xi}R_{\infty}^{2}$ is then,

$$\overline{\psi}\left(\overline{\xi},\overline{\eta}\right)=-\int_{\overline{\xi}_{\mathrm{A}}}^{\overline{\xi}_{\mathrm{E}}}\frac{\overline{q}\left(\overline{\zeta}\right)\left(\overline{\xi}-\overline{\zeta}\right)}{\left[\left(\overline{\xi}-\overline{\zeta}\right)^{2}+\overline{\eta}^{2}\right]^{1/2}}\mathrm{d}\overline{\zeta}+\frac{\overline{\eta}^{2}}{2}+\mathrm{const.} \tag{7.51}$$

The projectile tip where $\overline{\eta}=0$ belonging to the streamline $\overline{\psi}=0$, determines the constant in Eq. (7.51) as,

$$\mathrm{const}=-\int_{\overline{\xi}_{\mathrm{A}}}^{\overline{\xi}_{\mathrm{E}}}\overline{q}\left(\overline{\zeta}\right)\mathrm{d}\overline{\zeta}. \tag{7.52}$$

The entire projectile surface, $\overline{\eta}=\overline{R}\left(\overline{\xi}\right)$, also belongs to the streamline $\overline{\psi}=0$. Accordingly, Eqs. (7.51) and (7.52) yield the following integral equation for $\overline{q}\left(\overline{\zeta}\right)$,

$$\int_{\overline{\xi}_{\mathrm{A}}}^{\overline{\xi}_{\mathrm{E}}}\left\{\frac{\overline{\xi}-\overline{\zeta}}{\left[\left(\overline{\xi}-\overline{\zeta}\right)^{2}+\overline{R}^{2}\left(\overline{\xi}\right)\right]^{1/2}}+1\right\}\overline{q}\left(\overline{\zeta}\right)\mathrm{d}\overline{\zeta}=\frac{\overline{R}^{2}\left(\overline{\xi}\right)}{2}, \tag{7.53}$$

where $\overline{R}\left(\overline{\xi}\right)$ is the radial coordinate of the projectile surface [186]. Note that Eq. (7.53) is a Fredholm integral equation of the first kind for the unknown, $\overline{q}\left(\overline{\zeta}\right)$, and can be solved using

standard mathematical methods [187, 188][1]. Moreover, Eq. (7.53) does not involve a slender–body approximation. It should be emphasized that every bullet type has a different shape which means that it corresponds to a unique function $\overline{R}\left(\overline{\xi}\right)$, and thus, to a unique distribution of sources and sinks $\overline{q}\left(\overline{\zeta}\right)$. After Eq. (7.53) is solved and the distribution $\overline{q}\left(\overline{\zeta}\right)$ is found, the potential $\overline{\varphi}$ is fully determined and the velocity field about the bullet generated by the system of sources and sinks established is found as,

$$\mathbf{v}_{\mathrm{T}} = \dot{\xi}\left[\frac{\partial\overline{\varphi}}{\partial\overline{\xi}}\mathbf{e}_{\xi} + \frac{\partial\overline{\varphi}}{\partial\overline{\eta}}\mathbf{e}_{\eta}\right], \tag{7.54}$$

where subscript T corresponds to the target, the boldfaced characters denote vectors, and $\mathbf{e}_{\xi}$ and $\mathbf{e}_{\eta}$ are unit vectors in the axial and cylindrical radial directions.

Accordingly, the velocity field associated with the system of sources and sinks established takes the following form in the spherical coordinates,

$$\mathbf{v}_{\mathrm{T}} = \dot{\xi}\left[\left(\overline{r}\sin^2\theta\Gamma_1 + \cos\theta\Gamma_2\right)\mathbf{e}_r + \left(\overline{r}\sin\theta\cos\theta\Gamma_1 - \sin\theta\Gamma_2\right)\mathbf{e}_{\theta}\right], \tag{7.55}$$

where,

$$\Gamma_1 = \int_{-\overline{r}_{\mathrm{A}}}^{\overline{r}_{\mathrm{E}}} \frac{\overline{q}\left(\overline{\zeta}\right)}{\left[\left(\overline{r}\cos\theta - \overline{\zeta}\right)^2 + \overline{r}^2\sin^2\theta\right]^{3/2}}\mathrm{d}\overline{\zeta}, \tag{7.56}$$

---

[1]The evaluation of Eq. (7.53) is not trivial, therefore, its solution is discussed in Appendix B.

$$\Gamma_2 = \int_{-\overline{r}_{\mathrm{A}}}^{\overline{r}_{\mathrm{E}}} \frac{\left(\overline{r}\cos\theta - \overline{\zeta}\right)\overline{q}\left(\overline{\zeta}\right)}{\left[\left(\overline{r}\cos\theta - \overline{\zeta}\right)^2 + \overline{r}^2\sin^2\theta\right]^{3/2}} \mathrm{d}\overline{\zeta}, \tag{7.57}$$

$\overline{r}_{\mathrm{E}} = \overline{\xi}_{\mathrm{E}}$, $\overline{r}_{\mathrm{A}} = -\overline{\xi}_{\mathrm{A}}$, and $\mathbf{e}_r$ and $\mathbf{e}_\theta$ are the spherical radial and axial unit vectors in the spherical coordinate system depicted in Fig. 26.

The fragmentation of blood in the target into individual droplets is the result of angular stretching due to the bullet. This triggers a cascade of instabilities and cannot be sustained indefinitely, but rather until the kinetic energy of deformation of progressively smaller scales diminishes to the level of the surface energy at this scale. Thus, at the smallest possible scale, surface tension would cease the fragmentation process and the smallest indivisible droplet radius a_0, would be found from the following equality according to Sec. 7.3.1,

$$\frac{1}{2}\rho a_0^3 \left(\dot{\gamma} a_0\right)^2 = \sigma a_0^2, \tag{7.58}$$

where ρ and σ are the density and surface tension of blood (1060 kg/m^3 and 60.45 mN/m, respectively as per Ch. 4), and $\dot{\gamma}$ is the local rate of strain. The rate of deformation tensor $\mathbf{D}_{\mathrm{T}}$ determines the local rate of strain throughout the target as,

$$\mathbf{D}_{\mathrm{T}} = \frac{\partial v_r}{\partial r}\mathbf{e}_r \otimes \mathbf{e}_r + \frac{1}{r}\left(v_r + v_\theta \cot\theta\right)\mathbf{e}_\varepsilon \otimes \mathbf{e}_\varepsilon + \frac{1}{r}\left(v_r + \frac{\partial v_\theta}{\partial \theta}\right)\mathbf{e}_\theta \otimes \mathbf{e}_\theta, \tag{7.59}$$

where the velocity components corresponding to Eq. (7.55) and their derivatives are,

$$v_r = \dot{\xi}\left(\overline{r}\sin^2\theta\Gamma_1 + \cos\theta\Gamma_2\right), \tag{7.60}$$

$$v_\theta = \dot{\xi}\left(\overline{r}\sin\theta\cos\theta\Gamma_1 - \sin\theta\Gamma_2\right), \tag{7.61}$$

$$\frac{\partial v_r}{\partial r} = -\frac{\dot{\xi}}{R_\infty}\left[\left(1+\cos^2\theta\right)\Gamma_1 - \frac{\cos\theta}{\overline{r}}\Gamma_2 - 3\overline{r}\sin^2\theta\cos\theta\Gamma_3 + \sin^2\theta\Gamma_4\right], \tag{7.62}$$

$$\frac{\partial v_\theta}{\partial \theta} = \dot{\xi}\left[\overline{r}\cos\left(2\theta\right)\Gamma_1 - \cos\theta\Gamma_2 - 3\overline{r}^2\sin^2\theta\cos\theta\Gamma_3 + \overline{r}\sin^2\theta\Gamma_4\right], \tag{7.63}$$

and,

$$\Gamma_3 = \int_{-\overline{r}_\mathrm{A}}^{\overline{r}_\mathrm{E}} \frac{\overline{\zeta}\overline{q}\left(\overline{\zeta}\right)}{\left[\left(\overline{r}\cos\theta - \overline{\zeta}\right)^2 + \overline{r}^2\sin^2\theta\right]^{5/2}}\mathrm{d}\overline{\xi}, \tag{7.64}$$

$$\Gamma_4 = \int_{-\overline{r}_\mathrm{A}}^{\overline{r}_\mathrm{E}} \frac{\left(\overline{r}^2 + \overline{\zeta}\overline{r}\cos\theta - 2\overline{\zeta}^2\right)\overline{q}\left(\overline{\zeta}\right)}{\left[\left(\overline{r}\cos\theta - \overline{\zeta}\right)^2 + \overline{r}^2\sin^2\theta\right]^{5/2}}\mathrm{d}\overline{\xi}, \tag{7.65}$$

Note that in Eq. (7.59), $\mathbf{e}_\varepsilon$ is the polar unit vector of the spherical coordinate system defined in Fig. 26.

The effective rate of strain of blood in the target, $\dot{\gamma}$, is related to the modulus of the rate of strain tensor, $\sqrt{\mathbf{D}_{\mathrm{T}} : \mathbf{D}_{\mathrm{T}}^{\mathrm{T}}}$ [189], and is expressed as,

$$\dot{\gamma} = \sqrt{\left(\frac{\partial v_r}{\partial r}\right)^2 + \frac{1}{(\bar{r}R_\infty)^2}\left(v_r + v_\theta \cot\theta\right)^2 + \frac{1}{(\bar{r}R_\infty)^2}\left(v_r + \frac{\partial v_\theta}{\partial \theta}\right)^2}. \tag{7.66}$$

Surface tension prevents droplet separation below a certain size, a_0 [cf. Eq. (7.58)], which determines the smallest possible droplets for a given rate of strain as,

$$a_0 = \left(\frac{\sigma}{\rho\dot{\gamma}^2}\right)^{1/3}, \tag{7.67}$$

and the corresponding volume of the smallest possible droplet, V_0, is,

$$V_0 = \frac{4\pi\sigma}{3\rho\dot{\gamma}^2}. \tag{7.68}$$

In the framework of percolation theory, the smallest possible drop is designated as a site [118]. According to the probability of target space being randomly filled by such "material sites", bigger clusters (bigger drops) can be formed, sometimes even with some lacunae inside. If the probability is equal to one, it would mean that the entire liquid mass would be a single intact body.

A liquid mass initially thrown in such a way that it acquires a shape of a growing "amoeba" is prone to disintegrate. Here, it is implied that liquid motion becomes chaotic and incorporates multiple scales (a cascade of instabilities), while adhering to the liquid's incompressibility. Therefore, the more the "amoeba" spreads, the less is the probability, P, that a "site" of the

size of the smallest possible droplet of the size a_0 is occupied by it. The probability, P, that the site is occupied is equal to the ratio of the liquid volume (which is conserved) to the volume of the envelope surrounding the "amoeba". As long as the "amoeba" is stretching, the probability P, which is a function of time t, decreases. According to percolation theory, at a certain critical value of $P = P^*$, an intact liquid body (which can already have some lacunae) cannot exist anymore, and will disintegrate into finite clusters of different sizes going down to a_0, but not below it [181,182]. The statistics of the finite clusters (the resulting drops) is known [181,182], and it depends locally on $P(t)$ which continues to diminish. In the case of forward spatter the blood target undergoes mostly azimuthal stretching (accompanied by the corresponding radial compression due to the incompressibility embedded in the rate of strain tensor, $\mathbf{D}_{\mathrm{T}}$, which is expressed in Eq. (7.66) for $\dot{\gamma}$. Due to the cascade of instabilities, perturbations begin to develop, and lacunae begin to appear and increase in size. Accordingly, the continuous liquid target description is replaced by one rooted in percolation theory, still having in mind that the entire chain of events has been triggered by $\dot{\gamma}$. Finally, as the probability predicts, the intact mass of liquid disintegrates, and a cluster of blood drops appear. This description can be quantified using an element of target volume, $\mathrm{d}V_{\mathrm{T}}$, undergoing fragmentation as a function of $\dot{\gamma}$ primarily due to the above–mentioned angular stretching. Percolation theory can be applied to the corresponding fragmentation process, which allows one to determine the number

of droplets, and their size distributions [72, 118, 181, 182]. The current volume of the target undergoing fragmentation, $\mathrm{d}V_{\mathrm{T}}$, is found as the following,

$$\mathrm{d}V_{\mathrm{T}} = \mathrm{d}V_{\mathrm{T0}} \left(1 + \int_0^t \dot{\gamma} \mathrm{d}t\right)^3, \tag{7.69}$$

where $\mathrm{d}V_{\mathrm{T0}}$ is the initial volume. The probability of a site occupied by the smallest blood droplet is,

$$P\left(t\right) = \frac{\mathrm{d}V_{\mathrm{T0}}}{\mathrm{d}V_{\mathrm{T0}} \left(1 + \int_0^t \dot{\gamma} \mathrm{d}t\right)^3}. \tag{7.70}$$

Since the lacunae growth continues as the bullet penetration process progresses, the probability at which a material element occupies a virtual site in the domain encompassed by the fluid decreases. Accordingly, at a certain critical time moment the lowest critical probability, P^*, is reached, at which an "infinite" (intact) blood body ceases to exist, and it splits into a number of fragments. This target fragmentation threshold is known from percolation theory to be $P^* = 0.311$ [181, 182], and has already been used in the theory corresponding to bullets shaped as an ovoid of Rankine described in Sec. 7.3.1.

The basic flow is incompressible, and the motion of material elements in it can be tracked linking the Lagrangian and Eulerian descriptions. Simultaneously, locally (in every element) a switch to liquid disintegration is probed according to the corresponding value of the probability, P. The Lagrangian tracking and the switch to disintegration are described by Eqs. (7.71)–(7.73). Specifically, using the Lagrangian description of individual material particles of blood, the

probability field $P(r,\theta,t)$ with the current angular and radial positions of a material element, θ_{L}, and r_{L}, respectively, can be found. Note that subscript L refers to the current Lagrangian position. The following set of ordinary differential equations describes their evolution in time,

$$\frac{\mathrm{d}}{\mathrm{d}t}\left(P^{-1/3}\right) = \dot{\gamma}|_{\mathrm{L}}\,, \tag{7.71}$$

$$\frac{\mathrm{d}r_L}{\mathrm{d}t} = \mathbf{v}_{\mathrm{T}} \cdot \mathbf{e}_r + \dot{\xi}\cos\theta_{\mathrm{L}}, \tag{7.72}$$

$$\frac{\mathrm{d}\theta_L}{\mathrm{d}t} = \frac{1}{r_{\mathrm{L}}}\left(\mathbf{v}_{\mathrm{T}} \cdot \mathbf{e}_\theta - \dot{\xi}\sin\theta_{\mathrm{L}}\right). \tag{7.73}$$

It should be emphasized that subscript L in Eq. (7.71) denotes the rate of strain at the position with coordinates θ_{L}, and r_{L}. Noting that $\dot{\xi}\mathrm{d}t = \mathrm{d}\xi$, Eqs. (7.71)–(7.73) take the following dimensionless form,

$$\frac{\mathrm{d}}{\mathrm{d}\bar{\xi}}\left(P^{-1/3}\right) = \frac{R_\infty}{\dot{\xi}}\,\dot{\gamma}|_{\mathrm{L}}\,, \tag{7.74}$$

$$\frac{\mathrm{d}\bar{r}_{\mathrm{L}}}{\mathrm{d}\bar{\xi}} = \bar{r}_{\mathrm{L}}\sin^2\theta_{\mathrm{L}}\;\Gamma_1|_{\mathrm{L}} + (1+\Gamma_2|_{\mathrm{L}})\cos\theta_{\mathrm{L}}, \tag{7.75}$$

$$\frac{\mathrm{d}\theta_{\mathrm{L}}}{\mathrm{d}\bar{\xi}} = \frac{1}{\bar{r}_{\mathrm{L}}}\left[\bar{r}_{\mathrm{L}}\sin\theta_{\mathrm{L}}\cos\theta_{\mathrm{L}}\;\Gamma_1|_{\mathrm{L}} - (1+\Gamma_2|_{\mathrm{L}})\sin\theta_{\mathrm{L}}\right]. \tag{7.76}$$

The following initial conditions must be imposed on Eqs. (7.74)–(7.76),

$$\overline{\xi} = 0: \quad P = 1,\ \overline{r}_{\mathrm{L}} = \overline{r}_0,\ \theta_{\mathrm{L}} = \theta_0, \tag{7.77}$$

where $\overline{r}_0$ and θ_0 are the initial radial and axial coordinates of a material element.

If a fragmented section of the target is comprised of s smallest–possible droplets (i.e. of the size a_0), its volume, V, can be determined using Eq. (7.68), as,

$$V = \frac{4\pi\sigma}{3\rho\dot{\gamma}^2}s, \tag{7.78}$$

and its corresponding mass, m is found as,

$$m = \frac{4\pi\sigma}{3\dot{\gamma}^2}s. \tag{7.79}$$

According to percolation theory [118,181,182], the probability that a fragment is composed of s to $s+\mathrm{d}s$ minimally–sized (i.e. of size a_0) possible droplets is $w_s\mathrm{d}s$. The probability density function is expressed as,

$$w_s = Ks^{-\tau+1}\exp\left(-bs^{\psi}\right), \tag{7.80}$$

where $\tau = 3/2$, $b = 20.84\,|P^* - P|^{1/0.43}$, and $\psi = 1$, which are parameters (called the critical exponents) established in the framework of percolation theory [118, 181, 182], and K is the normalization parameter such that $\sum_{s=1}^{\infty} w_s = 1$, defined as,

$$K = \frac{1}{\int_1^{\infty} s^{-\tau+1} \exp\left(-bs^{\psi}\right) \mathrm{d}s}. \tag{7.81}$$

Note that percolation theory is geometric in nature and thus absolutely universal, no matter the physical type of discretized lattice as long as the discretization process is completely random. In particular, in the present case, the random discretization of the target implies universal values of the critical exponents used in the probability density function describing the drop–size distribution resulting from a multi–stage discretization process [118, 181, 182].

Then, the number of fragments of mass m_f within a differential target volume, $\mathrm{d}V_{\mathrm{T}}$ in the fragmented part of the target is,

$$\mathrm{d}N\left(m_{\mathrm{f}}\right) = \frac{3\rho\dot{\gamma}^2}{4\pi\sigma} \mathrm{d}V_{\mathrm{T}} K \int_1^{s_{\mathrm{f}}} s^{-\tau} \exp\left(-bs^{\psi}\right) \mathrm{d}s, \tag{7.82}$$

where,

$$s_{\mathrm{f}}\left(m_{\mathrm{f}}, \overline{R}\right) = \max\left[1,\ \frac{3\dot{\gamma}^2 m_{\mathrm{f}}}{4\pi\sigma}\right]. \tag{7.83}$$

The total mass of the fragmented zone accounting for all the fragments starting from the mass of the smallest indivisible one of size of a_0 to the fragment mass m_f, within the volume element is,

$$\mathrm{d}M\left(m_\mathrm{f}\right) = \rho \mathrm{d}V_\mathrm{T} K \int_1^{s_\mathrm{f}} s^{-\tau+1} \exp\left(-bs^{\psi}\right) \mathrm{d}s. \tag{7.84}$$

Evaluating the integrals in Eqs. (7.82) and (7.84) over the fragmented target volume results in,

$$N\left(m_\mathrm{f}\right) = \frac{3\rho}{4\pi\sigma} \int_{V_\mathrm{T}} \left[\dot{\gamma}^2 K \int_1^{s_\mathrm{f}} s^{-\tau} \exp\left(-bs^{\psi}\right)\right] \mathrm{d}V_\mathrm{T}, \tag{7.85}$$

$$M\left(m_\mathrm{f}\right) = \rho \int_{V_\mathrm{T}} \left[K \int_1^{s_\mathrm{f}} s^{-\tau+1} \exp\left(-bs^{\psi}\right) \mathrm{d}s\right] \mathrm{d}V_\mathrm{T}, \tag{7.86}$$

and yields,

$$\begin{aligned} N\left(m_\mathrm{f}\right) = & \frac{3\rho}{2\pi\sigma} \int_{V_\mathrm{T}} \sqrt{\frac{b}{\pi}} \frac{\dot{\gamma}^2}{\operatorname{erfc}\left(\sqrt{b}\right)} \left\{\sqrt{b\pi} \left[\operatorname{erf}\left(\sqrt{b}\right) - \operatorname{erf}\left(\sqrt{bs_\mathrm{f}}\right)\right]\right. \\ & \left. + \exp\left(-b\right) - s_\mathrm{f}^{-1/2} \exp\left(bs_\mathrm{f}\right)\right\} \mathrm{d}V_\mathrm{T}, \end{aligned} \tag{7.87}$$

$$M\left(m_\mathrm{f}\right) = \rho \int_{V_\mathrm{T}} \frac{\operatorname{erf}\left(\sqrt{bs_\mathrm{f}}\right) - \operatorname{erf}\left(\sqrt{b}\right)}{\operatorname{erfc}\left(\sqrt{b}\right)} \mathrm{d}V_\mathrm{T}. \tag{7.88}$$

The fragmented target volume can be approximated as cylindrical because directly in front of the leading edge of the projectile, many small, extremely fast moving droplets travel together with the bullet [this approximation has been introduced in Sec. 7.3.1, cf. Fig. 25(a)]. These droplets do not contribute to the overall forward spattered bloodstain pattern and as such, numerical integration for a cylindrical target element, $\mathrm{d}V_{\mathrm{T}}$, was implemented in Eqs. (7.87) and (7.88) similarly to Sec. 7.3.1.

7.4.2 Generalized Effect of Blood Elasticity

The fractured portion of the target was discretized into ring–like sections termed bins and denoted by subscript i. The initial velocities of the droplets within each bin are found from the time–dependent velocity field as,

$$u_i|_{\mathrm{initial}} = \sqrt{\mathrm{v}_{\mathrm{T}}^2 + \dot{\xi}^2 - 2\mathrm{v}_{\mathrm{T}}\dot{\xi}\cos\theta}. \tag{7.89}$$

These droplets are issued at initial inclination angles, β_i, determined as,

$$\beta_i = \cos^{-1}\left(\frac{u_i^2|_{\mathrm{initial}} + \dot{\xi}^2 - \mathrm{v}_{\mathrm{T}}^2}{2\,u_i|_{\mathrm{initial}}\,\dot{\xi}}\right). \tag{7.90}$$

It should be emphasized that Eqs. (7.89) and (7.90) are unique for each bullet since $\mathbf{v}_{\mathrm{T}}$ is unique. Note also that the characteristic droplet size in the ejected bins, $l_{*,i}$, can be found as,

$$l_{*,i} = \left[\frac{6\,(M_i/N_i)}{\pi\rho}\right]^{1/3}. \tag{7.91}$$

The web of blood droplets streaming from the fragmented target surface is initially inter–connected by tails on the trailing edge of individual droplets. Viscoelastic fluids, such as blood, subjected to strong elongational flows (for which the Deborah number, De, is $De \gg 1$) characteristic of forward spatter result in significant elastic stresses similarly to Sec. 7.3.3. As a result, the individual droplet tails undergo brittle fracture which has been experimentally observed for various liquids under similar circumstances [177–180]. Up to the fracture moment, tails decelerate the droplets and diminish their initial velocities when they finally detach. This effect is quantified in the following equation as shown in Sec. 7.3.3,

$$u_i = u_i|_{\text{initial}} \cos\left(t_i/T_i\right), \quad T_i = \left(\frac{2}{3}\frac{\rho l_{*,i}^2}{E}\right)^{1/2}, \tag{7.92}$$

where t_i is the droplet detachment time, the determination of which is discussed in Sec. 7.5 and E is the Young's modulus of blood, taken as $E = 2.6$ GPa (cf. Sec. 7.3.3).

Following Ch. 6 and Sec. 7.3.2, it is assumed that bins ejected from the target form a blood drop spray entraining air due to viscous suction and thus create a two–phase interpenetrating continua. This two–phase flow is subjected to gravity, air drag, and the collective effect of the aerodynamic droplet–droplet interaction in flight. The corresponding trajectory equations are described in detail in Ch. 6. The correlation for the air drag experienced by an individual

droplet is given by the Schiller–Naumann formula which is in the range of validity of the forward spattering phenomena [72],

$$C_{\mathrm{D},i} = \frac{24}{Re_i}\left(1 + 0.15 Re_i^{0.687}\right), \tag{7.93}$$

where Re_i is the bin Reynolds number. Note that this correlation neglects droplet oscillation in flight, as well as their possible secondary atomization.

7.5 Results and Discussion

At the onset of the bullet penetrating the target, a nearly instantaneous spray is formed that contains many small droplets traveling at a high initial velocity (cf. Ch 5). The theoretical model described in Sec. 7.3 and 7.4 predicts that these small droplets form in the target directly ahead of the bullet. These small droplets are rapidly decelerated by air drag and fall down very close to the target. Moreover, high–speed videos of bullet penetration phenomena show that the majority of the resultant blood drop spray stems from the area surrounding the bullet [7] and thus droplets issued from the cross–hatched domain in Fig. 25(a) are disregarded. On the other hand, bigger drops formed and issued from the "cylindrical" cross–hatched domain shown in Fig. 25(b) were fully accounted for and their trajectories tracked. This cylindrical domain was discretized into 20 ringlike slices (bins) spanning the length of the target, as shown in Fig. 23.

7.5.1 Unique Solution Results

To compare the experimental data to the theoretical results, several governing parameters must be specified. Namely, the velocity of the bullet, $\dot{x} = 351$ m/s was used in the simulations,

as well as the height at which the bullet impacted the target, $H_0 = 152.4$ cm. Since the theoretical model implies the bullet is shaped like an ovoid of Rankine, the latter was fitted to the real bullet shape. Although close, the present bullet was not a perfect ovoid of Rankine. It is unphysical to have the ovoid of Rankine bullet in the numerical simulation to extend past the surface of the actual bullet since the tip shape practically completely determines the flow field, which is substantiated by multiple well–established phenomena in the field of terminal ballistics [190] and is a fundamental assumption in such models as the cavity expansion model developed there. A very good agreement of the shape of the ovoid of Rankine can be achieved with the leading part of the real bullet (Fig. 27). This, however, reached only 3/4 of the real bullet radius (i.e. $R_\infty = 3.375$ mm) at "infinity", which was considered to be tolerable. The thickness of the target was set to be equal to R_∞ and the droplet bins issued from only over the top and below the bottom of the bullet [at the azimuthal angles $\Phi = 90°$ and 270°; cf. Fig. 14(b)] were tracked numerically. This was motivated by the fact that the experiment was designed in such a way that only a strip of paper directly under the trajectory of the bullet was used to acquire the data.

The configuration of the fragmented "cylindrical" volume (cf. Fig. 25) of the target was predicted at $t = 0.2$ ms after the bullet impact using Eqs. (7.17) and (7.19). The mass and number of droplets issued from each bin was predicted using Eqs. (7.39) and (7.40). The initial velocities and inclination angles of the droplets of each bin were predicted by Eqs. (7.42) and (7.43) with characteristic sizes calculated by Eq. (7.44). It should be emphasized that the droplets originating from the bins that are closer to the rear surface of the target move

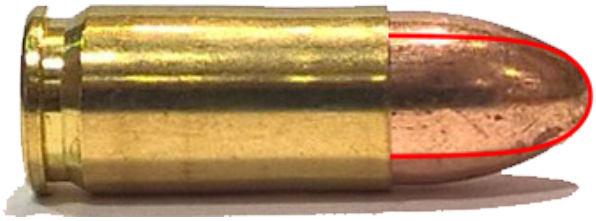

Figure 27. A 9 mm Luger copper FMJ bullet and cartridge casing used in the experiment with the ovoid of Rankine shown by the line superimposed on its leading edge.

forward slower than the ones originating from the other side. Immediately following the moment of fracture, in a very dense cloud of droplets, such a velocity distribution inevitably causes chaotic multiple drop–drop collisions. Moreover, the following three circumstances should be mentioned: (i) the fragmentation of a target due to a bullet impact is a large–scale phenomenon, albeit the volume of material that actually leaves the target is quite small. An example of this is seen in the seminal images photographed by Harold Edgerton [191]. In an image of a .30 caliber bullet impacting a sheet of plexiglass, one can see that there are small fragments leaving the target in the direction of the bullet motion (the forward "spatter") only in the very near vicinity of the bullet impact point. On the other hand, there is a fractured zone that is massive in comparison to the material that actually leaves the target. (ii) The case of the forward spattering of blood due to a gunshot is not dissimilar to the bullet impacting a plexiglass pane due to the fact that at high values of the Deborah number characteristic of bullet impact, blood undergoes brittle fracture, as discussed in Sec. 7.3.3 and 7.4.2. A rough estimate can be done of the volume of blood that is splashed forward, using the high–speed videos of blood spatter due

to a gunshot, which were taken by the MFRC [148] and analyzed in Ch. 5. From experiment 7Aa1 there, which closely resembles the one here, one estimates that the target looks to be filled with ~ 10 mL of blood and that only 0.33 cm^3 of blood was splashed (taking the average sizes and estimating the number of droplets splashed), which means that only about 3.3% of blood was actually splashed. It should be emphasized, however, that this is a rough "higher" value, and in some cases it can be much lower. Using the exact number of droplets and average area from Ch. 5, for instance, shows that in experiment 7Aa1, the percentage of droplets that leave the target becomes 0.01%. (iii) An additional factor preventing detachment of multiple droplets from the bulk is the formation of long tails that are stabilized by the elastic forces and do not break up (the situation discussed in Sec. 7.3.3 and 7.4.2) and illustrated by the images of disintegrating jets of dilute polymer solutions in Ref. [183]. Summarizing, one can state that in any case, the volume of material that escapes the target is extremely small when compared to the volume of the entire fractured part of the target. As a result, it is assumed that 5% of the fractured target results in droplets that form the forward spatter spray.

The relaxation time of swine blood (which shares similarities with human blood [133]) is about $\lambda = 15$ ms as shown in Ref. [1], bullet penetration happens on the scale of 10^{-5} s, and the fracture process of the blood drop tail is on the order of microseconds, as Eq. (7.48) reveals given the known input parameters. The droplet tail detachment time is naturally an increasing

function of the droplet size, $l_{*,i}$, and the plausible interpolation function that satisfies these criteria and generates the cutoff time in Eq. (7.48) and is shown in Fig. 28 is the following,

$$t_{\mathrm{det},i} = -13.4\,(l_{*,i})^2 + 8.34\,(l_{*,i}) + 1.70 \times 10^{-3}, \tag{7.94}$$

where $t_{\mathrm{det},i}$ is in μs and $l_{*,i}$ in cm, and the coefficients have the corresponding units. This function was determined through testing the required initial velocities calculated with Eq. (7.48), which produce trajectories corresponding to the experimental range seen in the experimental data. It should be emphasized that according to Fig. 28, $De = \lambda/t_{\mathrm{det},i} \gg 1$, indeed, which corresponds to the brittle fracture regime. Note that this function satisfies the following plausible criteria: (i) it grows with the droplet size, which is physical, and (ii) it works on the scale of microseconds, i.e. once again, on physical grounds.

Drop trajectories were numerically determined using the Kutta–Merson algorithm described in Appendix A. The predicted dependence of the number of stains on the floor to their final distance from the rear side of the target is shown in Fig. 29 in comparison with the experimental data, with the agreement being quite satisfactory.

The resultant stain area on the floor was measured experimentally and predicted following the procedure of Ch. 6, which employs the calculated impact angle of blood drops on the floor, α_i [173] and the drop spread factor for normal impact ξ_i. Namely, a blood drop impinging onto a horizontal surface shown in Fig. 30 reveals the longest size of the drop stain $\Delta X_i = (\xi_i l_{*,i})\,/\sin\alpha_i$, where $\xi_i = 0.61\,(We_i/Oh_i)^{0.166}$ [43,171] with We_i and Oh_i being the final Weber and Ohnesorge numbers, respectively, based on the droplet parameters. This spread factor was first proposed

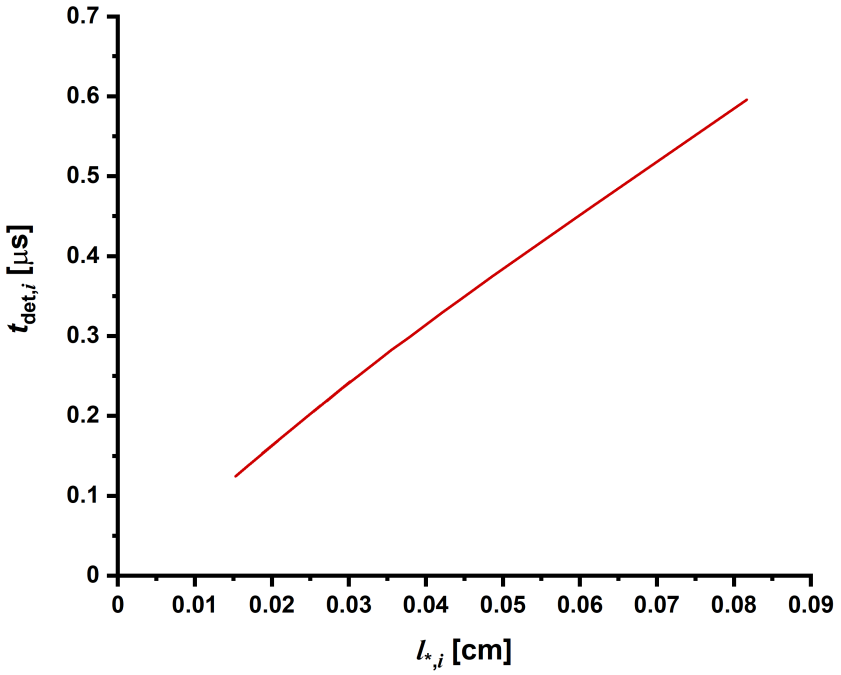

Figure 28. The dependence of the droplet tail detachment time on its characteristic size used in the simulations in conjunction with Eq. (7.44).

by Scheller and Bousfield [171] with the validity range for viscosity of 1–300 mPa × s and the correlation coefficient of 0.963 for all of their experimental data. There is a plethora of various other spread factor correlations to choose from and they all have different ranges of validity. Some of these correlations are experimental and some others span the results of numerical simulations [192, 193], but Ref. [194] showed that all of those later correlations are in full agreement with the Scheller–Bousfield correlation used here.

It should be emphasized that the Ohnesorge number involves viscosity μ_{blood}, which was taken as the asymptotic value obtained in the simple shear flow, $\mu_{\text{blood}} = 5$ mPa × s (cf. Ch. 4),

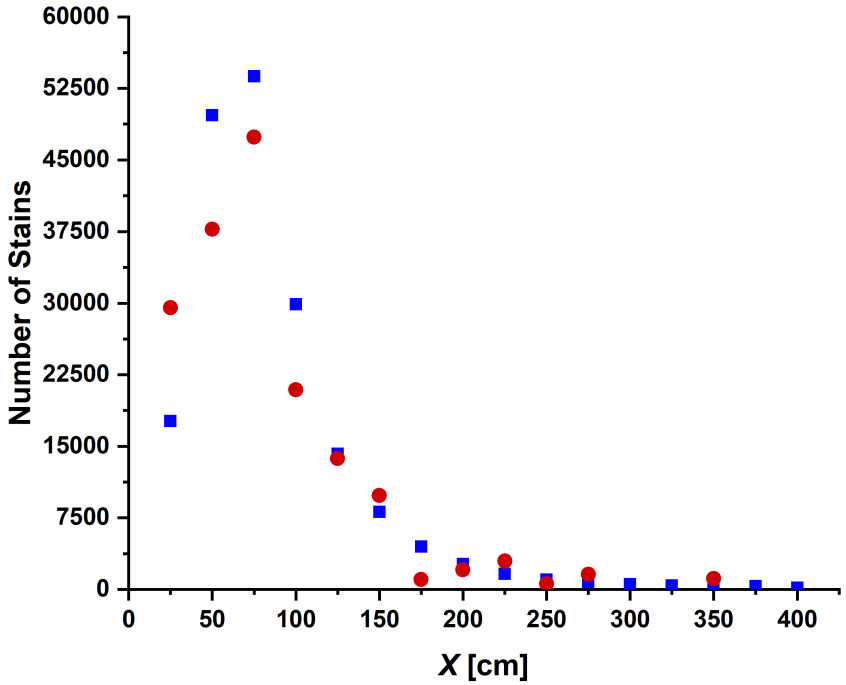

Figure 29. The number of stains deposited on the floor vs. the distance from the rear side of the target in forward blood spatter. The red circles correspond to the predicted results, and the blue squares to the experimental data. It should be emphasized that these data correspond to the combined results of five experiments.

because high shear rates accompany droplet spreading on impact [172, 195]. This leads to the following expression for the stain area,

$$A_i = \frac{\pi l_{*,i}^2 \xi_i^2}{4\sin\alpha_i}. \tag{7.95}$$

Note also that for the effect of the impact obliquity on drop spreading at the surface, there are no fully reliable correlations, especially accounting for the detailed behavior of the advancing

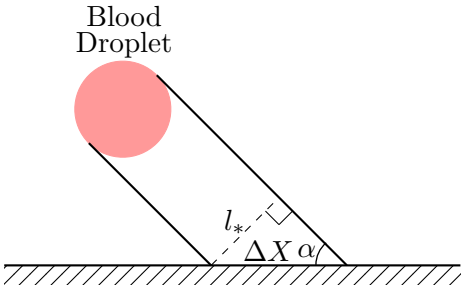

Figure 30. Schematic of stain formation due to a blood droplet impacting onto a horizontal surface.

and receding contact angles (which are unknown for blood). Therefore, Eq. (7.95) is used to account for the effect of the impact obliquity by indirectly introducing into consideration the largest semiaxis of an elliptical stain, as is currently done in the framework of BPA [18, 196].

The predicted and measured stain area are shown as a function of the distance from the rear side of the target in Fig. 31 with the agreement being fairly good. The spatial distribution in the stain area plot in Fig. 31 reveals that the initially slower, larger droplets fly further than the initially faster, smaller ones (cf. Fig. 29), which can be explained by two effects. First, the smaller drops have a lower inertia with respect to the effect of air drag and as such the trajectories of smaller drops are more affected by drag and fall shorter than those of larger drops. Second, the collective aerodynamic effect also participates in the spatial distribution in the stain area plot in Fig. 31, because the initially leading droplets create the aerodynamic wake, which reduces the drag and facilitates the flight of the subsequent larger droplets. Note that the model uses probability only to determine which part of the target is fragmented and

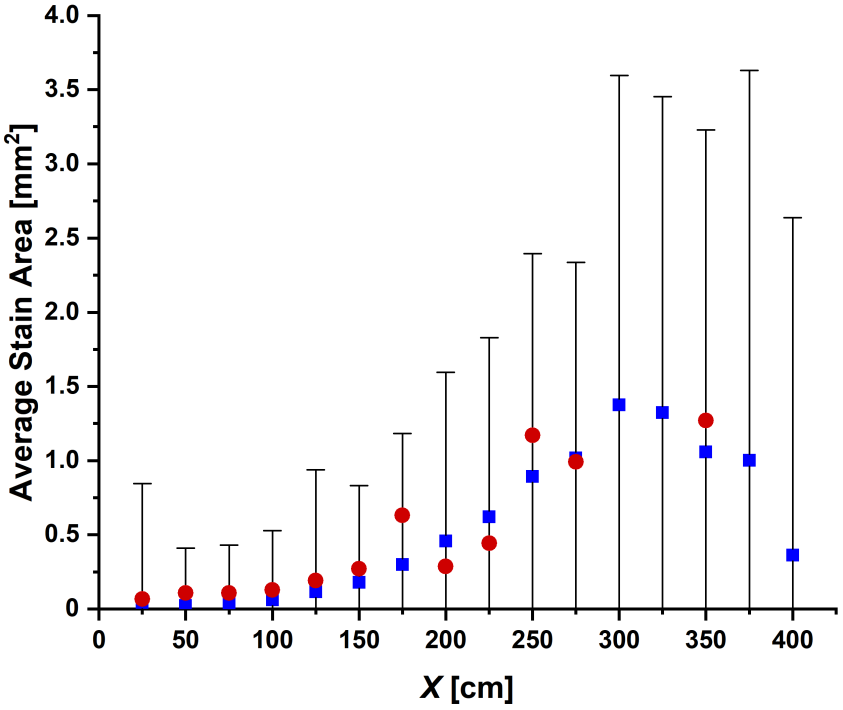

Figure 31. The average stain area as a function of distance from the rear side of the target in forward blood spatter. The red circles depict the predictions and the blue squares are the experimental data. The error bars for the experimental data indicate the standard deviation in the stain area arising from the five experiments.

produces detached droplets under a given bullet geometry and motion. Other than that, droplet motion is fully deterministic, and Figs. 29 and 31 represent the fully deterministic predictions. This is, essentially, similar to how detached droplets are generated, travel, and are deposited in reality.

It should be emphasized that the parameters in such experiments are very difficult to control, which results in the large standard deviations. These standard deviations do not follow a Gaussian distribution, first of all because area is an inevitably positive quantity. Also, it should

be emphasized that all the outlier stain areas were included. It seems nearly impossible to create perfectly repeatable experiments because things that are seemingly minute, such as the gunpowder in the cartridge, easily change the muzzle velocity of the bullet. Or, for instance, the grain (the mass of the projectile) can be different even for the same bullet type, which is something entirely dictated by the manufacturer and would completely change the inertia of the impacting projectile. These parameters are out of the control of the police shooters conducting these experiments. Blood properties can also vary from sample to sample, which further compromises reproducibility and increases error bars, as in Fig. 31.

The offset stain area in the numerical results as compared to the experimental data may be attributed to the physical considerations under which Eq. (7.95) was determined. For instance, the numerical calculations neglect the evaporation of the drops during flight. Moreover, the effect of hematocrit on surface tension is unknown, even though it is plausible that it does have an effect because the surface tension of water is higher than that of blood. The addition of whey protein isolate, for instance, is known to reduce the surface tension along with temperature [197]. It should be emphasized that the most commonly used spread factor correlations are empirical and valid only for the flow regimes that they were experimentally tested on. As such, it is nearly impossible to really prove that one correlation is better or more appropriate than the other unless the correlation is tested and found for each possible deposition scenario. Note also that using the dependence of the blood viscosity on temperature and hematocrit from Ref. [195] and of the surface temperature of blood on temperature from Ref. [198], it was found that the theoretical predictions of the dependence of the average stain area on distance

(cf. Fig. 31) change insignificantly between the two limiting cases of the room and body temperature. Accordingly, the effect of drop cooling during flight on the results is insignificant.

It should be emphasized that the experimental data were collected by adding the values found in five experiments and that the number of stains in Fig. 29 was predicted accordingly, whereas the stain area in Fig. 31 was averaged. An artificial discretization of the experimental and theoretical results, as shown in Fig. 23, can contain some stains resulting from a certain bin into a strip with the other stains, thus creating the resulting fluctuations, as for example those seen in the theoretical predictions in Fig. 31 at $x = 175$ and 250 cm.

7.5.2 Generalized Solution Results

The number of droplets formed in the forward spattering of blood due to a bullet of an arbitrary shape is found via numerical integration over the fractured target zone using Eq. (7.87). The mass of these droplets is then found using Eq. (7.88) which allows for the characteristic droplet sizes to be determined through Eq. (7.91). Droplets within each discretized target bin are ejected with the initial velocity calculated in Eq. (7.89) at initial inclination angles found from Eq. (7.90). Due to the viscoelasticity of blood, droplet tails act to slow down the droplets according to Eq. (7.92) until the tail fractures. The two–phase air–droplet jet then propagates through air which is described in detail in Ch. 6 with the drag coefficient given by Eq. (7.93). Note that the bullet shape and velocity are tremendously important in determining blood spatter patterns as they dictate the velocity field within the target. This is because the bullet shape defines the system of sinks and sources, $\overline{q}\left(\overline{\zeta}\right)$, which generates the flow potential via Eq. (7.53),

and influences the velocity field within the blood target as seen in Eqs. (7.55)–(7.57). Note specifically that Eq. (7.55) incorporates $\dot{\xi}$ which is the velocity of the bullet.

This procedure allows for the proper evaluation of chaotic disintegration of blood in the target due to the penetration of bullets of arbitrary shape. The analytical benchmark for this numerical procedure is provided by the bullet shaped as an ovoid of Rankine. The comparison of the velocity vectors and probability field of the benchmark analytical case of an ovoid of Rankine with the generalized numerical predictions for the same bullet is shown in Fig. 32. Note that the effective rate of strain in Sec. 7.3 used an order of magnitude estimate and the difference between the exact equation Eq. (7.66) and the one used in Sec. 7.3 is $\sqrt{6}/4$. Therefore, the comparison requires Eq. (7.66) to be multiplied by $4/\sqrt{6}$ and for consistency, this was held for the generalized numerical calculations of the 7.62 $\times$ 39 mm and .45 auto bullets. The velocity vectors and probability field in Fig. 32 reveal that the present fully–numerical procedure applicable for bullets of an arbitrary shape is in good agreement with the results of the analytical benchmark case of the bullet shaped as an ovoid of Rankine.

Then, in the calculations related to the 7.62 $\times$ 39 mm bullet shown in Fig. 22(b), the exact muzzle velocity and bullet shape ($R_\infty = 0.396$ cm) were used. The system of sinks and sources $\overline{q}\left(\overline{\zeta}\right)$, found from solving Eq. (7.53), using the known bullet geometry is shown in Fig. 33(a) and a representative system of material points in the target in Fig. 33(b) illustrates the corresponding deformation field.

The prediction of the spatial distribution of the number of stains and their respective area requires a physically plausible cutoff time t_i of blood droplets from the web of viscoelastic

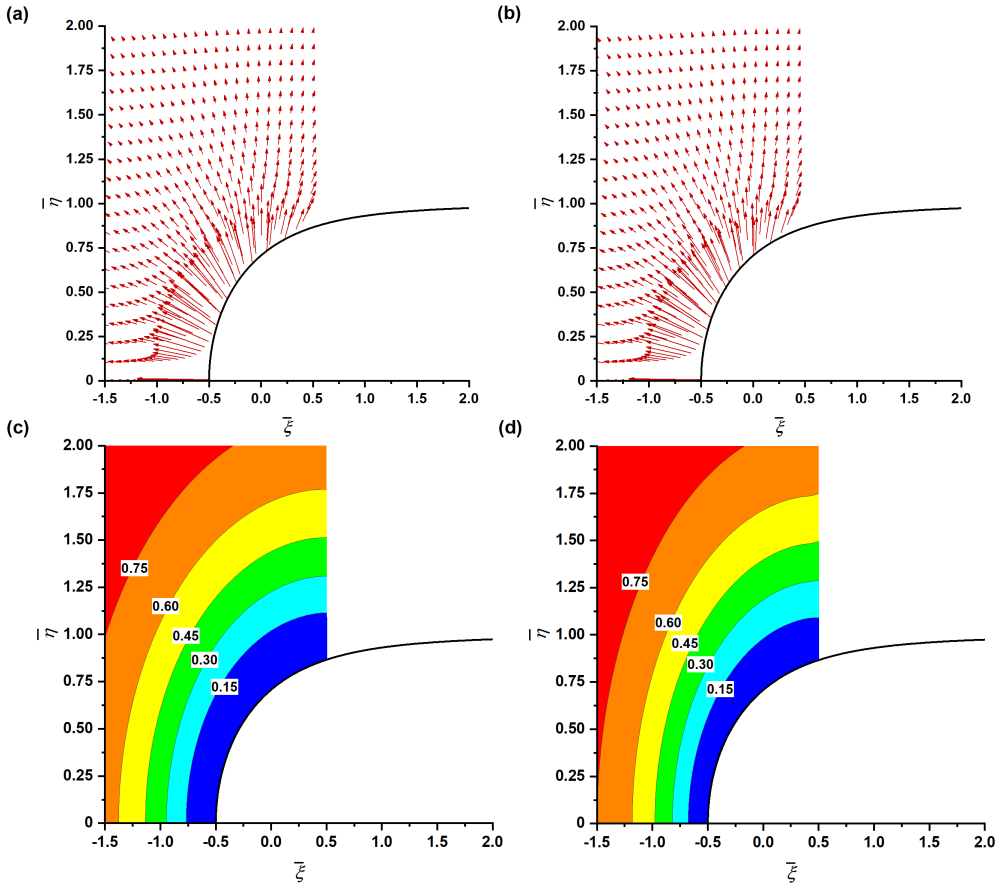

Figure 32. Comparisons for a bullet shaped as an ovoid of Rankine. Predictions were done using the analytical results of Sec. 7.3 and the generalized numerical model of Sec. 7.4. (a) Velocity vector plot from the analytical results of Sec. 7.3, (b) velocity vector plot found from the generalized numerical model using Eqs. (7.60) and (7.61), (c) probability contours from the analytical results of Sec. 7.3, (d) probability contours from the generalized numerical model using Eq. (7.74). The depth of bullet penetration is $\overline{\xi} = 1.0$ and the contour levels are indicated about the current position of the bullet. The ovoid of Rankine bullet is shown by the thick black line.

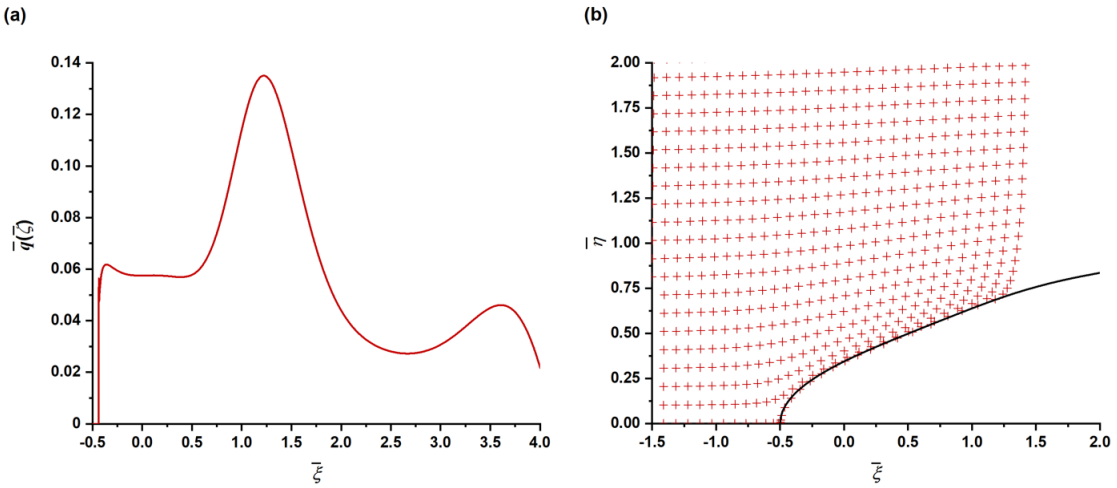

Figure 33. Results of the generalized numerical model applied to the 7.62 × 39 mm bullet shown in Fig. 22(b). (a) The predicted distribution of sinks and sources found from the solution of Eq. (7.53), and (b) a representative system of material points in the target at a penetration depth of $\overline{\xi} = 2.0$.

ligaments similar to those observed in Ref. [183]. Then, through Eq. (7.48), the initial blood droplet velocity can be determined. It should be emphasized that such droplet tails undergo strong uniaxial elongation which is characterized by extremely high values of the Deborah number $De \gg 1$, which essentially means a practically brittle (cohesive) fracture [177–180]. In general, it is physically plausible that the tail detachment time becomes larger for large blood droplets, and this occurs on the order of microseconds which corresponds to the bullet penetration timescale. Accordingly, based on the available empirical information on droplet

deposition ranges affected by the values of t_i, the following empirical correlation of the tail detachment time with the droplet size is proposed,

$$t_i = -3.85\,(l_{*,i})^2 + 8.04\,(l_{*,i}) - 4.72 \times 10^{-4}, \tag{7.96}$$

where t_i is in μs and $l_{*,i}$ in cm. Accordingly, the characteristic droplet detachment is on the scale of microseconds. It should be emphasized that Eq. (7.96) is the droplet tail detachment time needed for the evaluation as per Eq. (7.92).

Due to the chaotic dispersion of blood droplets in the first time moments of the spray and the volume of blood leaving the target being significantly smaller than the entire fractured zone, it is assumed that 0.5% of blood within the fractured target results in the blood spray. From high–speed video evidence of Ch. 5, this value is in the $0.01 - 5.0\%$ range, and accordingly, 0.5% is within the plausible range. All other parameters required for the analysis were kept the same as Sec. 7.5.1 and are discussed in more detail there. The experimental data and the theoretical predictions for the 7.62 $\times$ 39 mm bullet shaped as in Fig. 22(b) are compared in Fig. 34, where the distribution of the number of stains along the floor from the rear side of the target is shown.

The stain area can be calculated following the method employed in Sec. 7.5.1 which utilizes the Scheller–Bousfield spread factor, χ_i, as a function of the impact Weber and Ohnesorge

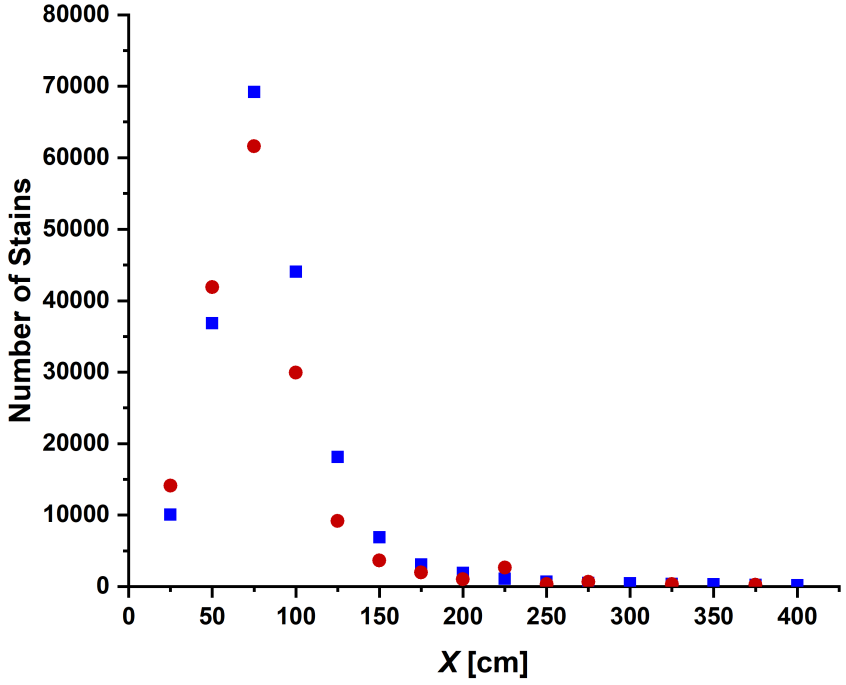

Figure 34. Number of stains as a function of the distance from the rear face of the target for the 7.62 × 39 mm bullet where the blue squares correspond to the experimental data and the red circles to the theoretical predictions. It should be emphasized that the data is the sum of five experimental trials. Accordingly, the theoretical prediction is taken five–fold.

numbers as $\chi_i = 0.6\,(We_i/Oh_i)^{0.166}$, [171]. Accounting for the impact angle of the stain results in the following formula,

$$A_i = \frac{\pi l_{*,i}^2 \chi_i^2}{4\sin\alpha_i}, \tag{7.97}$$

where α_i is the predicted impact angle of the droplet. The stain area was then averaged according to the strips outlined in Fig. 23 and the comparison between the numerical and experimental predictions is shown in Fig. 35.

In order to test the universality of the model to bullets of an arbitrary shape, the tail detachment time function required for Eq. (7.92) should be generalized as a function of the maximum characteristic strain rate, $\dot{\gamma}|_{\max} = \dot{\xi}/R_\infty$. This was done by linearly matching Eq. (7.96) and the one used in Sec. 7.5.1, $t_i = -13.4\,(l_{*,i})^2 + 8.34\,(l_{*,i}) + 1.70 \times 10^{-3}$ (where t_i is in μs), which yields the following generalized function,

$$t_i = A\,(l_{*,i})^2 + B\,(l_{*,i}) + C, \tag{7.98}$$

where t_i is in μs, $l_{*,i}$ is in cm, $A = 9.256 \times 10^{-5}\,(\dot{\gamma}|_{\max}) - 20.620$, $B = -2.908 \times 10^{-6}\,(\dot{\gamma}|_{\max}) + 8.567$, $C = -2.105 \times 10^{-8}\,(\dot{\gamma}|_{\max}) + 3.342 \times 10^{-3}$, and $\dot{\gamma}|_{\max}$, is in s^{-1}. It should be emphasized that this equation is uniformly valid because it accounts for the fact that different bullets have different shapes and move with different velocities, thus generating different characteristic strain rates in the surrounding blood. Note that these functions were established using the physical parameters of the bullet to find the overall maximal value of $\dot{\gamma}|_{\max}$.

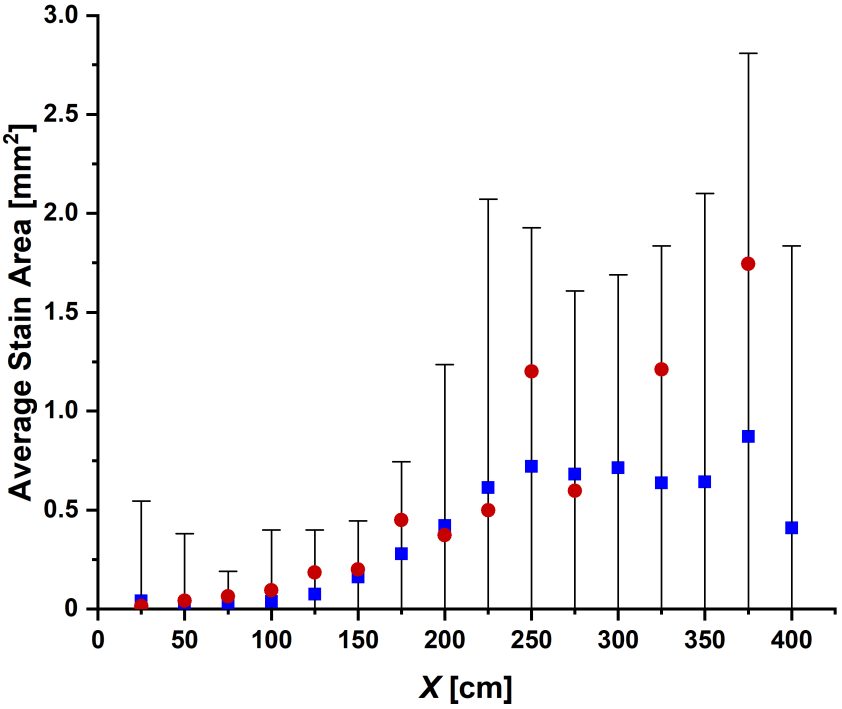

Figure 35. Average stain area as a function of distance from the rear face of the target for the 7.62 × 39 mm bullet where the blue squares correspond to experimental data and the red circles to the theoretical predictions. The error bars on the experimental data are the standard deviation.

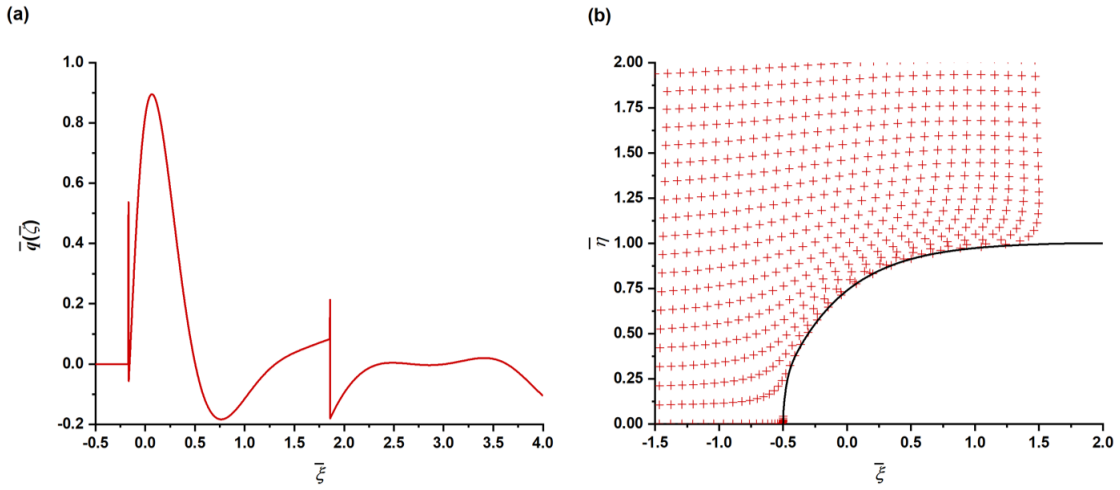

Figure 36. Results of the generalized numerical model applied to the .45 auto bullet. (a) The predicted distribution of sinks and sources found from the solution of Eq. (7.53), and (b) a representative system of material points in the target at a penetration depth of $\overline{\xi} = 2.0$.

Applying Eq. (7.98) for the .45 auto bullet with its radius, $R_\infty = 0.5715$ cm, and its velocity of $\dot{\xi} = 234.47$ m/s, results in the tail detachment time function of,

$$t_i = -16.82\,(l_{*,i})^2 + 8.45\,(l_{*,i}) + 2.84 \times 10^{-3}. \tag{7.99}$$

All other model parameters were kept the same since the .45 auto bullet is similar in shape to the bullet used and described in Sec. 7.5.1 as the ovoid of Rankine bullet. The solution of Eq. (7.53), i.e. the predicted distribution of sinks and sources, for the known bullet geometry of the .45 auto bullet is shown in Fig. 36(a). The corresponding representative target points showing the deformation predicted by the model are depicted in Fig. 36(b).

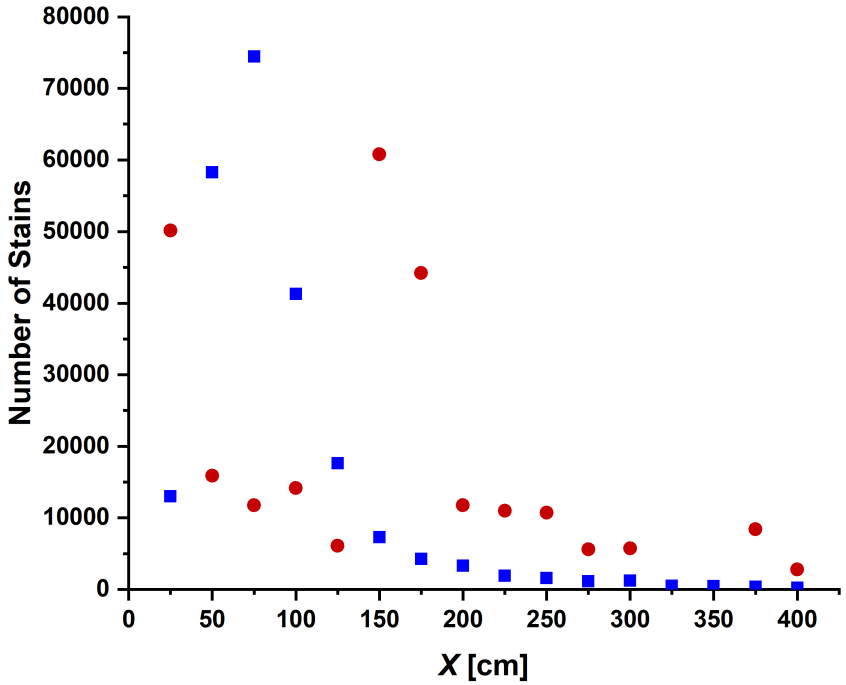

Figure 37. Number of stains as a function of the distance from the rear face of the target for the .45 auto bullet. The blue squares correspond to the experimental data and the red circles to the theoretical predictions. It should be emphasized that the data is the sum of five trials. Accordingly, the theoretical prediction is taken five–fold.

The predicted number of stains for the .45 auto is compared with the corresponding experimental data in Fig. 37.

The application of Eq. (7.97) for the calculation of the average stain area (exactly as done for the 7.62 × 39 mm bullet and 9 mm one in Sec. 7.5.1) yields the results for the .45 auto bullet shown in Fig. 38.

It should be emphasized that the results shown in Figs. 37 and 38 were obtained by using the generalized model for a given type of bullet and its velocity without any additional fitting.

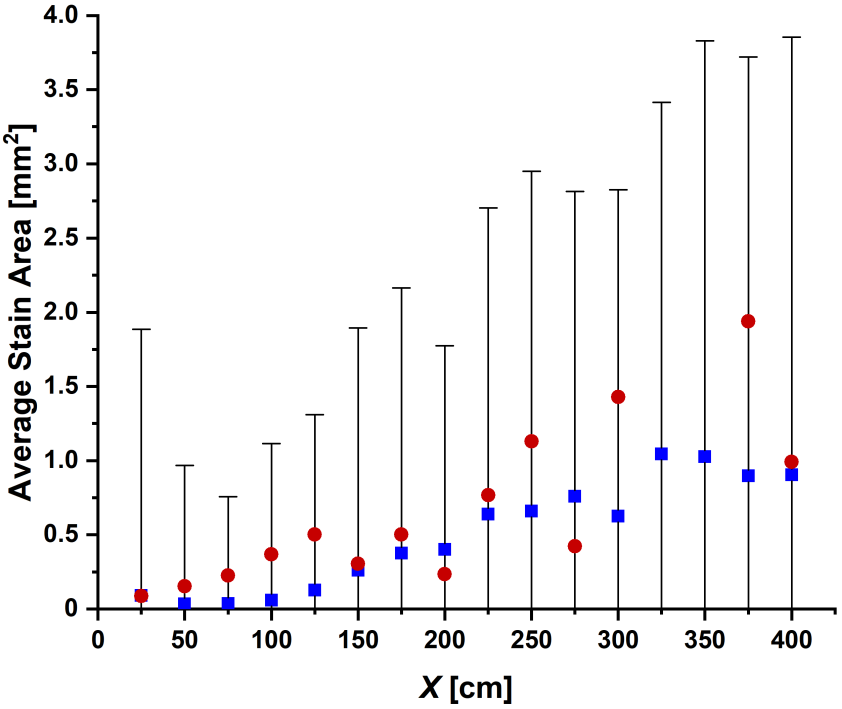

Figure 38. Average stain area as a function of distance from the rear face of the target for the .45 auto bullet where the blue squares correspond to experimental data and the red circles to the theoretical predictions. The error bars on the experimental data are the standard deviation.

The plausible results show that the generalized model described in Sec. 7.4 holds great promise for predicting the resultant forward blood spatter pattern for arbitrary bullets.

7.6 Conclusion

A theoretical model of forward blood spatter due to a gunshot was described. The model is based on the approach previously applied to the problems of terminal ballistics in the framework of percolation theory. In addition, the present model incorporates the effect of the viscoelasticity of blood on droplet detachment from the target and the collective aerodynamic interaction of droplets flying through air. The model has a unique solution for an ovoid of Rankine and was generalized to accommodate a projectile of arbitrary shape.

The unique solution was tested with experimental data acquired from gunshots of a 9 mm FMJ bullet shot by a Glock model 19 into a cavity filled with human blood. The comparison of the predicted and measured number of blood stains and their respective stain area found at certain distances from the rear side of the target along the bullet path revealed good agreement. The generalized numerical model was validated by comparison to the previously developed analytical benchmark case of the bullet shaped as an ovoid of Rankine. Then, the predictions of the generalized numerical model were compared to the experimental data of the present work for a 7.62 $\times$ 39 mm bullet. The comparison of the numerical results with the experimental data for the distribution of the number of droplets and their respective stain areas on the floor revealed good agreement. The model was then tested with a .45 auto bullet which is similar in shape to the 9 mm bullet approximated as an ovoid of Rankine with a tail detachment time being related to the effective strain rate. This also produced plausible results, which shows

that the generalized model is universally valid for bullets of any given shape moving with any given velocity. This shows that the generalized model of forward blood spattering based on percolation theory of chaotically disintegrating liquid holds great promise for the modeling of gunshot forward spatters in relation to forensic investigations.

It should be emphasized that the compared experimental results are preliminary, and in order to fully validate the proposed model, more varied experiments should be conducted in the future. The theoretical predictions are produced in the framework of a unified approach, based on physical principles, i.e. the chaotic disintegration of blood described through percolation theory, the viscoelasticity of blood, the velocity field, the individual droplet flight affected by the gravity force, and air drag and the collective effect, which stems from the aerodynamic droplet–droplet interaction. These predictions are based on the same set of input parameters, and they are not trivial, e.g. the maximum of the number of stains and the deposition of the largest of the droplets. These nontrivial effects stem from the collective aerodynamic effect in which the leading drops create an aerodynamic wake, which lowers the drag on the subsequent ones, and as such, the slower and larger droplets can fly to a distance farther than the initially faster smaller droplets. Moreover, the model also predicts the droplet impact angle and its final velocity responsible for the stain area. To date, there is no other theoretical model capable of predicting any of these outcomes of the forward spattering of blood due to a gunshot based on sound physical principles.

CHAPTER 8

INTERACTION OF MUZZLE GASES

This chapter has been submitted for publication in Ref. [4].

8.1 Introduction

Self–similar turbulent vortex rings are investigated theoretically in the framework of the semi–empirical turbulence theory for the modified Helmholtz equation. The velocity and vorticity fields are established, as well as the transport of passive admixture by turbulent vortex rings. Turbulent vortex rings of propellant gases originating from the muzzle of a gun after a gunshot are an important phenomenon to consider in crime scene reconstruction. In this work, it is shown that this has a significant repercussion on the outcome of backward spattered blood droplets from a gunshot. Turbulent vortex rings of propellant gases skew the distribution of blood stains on the ground and can either propel blood droplets further from the target, or even turn them backwards toward the target. This is revealed through the final bloodstain locations and their respective distribution of the number of stains and their area as a function of distance from the target using two different shooter–to–target distances. An image of the propagating muzzle gases after bullet ejection is overlaid with the predicted flow field which reveals good agreement. Gunshot residue is an important factor in determining the events of a violent crime due to a gunshot and are considered to be entrained by the propellant gases.

The self–similar solutions for the flow, vorticity, and concentration of gunpowder particles are predicted and the results are shown to be within the measured range of experimental data.

8.2 Theoretical Model

8.2.1 Self–Similar Motion of Turbulent Vortex Rings

The structure of self–similar turbulent vortex rings is determined in the framework of the semi–empirical theory of turbulence using the turbulent eddy viscosity in the momentum balance equation,

$$\frac{\partial \mathbf{v}}{\partial t} + (\mathbf{v} \cdot \nabla)\,\mathbf{v} = \mathbf{F} - \frac{1}{\rho}\nabla p + \nu \nabla^2 \mathbf{v}, \tag{8.1}$$

supplemented with the continuity equation for the incompressible mean flow,

$$\nabla \cdot \mathbf{v} = 0, \tag{8.2}$$

where bold characters denote vectors, $\boldsymbol{v}$ is the average flow velocity, $\boldsymbol{F}$ represents the body force, t is time, ρ is the fluid density, p is the pressure, and ν is the turbulent eddy viscosity, $\nu\,(t) = \lambda W\,(t)\,R\,(t)$, where λ is an empirical constant, W is the axial velocity of the vortex ring, and R is its radius.

The vortex ring is assumed to be axisymmetric in average. Then, the cylindrical coordinate system shown in Fig. 39 (from the z–r coordinate origin) is introduced, with the z–coordinate being reckoned along the ring axis, and the r–coordinate in the radial direction. The vorticity, $\boldsymbol{\Omega} = \nabla \times \mathbf{v}$, has only the azimuthal component which is denoted as Ω. The velocity components

are generated by the stream function ψ, as $v_z = r^{-1}\partial\psi/\partial r$, and $v_r = -r^{-1}\partial\psi/\partial z$ [83], which satisfy Eq. (8.1). Then, Eq. (8.1) takes the form of the modified Helmholtz equation,

$$\frac{\partial\Omega}{\partial t} + \frac{\partial\psi}{\partial r}\frac{\partial}{\partial z}\left(\frac{\Omega}{r}\right) - \frac{\partial\psi}{\partial z}\frac{\partial}{\partial r}\left(\frac{\Omega}{r}\right) = \nu\left[\frac{\partial^2\Omega}{\partial z^2} + \frac{\partial^2\Omega}{\partial r^2} + \frac{\partial}{\partial r}\left(\frac{\Omega}{r}\right)\right], \tag{8.3}$$

while the definition of vorticity yields,

$$\frac{\partial^2\psi}{\partial z^2} + \frac{\partial^2\psi}{\partial r^2} - \frac{1}{r}\frac{\partial\psi}{\partial r} = -r\Omega. \tag{8.4}$$

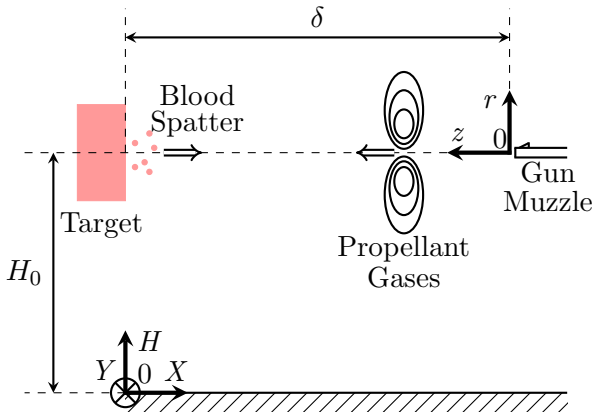

Figure 39. Schematic of the coordinate systems used for the description of the turbulent vortex ring of propellant gases moving toward the target and of the backward spatter of blood. The cylindrical coordinates r and z are associated with the radial and axial directions of the turbulent vortex ring and its origin is at the muzzle of the gun. The Cartesian coordinate system X–Y–H is used for the description of the trajectories of blood droplets in backward spatter resulting from a bullet impacting the target (the blood source).

The hydrodynamic vortex impulse is defined as,

$$\mathbf{P} = \frac{1}{2}\int \mathbf{r} \times \mathbf{\Omega} \mathrm{d}V, \tag{8.5}$$

where the integration is performed over an unbounded volume. The vortex impulse $\boldsymbol{P}$ is the integral invariant of the equations of motion, Eqs. (8.3) and (8.4) [77, 199]. Therefore, the impulse can be fully determined by the initial vorticity distribution in the turbulent vortex ring $\Omega_0 (r, z)$,

$$P_0 = \pi \int_{-\infty}^{\infty} \int_{0}^{\infty} r^2 \Omega_0 (r, z) \, \mathrm{d}r\mathrm{d}z, \tag{8.6}$$

where subscript zero here indicates the initial value.

It should be emphasized that the initial radius of the turbulent vortex ring is comparable to the radius of the muzzle exit and much smaller than the radius of the turbulent vortex ring as it propagates toward the target. Therefore, the initial radius can be neglected, the idealization which makes the problem self–similar [140]. Then, the dimensionless self–similar coordinates, $\overline{r}$ and $\overline{z}$ are introduced, as well as other functions, following standard considerations of the theory of self–similar flows [164, 200],

$$\overline{r} = \frac{r}{(P_0 t)^{1/4}}; \ \overline{z} = \frac{z}{(P_0 t)^{1/4}}; \ \Omega = \frac{1}{t}\overline{\Omega} (\overline{r}, \overline{z}) ; \ \psi = \frac{P_0^{3/4}}{t^{1/4}} \overline{\psi} (\overline{r}, \overline{z}) ; \ \nu = \lambda_0 \left(\frac{P_0}{t} \right)^{1/2}, \tag{8.7}$$

where λ_0 is a dimensionless empirical constant.

Accordingly, Eqs. (8.3) and (8.4) take the following dimensionless self–similar forms,

$$\lambda_0 \left[\frac{\partial^2 \overline{\Omega}}{\partial \overline{z}^2} + \frac{\partial^2 \overline{\Omega}}{\partial \overline{r}^2} + \frac{1}{\overline{r}} \frac{\partial \overline{\Omega}}{\partial \overline{r}} - \frac{\overline{\Omega}}{\overline{r}^2} \right] + \overline{\Omega} + \frac{1}{4} \left[\overline{z} \frac{\partial \overline{\Omega}}{\partial \overline{z}} + \overline{r} \frac{\partial \overline{\Omega}}{\partial \overline{r}} \right] = \frac{1}{\overline{r}} \left[\frac{\partial \overline{\psi}}{\partial \overline{r}} \frac{\partial \overline{\Omega}}{\partial \overline{z}} - \frac{\partial \overline{\psi}}{\partial \overline{z}} \frac{\partial \overline{\Omega}}{\partial \overline{r}} - \frac{\overline{\Omega}}{\overline{r}} \frac{\partial \overline{\psi}}{\partial \overline{z}} \right], \quad (8.8)$$

$$\frac{\partial^2 \overline{\psi}}{\partial \overline{z}^2} + \frac{\partial^2 \overline{\psi}}{\partial \overline{r}^2} - \frac{1}{\overline{r}} \frac{\partial \overline{\psi}}{\partial \overline{r}} = -\overline{r}\overline{\Omega}. \quad (8.9)$$

The solutions of Eqs. (8.8) and (8.9) are subjected to the following boundary conditions,

$$\overline{z}^2 + \overline{r}^2 \to \infty : \quad \overline{\Omega} \to 0 \text{ and } \overline{\psi} \to 0, \quad (8.10)$$

$$\overline{r} = 0 : \quad \overline{\Omega} = 0 \text{ and } \overline{\psi} = 0, \quad (8.11)$$

and should satisfy the following integral invariant condition associated with Eq. (8.6),

$$\pi \int_{-\infty}^{\infty} \int_{0}^{\infty} \overline{r}^2 \overline{\Omega} d\overline{r} d\overline{z} = 1. \quad (8.12)$$

Equations (8.8) and (8.9) can only be solved numerically. However, an analytical solution can be constructed when a plausible approximation of the RHS of Eq. (8.8) is introduced. Namely, having in mind that the axial velocity of turbulent vortex rings is typically much

higher than the radial one, i.e. $v_z \gg v_r$, and thus $\partial\overline{\psi}/\partial\overline{r} \gg \partial\overline{\psi}/\partial\overline{z}$, Eq. (8.8) is approximated by the following equation,

$$\lambda_0 \left[\frac{\partial^2\overline{\Omega}}{\partial\overline{z}^2} + \frac{\partial^2\overline{\Omega}}{\partial\overline{r}^2} + \frac{1}{\overline{r}}\frac{\partial\overline{\Omega}}{\partial\overline{r}} - \frac{\overline{\Omega}}{\overline{r}^2}\right] + \overline{\Omega} + \frac{1}{4}\left[\overline{z}\frac{\partial\overline{\Omega}}{\partial\overline{z}} + \overline{r}\frac{\partial\overline{\Omega}}{\partial\overline{r}}\right] = \frac{1}{\overline{r}_{\mathrm{m}}}\left.\frac{\partial\overline{\psi}}{\partial\overline{r}}\right|_{\substack{\overline{r}=\overline{r}_{\mathrm{m}} \\ \overline{z}=\overline{z}_{\mathrm{m}}}} \frac{\partial\overline{\Omega}}{\partial\overline{z}}, \tag{8.13}$$

where $\overline{r}_{\mathrm{m}}$ and $\overline{z}_{\mathrm{m}}$ are the locations of the maximum of the vorticity function $\overline{\Omega}\left(\overline{r},\overline{z}\right)$.

The analytical solution of the system of Eqs. (8.9) and (8.13) reads,

$$\overline{\psi}\left(\overline{r},\overline{z}\right) = \frac{\overline{r}^2}{64\sqrt{2}\pi\lambda_0^{3/2}s^3}\left[\mathrm{erf}\left(s\right) - \frac{2s}{\sqrt{\pi}}\exp\left(-s^2\right)\right], \tag{8.14}$$

$$\overline{\Omega}\left(\overline{r},\overline{z}\right) = \frac{\overline{r}}{64\sqrt{2}\pi^{3/2}\lambda_0^{5/2}}\exp\left(-s^2\right), \tag{8.15}$$

where,

$$s = \sqrt{\frac{\left(\overline{z}-\overline{z}_{\mathrm{m}}\right)^2 + \overline{r}^2}{8\lambda_0}}, \tag{8.16}$$

$$\overline{r}_{\mathrm{m}} = 2\sqrt{\lambda_0}, \tag{8.17}$$

$$\overline{z}_{\mathrm{m}} = \frac{1}{2\sqrt{2e}\left(\pi\lambda_0\right)^{3/2}}\left[1 - \sqrt{\frac{\pi e}{8}}\mathrm{erf}\left(\frac{1}{\sqrt{2}}\right)\right]. \tag{8.18}$$

The empirical coefficient λ_0 is related to the ratio of the coordinates of the maximum vorticity locations, $\alpha = \overline{r}_{\rm m}/\overline{z}_{\rm m}$, as,

$$\lambda_0 = \sqrt{\alpha}\left[\frac{1-\sqrt{\pi e/8}\,\mathrm{erf}\left(1/\sqrt{2}\right)}{4\sqrt{2e}\pi^{3/2}}\right]^{1/2}. \tag{8.19}$$

It should be emphasized that the ratio α can be measured experimentally, which determines the only empirical parameters of the semi–empirical theory of turbulent vortex rings, λ_0, through Eq. (8.19).

The solution of Eqs. (8.9) and (8.13) resulting in Eqs. (8.14)–(8.18) was recently published in Ref. [77] without any derivation. The original derivation given is given in Ref. [200] and is difficult to obtain, therefore, its complete derivation is proven independently in this work and shown in Appendix C.

8.2.2 Gunpowder Particle Transport by a Turbulent Vortex Ring

The transport of gunpowder particles by a turbulent vortex ring is described using the following equation,

$$\frac{\partial c}{\partial t} + v_z\frac{\partial c}{\partial z} + v_r\frac{\partial c}{\partial r} = D\left[\frac{1}{r}\frac{\partial}{\partial r}\left(r\frac{\partial c}{\partial r}\right) + \frac{\partial^2 c}{\partial z^2}\right], \tag{8.20}$$

where c is the average gunpowder particle concentration in units of particles/cm^3, D is the turbulent diffusion coefficient, and $D = \gamma\nu$, where γ is the inverse turbulent Schmidt number.

The total number of gunpowder particles is invariant and thus, Eq. (8.20) possesses the following integral invariant,

$$N_0 = 2\pi \int_{-\infty}^{\infty} \int_{0}^{\infty} cr\mathrm{d}r\mathrm{d}z, \tag{8.21}$$

where N_0 is the total number of gunpowder particles released from the muzzle.

Similarly to the flow field, the gunpowder particle concentration in the present case is also self–similar, and thus Eq. (8.20) takes the following self–similar form,

$$\gamma\lambda_0 \left[\frac{\partial^2 \overline{c}}{\partial \overline{z}^2} + \frac{\partial^2 \overline{c}}{\partial \overline{r}^2} + \frac{1}{\overline{r}}\frac{\partial \overline{c}}{\partial \overline{r}}\right] + \frac{1}{4}\left[\overline{z}\frac{\partial \overline{c}}{\partial \overline{z}} + \overline{r}\frac{\partial \overline{c}}{\partial \overline{r}}\right] + \frac{3}{4}\overline{c} = \frac{1}{\overline{r}}\left[\frac{\partial \overline{\psi}}{\partial \overline{r}}\frac{\partial \overline{c}}{\partial \overline{z}} - \frac{\partial \overline{\psi}}{\partial \overline{z}}\frac{\partial \overline{c}}{\partial \overline{r}}\right], \tag{8.22}$$

where,

$$c = \frac{N_0}{2\pi \left(P_0 t\right)^{3/4}}\overline{c}. \tag{8.23}$$

The solution of Eq. (8.22) should satisfy the following boundary conditions,

$$\overline{z}^2 + \overline{r}^2 \to \infty : \quad \overline{c} \to 0, \tag{8.24}$$

$$\overline{r} = 0 : \quad \overline{c} = \max. \tag{8.25}$$

As in the momentum balance equation discussed in Sec. 8.2.1, we account for the fact that $v_z \gg v_r$, and thus, $\partial\overline{\psi}/\partial\overline{r} \gg \partial\overline{\psi}/\partial\overline{z}$, and reduce Eq. (8.22) to the following form,

$$\gamma\lambda_0 \left[\frac{\partial^2\overline{c}}{\partial\overline{z}^2} + \frac{\partial^2\overline{c}}{\partial\overline{r}^2} + \frac{1}{\overline{r}}\frac{\partial\overline{c}}{\partial\overline{r}}\right] + \frac{1}{4}\left(\overline{z} - \frac{4}{\overline{r}_{\mathrm{m}}}\left.\frac{\partial\overline{\psi}}{\partial\overline{r}}\right|_{\substack{\overline{r}=\overline{r}_{\mathrm{m}}\\ \overline{z}=\overline{z}_{\mathrm{m}}}}\right)\frac{\partial\overline{c}}{\partial\overline{z}} + \frac{\overline{r}}{4}\frac{\partial\overline{c}}{\partial\overline{r}} + \frac{3}{4}\overline{c} = 0. \tag{8.26}$$

Introduce the following variables to find an analytical solution of Eq. (8.26),

$$\xi = \frac{1}{m}\left(\overline{z} - 4K\right); \quad \eta = \frac{1}{m}\overline{r}, \tag{8.27}$$

where $K = \overline{r}_{\mathrm{m}}^{-1}\left.\partial\overline{\psi}/\partial\overline{r}\right|_{\substack{\overline{r}=\overline{r}_{\mathrm{m}}\\ \overline{z}=\overline{z}_{\mathrm{m}}}}$ and $m = \sqrt{8\gamma\lambda_0}$.

The solution is sought in the form,

$$\overline{c} = \exp\left(-\frac{\xi^2+\eta^2}{2}\right)\Gamma\left(\xi,\eta\right). \tag{8.28}$$

Accordingly, Eq. (8.26) yields the following equation for the function $\Gamma\left(\zeta,\eta\right)$,

$$\frac{1}{\eta}\frac{\partial}{\partial\eta}\left(\eta\frac{\partial\Gamma}{\partial\eta}\right) + \frac{\partial^2\Gamma}{\partial\xi^2} + \left(3 - \xi^2 - \eta^2\right)\Gamma = 0, \tag{8.29}$$

Defining $\Gamma\left(\xi,\eta\right) = \Gamma_1\left(\xi\right)\Gamma_2\left(\eta\right)$, then Eq. (8.29) yields the following two ordinary differential equations,

$$\frac{\mathrm{d}^2\Gamma_1}{\mathrm{d}\xi^2} - \xi^2\Gamma_1 = -\left(A+3\right)\Gamma_1, \tag{8.30}$$

$$\frac{1}{\eta}\frac{\mathrm{d}}{\mathrm{d}\eta}\left(\eta\frac{\mathrm{d}\Gamma_2}{\mathrm{d}\eta}\right)-\eta^2\Gamma_2=A\Gamma_2, \tag{8.31}$$

where A is a separation constant.

The integral invariant of Eq. (8.21) takes the following form,

$$\int_{-\infty}^{\infty}\exp\left(-\frac{\xi^2}{2}\right)\Gamma_1\mathrm{d}\xi\int_{0}^{\infty}\exp\left(-\frac{\eta^2}{2}\right)\eta\Gamma_2\mathrm{d}\eta=\frac{1}{\left(8\gamma\lambda_0\right)^{3/2}}. \tag{8.32}$$

Equation (8.30) is known in the theory of one–dimensional quantum oscillators and its solution satisfying Eq. (8.32) is readily available [187, 201],

$$\Gamma_1\left(\xi\right)=B_1\frac{\exp\left(-\xi^2/2\right)H_j\left(\xi\right)}{\pi^{1/4}\left(2^M j!\right)^{1/2}}, \tag{8.33}$$

where B_1 is a constant, H_j are the Hermite polynomials, and $A+3=2j+1$, where $j=0,1,2,\ldots$.

Equation (8.31) is also known in the theory of cylindrical quantum oscillators [202], and its solution satisfying Eq. (8.32) exists only when $-A=2\left(2i+1\right)$, where $i=0,1,2,\ldots$. Then, it is seen that the only appropriate choice is $i=j=0$, which yields $A=-2$, and Eq. (8.31) results in,

$$\Gamma_2\left(\eta\right)=B_2\exp\left(-\eta^2/2\right), \tag{8.34}$$

where B_2 is a constant.

Therefore, $\Gamma(\xi,\eta)$ becomes,

$$\Gamma(\xi,\eta) = B\exp\left(-\frac{\xi^2+\eta^2}{2}\right), \tag{8.35}$$

where B is a constant which incorporates all the previous factors and is determined from the integral invariant, Eq. (8.32), as,

$$B = \frac{2}{\sqrt{\pi}\left(8\gamma\lambda_0\right)^{3/2}}. \tag{8.36}$$

Then, Eqs. (8.28), (8.35), and (8.36) result in,

$$\overline{c} = \frac{2}{\sqrt{\pi}\left(8\gamma\lambda_0\right)^{3/2}}\exp\left[-\left(\xi^2+\eta^2\right)\right]. \tag{8.37}$$

Through the variable transformation in Eq. (8.27), the latter equation yields the solution for the concentration of gunpowder particles transported by a turbulent vortex ring in the following form,

$$\overline{c} = \frac{2}{\sqrt{\pi}\left(8\gamma\lambda_0\right)^{3/2}}\exp\left[-\frac{\left(\overline{z}-4K\right)^2+\overline{r}^2}{8\gamma\lambda_0}\right]. \tag{8.38}$$

8.2.3 Deflection of Blood Droplets in Backward Spatter

When a bullet impacts a target and blood is splashed in the direction opposite of bullet motion, i.e. backward spatter, the turbulent vortex ring of propellant powder following the bullet can encounter the airborne blood droplets moving in the opposite direction. These blood

droplets form due to the Rayleigh–Taylor instability which occurs in backward spatter because the denser blood is accelerated towards air as explained in Ch. 6. The theory of this instability has been used to predict the formation of blood droplets in two different cases of backward spatter by sharp and blunt bullets (cf. Ch. 6). In that chapter, backward spatter is considered as a system of two–interpenetrating continua, with a cloud of blood droplets propagating through air experiencing aerodynamic drag, producing viscous suction and causing air entrainment. The leading blood droplets experience the highest drag and entrain air in their wake which reduces the air drag experienced by the following droplets. This collective effect, resembling a flock of geese flying in V formation, allows the droplets to fly further [70].

Following the work of Sec. 6.6, the drag force acting on a droplet along its trajectory, $\mathbf{F}_{\mathrm{D},i}$, with entrained air is,

$$\mathbf{F}_{\mathrm{D},i} = \frac{1}{8}\pi l_{*,i}^2 C_{\mathrm{D},i}\rho_{\mathrm{a}}\left(\mathbf{u}_i - \mathbf{U}_i\right)\left|\mathbf{u}_i - \mathbf{U}_i\right|, \tag{8.39}$$

where $l_{*,i}$ is an individual droplet diameter determined by the Rayleigh–Taylor instability, $C_{\mathrm{D},i}$ is the drag coefficient, ρ_{a} is the density of air, u_i is the instantaneous average velocity of the blood droplets in a cloud i along the droplet trajectory, and $\mathbf{U}_i$ is the instantaneous averaged velocity of entrained air in the cloud along the trajectory.

The momentum balance of blood droplets in a cloud with air entrainment is then,

$$\frac{\mathrm{d}^2X}{\mathrm{d}T^2}\mathbf{i}+\frac{\mathrm{d}^2Y}{\mathrm{d}T^2}\mathbf{j}+\frac{\mathrm{d}^2H}{\mathrm{d}T^2}\mathbf{k}=-\frac{1}{8}\pi l_{*,i}^2 C_{\mathrm{D},i}\frac{n_i}{M_i}\rho_{\mathrm{a}}\left[\left(\frac{\mathrm{d}X}{\mathrm{d}T}\mathbf{i}+\frac{\mathrm{d}Y}{\mathrm{d}T}\mathbf{j}+\frac{\mathrm{d}H}{\mathrm{d}T}\mathbf{k}\right)-U_i\boldsymbol{\tau}\right]\times \left[\sqrt{\left(\frac{\mathrm{d}X}{\mathrm{d}T}\right)^2+\left(\frac{\mathrm{d}Y}{\mathrm{d}T}\right)^2+\left(\frac{\mathrm{d}H}{\mathrm{d}T}\right)^2}-U_i\right]-g\mathbf{k} \tag{8.40}$$

where M_i is the mass of blood in the cloud, T is the time reckoned from the moment these droplets have been spattered, n_i is the number of blood droplets in the cloud, $\boldsymbol{\tau}$ is the unit vector tangent to the trajectory, and $\mathbf{i}$, $\mathbf{j}$, and $\mathbf{k}$ are the unit vectors of the X–Y–H directions shown in Fig. 39. Note that a temporal offset exists between the formation of the turbulent vortex ring and the backward spatter of blood droplets. Therefore, the time t, in which the evolution and propagation of the turbulent vortex ring is tracked, and the time T, in which droplet motion is calculated, are related as,

$$t=T+\frac{\delta}{V_A}, \tag{8.41}$$

where V_A is the velocity of the bullet approaching the target, and δ is the distance between the muzzle exit and the target (cf. Fig. 39).

If the airborne blood droplets encounter a turbulent vortex ring, the counter–flow of air generated by the latter sheds the air entrained by the cloud, i.e. the velocity and volume of

the entrained air, $U_i \to 0$, and $V \to 0$. Then, the drag force acting on the droplets become associated with the velocity of the counter–flow generated by the turbulent vortex ring as,

$$\mathbf{F}_{\mathrm{D},i} = \frac{1}{8}\pi l_{*,i}^2 \rho_{\mathrm{a}} \left(\mathbf{u}_i + \mathbf{v}\right) \left|\mathbf{u}_i + \mathbf{v}\right|, \tag{8.42}$$

where $\mathbf{v}$ is the velocity vector of the turbulent vortex ring. It should be emphasized that Eq. (8.42) does not include the effect of the air entrained by flying droplets before the strong interaction with the oncoming vortex ring because the entrained air is easily shed back by the ring long before the droplets are affected by the collision.

The momentum balance of blood droplets in a cloud interacting with a turbulent vortex ring is expressed as,

$$\begin{aligned}
\frac{\mathrm{d}^2 X}{\mathrm{d}T^2}\mathbf{i} + \frac{\mathrm{d}^2 Y}{\mathrm{d}T^2}\mathbf{j} + \frac{\mathrm{d}^2 H}{\mathrm{d}T^2}\mathbf{k} = -\frac{1}{8}\pi l_{*,i}^2 C_{\mathrm{D},i} \frac{n_i}{M_i} \rho_{\mathrm{a}} \times \\
\left[\left(\frac{\mathrm{d}X}{\mathrm{d}T}\mathbf{i} + \frac{\mathrm{d}Y}{\mathrm{d}T}\mathbf{j} + \frac{\mathrm{d}H}{\mathrm{d}T}\mathbf{k} \right) + \left(v_z \mathbf{i} + v_r \frac{\mathrm{d}Y}{\mathrm{d}T} \left[\left(\frac{\mathrm{d}Y}{\mathrm{d}T} \right)^2 + \left(\frac{\mathrm{d}H}{\mathrm{d}T} \right)^2 \right]^{-1/2} \mathbf{j} + \cdots \right. \right. \\
\left. \left. v_r \frac{\mathrm{d}H}{\mathrm{d}T} \left[\left(\frac{\mathrm{d}Y}{\mathrm{d}T} \right)^2 + \left(\frac{\mathrm{d}H}{\mathrm{d}T} \right)^2 \right]^{-1/2} \mathbf{k} \right) \right] \times \\
\left[\left(\frac{\mathrm{d}X}{\mathrm{d}T} + v_z \right)^2 + \left(\frac{\mathrm{d}Y}{\mathrm{d}T} + v_r \frac{\mathrm{d}Y}{\mathrm{d}T} \left[\left(\frac{\mathrm{d}Y}{\mathrm{d}T} \right)^2 + \left(\frac{\mathrm{d}H}{\mathrm{d}T} \right)^2 \right]^{-1/2} \right)^2 + \cdots \right. \\
\left. \left(\frac{\mathrm{d}H}{\mathrm{d}T} + v_r \frac{\mathrm{d}H}{\mathrm{d}T} \left[\left(\frac{\mathrm{d}Y}{\mathrm{d}T} \right)^2 + \left(\frac{\mathrm{d}H}{\mathrm{d}T} \right)^2 \right]^{-1/2} \right)^2 \right]^{1/2} - g\mathbf{k}
\end{aligned} \tag{8.43}$$

The projections of Eqs. (8.40) and (8.43) on the X–Y–H axes and the appropriate initial conditions are described in Appendix D.

In the case of a strong interaction of the blood droplets and the turbulent vortex ring, the blood droplet velocity u_i will slow down to zero. Then, droplet motion along the trajectory will cease, and the droplets will be pushed by the turbulent vortex ring in the opposite direction. The interaction of the turbulent vortex ring and the turned–around blood droplets is relatively short because the turbulent vortex ring propagates rapidly, and its velocity field is practically not felt outside of the vortex body. Then, the droplets will continue moving toward the target entraining the surrounding air once again according to the mechanisms described in Eq. 8.40. Also, the droplets which passed through the vortex ring will continue moving from the target entraining the surrounding air once again according to the mechanisms described in Eq. (8.40).

8.3 Results and Discussion

8.3.1 Propagation of Propellant Gases

The dimensionless empirical parameter λ_0 involved in the semi–empirical theory of turbulent vortices is found using Eq. (8.19) and data for the coordinates of the locations of the maximum vorticity, $\alpha = \overline{r}_{\rm m}/\overline{z}_{\rm m}$. The latter was found experimentally as $\alpha \approx 10^{-2} - 10^{-3}$ [76, 77]. For the value of $\alpha = 5.5 \times 10^{-3}$, which corresponds to the value of $\lambda_0 = 4.4 \times 10^{-3}$, the field of the self–similar stream function found from Eq. (8.14) is shown in Fig. 40. Note that unless otherwise specified, this value of α, and thus λ_0, is used hereinafter in this work. The vorticity of such a turbulent vortex ring was reported to be highly localized [203], which is corroborated in Fig. 41, plotted using Eq. (8.15).

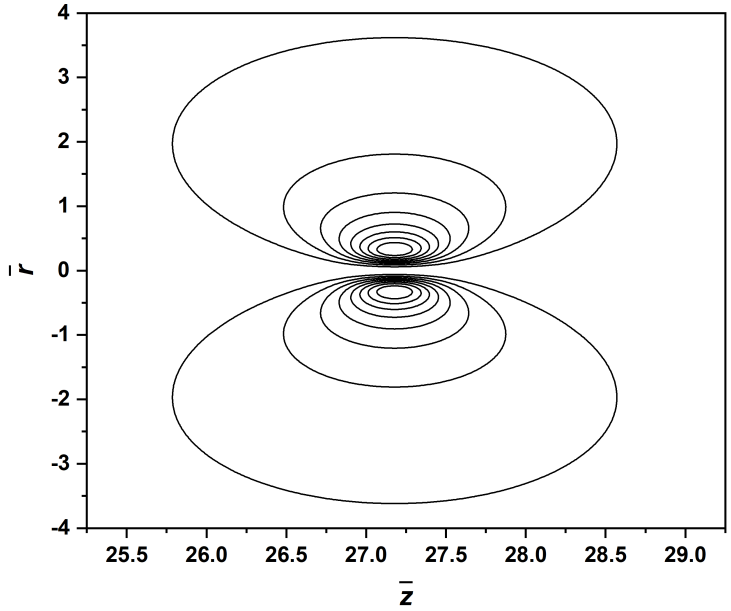

Figure 40. Self–similar streamlines of the turbulent vortex ring with $\alpha = 5.5 \times 10^{-3}$ ($\lambda_0 = 4.4 \times 10^{-3}$). The values of the streamlines from the outward line going inward are 0.022–0.176 in steps of 0.022.

The field of the self–similar concentration of gunpowder particles found from Eq. (8.19) with $\gamma = 1$ (corresponding to the turbulent Schmidt number equal to one, a plausible approximation for turbulent flows [140]) is shown in Fig. 42.

Using the self–similar solution, the time dependent flow pattern can be reconstructed with Eq. (8.7), and the resultant flow field can be overlaid on experimental pictures of muzzle gases. Such data is available in Ref. [79] where a 5.56 mm caliber M–16 rifle firing ball ammunition was photographed during the early development of the muzzle flow pattern close to the muzzle of the rifle. There were four photographs taken at 10, 37, 105, and 237 μs after the bullet left the

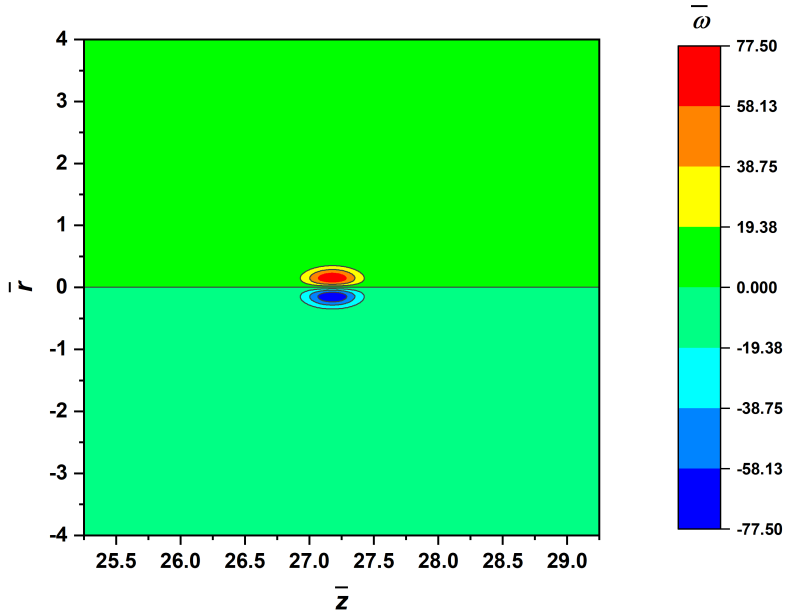

Figure 41. Self–similar vorticity field of the turbulent vortex ring with $\alpha = 5.5 \times 10^{-3}$ ($\lambda_0 = 4.4 \times 10^{-3}$).

muzzle and the final image at 237 μs shows a plume of muzzle gases and the turbulent vortex ring. The theoretical flow pattern predicted using Eq. (8.14) overlaid on this experimental image is shown in Fig. 43. Note that other structures inherent of the propagation of muzzle gases (such as the precursor blast wave) discussed in Sec. 2.5, are also seen in Fig. 43. The impulse of the vortex ring was found by fitting the flow pattern to the experimental image which yielded $P_0 = 75$ cm^4/s. The corresponding streamlines predicted with the values of α (and thus λ_0) and P_0 mentioned above, properly fit the dark area in Fig. 43.

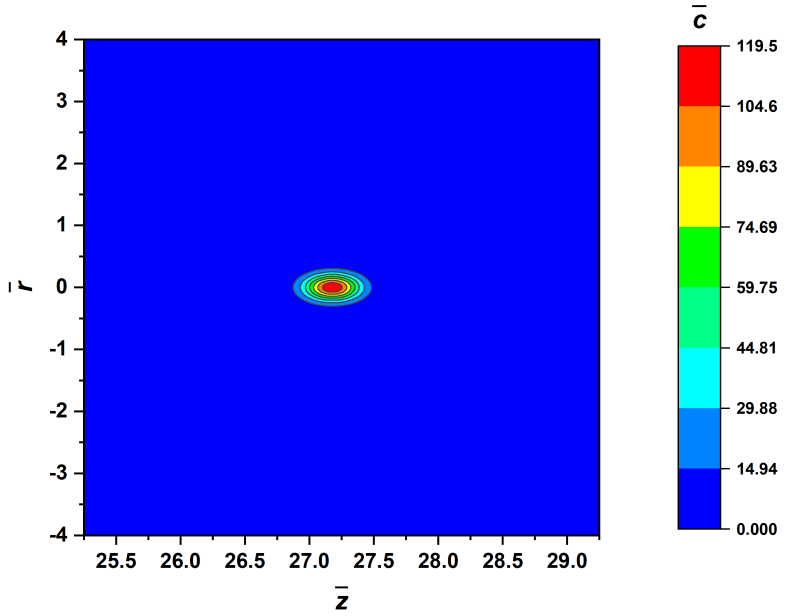

Figure 42. Field of the self–similar concentration of gunpowder particles in the turbulent vortex ring with $\alpha = 5.5 \times 10^{-3}$ ($\lambda_0 = 4.4 \times 10^{-3}$), and $\gamma = 1$.

The propagation of the turbulent vortex ring can be followed by the locations of the maximum vorticity versus time, which are found from Eq. (8.7), (8.17), and (8.18) as,

$$z_{\rm m}(t) = \overline{z}_{\rm m} (P_0 t)^{1/4}, \quad r_{\rm m}(t) = \overline{r}_{\rm m} (P_0 t)^{1/4}. \tag{8.44}$$

For the turbulent vortex ring shown in Fig. 43, the values of $\overline{z}_{\rm m} = 27.18$ and $\overline{r}_{\rm m} = 0.1495$ (corresponding to $\alpha = 5.5 \times 10^{-3}$, and thus, $\lambda_0 = 4.4 \times 10^{-3}$), with $P_0 = 75$ cm^4/s, yield the axial and radial positions of the maximum vorticity through Eq. (8.44), as is shown in Fig. 44.

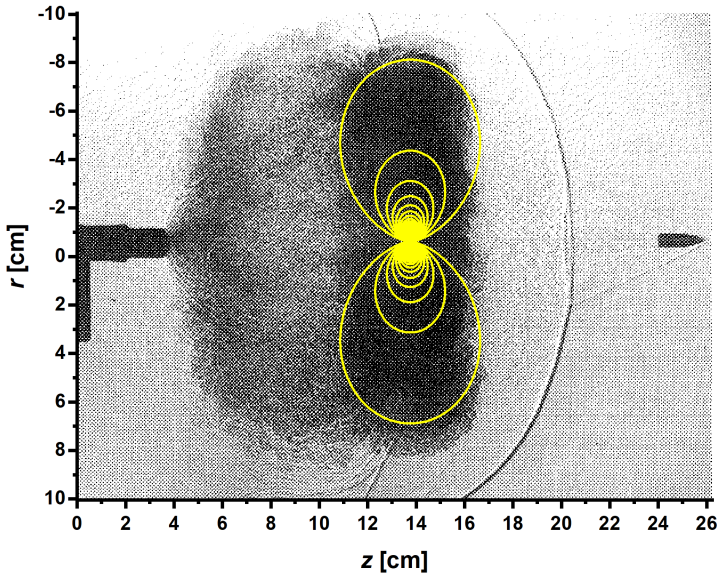

Figure 43. Theoretically predicted flow pattern of the turbulent vortex ring at 237 μs after the bullet left the muzzle of the gun. The experimental image is taken from Ref. [79]. The values of the stream function corresponding to the streamlines from the outward line to the inward one are, $\psi = 0.8 - 37.4$ cm^3/s in steps of 0.8 cm^3/s.

The concentration of gunpowder particles swept by a turbulent vortex ring depends on the total number of particles within the cartridge, N_0. This value can be evaluated knowing the volume of a single gunpowder particle and the volume of the cartridge which holds all gunpowder particles. For spherical gunpowder particles of 1 mm in diameter (which have a density around 1 g/cm^3 [204]), and the volume of the cartridge is approximately 1 mL, an estimate of the number of the particles is then $N_0 \approx 1500$ particles. The concentration of gunpowder particles (as a function of time) swept by the turbulent vortex ring of propellant gases with an impulse in the $P_0 = 50 - 125$ cm^4/s range (which incorporates the value of $P_0 = 75$ cm^4/s established

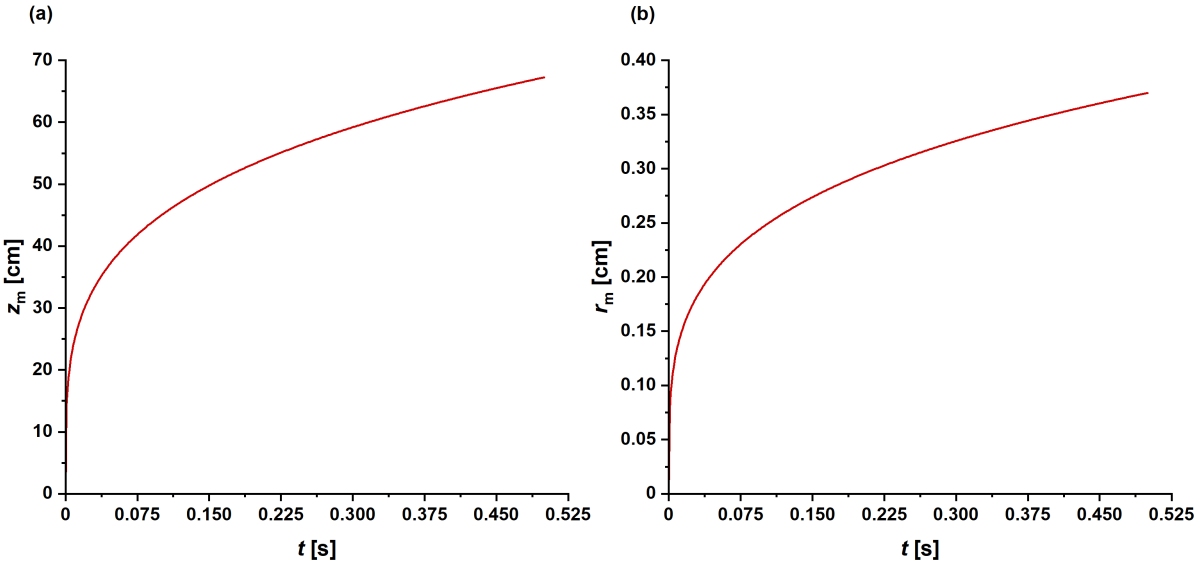

Figure 44. Location of the maximum vorticity in the turbulent vortex ring of the propellant gases over time. (a) The axial position, (b) the radial position.

in Fig. 43), is shown in Fig. 45. It is calculated using Eqs. (8.23) and (8.38). The order of magnitude of the concentration is within the realm of what was observed experimentally, as Ref. [79] has reported $10^5 - 10^8$ particles/cm^3.

8.3.2 Effect of Propellant Gases on the Backward Spatter of Blood

To study the effect of a turbulent vortex ring of propellant gases on the backward spatter of blood droplets, the case of a blunt bullet impacting a target normally from 30 cm is considered with the same set of parameters as in Sec. 6.8. Namely, the blood spatter splash angle is $\Delta\theta = 15°$, the approaching bullet velocity is $V_A = 1000$ m/s, and the droplet size $l_{*,i}$ ranges from ~ 0.2 to 0.4 mm, which is the size range present in backward blood spatter due to a gunshot (cf. Ch. 6). The initial height (the droplet origin) was set to be $H_0 = 100$ cm. The

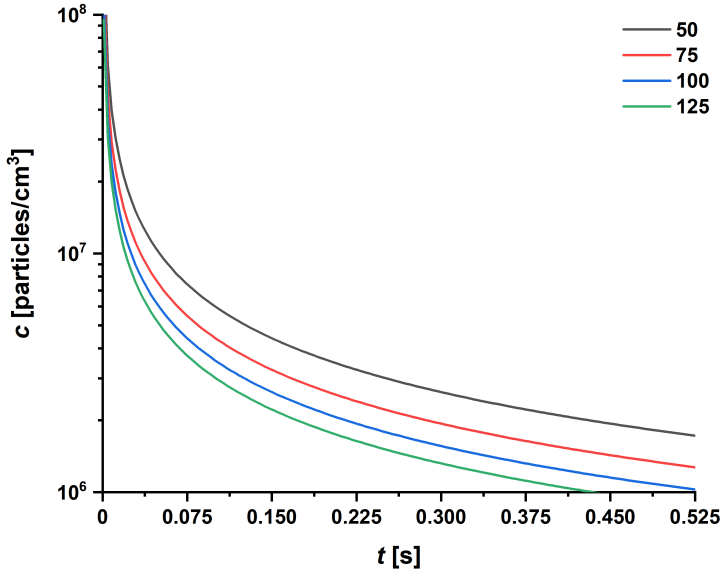

Figure 45. Gunpowder concentration in the turbulent vortex ring of propellant gases for $N_0 = 1500$ particles and the range of P_0 is indicated in the legend. The units for P_0 are cm^4/s.

equations for the droplet trajectory calculations in Sec. 6.6 were modified to incorporate an interaction with the turbulent vortex ring affecting the aerodynamic drag force, as described in Sec. 8.2.3. In order to reveal the effect of the impulse of the turbulent vortex ring, P_0, it was varied from 75 cm^4/s to 150 cm^4/s, and the final locations of the blood droplets predicted with and without accounting for the interaction with a turbulent vortex ring are shown in Fig. 46.

When the interactions with the turbulent vortex ring is accounted for, the blood droplet bins can be deflected further from the target than without such interactions, as seen in Fig. 46(b), for example. On the contrary, the blood droplet bins can be overcome by the turbulent vortex ring and turn towards the target. These bins can either be deflected and spread outwards (in

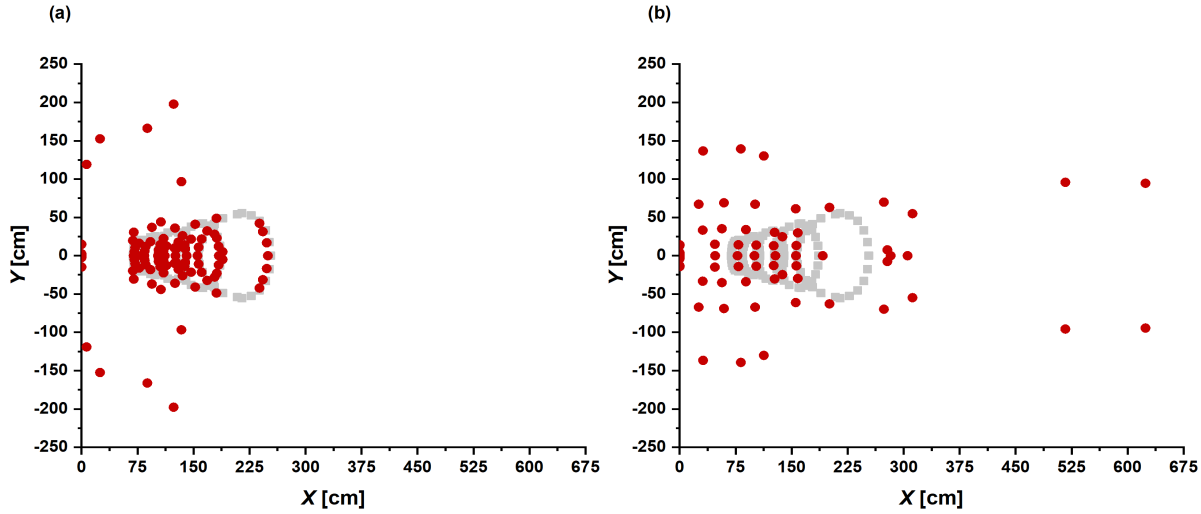

Figure 46. Final blood droplet bin locations on the floor accounting for an interaction with and without a turbulent vortex ring. The impulse of the turbulent vortex ring is (a) $P_0 = 75$ cm^4/s, and (b) $P_0 = 150$ cm^4/s. The red circles and gray squares represent the cases with and without the interaction with the turbulent vortex ring, respectively.

the Y–direction as shown in Fig. 46), or hit the target as indicated by the large quantity of red circles located around $X = 0$ in Fig. 46. The predicted spatial and average stain area presented in the form of histograms binned every 20 cm from the target are shown in Figs. 47 and 48, respectively.

The interactions with the turbulent vortex rings result in large changes in their final locations, and the resultant distribution of the average stain area. For the impulse of $P_0 = 75$ cm^4/s, 18% of the droplets splashed fall within 20 cm of the target, whereas for the impulse of $P_0 = 150$ cm^4/s, 41% of the droplets splashed fall within that range. A higher value of the vortex impulse is equivalent to a closer shooting distance (for self–similar vortex rings).

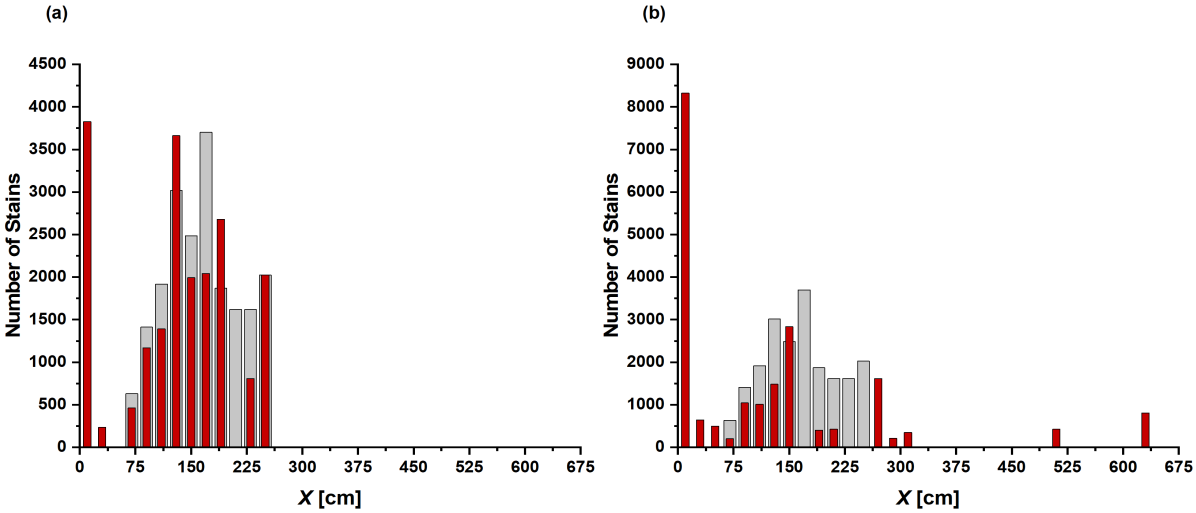

Figure 47. Spatial distribution of the number of bloodstains from a gunshot formed on the floor by backward spatter. (a) The case of a turbulent vortex ring with the impulse of $P_0 = 75$ cm^4/s, and (b) with the impulse of $P_0 = 150$ cm^4/s. The gray bars indicate the distributions predicted without an interaction with the vortex ring, and the red bars are for the case where the interaction was accounted for.

Accordingly, these results show that a closer shooting distance result in more blood droplets turning around and travelling towards the target, an effect important for CSI.

8.4 Conclusion

In this work, self–similar turbulent vortex rings of propellant gases are studied because they comprise the main mechanism responsible for two practically important effects: (i) transport of gunshot residue, and (ii) deflection of backward spattered blood droplets. The self–similar velocity and the gunpowder concentration fields were predicted and compared to experimental data which revealed a good agreement. The previously introduced theory of backward blood splashing due to a blunt bullet was modified to account for the effect of a turbulent vortex

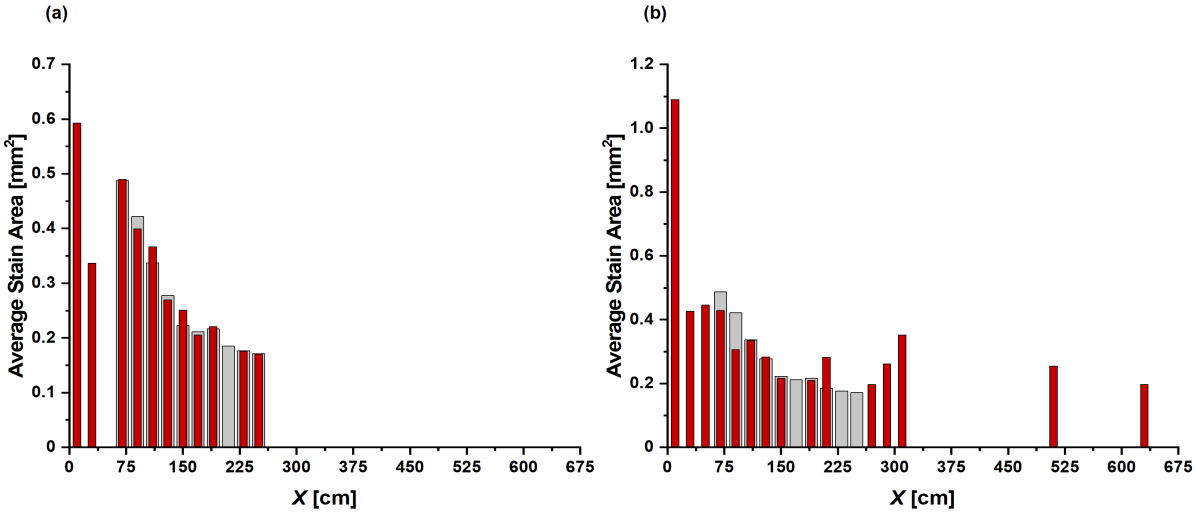

Figure 48. Spatial distribution of the average stain area from a gunshot formed on the floor by backward spatter. (a) The case of a turbulent vortex ring with the impulse of $P_0 = 75$ cm^4/s, and (b) with the impulse of $P_0 = 150$ cm^4/s. As in Fig. 47, the gray bars indicate the distributions predicted without an interaction with the vortex ring, and the red bars are for the case where the interaction was accounted for.

ring of propellant gases on the flight of blood droplets and their resultant deposition on the floor. The predicted final locations of backward splashed blood droplets calculated with and without the interaction of the turbulent vortex ring of propellant gases were compared. The results revealed a clear link between the turbulent vortex ring impulse, the blood distribution and average stain size on the floor. It was shown that doubling the impulse results in more than double the number of stains located 20 cm away from the target (i.e. relatively close to it). The same link, due to the self–similarity, exists between the final location of blood droplets affected by shooting from a closer range.

CHAPTER 9

BLOOD JETTING

This chapter has been previously published in Ref. [5], reprinted by permission from Springer Nature [Friction coefficient of an intact free liquid jet moving in air. Comiskey, P. M., and Yarin, A. L., Experiments in Fluids, 59, 65], copyright (2018) Springer Nature.

9.1 Introduction

A novel method of determining the friction coefficient of intact free liquid jets moving in quiescent air is proposed. The middle–size jets of this kind are relevant for such applications as decorative fountains, fiber–forming, fire suppression, agriculture, and forensics. The present method is based on measurements of trajectories created using a straightforward experimental apparatus emulating such jets at a variety of initial inclination angles. Then, the trajectories are described theoretically, accounting for the longitudinal traction imposed on such jets by the surrounding air. The comparison of the experimental data with the theoretical predictions show that the results can be perfectly superimposed with the friction coefficient $C_{\rm fd} = 5Re_{\rm d}^{-1/2 \pm 0.05}$, in the $621 \leq Re_{\rm d} \leq 1289$ range, with $Re_{\rm d}$ being the Reynolds number based on the local cross–sectional diameter of the jet. The results also show that the farthest distance such jets can reach corresponds to the initial inclination angle $\alpha = 35^{\circ}$ which is in agreement with already published data.

9.2 Experiment

Intact jets were experimentally issued using a three–tiered nozzle system shown in Fig. 49. The working fluid was kept in a storage vessel and supplied to the nozzle system using a submerged circulation pump (Marineland Maxi–Jet 600). The first tier of the nozzle system which the working fluid encountered consisted of a porous medium which acted to smooth the pulsing, slightly–transient flow from the circulation pump. Then, the second stage was an elongated honeycomb mesh intended to prevent any possible swirling or secondary flows. The final stage consisted of an enclosed cavity which filled uniformly and smoothly as it supplied the working fluid into the nozzle. Two different solid–stream spray nozzles with cross–sectional areas of 0.04 and 0.13 cm^2 (McMaster–Carr 7611T43 and 7611T46) were used. The free liquid jets were collected in a second storage vessel which had another submerged circulation pump (Marineland Maxi–Jet 600) to pump the working fluid back to the first storage tank, thus creating closed–loop system schematically shown in Fig. 49.

There were two replicated experiments, one for each nozzle type with four different initial inclination angles, with a total of nine experiments, as listed in Table VI. The two nozzle types were tested at the initial inclination angles of $\alpha \approx 0°,\ 20°,\ 40°,$ and $60°$. The inclination angle values were measured with a digital level on site and later corrected to more precise values based upon the images taken during each experiment, which resulted in the corrected values listed in Table VI. The pressure head between the first submerged circulation pump and the nozzle system had to be overcome by the pump. Accordingly, simply raising the three–tiered nozzle system reduced the flow rate of the working fluid through the nozzle. As a result, low–

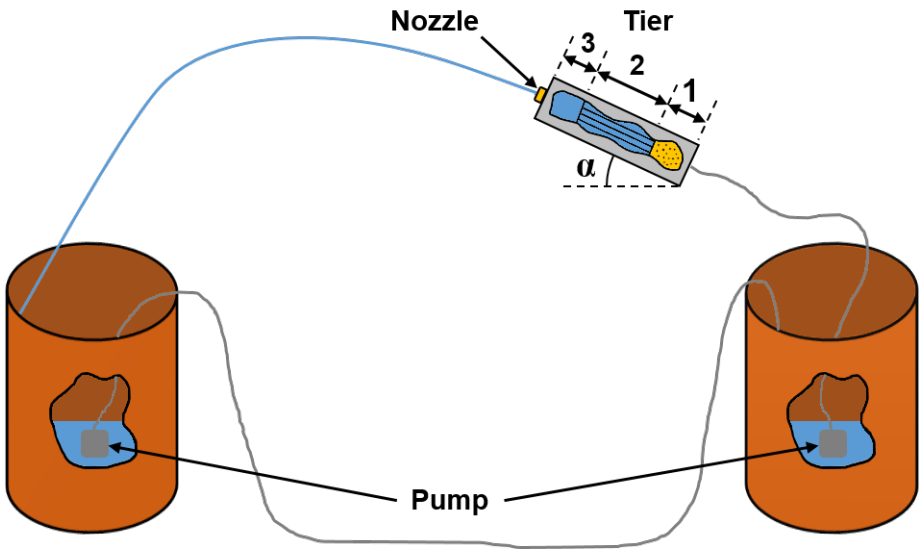

Figure 49. Schematic of the experimental setup. The free liquid jet issued from the nozzle is shown in blue and the gray lines indicate tubing. Tier 1 corresponds to the porous medium, tier 2 the elongated honeycomb mesh, and tier 3 the enclosed cavity. Fig. from Ref. [5].

velocity jet experiments could easily be performed by inducing in this way a large opposite pressure head as is the case of experiment 9 in Table VI. Note that for all other experiments, the pressure head was effectively kept constant, however, slight deviations led to a difference in jet velocity even for the same nozzle type. The velocity was determined through measuring the volumetric flow rate approximately 30 times for each experiment and using the known nozzle outlet area. The values were then averaged, with the results and the corresponding standard deviations being listed in Table VI. No discharge coefficients were needed in this calculation, because the internal geometry of the nozzles was smooth and gradual, resulting in a discharge

coefficient very close to unity, which was corroborated by the jet images of the type shown in Fig. 50. The working fluid used in all experiments was water.

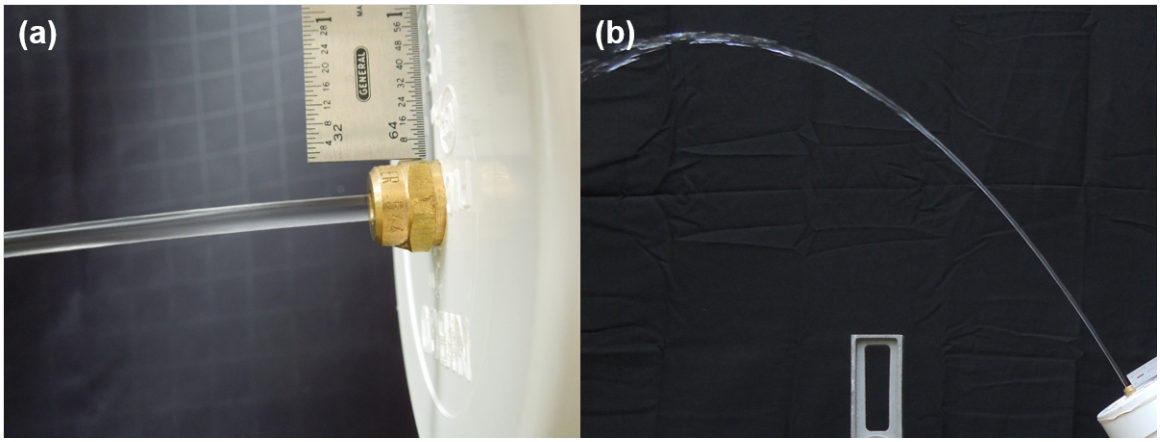

Figure 50. Water jets used in experiment 5 (a) and experiment 8 (b). Fig. from Ref. [5].

9.3 Theoretical Model

The momentless quasi–one–dimensional theory of planar bending liquid jets yields the following continuity Eq. (9.1), and two projections (tangential and normal to the jet trajectory) of the momentum balance equation [118],

$$\frac{\partial \lambda f}{\partial t} + \frac{\partial f W}{\partial x} = 0, \tag{9.1}$$

TABLE VI

Experimental parameters. Note that the values of α listed here were measured from experimental images and Re_{d} is the jet Reynolds number based on the jet velocity, diameter at the nozzle exit, and the kinematic viscosity of air. Table from Ref. [5].

Experiment number	Cross-sectional nozzle area [cm^2]	α [deg]	Jet velocity [cm/s]	Re_{d}
1	0.04	2.00	438.69 ± 12.78	743
2	0.04	19.00	412.85 ± 5.96	652
3	0.04	38.73	404.22 ± 6.08	650
4	0.04	58.28	390.38 ± 7.63	621
5	0.13	-4.14	398.29 ± 12.8	1180
6	0.13	22.87	422.82 ± 19.37	1289
7	0.13	41.86	386.85 ± 15.05	1097
8	0.13	58.00	373.37 ± 9.96	1075
9	0.13	0.00	238.75 ± 8.46	713

$$\frac{\partial \lambda f V_\tau}{\partial t} - \frac{f V_n}{\lambda}\frac{\partial \lambda V_n}{\partial x} + \frac{\partial f V_\tau W}{\partial x} - \lambda f W k V_n = \frac{1}{\rho}\frac{\partial P}{\partial x} + \lambda f F_\tau + \frac{1}{\rho}\lambda q_\tau, \tag{9.2}$$

$$\frac{\partial \lambda f V_n}{\partial t} - \frac{f V_\tau}{\lambda}\frac{\partial \lambda V_n}{\partial x} + \frac{\partial f V_n W}{\partial x} + \lambda f W k V_\tau = \frac{1}{\rho}\lambda k P + \lambda f F_n + \frac{1}{\rho}\lambda q_n. \tag{9.3}$$

Here, λ is the arc length of the jet axis, $\lambda = \sqrt{1 + (\partial H/\partial x)^2}$, H and x are the vertical and horizontal coordinates of the jet axis, f is the cross–sectional area of the jet, with the cross section being approximately circular, and thus, $f = \pi a^2$, with a being the cross–sectional radius. In addition, $W = V_\tau - V_n\,(\partial H/\partial x)$, with subscripts τ and n corresponding to the tangential and normal velocity components, respectively, k is the curvature of the jet axis,

i.e. $k = \left(\partial^2 H/\partial x^2\right)\left[1+\left(\partial H/\partial x\right)^2\right]^{-3/2}$, ρ is the liquid density, and F_τ and F_n denote the tangential and normal components of the acceleration associated with the body force (gravity, in the present case). Similarly, q_τ and q_n denote the tangential and normal components of the force imposed by the surrounding air on a unit length of the jet.

In the momentum balance, Eqs. (9.2) and (9.3), P is the longitudinal force acting in the jet cross section given as,

$$P = \left[3\mu\frac{1}{\lambda}\frac{\partial V_\tau}{\partial x} - kV_n \text{sign}\left(\frac{1}{\lambda}\frac{\partial V_\tau}{\partial x} - kV_n\right) - \sigma G\right] f + P_\sigma, \tag{9.4}$$

where μ is the liquid viscosity, σ is the surface tension, and G is the double mean curvature of the surface of the jet, and $P_\sigma = 2\pi a\sigma\left[1+\lambda^{-2}\left(\partial a/\partial x\right)^2\right]^{-1/2}$. It should be emphasized that here the liquid is assumed to be Newtonian, as in the present experiments with water. For any other non–Newtonian fluid (e.g. blood, which is pseudoplastic and viscoelastic as discussed in Ch. 4), Eq. (9.4) should be modified as described in [118][1].

For a steady–state jet $\partial H/\partial t = \lambda V_n = 0$. In addition, if the jet is thick enough, as in the present experiments, the effect of surface tension can be neglected. Then, Eqs. (9.1)–(9.4) take the following form,

$$Q = fV_\tau, \tag{9.5}$$

---

[1]The non–Newtonian extension is described in Appendix E.

$$\rho Q \frac{\mathrm{d}V_\tau}{\mathrm{d}x} = \frac{\mathrm{d}P}{\mathrm{d}x} + \rho\lambda f g_\tau + \lambda q_\tau, \tag{9.6}$$

$$\rho k f V_\tau^2 = kP + f\rho g_n, \tag{9.7}$$

$$P = 3\mu \frac{1}{\lambda} \frac{\mathrm{d}V_\tau}{\mathrm{d}x} f, \tag{9.8}$$

where Q is the volumetric flow rate in the jet.

Projecting the acceleration of the body force onto the normal and tangent to the jet axis (the trajectory arc), one obtains $g_n = -g/\lambda$, and $g_\tau = -g\,(1/\lambda)\,(\mathrm{d}H/\mathrm{d}x)$, respectively, with g being gravity acceleration. This transforms Eqs. (9.6) and (9.7) to the following form,

$$\rho Q \frac{\mathrm{d}V_\tau}{\mathrm{d}x} = \frac{\mathrm{d}P}{\mathrm{d}x} - \rho f g \frac{\mathrm{d}H}{\mathrm{d}x} + \lambda q_\tau, \tag{9.9}$$

$$\left(\rho f V_\tau^2 - P\right) k = -\frac{fg\rho}{\lambda}. \tag{9.10}$$

In the steady–state case, the only non–zero tangential aerodynamic force, q_τ, acting on a unit jet length can be expressed as $q_\tau = -\tau_{\mathrm{shear}} 2\pi a$, where τ_{shear} is the shear stress acting at

the jet surface. It is related to the friction coefficient C_{fd} as $\tau_{\mathrm{shear}} = (1/2)\,\rho_{\mathrm{a}} V_\tau^2 C_{\mathrm{fd}}$. In addition, noting that $a = \sqrt{Q/(V_\tau \pi)}$, Eqs. (9.9) and (9.10) are transformed to,

$$\frac{\mathrm{d}}{\mathrm{d}x}\left(\rho Q V_\tau - P\right) = -\frac{\rho g Q}{V_\tau}\frac{\mathrm{d}H}{\mathrm{d}x} - \pi^{1/2}\lambda\rho_{\mathrm{a}} V_\tau^{3/2} Q^{1/2} C_{\mathrm{fd}}, \tag{9.11}$$

$$\frac{\mathrm{d}^2 H}{\mathrm{d}x^2} = -\frac{Q}{V_\tau}\frac{\rho g\left[1 + (\mathrm{d}H/\mathrm{d}x)^2\right]}{(\rho Q V_\tau - P)}. \tag{9.12}$$

Moreover, for water used in the present experiments, viscous effects can be essentially neglected, i.e. according to Eq. (9.8), $P = 0$, which reduces the order of the differential equation relative to V_τ to the first one. Then, the boundary conditions for the system of Eqs. (9.11) and (9.12) are imposed only at the nozzle exit and read,

$$x = 0: \quad V_\tau = V_{\tau 0},\ H = H_0,\ \frac{dH}{dx} = \tan\alpha. \tag{9.13}$$

The governing equations, Eqs. (9.11) and (9.12) subjected to the boundary conditions listed in Eq. (9.13) are solved numerically using the Kutta–Merson method with an automatically adjustable stepping in x.

9.4 Results and Discussion

The experimental apparatus described in Sec. (9.2) performs best with water as a working fluid. An image at the onset of the water jet used to determine the initial inclination angle and jet diameter is shown in Fig. 50(a), and an image of the trajectory arc of the water jet used to determine the experimental jet location is shown in Fig. 50(b).

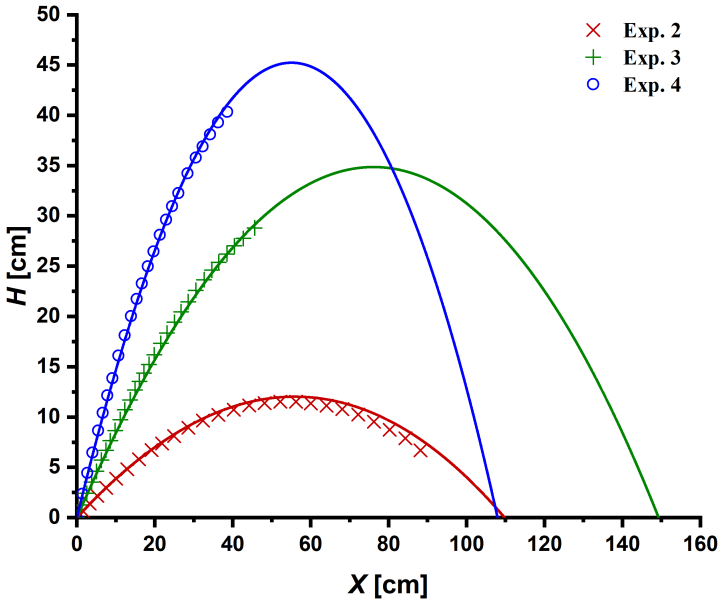

Figure 51. Three superimposed trajectories for the intact free water jets. The legend refers to experiments 2 through 4 from Table VI. The experimental data are shown by symbols and solid lines correspond to the numerical predictions. Fig. from Ref. [5].

The experimental results for the trajectories of water jets issued from the nozzle with the cross–sectional exit area of $f_0 = 0.04$ cm^2 at the inclination angles of $\alpha = 19.00°$, $38.73°$, and $58.28°$ are shown in Fig. 51. The experimental results for the nozzle with the larger cross–sectional area, $f_0 = 0.13$ cm^2, at the initial inclination angles of $\alpha = 22.97°$, $41.86°$, and $58.00°$, are shown in Fig. 52. In the numerical simulations of the problem, Eqs. (9.11)–(9.13), the input velocities used were within the standard deviation of the experimentally measured values. The dependence for the friction coefficient was chosen as $C_{\rm fd} = \gamma Re_{\rm d}^{-\beta}$. The best fit of the predicted trajectories with the experimental data for all the experiments shown in

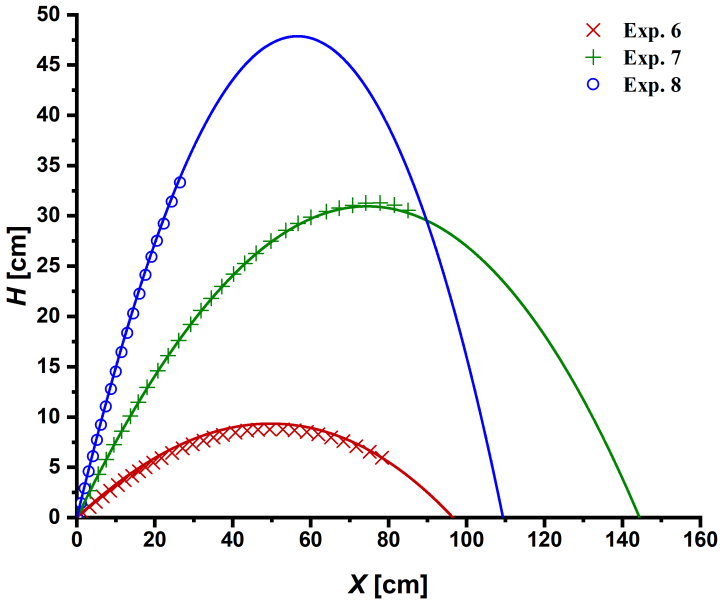

Figure 52. Three superimposed trajectories for the intact free water jets. The legend refers to experiments 6 through 8 from Table VI. The experimental data are shown by symbols and solid lines correspond to the numerical predictions. Fig. from Ref. [5].

Figs. 51, 52, and 53 was achieved with $\gamma = 5.0$ and $\beta = 1/2 \pm 0.05$, which means that the dependence $C_{\rm fd} = 5Re_{\rm d}^{-1/2 \pm 0.05}$ was established and it was uniformly valid for all experiments.

The results for $f_0 = 0.04$ cm^2 and 0.13 cm^2 with the corresponding initial angles of inclination of $\alpha = 2.00°$ and $-4.14°$, respectively, as well as for the low–velocity jet with $f_0 = 0.13$ cm^2 and $\alpha = 0.00°$ are shown in Fig. 53. Here, again, one finds the agreement of the predictions with the experimental data to be excellent when $C_{\rm fd} = 5Re_{\rm d}^{-1/2 \pm 0.05}$ is used. Note that in Figs. 51–53, the experimental data are given for only the intact parts of the jets.

The accurate prediction of all jet trajectories with the uniformly valid friction coefficient $C_{\rm fd} = 5Re_{\rm d}^{-1/2 \pm 0.05}$ allows one to use the numerical simulations to find the optimal inclination

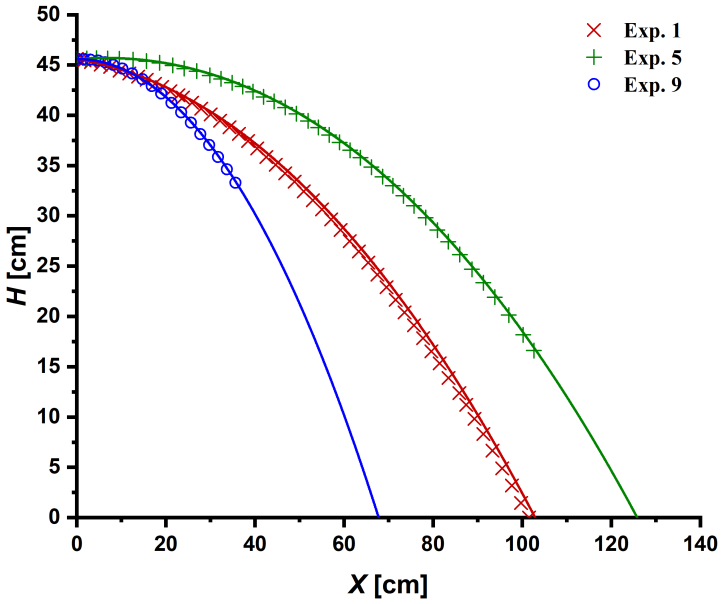

Figure 53. Three superimposed trajectories for the intact free water jets. The legend refers to experiments 1, 5, and 9 from Table VI. The experimental data are shown by symbols and solid lines correspond to the numerical predictions. Fig. from Ref. [5].

angle for reaching the farthest distance. Figure 54 shows the corresponding results, which were obtained by varying only the initial inclination angle with the other parameters being fixed for two different jet Reynolds numbers corresponding to the experimentally studied range. Figure 54 reveals the optimal inclination angle of $\alpha = 35°$. This prediction is within the $\alpha = 30 - 40°$ range of Ref. [104] and is in agreement with the experimental data of Ref. [102] ($\alpha = 35°$). Note also that the optimum angle is essentially the same as for the large scale two–phase sprinkler jets as shown by Ref. [70] where they found $\alpha = 36°$.

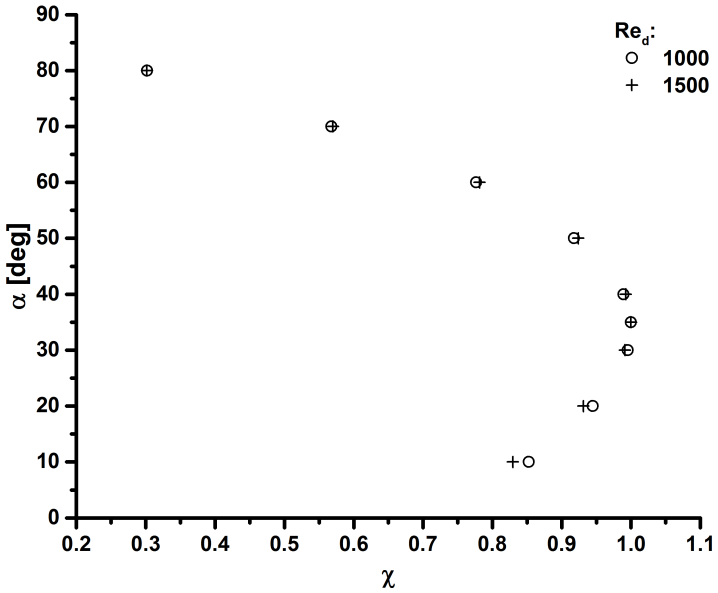

Figure 54. Jet distance versus the initial inclination angle. The horizontal axis χ is the jet distance rendered dimensionless by the maximum value corresponding to $\alpha = 35°$. The friction coefficient was $C_{\rm fd} = 5Re_{\rm d}^{-1/2\ \pm\ 0.05}$. Fig. from Ref. [5].

9.5 Conclusion

Experiments conducted in this work with water jets combined with the predictions of the quasi–one–dimensional theory developed here revealed that the friction factor $C_{\rm fd}$ for the intact curved free liquid jets moving in air is given by the following dependence on the Reynolds number, $Re_{\rm d}$, based on the jet velocity, diameter, and air viscosity: $C_{\rm fd} = 5Re_{\rm d}^{-1/2\ \pm\ 0.05}$ (in the $621 \leq Re_{\rm d} \leq 1289$ range). This dependence for the friction coefficient reveals the optimal inclination angle corresponding to the farthest reaching jet, $\alpha = 35°$, which is in agreement with previous experimental results. It should be emphasized that the established dependence $C_{\rm fd} = C_{\rm fd}\,(Re_{\rm d})$ is radically different from those established for melt spinning, where tiny

filaments (of about 100 μm in diameter) move with velocity of the order of 1 km/min. Note that the present result $C_{\rm fd} = 5Re_{\rm d}^{-1/2 \pm 0.05}$ corresponds to jets of about 0.32 cm in diameter moving in air with velocities of about 4 m/s, and is applicable to jets originating from decorative fountains, smaller sprinklers, as well as blood jets originating from knives or other cutting instruments used as a murder weapon, which is of interest in forensic applications.

CHAPTER 10

CONCLUSION

In the present work, the application of fluid mechanics to issues in forensic science were demonstrated. First, various physical properties of blood were quantified. The rheological behavior in simple shear flow was explored, and it was found that blood follows a power–law shear thinning behavior when in shear flow. Ramifications of the elongational viscosity shown to be up to three orders of magnitude larger than shear viscosity known in literature are discussed in the context of forensic science.

Then, the analysis of experimental evidence of the atomization of blood due to a gunshot was considered. This was done by performing PIV and image processing analysis techniques on high–speed videos found in literature. It was revealed that the maximum velocity of forward spattered blood droplets can be $\sim 47 \pm 5$ m/s, whereas the maximum velocity of backward spattered blood droplets is $\sim 24 \pm 8$ m/s. The sizes of the blood droplets spattered are approximately the same for both backward and forward spatter situations. The spatter angles of the blood droplet spray were also measured and it was shown that the close–to–cone semi–angles seen for backward spatter ranges from $\sim 30 - 57°$, whereas in forward spatter it is around $\sim 30°$. It was also seen that the muzzle gases from the chemical reaction propelling the bullet can greatly influence the trajectories of blood droplets in backward spatter, and that a collective aerodynamic effect exists for groups of blood droplets.

With the knowledge gained in the characterization of blood properties and a quantitative analysis of experimental data on the atomization of blood spatter due to a gunshot, backward blood spatter models were developed. Ultimately, two different models for idealized bullet shapes, one a slender cone, and the other a blunt cylinder, were created. The first model belongs to the class of Wagner–type problems, and the second is an instantaneous impact problem, both of which allow for the initial velocity and acceleration of the blood to be determined. The atomization of blood is then attributed to the Rayleigh–Taylor instability which arises when a more–dense fluid is accelerated towards a lighter one. In the considered scenario, the instability arises because blood is accelerated towards air due to the action of the bullet impacting the blood target. Then, the blood droplet trajectories are determined and calculated including air entrainment due to viscous suction, gravity, air drag, and drop–drop interaction in flight. The theoretical results were compared with experimental data for the distribution of the number of stains, their stain area, and their impact angle, and the agreement is good. Statistics on the two models are then explored to facilitate and extend their usage.

The problem of forward blood spatter was then investigated. From the quantitative analysis of the atomization of blood due to a gunshot with PIV, it was shown that blood droplets traveling in the direction of bullet motion are much faster than their backward spatter counterparts. The Rayleigh–Taylor instability triggers a cascade of instabilities in this case which leads to the chaotic disintegration of the blood. Within the framework of percolation theory, the fragmentation of the blood target is predicted and the viscoelasticity of blood is considered because the faster initial blood droplet velocities result in a build–up of elastic stresses which

form a "web" of blood. The motion of the resultant blood droplets is calculated as before in the case of backward spattered blood. The model is then generalized to predict the breakup of the blood target for any bullet shape and compared with experimental data for the distribution of the number of stains and their respective stain areas.

Muzzle gases were shown to be very important in the case of backward spattered blood droplets from the analysis of the high–speed videos with PIV. It was determined that a turbulent vortex ring of propellant gases is the main component of the muzzle gases which interact with the blood droplets and should be explored. The turbulent vortex ring is self–similar and the velocity and vorticity fields are calculated. Passive admixture of gunpowder particles is then assumed to be swept by the turbulent vortex ring and its self–similar concentration is determined. Then, the equations of motion for prediction of the trajectories of blood droplets are modified to account for the flow field of the turbulent vortex ring. The results show that there is a significant impact on the distribution of the number of blood stains and their respective area due to a turbulent vortex ring.

Finally, intact jets of liquid were considered. The equations of motion for the trajectory of an intact liquid jet were derived accounting for a friction coefficient which depends upon the size of the jet. The friction coefficient was empirically found with experimental data taken in this work. The results prove excellent agreement and the model is applicable for intact jets of blood as well because the role of the jet disintegration there is negligibly small.

APPENDICES

Appendix A

KUTTA–MERSON METHOD

The numerical scheme for solving the system of ODE's discussed in Sec. 6.6 and 9.3 is the Kutta–Merson method (sometimes called Runge–Kutta–Merson). The method was originally developed by R.H. Merson in 1957 [205] and is an explicit fourth order, five step, Runge–Kutta method. The numerical scheme is described in Ref. [206] and shown below,

$$
\begin{aligned}
y_{n+1} - y_n =& \frac{h}{6}\left(k_1 + 4k_4 + k_5\right), \\
k_1 =& f\left(x_n,\ y_n\right), \\
k_2 =& f\left(x_n + \frac{1}{3}h,\ y_n + \frac{1}{3}hk_1\right), \\
k_3 =& \left(x_n + \frac{1}{3}h,\ y_n + \frac{1}{6}hk_1 + \frac{1}{6}hk_2\right), \\
k_4 =& \left(x_n + \frac{1}{2}h,\ y_n + \frac{1}{8}hk_1 + \frac{3}{8}hk_3\right), \\
k_5 =& \left(x_n + h,\ y_n + \frac{1}{2}hk_1 - \frac{3}{2}hk_3 + 2hk_4\right),
\end{aligned}
\tag{A.1}
$$

where h is the step length, and n denotes the step.

Appendix A (Continued)

The numerical scheme of Eq. (A.1) solves the initial value problem,

$$y' = f\left(x,\ y\right), \tag{A.2}$$

which is subject to the initial condition, $y\left(a\right) = b$. The local truncation error is,

$$T_{n+1} = \frac{h}{30}\left(-2k_1 + 9k_3 - 8k_4 + k_5\right). \tag{A.3}$$

Appendix B

EVALUATION OF THE FREDHOLM INTEGRAL EQUATION FOR THE GENERALIZED CHAOTIC DISINTEGRATION OF A LIQUID

The generalized chaotic disintegration of a liquid is governed by a Fredholm integral equation of the first kind to solve for the system of sinks and sources, $\overline{q}\left(\overline{\zeta}\right)$, which form a unique distribution for an arbitrary body as discussed in Sec. 7.4.1. Standard mathematical methods for the solution of equations of this type such as the integral–transform or generating–function methods described in Refs. [187,188] may not adequately solve Eq. (7.53) for all possibilities of the projectile surface, $\overline{R}\left(\overline{\xi}\right)$. Therefore, an iterative numerical technique was developed based off of conversations with Dr. Ilia Roisman and is described below.

The arbitrary projectiles are assumed to be semi–infinite (that is, there is no "end" to the arbitrary bullet), therefore as $\overline{\xi} \to \infty$, $\overline{R} = 1$. The limit of the integral in Eq. (7.53) then tends towards 2 which means that $\int_{\overline{\xi}_{\mathrm{A}}}^{\overline{\xi}_{\mathrm{E}}} \overline{q}\left(\overline{\zeta}\right) \mathrm{d}\overline{\zeta} = 1/4$. Equation (7.53) then becomes,

$$\int_{\overline{\xi}_{\mathrm{A}}}^{\overline{\xi}_{\mathrm{E}}} \frac{\left(\overline{\xi} - \overline{\zeta}\right)}{\left[\left(\overline{\xi} - \overline{\zeta}\right)^2 + \overline{R}^2\right]^{1/2}} \overline{q}\left(\overline{\zeta}\right) \mathrm{d}\overline{\zeta} = \frac{\overline{R}^2}{2} - \frac{1}{4}. \tag{B.1}$$

The smoothness on the RHS of Eq. (B.1) presents issues, especially when $\overline{\zeta} = \overline{\xi}$. This problem can be mitigated by expanding the left–hand side (LHS) of Eq. (B.1) via integration

Appendix B (Continued)

by parts and defining $\Theta\left(\overline{\zeta}\right) = \int_{\overline{\xi}_{\mathrm{A}}}^{\overline{\zeta}} \overline{q}\left(\eta\right) \mathrm{d}\eta$, where η is a dummy–variable. Then, Eq. (B.1) becomes,

$$\int_{\overline{\xi}_{\mathrm{A}}}^{\overline{\xi}_{\mathrm{E}}} \frac{\Theta\left(\overline{\zeta}\right)}{\left[\left(\overline{\xi}-\overline{\zeta}\right)^2+\overline{R}^2\right]^{3/2}} \mathrm{d}\overline{\zeta} = \frac{1}{2} - \frac{1}{4\overline{R}^2}\left(1+\frac{\left(\overline{\xi}-\overline{\xi}_{\mathrm{E}}\right)}{\left[\left(\overline{\xi}-\overline{\xi}_{\mathrm{E}}\right)^2+\overline{R}^2\right]^{1/2}}\right). \tag{B.2}$$

At the tip of the arbitrary projectile, $\overline{\xi}_{\mathrm{A}}$, the value of the function $\Theta \to 0$. Therefore an intermediate point, $\overline{\xi}^*$, located between $\overline{\xi}_{\mathrm{E}}$ and $\overline{\xi}_{\mathrm{A}}$ can be introduced where $\Theta\left(\overline{\xi}\right) = 0$ at $\overline{\xi}_{\mathrm{A}} \leq \overline{\xi} \leq \overline{\xi}^*$. Splitting Eq. (B.2) at $\overline{\xi}_*$, the approximate solution in the region of $\overline{\xi}_{\mathrm{A}} \leq \overline{\xi} \leq \overline{\xi}^*$ is then,

$$\int_{\overline{\xi}_{\mathrm{A}}}^{\overline{\xi}_{\mathrm{E}}} \frac{1}{\left[\left(\overline{\xi}-\overline{\zeta}\right)^2+\overline{R}^2\right]^{3/2}} \Theta\left(\overline{\zeta}\right) \mathrm{d}\overline{\zeta} \approx f\left(\overline{\xi}\right), \tag{B.3}$$

where $f\left(\overline{\xi}\right)$ can be approximated as the RHS of Eq. (B.2) because of the assumption that the arbitrary projectile is a semi–infinite body of revolution (i.e. when $f\left(\overline{\xi}\right)\big|_{\overline{\xi}_{\mathrm{E}}} \to \infty$, then $f\left(\overline{\xi}\right) = 1/2$ and the distribution of the system of sinks and sources then adheres to that of a slender body of revolution as described in Ref. [153]).

The integral of Eq. (B.3) peaks as $\overline{\zeta} \to \overline{\xi}$. Since the principle contribution of the integral occurs on such a short duration of $\overline{\xi}$, the integral bounds can be extended to $\pm\,\infty$ and then $\Theta\left(\overline{\zeta}\right) \approx \Theta\left(\overline{\xi}\right)$. Therefore, Eq. (B.3) can be solved for $\Theta\left(\overline{\xi}\right)$ as,

$$\Theta\left(\overline{\xi}\right) \approx f\left(\overline{\xi}\right) \frac{\overline{R}\left(\overline{\xi}\right)^2}{2}. \tag{B.4}$$

Appendix B (Continued)

To solve for the unknown $\overline{\xi}^*$, the axial velocity component of Eq. (7.54) is used as,

$$\mathbf{v}_\xi = \dot{\xi}\left[\int_{\overline{\xi}_\mathrm{A}}^{\overline{\xi}_\mathrm{E}} \frac{\left(\overline{\xi}-\overline{\zeta}\right)}{\left[\left(\overline{\xi}-\overline{\zeta}\right)^2+\overline{R}^2\right]^{3/2}}\overline{q}\left(\overline{\zeta}\right)\mathrm{d}\overline{\zeta}+1\right]\mathbf{e}_\xi. \tag{B.5}$$

Since at the projectile tip $\mathbf{v}_\xi = 0$, and the system of sinks and sources exists when $\overline{\xi} \geq \overline{\xi}^*$ and $\overline{\xi}_\mathrm{A} < \overline{\xi}^*$, then Eq. (B.5) becomes,

$$0 = -\int_{\overline{\xi}^*}^{\overline{\xi}_\mathrm{E}} \left(\overline{\xi}_\mathrm{A}-\overline{\zeta}\right)^{-2}\overline{q}\left(\overline{\zeta}\right)\mathrm{d}\overline{\zeta}+1. \tag{B.6}$$

Integrating Eq. (B.6) by parts and noting that $\Theta\left(\overline{\zeta}\right) \approx \Theta\left(\overline{\xi}\right)$, $\overline{\xi}^*$ can be solved for with the following equation,

$$2\int_{\overline{\xi}^*}^{\overline{\xi}_\mathrm{E}} \frac{\Theta\left(\overline{\zeta}\right)}{\left(\overline{\xi}_\mathrm{A}-\overline{\zeta}\right)^3}\mathrm{d}\overline{\zeta}+1 = \frac{1}{4\left(\overline{\xi}_\mathrm{A}-\overline{\xi}_\mathrm{E}\right)^2}. \tag{B.7}$$

The numerical scheme to solve Eq. (7.53) is now complete. In summary, this iterative algorithm starts by finding the approximate value of Θ for all $\overline{\xi}$ from Eq. (B.4). Then, $\overline{\xi}^*$ can be determined by guessing a value in Eq. (B.7) which results in an approximate value for the RHS of Eq. (B.7) which can be compared to the "true" RHS,

$$f\left(\overline{\xi}\right) = \frac{1}{2}-\frac{1}{4\overline{R}^2}\left(1+\frac{\left(\overline{\xi}-\overline{\xi}_\mathrm{E}\right)}{\left[\left(\overline{\xi}-\overline{\xi}_\mathrm{E}\right)^2+\overline{R}^2\right]^{1/2}}\right)-\int_{\overline{\xi}^*}^{\overline{\xi}_\mathrm{E}} \frac{\Theta\left(\overline{\zeta}\right)}{\left[\left(\overline{\xi}-\overline{\zeta}\right)^2+\overline{R}^2\right]^{3/2}}\mathrm{d}\overline{\zeta}. \tag{B.8}$$

Appendix B (Continued)

The next iterative step of $\Theta\left(\overline{\xi}\right)$ can then be solved for using,

$$\Theta^{j+1}\left(\overline{\xi}\right) = \Theta^{j}\left(\overline{\xi}\right) + f\left(\overline{\xi}\right)\frac{\overline{R}^{2}}{2}, \tag{B.9}$$

which comes from Eq. (B.4), and j is the iteration step. The scheme is solved such that the difference between the approximate RHS and true RHS is minimized. Once an acceptable margin of error is met, $\overline{q}\left(\overline{\zeta}\right)$ can now be found through the definition of Θ.

Appendix C

DETAILS ABOUT THE SELF–SIMILAR SOLUTION OF MUZZLE GASES

(This appendix has been submitted for publication in Ref. [4].)

In order to find the solution of Eqs. (8.9) and (8.13), new variables are introduced as,

$$\xi = \frac{1}{M}\left(\overline{z} - 4K\right); \quad \eta = \frac{1}{M}\overline{r}, \tag{C.1}$$

where $K = \overline{r}_{\mathrm{m}}^{-1}\ \partial\overline{\psi}/\partial\overline{r}\big|_{\substack{\overline{r}=\overline{r}_{\mathrm{m}} \\ \overline{z}=\overline{z}_{\mathrm{m}}}}$ and $M = \sqrt{8\lambda_0}$.

Also, a new function ω is introduced as,

$$\overline{\Omega} = \exp\left(-\frac{\zeta^2 + \eta^2}{2}\right)\omega\left(\zeta, \eta\right). \tag{C.2}$$

Then, Eq. (8.13) takes the form,

$$\frac{1}{\eta}\frac{\partial}{\partial\eta}\left(\eta\frac{\partial\omega}{\partial\eta}\right) + \frac{\partial^2\omega}{\partial\xi^2} + \left(5 - \xi^2 - \eta^2 - \frac{1}{\eta^2}\right)\omega = 0. \tag{C.3}$$

Equation (C.3) is solved using variable separation, $\omega\left(\xi, \eta\right) = \omega_1\left(\xi\right)\omega_2\left(\eta\right)$, which yields the following,

$$\frac{\mathrm{d}^2\omega_1}{\mathrm{d}\xi^2} - \xi^2\omega_1 = -\left(E + 5\right)\omega_1, \tag{C.4}$$

Appendix C (Continued)

$$\frac{1}{\eta}\frac{\mathrm{d}}{\mathrm{d}\eta}\left(\eta\frac{\mathrm{d}\omega_2}{\mathrm{d}\eta}\right)-\eta^2\omega_2-\frac{\omega_2}{\eta^2}=E\omega_2, \tag{C.5}$$

where E is a separation constant.

The integral invariant, i.e. the vortex impulse of Eq. (8.12), becomes,

$$\int_{-\infty}^{\infty}\exp\left(-\frac{\xi^2}{2}\right)\omega_1\mathrm{d}\xi\int_{0}^{\infty}\exp\left(-\frac{\eta^2}{2}\right)\eta^2\omega_2\mathrm{d}\eta=\frac{1}{\pi\left(8\lambda_0\right)^2}. \tag{C.6}$$

Equation (C.4) is known in the theory of one–dimensional quantum oscillators and its solution is readily available [187, 201]. The only solution which can satisfy Eq. (C.6) is,

$$\omega_1\left(\xi\right)=F_1\frac{\exp\left(-\xi^2/2\right)H_k\left(\xi\right)}{\pi^{1/4}\left(2^k k!\right)^{1/2}}, \tag{C.7}$$

where F_1 is a constant, H_k are the Hermite polynomials, and $E+5=2k+1$, with $k=0,1,2,\ldots$.

Equation (C.5) is also known in the theory of cylindrical quantum oscillators [202], and its solution satisfying Eq. (C.6) exists only when $-E=2\left(2n+2\right)$, with $n=0,1,2,\ldots$. Then, it is seen that the only appropriate choice would be $k=n=0$, which yields $E=-4$. Equation (C.7) then becomes,

$$\omega_1\left(\xi\right)=F_2\exp\left(-\xi^2/2\right), \tag{C.8}$$

Appendix C (Continued)

whereas the solution of Eq. (C.5) has the form,

$$\omega_2(\eta) = F_3 \eta \exp\left(-\eta^2/2\right), \tag{C.9}$$

where F_2 and F_3 are constant.

From Eqs. (C.2), (C.8), and (C.9) one finds that,

$$\overline{\Omega}(\xi,\eta) = I\eta \exp\left[-\left(\xi^2+\eta^2\right)\right], \tag{C.10}$$

where I is a constant and is found using Eq. (C.6) as,

$$I = \frac{1}{32\pi^{3/2}\lambda_0^2}. \tag{C.11}$$

Accordingly, Eqs. (C.1), (C.10), and (C.11) yield Eq. (8.15) where $K = \overline{z}_{\mathrm{m}}/4$.

To find the stream function corresponding to the vorticity of Eq. (C.10), introduce a new function Π,

$$\overline{\psi} = \eta^2 \Pi\left(\xi^2+\eta^2\right). \tag{C.12}$$

Then, the substitution of Eqs. (C.10)–(C.12) into Eq. (8.9) results in,

$$4\frac{\mathrm{d}}{\mathrm{d}\left(s^2\right)}\left[s^2\frac{\mathrm{d}\Pi}{\mathrm{d}\left(s^2\right)}\right] + 6\frac{\mathrm{d}\Pi}{\mathrm{d}\left(s^2\right)} = -GM^3\exp\left(-s^2\right), \tag{C.13}$$

where $s^2 = \xi^2+\eta^2$, and $G = 1/\left(32\pi^{3/2}\lambda_0^2\right)$.

Appendix C (Continued)

Introduce $\Pi_1(s) = \Pi\left(s^2\right)$, which transforms Eq. (C.13) to the following,

$$\frac{1}{2s}\left[2\frac{\mathrm{d}}{\mathrm{d}s}\left(s\frac{\mathrm{d}\Pi_1}{\mathrm{d}s}\right)+6\frac{\mathrm{d}\Pi_1}{\mathrm{d}s}\right] = -GM^3\exp\left(-s^2\right), \tag{C.14}$$

and has the appropriate solution in the form,

$$\Pi_1(s) = K_1\frac{\mathrm{erf}(s) - (2s/\sqrt{\pi})\exp\left(-s^2\right)}{s^3}, \tag{C.15}$$

where,

$$K_1 = \frac{\sqrt{\pi}GM^3}{8}. \tag{C.16}$$

Substituting Eqs. (C.1), (C.15), and (C.16) into Eq. (C.12), one obtains Eq. (8.14). Equations (8.15) and (8.16) show that the maximum vorticity corresponds to $\overline{z} = \overline{z}_{\mathrm{m}}$, which yields maximum to the function $\overline{r}\exp\left[-\overline{r}^2/(8\lambda_0)\right]$. This corresponding value of $\overline{r}$ is given by Eq. (8.17). Also, using the fact that $K = \overline{z}_{\mathrm{m}}/4 = \overline{r}_{\mathrm{m}}^{-1}\,\partial\overline{\psi}/\partial\overline{r}\big|_{\substack{\overline{r}=\overline{r}_{\mathrm{m}}\\ \overline{z}=\overline{z}_{\mathrm{m}}}}$, substituting Eqs. (8.14), (8.16), and (8.17), one obtains Eq. (8.18).

Appendix D

DETAILS ABOUT THE DEFLECTION OF BLOOD DROPLETS IN BACKWARD SPATTER BY THE TURBULENT VORTEX RING

(Portions of this appendix have been submitted for publication in Ref. [4].)

Projecting the momentum balance of blood droplets in a blob with air entrainment as shown in Eq. (8.40) onto the X–Y–H axes, one obtains,

$$\frac{\mathrm{d}^2X}{\mathrm{d}T^2} = -\chi\frac{\mathrm{d}X}{\mathrm{d}T}\left(1-\frac{U_i}{\Lambda_1}\right)(\Lambda_1 - U_i)\,, \tag{D.1}$$

$$\frac{\mathrm{d}^2Y}{\mathrm{d}T^2} = -\chi\frac{\mathrm{d}Y}{\mathrm{d}T}\left(1-\frac{U_i}{\Lambda_1}\right)(\Lambda_1 - U_i)\,, \tag{D.2}$$

$$\frac{\mathrm{d}^2H}{\mathrm{d}T^2} = -\chi\frac{\mathrm{d}H}{\mathrm{d}T}\left(1-\frac{U_i}{\Lambda_1}\right)(\Lambda_1 - U_i) - g, \tag{D.3}$$

where,

$$\chi = \frac{1}{8}\pi l_{*,i}^2 C_{\mathrm{D},i}\frac{n_i}{M_i}\rho_{\mathrm{a}}, \tag{D.4}$$

$$\Lambda_1 = \sqrt{\left(\frac{\mathrm{d}X}{\mathrm{d}T}\right)^2 + \left(\frac{\mathrm{d}Y}{\mathrm{d}T}\right)^2 + \left(\frac{\mathrm{d}H}{\mathrm{d}T}\right)^2}. \tag{D.5}$$

Appendix D (Continued)

Equations (D.1)–(D.3) are subjected to the following initial conditions,

$$T=0: \quad \begin{array}{l} X=0,\ Y=0,\ H=H_0 \\ \frac{\mathrm{d}X}{\mathrm{d}T}=u_{i,0}\sqrt{\cos^2\beta-\frac{\sin^2\beta}{\tan^2\Phi}},\ \frac{\mathrm{d}Y}{\mathrm{d}T}=u_{i,0}\frac{\sin\beta}{\tan\phi},\ \frac{\mathrm{d}H}{\mathrm{d}T}=u_{i,0}\sin\beta \end{array} . \tag{D.6}$$

The initial conditions listed in Eq. (D.6) utilize the initial blood droplet velocity calculated by the Rayleigh–Taylor instability, $u_{i,0}$, and the angles β, and ϕ are the initial inclination angle of the trajectory, $\beta = \arcsin\left[\sin\left(\Delta\theta\right)\sin\phi\right]$, and the polar angle in the circular cross–section of the bullet, respectively. Here, $\Delta\theta$ is the angle at which the blood droplet trajectories splashed relative to the bullet axis, as described in Ch. 6. Note that when $\Phi = 0, \pi, 2\pi, \ldots$, then $\mathrm{d}Y/\mathrm{d}T = u_{i,0}\sin\left(\Delta\theta\right)$.

The velocity of the entrained air can be determined through a momentum balance of air projected onto the tangent of the trajectory as,

$$\begin{aligned} \frac{\mathrm{d}}{\mathrm{d}T}\left(\rho_{\mathrm{a}}VU_i\right) = &\left(\sum_{i=1}^{N} n_i\right)\frac{1}{8}\pi l_{*,i}^2 C_{\mathrm{D},i}\rho_{\mathrm{a}}\times \\ &\left[\frac{1}{\Lambda_1}\left(\frac{\mathrm{d}X}{\mathrm{d}T}\right)^2+\frac{1}{\Lambda_1}\left(\frac{\mathrm{d}Y}{\mathrm{d}T}\right)^2+\frac{1}{\Lambda_1}\left(\frac{\mathrm{d}H}{\mathrm{d}T}\right)^2-U_i\right]\times \\ &\left|\frac{\mathrm{d}X}{\mathrm{d}T}+\frac{\mathrm{d}Y}{\mathrm{d}T}+\frac{\mathrm{d}H}{\mathrm{d}T}-U_i\right| \end{aligned} \tag{D.7}$$

where the volume of the entrained air,

$$V\left(T\right) = 0.33V_{\mathrm{blood}}\left(\frac{u_{i,0}|_{\max}}{V_{\mathrm{blood}}^{1/3}}\frac{\xi\left(T\right)}{u_i\left(T\right)}\right)^{3/2}, \tag{D.8}$$

Appendix D (Continued)

and the arc length of the trajectory denoted as ξ is found from the following equation,

$$\frac{\mathrm{d}\xi}{\mathrm{d}T} = \Lambda_1. \tag{D.9}$$

Equation (D.7) is subjected to the following initial conditions,

$$T = 0: \quad U_i = 0,\ V = 0,\ \xi = 0. \tag{D.10}$$

Equation (D.7) is solved directly for the product VU_i, and the equation for the volume of air in the blood droplet cloud, V in Eq. (D.8), is based off of the integral invariant of mass for an axisymmetric air jet and Prandtl's turbulent mixing length theory (cf. Ch. 6). The volume of blood splashed is V_{blood}, $u_{i,0}|_{\max}$ is the maximum initial blood droplet velocity calculated by the Rayleigh–Taylor instability, and the arc length of the trajectory is denoted as ξ.

Rendering Eqs. (D.1)–(D.10) dimensionless with the maximum initial blood droplet velocity $u_{i,0}|_{\max}$ for u_i, and U_i, the volume of blood $V_{\text{blood}}^{1/3}$ for X, Y, H, H_0, ξ, and $l_{*,i}$, and $V_{\text{blood}}^{1/3}/\ u_{i,0}|_{\max}$ for T, results in the following set of governing equations for the trajectory of a blood droplet cloud,

$$\frac{\mathrm{d}^2\overline{X}}{\mathrm{d}\overline{T}^2} = -\overline{\chi}\frac{\mathrm{d}\overline{X}}{\mathrm{d}\overline{T}}\left(1 - \frac{\overline{U}_i}{\overline{\Lambda}_1}\right)\left(\overline{\Lambda}_1 - \overline{U}_i\right), \tag{D.11}$$

$$\frac{\mathrm{d}^2\overline{Y}}{\mathrm{d}\overline{T}^2} = -\overline{\chi}\frac{\mathrm{d}\overline{Y}}{\mathrm{d}\overline{T}}\left(1 - \frac{\overline{U}_i}{\overline{\Lambda}_1}\right)\left(\overline{\Lambda}_1 - \overline{U}_i\right), \tag{D.12}$$

Appendix D (Continued)

$$\frac{\mathrm{d}^2\overline{H}}{\mathrm{d}\overline{T}^2} = -\overline{\chi}\frac{\mathrm{d}\overline{H}}{\mathrm{d}\overline{T}}\left(1-\frac{\overline{U}_i}{\overline{\Lambda}_1}\right)\left(\overline{\Lambda}_1-\overline{U}_i\right)-\frac{1}{Fr^2}, \tag{D.13}$$

$$\begin{aligned}\frac{\mathrm{d}\overline{U}_i\overline{V}}{\mathrm{d}\overline{T}} =& \frac{1}{8}\pi\bar{l}_{*,i}^2 C_{\mathrm{D},i}\left(\sum_{i=1}^{N} n_i\right)\times \\ & \left[\frac{1}{\overline{\Lambda}_1}\left(\frac{\mathrm{d}\overline{X}}{\mathrm{d}\overline{T}}\right)^2+\frac{1}{\overline{\Lambda}_1}\left(\frac{\mathrm{d}\overline{Y}}{\mathrm{d}\overline{T}}\right)^2+\frac{1}{\overline{\Lambda}_1}\left(\frac{\mathrm{d}\overline{H}}{\mathrm{d}\overline{T}}\right)^2-\overline{U}_i\right]\times \\ & \left|\frac{\mathrm{d}\overline{X}}{\mathrm{d}\overline{T}}+\frac{\mathrm{d}\overline{Y}}{\mathrm{d}\overline{T}}+\frac{\mathrm{d}\overline{H}}{\mathrm{d}\overline{T}}-\overline{U}_i\right|\end{aligned} \tag{D.14}$$

where,

$$\overline{\chi} = \frac{1}{8}\pi\bar{l}_{*,i}^2 C_{\mathrm{D},i} n_i \frac{\rho_{\mathrm{a}}}{\rho_{\mathrm{b}}}, \tag{D.15}$$

$$\overline{\Lambda}_1 = \sqrt{\left(\frac{\mathrm{d}\overline{X}}{\mathrm{d}\overline{T}}\right)^2+\left(\frac{\mathrm{d}\overline{Y}}{\mathrm{d}\overline{T}}\right)^2+\left(\frac{\mathrm{d}\overline{H}}{\mathrm{d}\overline{T}}\right)^2}, \tag{D.16}$$

$$\overline{V}\left(\overline{T}\right) = 0.33\left[\frac{\overline{\xi}\left(\overline{T}\right)}{\overline{\Lambda}_1\left(\overline{T}\right)}\right]^{3/2}, \tag{D.17}$$

$$\frac{\mathrm{d}\overline{\xi}}{\mathrm{d}\overline{T}} = \overline{\Lambda}_1, \tag{D.18}$$

Appendix D (Continued)

$$\overline{T}=0: \quad \begin{array}{l} \overline{X}=0,\ \overline{Y}=0,\ \overline{H}=\overline{H}_0 \\ \frac{\mathrm{d}\overline{X}}{\mathrm{d}\overline{T}}=\overline{u}_{i,0}\sqrt{\cos^2\beta-\frac{\sin^2\beta}{\tan^2\Phi}},\ \frac{\mathrm{d}\overline{Y}}{\mathrm{d}\overline{T}}=\overline{u}_{i,0}\frac{\sin\beta}{\tan\phi},\ \frac{\mathrm{d}\overline{H}}{\mathrm{d}\overline{T}}=\overline{u}_{i,0}\sin\beta \quad , \\ \overline{V}=0,\ \overline{U}_i=0,\ \overline{\xi}=0 \end{array} \tag{D.19}$$

where overbar denotes a dimensionless parameter, ρ_b is the density of blood, and Fr is the Froude number, $Fr=\sqrt{u_{i,0}^2\Big|_\mathrm{max}/\left(gV_\mathrm{blood}^{1/3}\right)}$. Equation (D.14) expresses the fact that the fastest moving blood droplets dominate the air entrainment and the terms $\mathrm{d}\overline{X}/\mathrm{d}\overline{T}$, $\mathrm{d}\overline{Y}/\mathrm{d}\overline{T}$, and $\mathrm{d}\overline{H}/\mathrm{d}\overline{T}$ in that equation represent the droplets "leading" the cloud.

Similarly, projecting Eq. (8.43) describing the interaction of the blood droplets with the vortex ring onto the X–Y–H axes read,

$$\frac{\mathrm{d}^2X}{\mathrm{d}T^2}=-\chi\left(\frac{\mathrm{d}X}{\mathrm{d}T}+v_z\right)\sqrt{\left(\frac{\mathrm{d}X}{\mathrm{d}T}+v_z\right)^2+\left(\frac{\mathrm{d}Y}{\mathrm{d}T}+\frac{v_r}{\Lambda_2}\frac{\mathrm{d}Y}{\mathrm{d}T}\right)^2+\left(\frac{\mathrm{d}H}{\mathrm{d}T}+\frac{v_r}{\Lambda_2}\frac{\mathrm{d}H}{\mathrm{d}T}\right)^2}, \tag{D.20}$$

$$\frac{\mathrm{d}^2Y}{\mathrm{d}T^2}=-\chi\frac{\mathrm{d}Y}{\mathrm{d}T}\left(1+\frac{v_r}{\Lambda_2}\right)\sqrt{\left(\frac{\mathrm{d}X}{\mathrm{d}T}+v_z\right)^2+\left(\frac{\mathrm{d}Y}{\mathrm{d}T}+\frac{v_r}{\Lambda_2}\frac{\mathrm{d}Y}{\mathrm{d}T}\right)^2+\left(\frac{\mathrm{d}H}{\mathrm{d}T}+\frac{v_r}{\Lambda_2}\frac{\mathrm{d}H}{\mathrm{d}T}\right)^2}, \tag{D.21}$$

$$\frac{\mathrm{d}^2H}{\mathrm{d}T^2}=-\chi\frac{\mathrm{d}H}{\mathrm{d}T}\left(1+\frac{v_r}{\Lambda_2}\right)\sqrt{\left(\frac{\mathrm{d}X}{\mathrm{d}T}+v_z\right)^2+\left(\frac{\mathrm{d}Y}{\mathrm{d}T}+\frac{v_r}{\Lambda_2}\frac{\mathrm{d}Y}{\mathrm{d}T}\right)^2+\left(\frac{\mathrm{d}H}{\mathrm{d}T}+\frac{v_r}{\Lambda_2}\frac{\mathrm{d}H}{\mathrm{d}T}\right)^2}-g, \tag{D.22}$$

Appendix D (Continued)

where,

$$\Lambda_2 = \sqrt{\left(\frac{\mathrm{d}Y}{\mathrm{d}T}\right)^2 + \left(\frac{\mathrm{d}H}{\mathrm{d}T}\right)^2}. \tag{D.23}$$

The six initial conditions for Eqs. (D.20)–(D.23) are the three final spatial positions and velocities when the entrained air surrounding the blood drop cloud is shed, i.e. when Eqs. (D.1)–(D.6) are not applicable anymore because of a turbulent vortex ring interaction and Eqs. (D.20)–(D.23) then describe the motion.

Rendering Eqs. (D.20)–(D.23) dimensionless with the same scales as for Eqs. (D.1)–(D.6), as well as using $u_{i,0}|_{\max}$ for v_r and v_z results in,

$$\frac{\mathrm{d}^2\overline{X}}{\mathrm{d}\overline{T}^2} = -\overline{\chi}\left(\frac{\mathrm{d}\overline{X}}{\mathrm{d}\overline{T}} + \overline{v}_z\right)\sqrt{\left(\frac{\mathrm{d}\overline{X}}{\mathrm{d}\overline{T}} + \overline{v}_z\right)^2 + \left(\frac{\mathrm{d}\overline{Y}}{\mathrm{d}\overline{T}} + \frac{\overline{v}_r}{\overline{\Lambda}_2}\frac{\mathrm{d}\overline{Y}}{\mathrm{d}\overline{T}}\right)^2 + \left(\frac{\mathrm{d}\overline{H}}{\mathrm{d}\overline{T}} + \frac{\overline{v}_r}{\overline{\Lambda}_2}\frac{\mathrm{d}\overline{H}}{\mathrm{d}\overline{T}}\right)^2}, \tag{D.24}$$

$$\frac{\mathrm{d}^2\overline{Y}}{\mathrm{d}\overline{T}^2} = -\overline{\chi}\frac{\mathrm{d}\overline{Y}}{\mathrm{d}\overline{T}}\left(1 + \frac{\overline{v}_r}{\overline{\Lambda}_2}\right)\sqrt{\left(\frac{\mathrm{d}\overline{X}}{\mathrm{d}\overline{T}} + \overline{v}_z\right)^2 + \left(\frac{\mathrm{d}\overline{Y}}{\mathrm{d}\overline{T}} + \frac{\overline{v}_r}{\overline{\Lambda}_2}\frac{\mathrm{d}\overline{Y}}{\mathrm{d}\overline{T}}\right)^2 + \left(\frac{\mathrm{d}\overline{H}}{\mathrm{d}\overline{T}} + \frac{\overline{v}_r}{\overline{\Lambda}_2}\frac{\mathrm{d}\overline{H}}{\mathrm{d}\overline{T}}\right)^2}, \tag{D.25}$$

$$\frac{\mathrm{d}^2\overline{H}}{\mathrm{d}\overline{T}^2} = -\overline{\chi}\frac{\mathrm{d}\overline{H}}{\mathrm{d}\overline{T}}\left(1 + \frac{\overline{v}_r}{\overline{\Lambda}_2}\right)\sqrt{\left(\frac{\mathrm{d}\overline{X}}{\mathrm{d}\overline{T}} + \overline{v}_z\right)^2 + \left(\frac{\mathrm{d}\overline{Y}}{\mathrm{d}\overline{T}} + \frac{\overline{v}_r}{\overline{\Lambda}_2}\frac{\mathrm{d}\overline{Y}}{\mathrm{d}\overline{T}}\right)^2 + \left(\frac{\mathrm{d}\overline{H}}{\mathrm{d}\overline{T}} + \frac{\overline{v}_r}{\overline{\Lambda}_2}\frac{\mathrm{d}\overline{H}}{\mathrm{d}\overline{T}}\right)^2} - \frac{1}{Fr^2}, \tag{D.26}$$

Appendix D (Continued)

where,

$$\overline{\Lambda}_2 = \sqrt{\left(\frac{\mathrm{d}\overline{Y}}{\mathrm{d}\overline{T}}\right)^2 + \left(\frac{\mathrm{d}\overline{H}}{\mathrm{d}\overline{T}}\right)^2}. \tag{D.27}$$

As usual, Eqs. (D.11)–(D.13) and (D.24)–(D.26) are supplemented with the kinematic equations relating coordinate variation with velocity to bring the system of second order ODE's down to first order ODE's.

Appendix E

NON–NEWTONIAN BLOOD JET MODEL EXTENSION

To extend the theory of an intact jet of liquid to accommodate a shear–thinning fluid such as blood, Eq. (9.4) for the longitudinal force acting in the jet cross section, P, must be changed to the following, according to Ref. [118],

$$P = \left[3^{\frac{n+1}{2}} K \frac{1}{\lambda} \frac{\partial V_\tau}{\partial x} - k\, V_n|^n \,\text{sign}\left(\frac{1}{\lambda} \frac{\partial V_\tau}{\partial x} - k V_n \right) - \sigma G \right] f + P_\sigma. \tag{E.1}$$

where n and K are the flow behavior, and flow consistency indices, respectively.

Through the simplifications described in Sec. 9.3, namely, for thick, steady–state jets, Eq. (E.1) becomes,

$$P = 3^{\frac{n+1}{2}} K \frac{1}{\lambda} \left| \frac{\mathrm{d}V_\tau}{\mathrm{d}x} \right|^n \text{sign}\left(\frac{dV_\tau}{dx} \right) f, \tag{E.2}$$

which replaces Eq. (9.8).

The rest of the analysis still holds, and therefore Eqs. (9.11) and (9.12) are still valid and P is simply replaced by Eq. (E.2) as opposed to $P = 0$. The governing equations can be rendered

Appendix E (Continued)

non–dimensional with H_0 for x and H, the initial velocity $V_0 = Q/f_0$ for V_τ, and $\left(K f_0 V_0^n\right)/H_0^n$ for P. This results in a dimensionless group, $\overline{K}$, defined as,

$$\overline{K} = \frac{K f_0^{2-n}}{\rho Q^{2-n} H_0^n}. \tag{E.3}$$

which can help determine if Eq. (E.2) is needed or not for intact jets of blood based off of an order of magnitude estimate. Using experimental ranges where $Q \sim 10^2$ cm^3/s, $\rho \sim 1$ g/cm^3, $f_0 \sim 10^{-1}$ cm^2, and $H_0 \sim 10$ cm, then $\overline{K} \sim 10^{-5}$. Therefore, an intact jet of blood for the flow range considered is practically inviscid and Eqs. (9.11) and (9.12) are still valid as evaluated in Ch. 9.

Appendix F

PUBLISHER PERMISSIONS

Permission granted by Springer Nature for the work which addresses blood rheology discussed in Sections 2.1, and 3.1, as well as Chapter 4 is Reference [1] in this thesis and can be found at: https://doi.org/10.1007/s00397-016-0964-1. Permission granted by the American Physical Society for the work which addresses the backspatter of blood for sharp bullets discussed in Sections 2.2, and 2.3, along with parts of Chapter 6 is Reference [2] in this thesis and can be found at: https://doi.org/10.1103/PhysRevFluids.1.043201. Permission granted by the American Physical Society for the work which addresses the forward spatter of blood for a bullet shaped as an ovoid of Rankine discussed in Section 2.4 and parts of Chapter 7, is Reference [3] in this thesis and can be found at: https://doi.org/10.1103/PhysRevFluids.3.063901. The work on the interaction of muzzle gases with backward spattered blood droplets discussed in Sections 2.5, and 3.4, as well as Chapter 8 and Appendix C and D and used as Reference [4] is currently not published but has been submitted for publication in the Journal of Fluid Mechanics. Permission granted by Springer Nature for the work which addresses intact liquid jets discussed in Sections 2.6, and 3.5, as well as Chapter 9 is Reference [5] in this thesis and can be found at: https://doi.org/10.1007/s00348-018-2519-y. Permission granted by the American Physical Society for the work which addresses the backspatter of blood for blunt bullets discussed in Section 3.3 and parts of Chapter 6 is Reference [6] in this thesis and can be found at: https://doi.org/10.1103/PhysRevFluids.2.073906. Permission granted

Appendix F (Continued)

by Elsevier for the work in high–speed video analysis of the atomization of blood due to a gunshot discussed in Section 3.2 and Chapter 5 is Reference [7] in this thesis and can be found at: `https://doi.org/10.1016/j.forsciint.2017.04.016`. The statistical work on the backward spatter of blood discussed in portions of Chapter 6 and used as Reference [8] is currently not published but has been submitted for publication in Forensic Science International. The work on the generalized model of the forward spatter of blood discussed in sections of Chapter 7 and used as Reference [9] is currently not published but has been submitted for publication in Physical Review Fluids

The subsequent statements are from the respective Publisher's granting permission for previously published articles of the present author used in this thesis.

Appendix F (Continued)

SPRINGER NATURE LICENSE TERMS AND CONDITIONS

Jan 25, 2019

This Agreement between Patrick M Comiskey ("You") and Springer Nature ("Springer Nature") consists of your license details and the terms and conditions provided by Springer Nature and Copyright Clearance Center.

License Number	4516071265545
License date	Jan 25, 2019
Licensed Content Publisher	Springer Nature
Licensed Content Publication	Rheologica Acta
Licensed Content Title	Blood rheology in shear and uniaxial elongation
Licensed Content Author	Alexander Kolbasov, Patrick M. Comiskey, Rakesh Prasad Sahu et al
Licensed Content Date	Jan 1, 2016
Licensed Content Volume	55
Licensed Content Issue	11
Type of Use	Thesis/Dissertation
Requestor type	academic/university or research institute
Format	print and electronic
Portion	full article/chapter
Will you be translating?	no
Circulation/distribution	<501
Author of this Springer Nature content	yes
Title	Fluid Mechanics of Blood Motion Resulting from Common Bloodletting Events
Institution name	University of Illinois at Chicago
Expected presentation date	Feb 2019
Requestor Location	Patrick M Comiskey 842 W Taylor St Room 2039 ERF, MC 251 CHICAGO, IL 60607 United States Attn: Patrick M Comiskey
Billing Type	Invoice
Billing Address	Patrick M Comiskey 842 W Taylor St Room 2039 ERF, MC 251 CHICAGO, IL 60607 United States Attn: Patrick M Comiskey
Total	0.00 USD
Terms and Conditions	

Springer Nature Terms and Conditions for RightsLink Permissions

Springer Nature Customer Service Centre GmbH (the Licensor) hereby grants you a non-exclusive, world-wide licence to reproduce the material and for the purpose and requirements specified in the attached copy of your order form, and for no other use, subject to the conditions below:

1. The Licensor warrants that it has, to the best of its knowledge, the rights to license reuse of this material. However, you should ensure that the material you are requesting is original to the Licensor and does not carry the copyright of another entity (as credited in the published version).

   If the credit line on any part of the material you have requested indicates that it was reprinted or adapted with permission from another source, then you should also seek permission from that source to reuse the material.

Appendix F (Continued)

2. Where **print only** permission has been granted for a fee, separate permission must be obtained for any additional electronic re-use.

3. Permission granted **free of charge** for material in print is also usually granted for any electronic version of that work, provided that the material is incidental to your work as a whole and that the electronic version is essentially equivalent to, or substitutes for, the print version.

4. A licence for 'post on a website' is valid for 12 months from the licence date. This licence does not cover use of full text articles on websites.

5. Where **'reuse in a dissertation/thesis'** has been selected the following terms apply: Print rights of the final author's accepted manuscript (for clarity, NOT the published version) for up to 100 copies, electronic rights for use only on a personal website or institutional repository as defined by the Sherpa guideline (www.sherpa.ac.uk/romeo/).

6. Permission granted for books and journals is granted for the lifetime of the first edition and does not apply to second and subsequent editions (except where the first edition permission was granted free of charge or for signatories to the STM Permissions Guidelines http://www.stm-assoc.org/copyright-legal-affairs/permissions/permissions-guidelines/), and does not apply for editions in other languages unless additional translation rights have been granted separately in the licence.

7. Rights for additional components such as custom editions and derivatives require additional permission and may be subject to an additional fee. Please apply to Journalpermissions@springernature.com/bookpermissions@springernature.com for these rights.

8. The Licensor's permission must be acknowledged next to the licensed material in print. In electronic form, this acknowledgement must be visible at the same time as the figures/tables/illustrations or abstract, and must be hyperlinked to the journal/book's homepage. Our required acknowledgement format is in the Appendix below.

9. Use of the material for incidental promotional use, minor editing privileges (this does not include cropping, adapting, omitting material or any other changes that affect the meaning, intention or moral rights of the author) and copies for the disabled are permitted under this licence.

10. Minor adaptations of single figures (changes of format, colour and style) do not require the Licensor's approval. However, the adaptation should be credited as shown in Appendix below.

Appendix — Acknowledgements:

For Journal Content:
Reprinted by permission from [**the Licensor**]: [**Journal Publisher** (e.g. Nature/Springer/Palgrave)] [**JOURNAL NAME**] [**REFERENCE CITATION** (Article name, Author(s) Name), [**COPYRIGHT**] (year of publication)

For **Advance Online Publication papers:**
Reprinted by permission from [**the Licensor**]: [**Journal Publisher** (e.g. Nature/Springer/Palgrave)] [**JOURNAL NAME**] [**REFERENCE CITATION** (Article name, Author(s) Name), [**COPYRIGHT**] (year of publication), advance online publication, day month year (doi: 10.1038/sj.[JOURNAL ACRONYM].)

For Adaptations/Translations:
Adapted/Translated by permission from [**the Licensor**]: [**Journal Publisher** (e.g. Nature/Springer/Palgrave)] [**JOURNAL NAME**] [**REFERENCE CITATION** (Article name, Author(s) Name), [**COPYRIGHT**] (year of publication)

Note: For any republication from the British Journal of Cancer, the following credit line style applies:

Reprinted/adapted/translated by permission from [**the Licensor**]: on behalf of Cancer Research UK: : [**Journal Publisher** (e.g. Nature/Springer/Palgrave)] [**JOURNAL NAME**] [**REFERENCE CITATION** (Article name, Author(s) Name), [**COPYRIGHT]** (year of publication)

For **Advance Online Publication** papers:
Reprinted by permission from The [**the Licensor**]: on behalf of Cancer Research UK: [**Journal Publisher** (e.g. Nature/Springer/Palgrave)] [**JOURNAL NAME**] [**REFERENCE CITATION** (Article name, Author(s) Name), [**COPYRIGHT**] (year of publication), advance online publication, day month year (doi: 10.1038/sj.[JOURNAL ACRONYM])

Appendix F (Continued)

Appendix F (Continued)

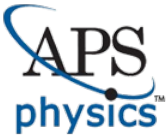

American Physical Society Reuse and Permissions License

25-Jan-2019

This license agreement between the American Physical Society ("APS") and Patrick Comiskey ("You") consists of your license details and the terms and conditions provided by the American Physical Society and SciPris.

Licensed Content Information

License Number:	**RNP/19/JAN/011352**
License date:	25-Jan-2019
DOI:	10.1103/PhysRevFluids.1.043201
Title:	Prediction of blood back spatter from a gunshot in bloodstain pattern analysis
Author:	P. M. Comiskey et al.
Publication:	Physical Review Fluids
Publisher:	American Physical Society
Cost:	USD $ 0.00

Request Details

Does your reuse require significant modifications: No

Specify intended distribution locations:	Worldwide
Reuse Category:	Reuse in a thesis/dissertation
Requestor Type:	Author of requested content
Items for Reuse:	Whole Article
Format for Reuse:	Electronic and Print
Total number of print copies:	Up to 1000

Information about New Publication:

University/Publisher:	University of Illinois at Chicago
Title of dissertation/thesis:	Fluid Mechanics of Blood Motion Resulting from Common Bloodletting Events
Author(s):	Patrick M. Comiskey
Expected completion date:	Feb. 2019

License Requestor Information

Name:	Patrick Comiskey
Affiliation:	Individual
Email Id:	pcomis2@uic.edu
Country:	United States

Appendix F (Continued)

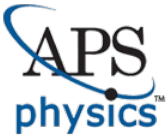

American Physical Society
Reuse and Permissions License

TERMS AND CONDITIONS

The American Physical Society (APS) is pleased to grant the Requestor of this license a non-exclusive, non-transferable permission, limited to Electronic and Print format, provided all criteria outlined below are followed.

1. You must also obtain permission from at least one of the lead authors for each separate work, if you haven't done so already. The author's name and affiliation can be found on the first page of the published Article.
2. For electronic format permissions, Requestor agrees to provide a hyperlink from the reprinted APS material using the source material's DOI on the web page where the work appears. The hyperlink should use the standard DOI resolution URL, http://dx.doi.org/{DOI}. The hyperlink may be embedded in the copyright credit line.
3. For print format permissions, Requestor agrees to print the required copyright credit line on the first page where the material appears: "Reprinted (abstract/excerpt/figure) with permission from [(FULL REFERENCE CITATION) as follows: Author's Names, APS Journal Title, Volume Number, Page Number and Year of Publication.] Copyright (YEAR) by the American Physical Society."
4. Permission granted in this license is for a one-time use and does not include permission for any future editions, updates, databases, formats or other matters. Permission must be sought for any additional use.
5. Use of the material does not and must not imply any endorsement by APS.
6. APS does not imply, purport or intend to grant permission to reuse materials to which it does not hold copyright. It is the requestor's sole responsibility to ensure the licensed material is original to APS and does not contain the copyright of another entity, and that the copyright notice of the figure, photograph, cover or table does not indicate it was reprinted by APS with permission from another source.
7. The permission granted herein is personal to the Requestor for the use specified and is not transferable or assignable without express written permission of APS. This license may not be amended except in writing by APS.
8. You may not alter, edit or modify the material in any manner.
9. You may translate the materials only when translation rights have been granted.
10. APS is not responsible for any errors or omissions due to translation.
11. You may not use the material for promotional, sales, advertising or marketing purposes.
12. The foregoing license shall not take effect unless and until APS or its agent, Aptara, receives payment in full in accordance with Aptara Billing and Payment Terms and Conditions, which are incorporated herein by reference.
13. Should the terms of this license be violated at any time, APS or Aptara may revoke the license with no refund to you and seek relief to the fullest extent of the laws of the USA. Official written notice will be made using the contact information provided with the permission request. Failure to receive such notice will not nullify revocation of the permission.
14. APS reserves all rights not specifically granted herein.
15. This document, including the Aptara Billing and Payment Terms and Conditions, shall be the entire agreement between the parties relating to the subject matter hereof.

Appendix F (Continued)

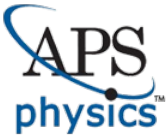

American Physical Society Reuse and Permissions License

25-Jan-2019

This license agreement between the American Physical Society ("APS") and Patrick Comiskey ("You") consists of your license details and the terms and conditions provided by the American Physical Society and SciPris.

Licensed Content Information

License Number:	**RNP/19/JAN/011353**
License date:	25-Jan-2019
DOI:	10.1103/PhysRevFluids.3.063901
Title:	Theoretical and experimental investigation of forward spatter of blood from a gunshot
Author:	P. M. Comiskey, A. L. Yarin, and D. Attinger
Publication:	Physical Review Fluids
Publisher:	American Physical Society
Cost:	USD $ 0.00

Request Details

Does your reuse require significant modifications: No

Specify intended distribution locations:	Worldwide
Reuse Category:	Reuse in a thesis/dissertation
Requestor Type:	Author of requested content
Items for Reuse:	Whole Article
Format for Reuse:	Print and Electronic
Total number of print copies:	Up to 1000

Information about New Publication:

University/Publisher:	University of Illinois at Chicago
Title of dissertation/thesis:	Fluid Mechanics of Blood Motion Resulting from Common Bloodletting Events
Author(s):	Patrick M. Comiskey
Expected completion date:	Feb. 2019

License Requestor Information

Name:	Patrick Comiskey
Affiliation:	Individual
Email Id:	pcomis2@uic.edu
Country:	United States

Appendix F (Continued)

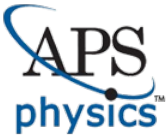

American Physical Society Reuse and Permissions License

TERMS AND CONDITIONS

The American Physical Society (APS) is pleased to grant the Requestor of this license a non-exclusive, non-transferable permission, limited to Print and Electronic format, provided all criteria outlined below are followed.

1. You must also obtain permission from at least one of the lead authors for each separate work, if you haven't done so already. The author's name and affiliation can be found on the first page of the published Article.
2. For electronic format permissions, Requestor agrees to provide a hyperlink from the reprinted APS material using the source material's DOI on the web page where the work appears. The hyperlink should use the standard DOI resolution URL, http://dx.doi.org/{DOI}. The hyperlink may be embedded in the copyright credit line.
3. For print format permissions, Requestor agrees to print the required copyright credit line on the first page where the material appears: "Reprinted (abstract/excerpt/figure) with permission from [(FULL REFERENCE CITATION) as follows: Author's Names, APS Journal Title, Volume Number, Page Number and Year of Publication.] Copyright (YEAR) by the American Physical Society."
4. Permission granted in this license is for a one-time use and does not include permission for any future editions, updates, databases, formats or other matters. Permission must be sought for any additional use.
5. Use of the material does not and must not imply any endorsement by APS.
6. APS does not imply, purport or intend to grant permission to reuse materials to which it does not hold copyright. It is the requestor's sole responsibility to ensure the licensed material is original to APS and does not contain the copyright of another entity, and that the copyright notice of the figure, photograph, cover or table does not indicate it was reprinted by APS with permission from another source.
7. The permission granted herein is personal to the Requestor for the use specified and is not transferable or assignable without express written permission of APS. This license may not be amended except in writing by APS.
8. You may not alter, edit or modify the material in any manner.
9. You may translate the materials only when translation rights have been granted.
10. APS is not responsible for any errors or omissions due to translation.
11. You may not use the material for promotional, sales, advertising or marketing purposes.
12. The foregoing license shall not take effect unless and until APS or its agent, Aptara, receives payment in full in accordance with Aptara Billing and Payment Terms and Conditions, which are incorporated herein by reference.
13. Should the terms of this license be violated at any time, APS or Aptara may revoke the license with no refund to you and seek relief to the fullest extent of the laws of the USA. Official written notice will be made using the contact information provided with the permission request. Failure to receive such notice will not nullify revocation of the permission.
14. APS reserves all rights not specifically granted herein.
15. This document, including the Aptara Billing and Payment Terms and Conditions, shall be the entire agreement between the parties relating to the subject matter hereof.

Appendix F (Continued)

SPRINGER NATURE LICENSE TERMS AND CONDITIONS

Jan 25, 2019

This Agreement between Patrick M Comiskey ("You") and Springer Nature ("Springer Nature") consists of your license details and the terms and conditions provided by Springer Nature and Copyright Clearance Center.

License Number	4516110719355
License date	Jan 25, 2019
Licensed Content Publisher	Springer Nature
Licensed Content Publication	Experiments in Fluids
Licensed Content Title	Friction coefficient of an intact free liquid jet moving in air
Licensed Content Author	P. M. Comiskey, A. L. Yarin
Licensed Content Date	Jan 1, 2018
Licensed Content Volume	59
Licensed Content Issue	4
Type of Use	Thesis/Dissertation
Requestor type	academic/university or research institute
Format	print and electronic
Portion	full article/chapter
Will you be translating?	no
Circulation/distribution	<501
Author of this Springer Nature content	yes
Title	Fluid Mechanics of Blood Motion Resulting from Common Bloodletting Events
Institution name	University of Illinois at Chicago
Expected presentation date	Feb 2019
Requestor Location	Patrick M Comiskey 842 W Taylor St Room 2039 ERF, MC 251 CHICAGO, IL 60607 United States Attn: Patrick M Comiskey
Billing Type	Invoice
Billing Address	Patrick M Comiskey 842 W Taylor St Room 2039 ERF, MC 251 CHICAGO, IL 60607 United States Attn: Patrick M Comiskey
Total	0.00 USD
Terms and Conditions	

Springer Nature Terms and Conditions for RightsLink Permissions

Springer Nature Customer Service Centre GmbH (the Licensor) hereby grants you a non-exclusive, world-wide licence to reproduce the material and for the purpose and requirements specified in the attached copy of your order form, and for no other use, subject to the conditions below:

1. The Licensor warrants that it has, to the best of its knowledge, the rights to license reuse of this material. However, you should ensure that the material you are requesting is original to the Licensor and does not carry the copyright of another entity (as credited in the published version).

   If the credit line on any part of the material you have requested indicates that it was reprinted or adapted with permission from another source, then you should also seek permission from that source to reuse the material.

Appendix F (Continued)

2. Where **print only** permission has been granted for a fee, separate permission must be obtained for any additional electronic re-use.

3. Permission granted **free of charge** for material in print is also usually granted for any electronic version of that work, provided that the material is incidental to your work as a whole and that the electronic version is essentially equivalent to, or substitutes for, the print version.

4. A licence for 'post on a website' is valid for 12 months from the licence date. This licence does not cover use of full text articles on websites.

5. Where **'reuse in a dissertation/thesis'** has been selected the following terms apply: Print rights of the final author's accepted manuscript (for clarity, NOT the published version) for up to 100 copies, electronic rights for use only on a personal website or institutional repository as defined by the Sherpa guideline (www.sherpa.ac.uk/romeo/).

6. Permission granted for books and journals is granted for the lifetime of the first edition and does not apply to second and subsequent editions (except where the first edition permission was granted free of charge or for signatories to the STM Permissions Guidelines http://www.stm-assoc.org/copyright-legal-affairs/permissions/permissions-guidelines/), and does not apply for editions in other languages unless additional translation rights have been granted separately in the licence.

7. Rights for additional components such as custom editions and derivatives require additional permission and may be subject to an additional fee. Please apply to Journalpermissions@springernature.com/bookpermissions@springernature.com for these rights.

8. The Licensor's permission must be acknowledged next to the licensed material in print. In electronic form, this acknowledgement must be visible at the same time as the figures/tables/illustrations or abstract, and must be hyperlinked to the journal/book's homepage. Our required acknowledgement format is in the Appendix below.

9. Use of the material for incidental promotional use, minor editing privileges (this does not include cropping, adapting, omitting material or any other changes that affect the meaning, intention or moral rights of the author) and copies for the disabled are permitted under this licence.

10. Minor adaptations of single figures (changes of format, colour and style) do not require the Licensor's approval. However, the adaptation should be credited as shown in Appendix below.

Appendix — Acknowledgements:

For Journal Content:
Reprinted by permission from [**the Licensor**]: [**Journal Publisher** (e.g. Nature/Springer/Palgrave)] [**JOURNAL NAME**] [**REFERENCE CITATION** (Article name, Author(s) Name), [**COPYRIGHT**] (year of publication)

For **Advance Online Publication papers:**
Reprinted by permission from [**the Licensor**]: [**Journal Publisher** (e.g. Nature/Springer/Palgrave)] [**JOURNAL NAME**] [**REFERENCE CITATION** (Article name, Author(s) Name), [**COPYRIGHT**] (year of publication), advance online publication, day month year (doi: 10.1038/sj.[JOURNAL ACRONYM].)

For Adaptations/Translations:
Adapted/Translated by permission from [**the Licensor**]: [**Journal Publisher** (e.g. Nature/Springer/Palgrave)] [**JOURNAL NAME**] [**REFERENCE CITATION** (Article name, Author(s) Name), [**COPYRIGHT**] (year of publication)

Note: For any republication from the British Journal of Cancer, the following credit line style applies:

Reprinted/adapted/translated by permission from [**the Licensor**]: on behalf of Cancer Research UK: : [**Journal Publisher** (e.g. Nature/Springer/Palgrave)] [**JOURNAL NAME**] [**REFERENCE CITATION** (Article name, Author(s) Name), [**COPYRIGHT]** (year of publication)

For **Advance Online Publication** papers:
Reprinted by permission from The [**the Licensor**]: on behalf of Cancer Research UK: [**Journal Publisher** (e.g. Nature/Springer/Palgrave)] [**JOURNAL NAME**] [**REFERENCE CITATION** (Article name, Author(s) Name), [**COPYRIGHT**] (year of publication), advance online publication, day month year (doi: 10.1038/sj.[JOURNAL ACRONYM])

Appendix F (Continued)

Appendix F (Continued)

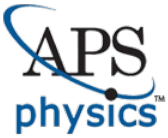

American Physical Society Reuse and Permissions License

25-Jan-2019

This license agreement between the American Physical Society ("APS") and Patrick Comiskey ("You") consists of your license details and the terms and conditions provided by the American Physical Society and SciPris.

Licensed Content Information

License Number:	**RNP/19/JAN/011354**
License date:	25-Jan-2019
DOI:	10.1103/PhysRevFluids.2.073906
Title:	Hydrodynamics of back spatter by blunt bullet gunshot with a link to bloodstain pattern analysis
Author:	P. M. Comiskey, A. L. Yarin, and D. Attinger
Publication:	Physical Review Fluids
Publisher:	American Physical Society
Cost:	USD $ 0.00

Request Details

Does your reuse require significant modifications: No

Specify intended distribution locations:	Worldwide
Reuse Category:	Reuse in a thesis/dissertation
Requestor Type:	Author of requested content
Items for Reuse:	Whole Article
Format for Reuse:	Print and Electronic
Total number of print copies:	Up to 1000

Information about New Publication:

University/Publisher:	University of Illinois at Chicago
Title of dissertation/thesis:	Fluid Mechanics of Blood Motion Resulting from Common Bloodletting Events
Author(s):	Patrick M. Comiskey
Expected completion date:	Feb. 2019

License Requestor Information

Name:	Patrick Comiskey
Affiliation:	Individual
Email Id:	pcomis2@uic.edu
Country:	United States

Appendix F (Continued)

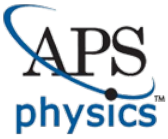

American Physical Society
Reuse and Permissions License

TERMS AND CONDITIONS

The American Physical Society (APS) is pleased to grant the Requestor of this license a non-exclusive, non-transferable permission, limited to Print and Electronic format, provided all criteria outlined below are followed.

1. You must also obtain permission from at least one of the lead authors for each separate work, if you haven't done so already. The author's name and affiliation can be found on the first page of the published Article.
2. For electronic format permissions, Requestor agrees to provide a hyperlink from the reprinted APS material using the source material's DOI on the web page where the work appears. The hyperlink should use the standard DOI resolution URL, http://dx.doi.org/{DOI}. The hyperlink may be embedded in the copyright credit line.
3. For print format permissions, Requestor agrees to print the required copyright credit line on the first page where the material appears: "Reprinted (abstract/excerpt/figure) with permission from [(FULL REFERENCE CITATION) as follows: Author's Names, APS Journal Title, Volume Number, Page Number and Year of Publication.] Copyright (YEAR) by the American Physical Society."
4. Permission granted in this license is for a one-time use and does not include permission for any future editions, updates, databases, formats or other matters. Permission must be sought for any additional use.
5. Use of the material does not and must not imply any endorsement by APS.
6. APS does not imply, purport or intend to grant permission to reuse materials to which it does not hold copyright. It is the requestor's sole responsibility to ensure the licensed material is original to APS and does not contain the copyright of another entity, and that the copyright notice of the figure, photograph, cover or table does not indicate it was reprinted by APS with permission from another source.
7. The permission granted herein is personal to the Requestor for the use specified and is not transferable or assignable without express written permission of APS. This license may not be amended except in writing by APS.
8. You may not alter, edit or modify the material in any manner.
9. You may translate the materials only when translation rights have been granted.
10. APS is not responsible for any errors or omissions due to translation.
11. You may not use the material for promotional, sales, advertising or marketing purposes.
12. The foregoing license shall not take effect unless and until APS or its agent, Aptara, receives payment in full in accordance with Aptara Billing and Payment Terms and Conditions, which are incorporated herein by reference.
13. Should the terms of this license be violated at any time, APS or Aptara may revoke the license with no refund to you and seek relief to the fullest extent of the laws of the USA. Official written notice will be made using the contact information provided with the permission request. Failure to receive such notice will not nullify revocation of the permission.
14. APS reserves all rights not specifically granted herein.
15. This document, including the Aptara Billing and Payment Terms and Conditions, shall be the entire agreement between the parties relating to the subject matter hereof.

Appendix F (Continued)

CITED LITERATURE

1. Kolbasov, A., Comiskey, P. M., Sahu, R. P., Sinha-Ray, S., Yarin, A. L., Sikarwar, B. S., Kim, S., Jubery, T. Z., and Attinger, D.: Blood rheology in shear and uniaxial elongation. Rheologica Acta, 55(11-12):901–908, 2016.

2. Comiskey, P. M., Yarin, A. L., Kim, S., and Attinger, D.: Prediction of blood back spatter from a gunshot in bloodstain pattern analysis. Physical Review Fluids, 1(4):043201, 2016.

3. Comiskey, P. M., Yarin, A. L., and Attinger, D.: Theoretical and experimental investigation of forward spatter of blood from a gunshot. Physical Review Fluids, 3(6):063901, 2018.

4. Comiskey, P. M. and Yarin, A. L.: Self–similar turbulent vortex rings: Interaction of propellant gases with blood backspatter and the transport of gunshot residue. Journal of Fluid Mechanics, Submitted 2019.

5. Comiskey, P. M. and Yarin, A. L.: Friction coefficient of an intact free liquid jet moving in air. Experiments in Fluids, 59(4):65, 2018.

6. Comiskey, P. M., Yarin, A. L., and Attinger, D.: Hydrodynamics of back spatter by blunt bullet gunshot with a link to bloodstain pattern analysis. Physical Review Fluids, 2(7):073906, 2017.

7. Comiskey, P. M., Yarin, A. L., and Attinger, D.: High–speed video analysis of forward and backward spattered blood droplets. Forensic Science International, 276:134–141, 2017.

8. Comiskey, P. M., Yarin, A. L., and Attinger, D.: Implications of two backward blood spatter models based on fluid dynamics for bloodstain pattern analysis. Forensic Science International, Submitted 2018.

9. Comiskey, P. M., Yarin, A. L., and Attinger, D.: Forward spattering of blood from a gunshot by a bullet of an arbitrary shape. Physical Review Fluids, Submitted 2019.

10. Piotrowski, E.: Über Entstehung, Form, Richtung u. Ausbreitung der Blutspuren nach Hiebwunden des Kopfes. Slomski, 1895.

11. Balthazard, V., Piedelievre, R., Desoille, H., and Derobert, L.: Study of projected drops of blood. Annales de Medecine Legale, Criminologie, Police Scientifique et Toxicologie, 19:265–323, 1939.

12. LeMoyne, S.: Homicide Investigation. Springfield, IL, Charles C. Thomas, 1944.

13. Kirk, P. L.: Affidavit Regarding State of Ohio vs. Samuel H. Sheppard. Court of Common Pleas, Criminal Branch, 1955. No. 64571, 26 April.

14. MacDonell, H. L. and Bialousz, L. F.: Flight Characteristics and Stain Patterns of Human Blood. Washington DC, National Institute of Law Enforcement and Criminal Justice, 1971.

15. Attinger, D., Moore, C., Donaldson, A., Jafari, A., and Stone, H. A.: Fluid dynamics topics in bloodstain pattern analysis: Comparative review and research opportunities. Forensic Science International, 231(1-3):375–396, 2013.

16. Varney, C. R. and Gittes, F.: Locating the source of projectile fluid droplets. American Journal of Physics, 79(8):838–842, 2011.

17. Cecchetto, B. T.: Nonlinear blood pattern reconstruction. The Univesity of British Columbia, 2010. M.S. Thesis.

18. Laan, N., de Bruin, K. G., Bartolo, D., Josserand, C., and Bonn, D.: Maximum diameter of impacting liquid droplets. Physical Review Applied, 2(4):044018, 2014.

19. Laan, N., de Bruin, K. G., Slenter, D., Wilhelm, J., Jermy, M., and Bonn, D.: Bloodstain pattern analysis: implementation of a fluid dynamic model for position determination of victims. Scientific Reports, 5:11461, 2015.

20. Attinger, D., Comiskey, P. M., Yarin, A. L., and Brabanter, K. D.: Determining the region of origin of blood spatters considering fluid dynamics and statistical uncertainties. Forensic Science International, Submitted 2018.

21. Attinger, D., Liu, Y., Faflak, R., Rao, Y., Struttman, B. A., Brabanter, K. D., Comiskey, P. M., and Yarin, A. L.: A data set of bloodstain patterns for teaching and research in bloodstain pattern analysis: Gunshot backspatters. Data in Brief, 22:269–278, 2019.

22. Comiskey, P. M., Yarin, A. L., and Attinger, D.: Atomization of blood spatter resulting from a gunshot. In ICLASS 14th Triennial International Conference on Liquid Atomization and Spray System Proceedings, 2018.

23. Bevel, T. and Gardner, R. M.: Bloodstain Pattern Analysis with an Introduction to Crime Scene Reconstruction. Boca Raton, FL, CRC Press, 2008.

24. Walker, H., Hall, W., and Hurst, J.: Clinical Methods: The History, Physical, and Laboratory Examinations. Boston, Butterworths, 1990.

25. Gruttola, S. D., Boomsma, K., and Poulikakos, D.: Computational sumulation of a non–Newtonian model of the blood separation process. Artifical Organs, 29(12):949–959, 2005.

26. Charm, S. and Kurland, G.: Viscometry of human blood for shear rates of 0–100,000 sec^{-1}. Nature, 206(4984):617–618, 1965.

27. Chien, S., King, R. G., Skalak, R., Usami, S., and Copley, A. L.: Viscoelastic properties of human blood and red cell suspensions. Biorheology, 12(6):341–346, 1975.

28. Brust, M., Schaefer, C., Doerr, R., Pan, L., Garcia, M., Arratia, P. E., and Wagner, C.: Rheology of human blood plasma: viscoelastic versus Newtonian behavior. Physical Review Letters, 110(7):078305, 2013.

29. Copley, A. L., King, R. G., Chien, S., Usami, S., Skalak, R., and Huang, C. R.: Microscopic observations of viscoelasticity of human blood in steady and oscillatory shear. Biorheology, 12(5):257–263, 1975.

30. Johnston, B. M., Johnston, P. R., Corney, S., and Kilpatrick, D.: Non–Newtonian blood flow in human right coronary arteries: Steady state simulations. Journal of Biomechanics, 37(5):709–720, 2004.

31. Johnston, B. M., Johnston, P. R., Corney, S., and Kilpatrick, D.: Non–Newtonian blood flow in human right coronary arteries: Transient simulations. Journal of Biomechanics, 39(6):1116–1128, 2006.

32. Leuprecht, A. and Perktold, K.: Computer simulation of non–Newtonian effects on blood flow in large arteries. Computer Methods in Biomechanics and Biomedical Engineering, 4(2):149–163, 2001.

33. Council, N. R.: Strengthening Forensic Science in the United States: A Path Forward. USA, National Academies Press, 2009. http://www.nap.edu/catalog/12589.html.

34. Thoroddsen, S. T., Etoh, T. G., and Takehara, K.: High–speed imaging of drops and bubbles. Annual Review of Fluid Mechanics, 40(1):257–285, 2008.

35. Lin, S. P. and Reitz, R. D.: Drop and spray formation from a liquid jet. Annual Review of Fluid Mechanics, 30(1):85–105, 1998.

36. Eggers, J. and Villermaux, E.: Physics of liquid jets. Reports on Progress in Physics, 71(3):036601, 2008.

37. Rein, M.: Phenomena of liquid drop impact on solid and liquid surfaces. Fluid Dynamics Research, 12(2):61–93, 1993.

38. Clasen, C., Bico, J., Entov, V. M., and McKinley, G. H.: 'Gobbling' drops: the jetting–dripping transition in flows of polymer solutions. Journal of Fluid Mechanics, 636:5–40, 2009.

39. Attinger, D., Haferl, S., Zhao, Z., and Poulikakos, D.: Transport phenomena in the impact of a molten droplet on a surface: Macroscopic phenomenology and microscopic considerations. Part II: Heat transfer and solidification. Annual Review of Heat Transfer, 11:145–205, 2000.

40. Chen, L. and Li, Z.: Bouncing droplets on nonsuperhydrophobic surfaces. Physical Review E, 82(1):016308, 2010.

41. Caviezel, D., Narayanan, C., and Lakehal, D.: Adherence and bouncing of liquid droplets impacting on dry surfaces. Microfluidics and Nanofluidics, 5(4):469–478, 2008.

42. Bartolo, D., Bouamrirene, F., Verneuil, É., Buguin, A., Silberzan, P., and Moulinet, S.: Bouncing or sticky droplets: Impalement transitions on superhydrophobic micropatterned surfaces. Europhysics Letters, 74(2):299–305, 2006.

43. Yarin, A. L.: Drop Impact Dynamics: Splashing, Spreading, Receding, Bouncing... Annual Review of Fluid Mechanics, 38:159–192, 2006.

44. Allain, C. and Limat, L.: Regular patterns of cracks formed by directional drying of a collodial suspension. Physical Review Letters, 74(15):2981–2984, 1995.

45. Gennes, P. G. D.: Coil–stretch transition of dilute flexible polymers under ultrahigh velocity gradients. The Journal of Chemical Physics, 60(12):5030–5042, 1974.

46. Apostolidis, A. J. and Beris, A. N.: Modeling of the blood rheology in steady–state shear flows. Journal of Rheology, 58(3):607–633, 2014.

47. Yilmaz, P. and Gundogdu, M. Y.: A critical review on blood flow in large arteries; relevance to blood rheology, viscosity models, and physiological conditions. Korea–Australia Rheology Journal, 20(4):197–211, 2008.

48. Errill, E. W.: Rheology of blood. Physiological Reviews, 49(4):863–888, 1969.

49. Meiselman, H. J., Neu, B., Rampling, M. W., and Baskurt, O. K.: RBC aggregation: laboratory data and models. Indian Journal of Experimental Biology, 45(1):9–17, 2007.

50. Bertola, V.: An experimental study of bouncing Leidenfrost drops: Comparison between Newtonian and viscoelastic liquids. International Journal of Heat and Mass Transfer, 52(7-8):1786–1793, 2009.

51. Jiang, T., Ouyang, J., Yang, B., and Ren, J.: The SPH method for simulating a viscoelastic drop impact and spreading on an inclined plate. Computational Mechanics, 45(6):573–583, 2010.

52. Yue, P., Zhou, C., Feng, J. J., Ollivier-Gooch, C. F., and Hu, H. H.: Phase–field simulations of interfacial dynamics in viscoelastic fluids using finite elements with adaptive meshing. Journal of Computational Physics, 219(1):47–67, 2006.

53. Cooper-White, J. J., Crooks, R. C., and Boger, D. V.: A drop impact study of worm–like viscoelastic surfactant solutions. Colloids and Surfaces A: Physicochemical and Engineering Aspects, 210(1):105–123, 2002.

54. Joseph, D. D., Belanger, J., and Beavers, G. S.: Breakup of a liquid drop suddenly exposed to a high–speed airstream. International Journal of Multiphase Flow, 25(6-7):1263–1303, 1999.

55. Mighri, F., Carreau, P. J., and Ajji, A.: Influence of elastic properties on drop deformation and breakup in shear flow. Journal of Rheology, 42(6):1477–1490, 1998.

56. Carré, A., Gastel, J. C., and Shanahan, M. E. R.: Viscoelastic effects in the spreading of liquids. Nature, 379(6564):432–434, 1996.

57. Today: Blood–spatter analyst supports Spector's story, 7/23/2007. `http://www.today.com/id/19921974/ns/today-today_entertainment/t/blood-spatter-analyst-supports-spectors-story/`.

58. Illes, M. B., Carter, A. L., Laturnus, P. L., and Yamashita, A. B.: Use of the Backtrack^{TM} computer program for bloodstain pattern analysis of stains from downward–moving drops. Canadian Society of Forensic Science Journal, 38(4):213–217, 2005.

59. Carter, A. L.: The directional analysis of bloodstain patterns theory and experimental validation. Canadian Society of Forensic Science Journal, 34(4):173–189, 2001.

60. Kanable, R.: BackTrack going forward. Law Enforcement Technology, pages 40–45, 2006.

61. Carter, A. L., Forsythe-Erman, J., Hawkes, V., and Yamashita, A. B.: Validation of the BackTrack suite of programs for bloodstain pattern analysis. Journal of Forensic Identification, 56(2):242, 2006.

62. Carter, A. L., Illes, M., Maloney, K., Yamashita, A. B., Allen, B., Brown, B., Davidson, L., Ellis, G., Gallant, J., Gradkowski, A., Hignell, J., Jory, S., Laturnus, P. L., Moore, C. C., Pembroke, R., Richard, A., Spenard, R., and Stewart, C.: Further validation of the BackTrack computer program for bloodstain pattern analysis: Precision and accuracy. International Association of Bloodstain Pattern Analysts News, 21:15–22, 2005.

63. Rowe, W. F.: Errors in the determination of the point of origin of bloodstains. Forensic Science International, 161(1):47–51, 2006.

64. de Bruin, K. G., Stoel, R. D., and Limborgh, J. C. M.: Improving the point of origin determination in bloodstain pattern analysis. Journal of Forensic Sciences, 56(6):1476–1482, 2011.

65. Behrooz, N.: Bloodstain pattern analysis for determination of point of origin. University of Toronto, 2009. B.S. thesis.

66. Attinger, D., Moore, C., Donaldson, A., and Stone, H. A.: Fluid dynamics aspects of bloodstain pattern analysis: Comparative review and research opportunities. In International Association of Bloodstain Pattern Analysts Training Conference, San Diego, 2013.

67. Poulikakos, D. and Waldvogel, J. M.: Heat transfer and fluid dynamics in the process of spray deposition. In Advances in Heat Transfer, volume 28, pages 1–74. Elsevier, 1996.

68. Behrooz, N., Hulse-Smith, L., and Chandra, S.: An evaluation of the underlying mechanisms of bloodstain pattern analysis error. Journal of Forensic Sciences, 56(5):1136–1142, 2011.

69. Denison, D., Porter, A., Mills, M., and Schroter, R. C.: Forensic implications of respiratory derived blood spatter distributions. Forensic Science International, 204(1-3):144–155, 2011.

70. Murzabaev, M. T. and Yarin, A. L.: Dynamics of sprinkler jets. Fluid Dynamics, 20(5):715–722, 1985.

71. Roisman, I. V., Araneo, L., and Tropea, C.: Effect of ambient pressure on penetration of a diesel spray. International Journal of Multiphase Flow, 33(8):904–920, 2007.

72. Yarin, A. L., Roisman, I. V., and Tropea, C.: Collision Phenomena in Liquids and Solids. Cambridge, Cambridge University Press, 2017.

73. hua Qi, L., Luo, J., ming Zhou, J., hui Hou, X., and jun Li, H.: Prediction and measurement of deflected trajectory and temperature history of uniform metal droplets in microstructures fabrication. The International Journal of Advanced Manufacturing Technology, 55(9-12):997–1006, 2011.

74. Davidson, P. L., Taylor, M. C., Wilson, S. J., Walsh, K. A. J., and Kieser, J. A.: Physical components of soft-tissue ballistic wounding and their involvement in the generation of blood backspatter. Journal of Forensic Sciences, 57(5):1339–1342, 2012.

75. Maxworthy, T.: The structure and stability of vortex rings. Journal of Fluid Mechanics, 51(1):15–32, 1972.

76. Maxworthy, T.: Turbulent vortex rings. Journal of Fluid Mechanics, 64(2):227–240, 1974.

77. Akhmetov, D. G.: Vortex Rings. Berlin, Springer, 2009.

78. Gleezer, A. and Coles, D.: An experimental study of a turbulent vortex ring. Journal of Fluid Mechanics, 211:243–283, 1990.

79. Klingenberg, G. and Heimerl, J. M.: Gun Muzzle Blast and Flash. Washington DC, American Institute of Aeronautics and Astronautics, Inc., 1992.

80. Taylor, G. I.: The formation of a blast wave by a very intense explosion. Proceedings of the Royal Society of London: Series A, Mathematical and Physical Sciences, 201:159–174, 1950.

81. Sedov, L. I.: Similarity and Dimensional Methods in Mechanics. New York, Academic Press, 1959.

82. von Neumann, J.: The Point Source Solution (Collected Works, Vol. VI). Oxford, Pergamon Press, 1963.

83. Loitsyanskii, L. G.: Mechanics of Liquids and Gases. Oxford, Pergamon, 1966.

84. Courant, R. and Friedrichs, K. O.: Supersonic Flow and Shock Waves. New York, Springer, 1976.

85. Klingenberg, G.: Investigation of combustion phenomena associated with the flow of hot propellant gases–III: Experimental survey of the formation and decay of muzzle flow fields and of pressure measurements. Combustion and Flame, 29:289–309, 1977.

86. Klingenberg, G. and Mach, H.: Investigation of combustion phenomena associated with the flow of hot propellant gases–I: Spectroscopic temperature measurements inside the muzzle flash of a rifle. Combustion and Flame, 27:163–176, 1976.

87. Klingenberg, G. and Schröder, G. A.: Investigation of combustion phenomena associated with the flow of hot propellant gases–II: Gas velocity measurements by laser–induced gas breakdown. Combustion and Flame, 27:177–187, 1976.

88. Eggins, P. L. and Jackson, D. A.: Laser–Doppler velocity measurements. Journal of Physics D: Applied Physics, 7(14):1894–1906, 1974.

89. Schmidt, E. M. and Shear, D. D.: Optical measurements of muzzle blast. AIAA Journal, 13(8):1086–1091, 1975.

90. Erdos, J. I. and Del Guidice, P. D.: Calculation of muzzle blast flowfields. AIAA Journal, 13(8):1048–1055, 1975.

91. Schwoeble, A. J. and Exline, D. L.: Forensic Gunshot Residue Analysis. Boca Raton, FL, CRC Press, 2000.

92. Dalby, O., Butler, D., and Birkett, J. W.: Analysis of gunshot residue and associated materials–A review. Journal of Forensic Science, 55(4):924–943, 2010.

93. Brożek-Mucha, Z.: Distribution and properties of gunshot residue originating from a Luger 9mm ammunition in the vicinity of the shooting gun. Forensic Science International, 183(1-3):33–44, 2009.

94. Schwoeble, A. J. and Powers, W. H.: A study of downrange GSR deposition as a function of firearm type and ammunition caliber. Miscroscopy and Microanalysis, 15(S2):800–801, 2009.

95. Gerard, R. V., McVicar, M. J., Lindsay, E., Randall, E. D., and Harvey, E.: The long range deposition of gunshot residue and the mechanism of its transportation. Canadian Society of Forensic Science Journal, 44(3):97–104, 2011.

96. Fojtášek, L., Vacínová, J., Kolář, P., and Kotrlý, M.: Distribution of GSR particles in the surroundings of shooting pistol. Forensic Science International, 132(2):99–105, 2003.

97. Taylor, M. C., Laber, T. L., Epstein, B. P., Zamzow, D. S., and Baldwin, D. P.: The effect of firearm muzzle gases on the backspatter of blood. International Journal of Legal Medicine, 125(5):617–628, may 2010.

98. Biedermann, A. and Taroni, F.: A probabilistic approach to the joint evaluation of firearm evidence and gunshot residues. Forensic Science International, 163(1-2):18–33, 2006.

99. Freeman, J. R.: Experiments relating to hydraulics of fire streams. Transactions of the American Society of Civil Engineers, 21(2):303–461, 1889.

100. Rouse, H. R., Howe, J. W., and Metzler, D. E.: Experimental investigation of fire monitors and nozzles. Transactions of the American Society of Civil Engineering, 77(10):1–29, 1951.

101. Arato, E. G., Crow, D. A., and Miller, D. S.: Investigations of a high performance water nozzle. techreport 1058–1064, The British Hydromechanics Research Association, 1970.

102. Theobald, C.: The effect of nozzle design on the stability and performance of turbulent water jets. Fire Safety Journal, 4(1):1–13, 1981.

103. Bilanski, W. K. and Kidder, E. H.: Factors that affect the distribution of water from a medium–pressure rotary irrigation sprinkler. Transaction of the American Society of Agricultural and Biological Engineers, 1:19–28, 1958.

104. Hatton, A. P. and Osborne, M. J.: The trajectories of large fire fighting jets. International Journal of Heat and Fluid Flow, 1(1):37–41, 1979.

105. Wahl, T. L., Frizell, K. H., and Cohen, E. A.: Computing the trajectory of free jets. Journal of Hydraulic Engineering, 134(2):256–260, 2008.

106. Hatton, A. P., Leech, C. M., and Osborne, M. J.: Computer simulation of the trajectories of large water jets. International Journal of Heat and Fluid Flow, 6(2):137–141, 1985.

107. Tuck, E. O.: The shape of free jets of water under gravity. Journal of Fluid Mechanics, 76(4):625–640, 1976.

108. Clanet, C.: On large–amplitude pulsating fountains. Journal of Fluid Mechanics, 366:333–350, 1998.

109. Trettel, B. and Ezekoye, O. A.: Theoretical range and trajectory of a water jet. In Proceedings of ASME 2015 International Mechanical Engineering Congress and Exposition, number Rep. IMECE2015–52103, Houston, TX, 2015. ASME.

110. Lissaman, P. B. S. and Shollenberger, C. A.: Formation flight of birds. Science, 168(3934):1003–1005, 1970.

111. Ziabicki, A.: Fundamentals of Fibre Formation: The Science of Fibre Spinning and Drawing. New York, John Wiley & Sons, 1976.

112. Ziabicki, A. and Kawai, H.: High-speed fiber spinning. New York, John Wiley & Sons, 1985.

113. Wonder, A. Y.: Blood Dynamics. London, Academic Press, 2001.

114. Hanson, D.: Bloodstain pattern analysis: recreating the scene of the crime. Law Enforcement Technology, 31:84, 86–88, 90, 2004.

115. James, S. H., Kish, P. E., and Sutton, T. P.: Principles of Bloodstain Pattern Analysis: Theory and Practice. Boca Raton, FL, CRC Press, 2005.

116. of Investigation, F. B.: Crime in the United States, January 2005. `https://www2.fbi.gov/ucr/05cius/`.

117. of Investigation, F. B.: Crime in the United States, January 2014. `https://ucr.fbi.gov/crime-in-the-u.s/2014/crime-in-the-u.s.-2014`.

118. Yarin, A. L.: Free Liquid Jets and Films: Hydrodynamics and Rheology. Harlow, NY, Longman Publishing Group, 1993.

119. Clanet, C. and Lasheras, J. C.: Transition from dripping to jetting. Journal of Fluid Mechanics, 383:307–326, 1999.

120. Rayleigh, L.: On the instability of jets. Proceedings of the London Mathematical Society, 1(1):4–13, 1878.

121. Rutland, D. F. and Jameson, G. J.: A non–linear effect in the capillary instability of liquid jets. Journal of Fluid Mechanics, 46:267–271, 1971.

122. Basaran, O. A.: Nonlinear oscillations of viscous liquid drops. Journal of Fluid Mechanics, 241:169–198, 1992.

123. Yarin, A. L.: Bending and buckling instabilities of free liquid jets: experiments and general quasi–one–dimensional model. In Springer Handbook of Atomization and Sprays: Theory and Applications, ed. N. Ashgriz, chapter 2, pages 55–73. Heidelberg, Springer, 2011.

124. Ashgriz, N. and Yarin, A. L.: Capillary instability of free liquid jets. In Springer Handbook of Atomization and Sprays: Theory and Applications, ed. N. Ashgriz, chapter 1, pages 3–53. Heidelberg, Springer, 2011.

125. Yarin, A. L., Pourdeyhimi, B., and Ramakrishna, S.: Fundamentals and Applications of Micro-and Nanofibers. Cambridge, Cambridge University Press, 2014.

126. Schlichting, H.: Boundary Layer Theory. New York, McGraw–Hill, 1979.

127. Glicksman, L. R.: The cooling of optical fibres. Glass Technology, 9:131–138, 1968.

128. Yarin, A. L.: Flow–induced on–line crystallization of rodlike molecules in fiber spinning. Journal of Applied Polymer Science, 46(5):873–878, 1992.

129. Tafreshi, H. V. and Pourdeyhimi, B.: The effects of nozzle geometry on waterjet breakup at high Reynolds number. Experiments in Fluids, 35(4):364–371, 2003.

130. de Borda, J. C.: Mémoire sur l'écoulement des fluides par les orifices des vases. M'em Acad Sci, pages 579–607, 1766.

131. Lamb, H.: Hydrodynamics. Cambridge, Cambridge University Press, 1959.

132. Kochin, N. E., Kibel, I. A., and Rose, N. V.: Theoretical Hydrodynamics. New York, Interscience, 1964.

133. Windberger, U., Bartholovitsch, A., Plasenzotti, R., Korak, K. J., and Heinze, G.: Whole blood viscosity, plasma viscosity and erythrocyte aggregation in nine mammalian species: reference values and comparison of data. Experimental Physiology, 88(3):431–440, 2003.

134. Feng, C., Michielsen, S., and Attinger, D.: Impact of carpet construction on fluid penetration: The case of blood. Forensic Science International, 284:184–193, 2018.

135. Huang, C. R., Chen, H. Q., Pan, W. D., Shih, T., Kristol, D. S., and Copley, A. L.: Effect of hematocrit on thixotopic properties properties of human blood. Biorheology, 24(6):803–810, 1987.

136. Wickham, L. L., Bauersachs, R. M., Wenby, R. B., Sowemimo-Coker, S., Meiselman, H. J., and Elsner, R.: Red cell aggregation and viscoelasticity of blood from seals, swine and man. Biorheology, 27(2):191–204, 1990.

137. Williams, E. and Taylor, M.: Standardising blood physical properties: implications for precision bloodstain pattern analysis research. In International Association of Bloodstain Pattern Analysts Training Conference, San Diego, 2013.

138. Ristenpart, W., Tulleners, F., Siu, S., Saifu, J., and Springer, F.: Quantitative analysis os high velocity bloodstain patterns. techreport 1–86, National Institute of Justice, 2013.

139. Brutin, D., Sobac, B., Loquet, B., and Sampol, J.: Pattern formation in drying drops of blood. Journal of Fluid Mechanics, 667:85–95, 2011.

140. eds. C. Tropea, A. L. Yarin, and J. F. Foss Springer Handbook of Experimental Fluid Mechanics. Heidelberg, Springer Science & Business Media, 2007.

141. Steffe, J. F.: Rheological Methods in Food Process Engineering. East Lansing, MI, Freeman Press, 1996.

142. Poole, R. J. and Ridley, B. S.: Development–length requirements for fully developed laminar pipe flow of inelastic non–Newtonian liquids. Journal of Fluids Engineering, 129(10):1281, 2007.

143. Fahraeus, R. and Lindqvist, T.: The viscosity of the blood in narrow capillary tubes. American Journal of Physiology, 96(3):562–568, 1931.

144. Morshed, K. N., Jr., D. B., Forleo, M., and Dasi, L. P.: Theory to predict shear stress on cells in turbulent blood flow. PLoS ONE, 9(8):e105357, 2014.

145. Hung, T. C., Hochmuth, R. M., Joist, J. H., and Sutera, S. P.: Shear–induced aggregation and lysis of platelets. ASAIO Journal, 22(1):285–290, 1976.

146. Ramstack, J. M., Zuckerman, L., and Mockros, L. F.: Shear–induced activation of platelets. Journal of Biomechanics, 12(2):113–125, 1979.

147. Wurzinger, L. J., Opitz, R., Blasberg, P., and Schmid-Schönbein, H.: Platelet and coagulation parameters following millisecond exposure to laminar shear stress. Thrombosis and Haemostasis, 54(2):381–386, 1985.

148. Ames Laboratory Midwest Forensics Resource Center: MFRC Blood Pattern Analysis Videos, January 2017. `https://www.ameslab.gov/mfrc/bpa-videos`.

149. Laber, T. L., Epstein, B. P., and Taylor, M. C.: High speed digital video analysis of bloodstain pattern formation from common bloodletting mechanisms. IABPA News, 24(2):4–12, 2008.

150. Thielicke, W. and Stamhuis, E. J.: PIVlab–Time–Resolved digital particle image velocimetry tool for MATLAB (v 1.41). http://dx.doi.org/10.6084/m9.figshare.1092508, 2014.

151. Schneider, C. A., Rasband, W. S., and Eliceiri, K. W.: NIH image to ImageJ: 25 years of image analysis. Nature Methods, 9(7):671–675, 2012.

152. Phansalkar, N., More, S., Sable, A., and Joshi, M.: Adaptive local thresholding for detection of nuclei in diversly stained cytology images. In Communications and Signal Processing (ICCSP), 2011 International Conference on, pages 218–220, Calicut, India, 2011. IEEE.

153. Batchelor, G. K.: An Introduction to Fluid Dynamics. Cambridge, Cambridge University Press, 2002.

154. Logvinovich, G. V.: Hydrodynamics of Flows with Free Boundaries. Kiev, Naukova Dumka, 1969. (in Russian).

155. Sagomonyan, A. Y.: Penetration. Moscow, Moscow University Publishing House, 1974. (in Russian).

156. Wagner, H.: Über stoß–und gleitvorgänge an der oberfläche von flüssigkeiten. ZAMM-Journal of Applied Mathematics and Mechanics/Zeitschrift für Angewandte Mathematik und Mechanik, 12(4):193–215, 1932.

157. Chandrasekhar, S.: Hydrodynamic and Hydromagnetic Stability. New York, Dover, 1981.

158. Nigmatullin, R.: Dynamics of Multiphase Systems, volume 1. New York, Hemisphere, 1990.

159. Lavernia, E. J., Gutierrez, E. M., Szekely, J., and Grant, N. J.: A mathematical model of the liquid dynamic compaction process. Part 1: Heat flow in gas atomization. International Journal of Rapid Solidification, 4(1-2):89–124, 1988.

160. McMillen, J. H. and Newton, H. E.: A spark shadowgraphic study of body waves in water. Journal of Applied Physics, 17(7):541–555, 1946.

161. Aristoff, J. M. and Bush, J. W. M.: Water entry of small hydrophobic spheres. Journal of Fluid Mechanics, 619:45–78, 2008.

162. McMillen, J. H., Kramer, R. L., and Allmand, D. E.: Impact flash at high speed water entry. Journal of Applied Physics, 22(3):360–361, 1951.

163. McMillen, J. H., Kramer, R. L., and Allmand, D. E.: Shadowgrams of spherical missiles entering water at supersonic speeds. Journal of Applied Physics, 21(12):1341–1342, 1950.

164. Yarin, A. L. and Weiss, D. A.: Impact of drops on solid surfaces: self–similar capillary waves, and splashing as a new type of kinematic discontinuity. Journal of Fluid Mechanics, 283:141–173, 1995.

165. Birkhoff, G. and Roberts, I.: Transient cavities in air–water entry. Navord Rep, 1490, 1951.

166. May, A.: Vertical entry of missiles into water. Journal of Applied Physics, 23(12):1362–1372, 1952.

167. Howison, S. D., Ockendon, J. R., and Wilson, S. K.: Incompressible water–entry problems at small deadrise angles. Journal of Fluid Mechanics, 222:215–230, 1991.

168. Korobkin, A. A. and Pukhnachov, V. V.: Initial stage of water impact. Annual Review of Fluid Mechanics, 20(1):159–185, 1988.

169. Marston, J. O. and Thoroddsen, S. T.: Ejecta evolution during cone impact. Journal of Fluid Mechanics, 752:410–438, 2014.

170. Karger, B., Nüsse, R., Schroeder, G., Wüstenbecker, S., and Brinkmann, B.: Backspatter from experimental close–range shots to the head: I. Macrobackspatter. International Journal of Legal Medicine, 109(2):66–74, 1996.

171. Scheller, B. L. and Bousfield, D. W.: Newtonian drop impact with a solid surface. AIChE Journal, 41(6):1357–1367, 1995.

172. Antonini, C., Amirfazli, A., and Marengo, M.: Drop impact and wettability: From hydrophilic to superhydrophobic surfaces. Physics of Fluids, 24(10):102104, 2012.

173. Rizer, C.: Police Mathematics. Springfield, IL, Charles C. Thomas, 1955.

174. Baldwin, D. P., Zamzow, D. S., Bajic, S. J., and Strawsine, E.: Investigation of impact spatter and the effects of controlled independent variables. In International Association of Bloodstain Pattern Analysts Training Conference, 2013.

175. Yarin, A. L., Roisman, I. V., Weber, K., and Hohler, V.: Model for ballistic fragmentation and behind-armor debris. International Journal of Impact Engineering, 24(2):171–201, 2000.

176. Milne-Thomson, L. M.: Theoretical Hydrodynamics. New York, Dover, fifth edition, 2017.

177. Kornfeld, M.: Elasticity and Strength of Liquids. Moscow, GITTL, 1951.

178. Kolsky, H. and Rader, D.: Fracture, volume 1, chapter Stress waves and fracture. New York, Academic, 1969.

179. Cherepanov, G.: Mechanics of Brittle Fracture. New York, McGraw–Hill, 1979.

180. Dukhovskiœ, I. A., Kovalev, P. I., and Rozhkov, A. N.: Disintegration of polymer liquids at high-speed impact. Polymer Science A, 46(1):43–59, 2004.

181. Staufer, D.: Scaling theory of percolation clusters. Physics Reports, 54(1):1–74, 1979.

182. Staufer, D.: Introduction to Percolation Theory. London, Taylor & Francis, 1985.

183. Hoyt, J. W., Taylor, J. J., and Runge, C. D.: The structure of jets of water and polymer solution in air. Journal of Fluid Mechanics, 63(4):635–640, 1974.

184. Farhat, M., Tinguely, M., and Rouvinez, M.: Cavitation induced by high speed impact of a solid surface on a liquid jet. In American Physical Society Division of Fluid Dynamics Conference, 2009.

185. Bradley, E. L. and Sacerio, J.: The velocity of ultrasound in human blood under varying physiologic parameters. Journal of Surgical Research, 12(4):290–297, 1972.

186. Roisman, I. V., Yarin, A. L., and Rubin, M. B.: Oblique penetration of a rigid projectile into an elastic–plastic target. International Journal of Impact Engineering, 19(9-10):769–795, 1997.

187. Arfken, G. B., Weber, H. J., and Harris, F. E.: Mathematical Methods for Physicists. Cambridge MA, Academic Press, seventh edition, 2013.

188. Polyanin, A. D. and Manzhirov, A. V.: Handbook of Integral Equations. Boca Raton, FL, Chapman and Hall CRC, second edition, 2008.

189. Astarita, G. and Marrucci, G.: Principles of Non–Newtonian Fluid Mechanics. New York, McGraw–Hill, 1974.

190. Rosenberg, Z. and Dekel, E.: Terminal Ballistics. Berlin, Springer, 2012.

191. of Technology, M. I.: The Edgerton Digital Collections Project, April 2018. `https://www.edgerton-digital-collections.org`.

192. Eggers, J., Fontelos, M. A., Josserand, C., and Zaleski, S.: Drop dynamics after impact on a solid wall: Theory and simulations. Physics of Fluids, 22(6):062101, 2010.

193. Lagubeau, G., Fontelos, M. A., Josserand, C., Maurel, A., Pagneux, V., and Petitjeans, P.: Spreading dynamics of drop impacts. Journal of Fluid Mechanics, 713:50–60, 2012.

194. Sahu, R. P., Sett, S., Yarin, A. L., and Pourdeyhimi, B.: Impact of aqueous suspension drops onto non–wettable porous membranes: Hydrodynamic focusing and penetration of nanoparticles. Colloids and Surfaces A: Physicochemical and Engineering Aspects, 467:31–45, 2015.

195. Kim, S., Ma, Y., Agrawal, P., and Attinger, D.: How important is it to consider target properties and hematocrit in bloodstain pattern analysis? Forensic Science International, 266:178–184, 2016.

196. Adam, C. D.: Experimental and theoretical studies of the spreading of bloodstains on painted surfaces. Forensic Science International, 229(1-3):66–74, 2013.

197. Adhikari, B., Howes, T., Shrestha, A., and Bhandari, B. R.: Effect of surface tension and viscosity on the surface stickiness of carbohydrate and protein solutions. Journal of Food Engineering, 79(4):1136–1143, 2007.

198. Rosina, J., Kvasnák, E., Suta, D., Kolárová, H., Málek, J., and Krajcu, L.: Temperature dependence of blood surface tension. Physiological Research, 56(1):S93–S98, 2007.

199. Alekseenko, S. V., Kuibin, P. A., and Okulov, V. L.: Theory of Concentrated Vortices: An Introduction. Heidelberg, Springer, 2007.

200. Lugovtsov, B. A.: Turbulent vortex rings. Institute of Hydrodynamics Siberian Branch USSR Academy of Sciences, 1974. Ph.D. Thesis.

201. Tikhonov, A. N. and Samarskii, A. A.: Equations of Mathematical Physics. Dover, 1990. New York.

202. Pauling, L. and Wilson, E. B.: Introduction to Quantum Mechanics. McGraw–Hill, 1935. New York.

203. Sullivan, J. P., Widnall, S. E., and Ezekiel, S.: Study of vortex rings using a laser Doppler velocimeter. AIAA Journal, 11(10):1384–1389, 1973.

204. Davis, T. L.: The Chemisty of Powder and Explosives, volume 1. New York, Wiley, 1941.

205. Merson, R. H.: An operational method for the study of integration processes. In Proc. Symp. Data Processing, pages 1–25, Salisbury, Australia, 1957. Weapons Research Establishment.

206. Lambert, J. D.: Computational Methods in Ordinary Differential Equations. London, John Wiley & Sons, 1973.

CURRICULUM VITAE

Patrick M. Comiskey

PhD Candidate

EDUCATION

Doctor of Philosophy Expected Feb. 2019
Mechanical Engineering
University of Illinois at Chicago
Dissertation Title: "Fluid Mechanics of Blood Motion Resulting from Common Bloodletting Events"
Advisor: Dist. Prof. Alexander L. Yarin

Bachelor of Science May 2014
Mechanical Engineering
Milwaukee School of Engineering

RESEARCH EXPERIENCE

Research Assistant Aug. 2014 - Present
Department of Mechanical and Industrial Engineering
University of Illinois at Chicago

- Collaborate and coordinate with faculty, staff scientists, and fellow graduate students across departments
- Contribute to multi-disciplinary projects based on fluid mechanics, solid mechanics, and heat transfer
- Design experiments to obtain fundamental knowledge of various physical phenomena
- Develop mathematical models to theoretically predict and further understand physical phenomena

TECHNICAL SKILLS

- **Design/Analysis Software:** SolidWorks, SolidEdge, Creo, ANSYS, ImageJ
- **Computer Languages:** Fortran, MATLAB, C++, Simulink, LabVIEW, Mathematica
- **Laboratory Equipment:** Rotational Viscometer, Capillary Viscometer, Extensional Rheometer, High-Speed Photography, Spectrofluorometer, Flow Visualization, Wind Tunnel, Engine Dynamometer, Electrical Equipment
- **Other:** Microsoft Office Suite, Windows OS, Mac OS, Linux OS, LaTeX

INDUSTRY EXPERIENCE

Design Engineer Intern Summer 2013, 2014
Apex Tool Works, Inc.
Rolling Meadows, IL

- Worked closely in a professional environment with a design engineer
- Designed parts for complex machinery
- Heavily utilized CAD software and other design tools

Engineering Intern Summer 2012
Wisconsin Space Grant Consortium
Milwaukee, WI

- Designed and built a high altitude balloon
- Devised scientific experiments carried to over 90,000 feet
- Budgeted and adhered to strict program schedule

TEACHING EXPERIENCE

Teaching Assistant, Introduction to Heat Transfer Fall 2018
Department of Mechanical and Industrial Engineering
University of Illinois at Chicago

- Held open office hours to answer any questions about the coursework
- Graded homework assignments and examinations

Teaching Assistant, Experimental Methods in Engineering Spring 2018
Department of Mechanical and Industrial Engineering
University of Illinois at Chicago

- Taught laboratory section of a class which goes in depth into properly applying the scientific method to design and perform experiments
- Instructed proper report and workbook guidelines
- Graded writing assignments and laboratory reports

Teaching Assistant, Fluid Mechanics Spring 2015, 2016
Department of Mechanical and Industrial Engineering
University of Illinois at Chicago

- Taught laboratory section of introductory fluid mechanics course
- Conducted recitation sessions to reinforce concepts and answer any questions
- Graded all homework assignments, laboratory reports, and exams

PUBLICATIONS

P.M. Comiskey, and A.L. Yarin, "Self-similar turbulent vortex rings: Interaction of propellant gases with blood backspatter and the transport of gunshot residue", *J. Fluid Mech.*, Submitted Jan. 2019.

P.M. Comiskey, A.L. Yarin, and D. Attinger, "Implications of two backward blood spatter models based on fluid dynamics for bloodstain pattern analysis", *Forensic Sci. Int.*, Submitted Sep. 2018.

D. Attinger, **P.M. Comiskey**, A.L. Yarin, and K. De Brabanter, "Determining the region of origin of blood spatters considering fluid dynamics and statistical uncertainties", *Forensic Sci. Int.*, Submitted Sep. 2018.

P.M. Comiskey, A.L. Yarin, and D. Attinger, "Forward spattering of blood from a gunshot by a bullet of an arbitrary shape", *Phys. Rev. Fluids*, Submitted Aug. 2018.

D. Attinger, Y. Liu, R. Faflak, Y. Rao, B.A. Struttman, K. De Brabanter, **P.M. Comiskey**, and A.L. Yarin, "A data set of bloodstain patterns for teaching and research in bloodstain pattern analysis: Gunshot backspatters", *Data in Brief*, 22, 269-278, 2019.

P.M. Comiskey, A.L. Yarin, and D. Attinger, "Atomization of blood spatter resulting from a gunshot", *ICLASS 2018 14th Triennial International Conference on Liquid Atomization and Spray System Proceedings*, 2018.

P.M. Comiskey, A.L. Yarin, and D. Attinger, "Theoretical and experimental investigation of forward spatter of blood from a gunshot", *Phys. Rev. Fluids*, 3(6), 063901, 2018.

P.M. Comiskey, and A.L. Yarin, "Friction coefficient of an intact free liquid jet moving in air", *Exp. Fluids*, 59, 65, 2018.

P.M. Comiskey, A.L. Yarin, and D. Attinger, "High-speed video analysis of forward and backward spattered blood droplets", *Forensic Sci. Int.*, 276, 134-141, 2017.

P.M. Comiskey, A.L. Yarin, and D. Attinger, "Hydrodynamics of back spatter by a blunt bullet gunshot with a link to bloodstain pattern analysis", *Phys. Rev. Fluids*, 2(7), 073906, 2017.

P.M. Comiskey, A.L. Yarin, S. Kim, and D. Attinger, "Prediction of blood back spatter from a gunshot in bloodstain pattern analysis", *Phys. Rev. Fluids*, 1(4), 043201, 2016.

A. Kolbasov, **P.M. Comiskey**, R.P. Sahu, S. Sinha-Ray, A.L. Yarin, B.S. Sikarwar, S. Kim, T.Z. Jubery, and D. Attinger, "Blood rheology in shear and uniaxial elongation", *Rheol. Acta*, 55(11), 901-908, 2016.

CONFERENCE PRESENTATIONS

P.M. Comiskey, A.L. Yarin, and D. Attinger, "Theoretical and experimental investigation of forward spatter of blood from a gunshot", *American Physical Society Division of Fluid Dynamics*, Atlanta, Georgia, Nov. 18-20, 2018.

P.M. Comiskey, "Applied fluid mechanics of the atomization of a blood spatter spray", *Korea University and University of Illinois at Chicago International Workshop*, Chicago, Illinois, Jul. 24, 2018.

P.M. Comiskey, A.L. Yarin, and D. Attinger, "Atomization of blood spatter resulting from a gunshot", *International Conference on Liquid Atomization & Spray Systems*, Chicago, Illinois, Jul. 22-26, 2018.

P.M. Comiskey, A.L. Yarin, and D. Attinger, "Investigation of blood spatter resulting from a gunshot", *Pittcon*, Orlando, Florida, Feb. 26-Mar. 1, 2018.

P.M. Comiskey, A.L. Yarin, and D. Attinger, "High-speed video analysis of forward and backward spattered blood droplets", *American Physical Society Division of Fluid Dynamics*, Denver, Colorado, Nov. 19-21, 2017.

P.M. Comiskey, "Blood spatter patterns due to a blunt gunshot", *Korea University and University of Illinois at Chicago International Workshop*, Chicago, Illinois, Apr. 20, 2017.

P.M. Comiskey, A.L. Yarin, S. Kim, and D. Attinger, "Blood back spatter caused by a blunt bullet gunshot", *American Physical Society March Meeting*, New Orleans, Louisiana, Mar. 13-17, 2017.

P.M. Comiskey, A.L. Yarin, S. Kim, and D. Attinger, "Predictions and measurements of blood backspatter from a gunshot in bloodstain pattern analysis", *American Physical Society Division of Fluid Dynamics*, Portland, Oregon, Nov. 20-22, 2016.

P.M. Comiskey, "Theoretical prediction of blood spatter patterns II", *Korea University and University of Illinois at Chicago International Workshop*, Chicago, Illinois, Apr. 21, 2016.

P.M. Comiskey, "Theoretical prediction of blood spatter patterns", *Korea University and University of Illinois at Chicago International Workshop*, Chicago, Illinois, Apr. 17, 2015.

HONORS AND AWARDS

Chancellor's Student Service Award Mar. 2018
University of Illinois at Chicago
- For students who have made an outstanding contribution to the University through service to the campus and community

Graduate College Student Presenters Award Feb. 2018
University of Illinois at Chicago

Graduate Student Council Travel Award Feb. 2018
University of Illinois at Chicago

Faydor Litvin Graduate Honor Award Nov. 2017
University of Illinois at Chicago
- For exceptional academic achievement and service to the Mechanical and Industrial Engineering department and graduate student community

Honors List 2013 - 2014
Milwaukee School of Engineering

Academic Scholarship 2010 - 2013
Milwaukee School of Engineering

UNIVERSITY SERVICE/PROJECTS

Mechanical and Industrial Engineering Graduate Association 2016 - 2018
University of Illinois at Chicago
President, Vice President
- Managed and ran the graduate student organization for the Mechanical and Industrial Engineering department
- Planned graduate student events with the intent of fostering a sense of community between the students
- Facilitated departmental projects such as the creation of a graduate student lounge and periodic graduate student research presentations

Graduate Student Council 2016 - 2018
University of Illinois at Chicago
Department Representative
- Represented the graduate student body of the Mechanical and Industrial Engineering department to all other graduate associations within the university
- Disseminated information to faculty and students within the department
- Voted on various problems or proposals pertaining to the university as a whole

Stirling Engine Microgrid Generator 2013 - 2014
Milwaukee School of Engineering
Senior Design Project
- Designed and optimized a Stirling engine to be used as a generator
- Studied the dynamics and machine design of the engine as well as the thermodynamic requirements
- Worked on a team of four adhering to a self-imposed timeline, budget, and various design restrictions

Society of Automotive Engineers 2010 - 2014
Milwaukee School of Engineering
Vice President, Treasurer
- Oversaw planning of events and coordinated information between four design teams
- Managed the organization's funding including bi-weekly meetings, several design teams, school promotions, and international meet-ups

SuperMileage Design Team 2010 - 2013
Milwaukee School of Engineering
Sponsorship Manager, Engine Team Leader
- Kept track of sponsors for the team and properly acquired funding from outside donations
- Lead the development for designing and machining improvements on the engine for a student designed and built car with the intent of achieving the most fuel efficient vehicle possible